

FORMATION OF LIGHT NUCLEI AND HYPERNUCLEI
IN RELATIVISTIC HEAVY-ION COLLISIONS



APIWIT KITTIRATPATTANA

A Thesis Submitted in Partial Fulfillment of the Requirements for the
Degree of Doctor of Philosophy in Physics
Suranaree University of Technology
Academic Year 2024

การผลิตอนุภาคนิวเคลียสเบาและไฮเปอร์นิวเคลียส
จากการชนกันของไอออนหนักเชิงสัมพัทธภาพ



นายอภิวิชญ์ กิตติรัตน์พัฒนา

วิทยานิพนธ์นี้เป็นส่วนหนึ่งของการศึกษาตามหลักสูตรปริญญาวิทยาศาสตรดุษฎีบัณฑิต
สาขาวิชาฟิสิกส์
มหาวิทยาลัยเทคโนโลยีสุรนารี
ปีการศึกษา 2567

FORMATION OF LIGHT NUCLEI AND HYPERNUCLEI
IN RELATIVISTIC HEAVY-ION COLLISIONS

Suranaree University of Technology has approved this thesis submitted in partial fulfillment of the requirements for the Degree of Doctor of Philosophy.

Thesis Examining Committee

B. Ce

(Prof. Dr. Christoph Blume)

Chairperson

C. Herold

(Assoc. Prof. Dr. Christoph Herold)

Member (Thesis Advisor)

M. Bleicher

(Prof. Dr. Marcus Bleicher)

Member (Thesis Co-Advisor)

A. Limphirat

(Assoc. Prof. Dr. Ayut Limphirat)

Member (Thesis Co-Advisor)

Yupeng Yan

(Prof. Dr. Yupeng Yan)

Member

H. Podlech

(Prof. Dr. Holger Podlech)

Member

K. Khosonthongkee

(Asst. Prof. Dr. Khanchai Khosonthongkee)

Member

Yupaporn Ruksakulpiwat

(Assoc. Prof. Dr. Yupaporn Ruksakulpiwat)

Vice Rector for Academic Affairs
and Quality Assurance

S. Maensiri

(Prof. Dr. Santi Maensiri)

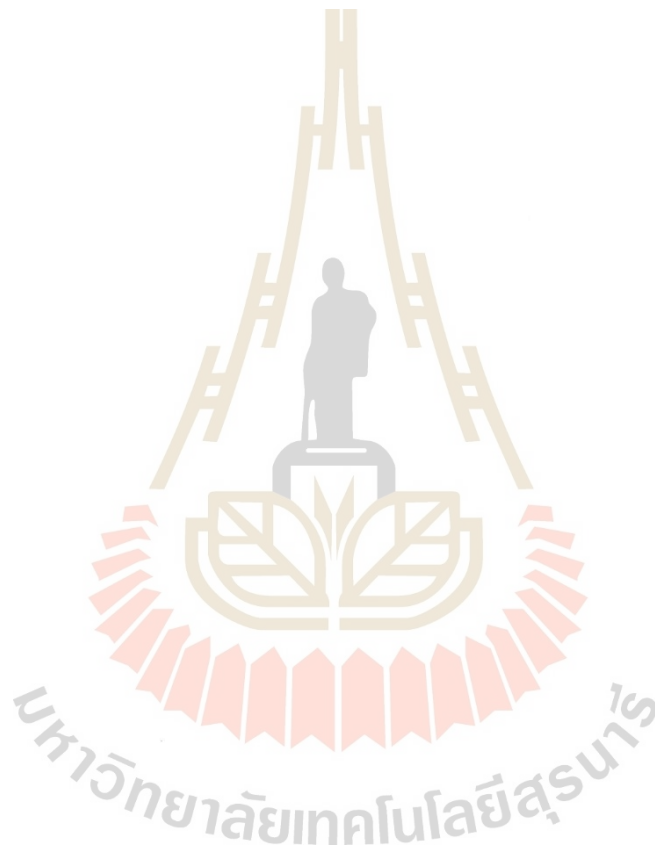
Dean of Institute of Science

อภิวิชัย กิตติรัตน์พัฒนา : การผลิตอนุภาคนิวเคลียสเบาและไฮเปอร์นิวเคลียสจากการชนกันของไอออนหนักเชิงสัมพันธภาพ (FORMATION OF LIGHT NUCLEI AND HYPERNUCLEI IN RELATIVISTIC HEAVY-ION COLLISIONS) อาจารย์ที่ปรึกษา : รองศาสตราจารย์ ดร.คริสทอฟ เฮโรลด์, อาจารย์ที่ปรึกษาร่วม : ศาสตราจารย์ ดร.มาคุส ไบลเซอร์, อาจารย์ที่ปรึกษาร่วม : รองศาสตราจารย์ ดร.อายุท ลิมพิรัตน์, 170 หน้า.

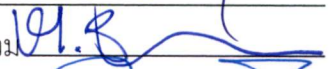
คำสำคัญ: การชนกันของไอออนหนัก/ การไหล/ การผลิตคริสเตอร์/ พลศาสตร์โมเลกุลควอนตัมเชิงสัมพันธภาพ

วิทยานิพนธ์นี้มุ่งเน้นไปที่การทำความเข้าใจพฤติกรรมร่วมกันระหว่างกาลอวกาศของการชนกันของไอออนหนักและ(ไฮเปอร์)นิวเคลียสรวมทั้งปัจจัยต่าง ๆ ที่ส่งผลกระทบต่อการศึกษาสมการสถานะ (EoS) ของสสารที่ช่วงพลังงานต่ำของโปรแกรมการสแกนด้วยพลังงาน BES รวมถึงสถาบัน FAIR และ HADES โดยใช้แบบจำลองการชน UrQMD เวอร์ชัน 3.5 เราทำการปรับปรุงแบบจำลองการรวมตัวเชิงเรขาคณิตเชิงพื้นที่ของ(แอนติ)นิวเคลียสและรัศมีแหล่งกำเนิด(แอนติ)นิวคลีออน ผลการวิจัยที่ได้จากการติดตั้งกับค่าพารามิเตอร์ของการรวมตัวจากการทดลอง B_2 และ \overline{B}_2 แสดงค่าสูงสุดของรัศมีหรือปริมาตรของไฟร์บอลที่อาจบ่งชี้ว่าเป็นพฤติกรรมวิกฤตได้ ณ พลังงานการชน $\sqrt{s_{NN}} = 27$ GeV ซึ่งรัศมีของไฟร์บอลที่ได้จากการศึกษามีนิยามสมมูลกับปริมาตรของ HBT ดังนั้นผลกระทบของการเปลี่ยนสถานะของสสารต่อรัศมี HBT จากสมการสถานะ (EoS) ต่าง ๆ ได้แก่ การชนแบบบิสระ (cascade) การชนกันภายใต้สมการสถานะแบบแข็ง (hard EoS), สมการสถานะอย่างอ่อน (soft EoS) และสมการสถานะแบบสนามเฉลี่ยไครัล (chiral mean field EoS) จึงถูกศึกษาโดยใช้การแทรกสอด HBT ของสองไพออน สมการสถานะของสนามเฉลี่ยไครัลที่มีการเปลี่ยนวิภูภาคได้ (CMF_PT2) แสดงพฤติกรรมวิกฤตทั้งในค่าของ R_0/R_5 และ $R_0^2 - R_5^2$ รวมถึงการยืดออกของฟังก์ชันการกระจายตัวของเวลาของไพออน ซึ่งสอดคล้องกับข้อมูลทดลองได้ดีกว่าสมการสถานะอื่น ๆ ความหนาแน่นของสสารนิวเคลียร์ (ρ_B) ถูกคาดการณ์ว่าอยู่ในช่วงประมาณ 2-3 เท่าของความหนาแน่นอิมิตัว (ρ_0) ณ ช่วงพลังงาน $\sqrt{s_{NN}} \approx 4$ เพื่อให้เกิดการเปลี่ยนสถานะดังกล่าวและไม่เกินความหนาแน่นของการเปลี่ยนแปลงวิภูภาคของ (CMF_PT3) ทำให้ทราบว่าความหนาแน่นที่จะสามารถสร้างได้ ณ ช่วงพลังงานนี้น้อยกว่า 4-5 เท่าของความหนาแน่นอิมิตัวนิวเคลียร์ นอกจากนี้เราเสนอให้ปรับปรุงการคำนวณและวัดค่าพารามิเตอร์การรวมตัว (B_A) สำหรับพลังงานต่ำโดยใช้สูตรที่พิจารณาจากกาลอวกาศของการชนและสมมูลของไอโซสปินเพื่อการคำนวณปริมาณนิวคลีออนทั้งหมดนับตั้งแต่ช่วงแรกของการชน ความสัมพันธ์กับพลังงานการชนกันของค่าพารามิเตอร์การรวมตัว (B_A) ที่ปรับปรุงแล้วที่พลังงานต่ำสอดคล้องกับค่าที่ทำนายจาก HBT ดังที่คาดไว้ เพื่อเป็นการยืนยันว่ากลไกการก่อตัวของคริสเตอร์เป็นกลไกที่เกิดขึ้นจริงมากกว่ากลไกเชิงอุณหพลศาสตร์ เราทำการวิเคราะห์เชิงกาลอวกาศของกลไกการผลิตคริสเตอร์โดยเสนอให้ใช้พลศาสตร์ของไอโซสปิน ($\Delta Y = (Y_{\pi^-} - Y_{\pi^+})$) เป็นตัวชี้วัด ค่าจุดสูงสุดที่สังเกตได้จาก d, t และ ^3He เมื่อเทียบ

กับ ΔY ของ UrQMD สอดคล้องกับการประมาณจากทฤษฎีตามสมมุติฐาน ซึ่งเป็นตัวบ่งชี้สนับสนุนว่ากลไกการรวมตัวเป็นกลไกที่ถูกต้อง สุดท้ายเราแสดงศักยภาพของการใช้ปฏิกิริยาที่เหนี่ยวนำด้วยโพออนในการทดลอง HADES ที่พลังงานต่ำและระบบขนาดเล็กสำหรับการศึกษาก่อตัวของ(ไฮเปอร์)นิวเคลียส ผลลัพธ์จากแบบจำลองการรวมตัวและแบบจำลองการแตกออกเชิงสถิติ (SMM) ชี้ให้เห็นว่าปริมาณผลผลิตของ(ไฮเปอร์)นิวเคลียสมีค่าใกล้เคียงกับแหล่งทดลองพลังงานสูง นอกจากนี้เมื่อเปรียบเทียบความสัมพันธ์ของขนาดของระบบกับอัตราส่วนของ ${}^3\text{H}/\Lambda$ จากปฏิกิริยา $\pi^- + \text{C}$ และ $\pi^- + \text{W}$ แสดงการลดทอนอย่างรุนแรงเมื่อขนาดของระบบเล็กลงซึ่งสอดคล้องและสนับสนุนการทำนายจากแบบจำลองการเชื่อมติดและหักล้างค่าทำนายของแบบจำลองเชิงอุณหพลศาสตร์



สาขาวิชาฟิสิกส์
ปีการศึกษา 2567

ลายมือชื่อนักศึกษา 
 ลายมือชื่ออาจารย์ที่ปรึกษา 
 ลายมือชื่ออาจารย์ที่ปรึกษาร่วม 
 ลายมือชื่ออาจารย์ที่ปรึกษาร่วม 

APIWIT KITTIRATPATTANA : FORMATION OF LIGHT NUCLEI AND HYPERNUCLEI IN RELATIVISTIC HEAVY-ION COLLISIONS. THESIS ADVISOR : ASSOC. PROF. CHRISTOPH HEROLD, THESIS CO-ADVISOR : PROF. MARCUS BLEICHER, THESIS CO-ADVISOR : ASSOC. PROF. AYUT LIMPHIRAT, Ph.D. 170 PP.

Keyword: Heavy-ion collision/ Collective flow/ Cluster formation/ Relativistic quantum molecular dynamics

The space-time picture of the fireball geometry and (hyper)nuclei formation in heavy-ion collisions is explored, considering various factors crucial for EoS studies at lower energies, specifically around FAIR and HADES energies, by utilizing the UrQMD v3.5 transport model. The spatial geometric coalescence model to study (anti)deuteron formation is improved and used to extract the (anti)nucleon source radii by fitting the (anti)deuteron formation rate with the available coalescence parameter data $B_2(\overline{B}_2)$. The findings suggest potential critical behavior on the emission source at $\sqrt{s_{NN}} = 27$ GeV. The antinucleon distributions from UrQMD support the presence of an annihilation region at the core of the emission source for all energies. The effects of a phase transition from cascade, hard, soft and chiral mean field EoS on the emission source are investigated by two-pion HBT interferometry. The chiral mean field with a phase transition (CMF_PT2) EoS exhibits critical behavior in R_O/R_S and $R_O^2 - R_S^2$ as well as a prolongation of the freeze-out time distribution of π^- from UrQMD simulations, showing good agreement with the experimental data. The analyses from both $R_O - R_S$ and the time distribution indicate that only the phase transition from the CMF_PT2 occurs, while the phase transition from the CMF_PT3 is never reached. Thus, according to their density-dependent nature, we conclude that the nuclear density ρ_B is around 2 — 3 times the saturation density ρ_0 at $\sqrt{s_{NN}} \approx 4$ GeV. We further propose corrections to the measurement of the coalescence parameter B_A for lower energies with the proper formula for estimating primordial protons and neutrons based on the isospin equilibration in the system. As expected, the collision energy dependence of the corrected B_A at low energies aligns well with HBT predictions. Cluster formation mechanisms are analyzed utilizing the different space-time pictures. The isospin triggering is proposed to solve the tension between the thermal emission at the chemical freeze-out and the coalescence at kinetic freeze-out. A dependence on $\Delta Y = Y_{\pi^-} - Y_{\pi^+}$ is expected if the clusters are formed by coalescence. The observed maxima of d, t, and ^3He with respect to ΔY from the UrQMD box coalescence model agree with our theoretical assumptions and provide an experimental method to distinguish coalescence

from thermal production. Lastly, The potential usage of pion-induced reactions at the HADES experiment for low energies and smaller system sizes for (hyper)nuclei formation studies is demonstrated. The UrQMD box coalescence model and the Statistical Multifragmentation Model (SMM) results show that (hyper)nuclei abundances are comparable to those at high-energy facilities. Additionally, the system size-dependence of ${}^3\Lambda\text{H}/\Lambda$ from $\pi^- + \text{C}$ and $\pi^- + \text{W}$ shows strong suppression at smaller system sizes, thus further supporting the coalescence model for hypernuclei production.



School of Physics
Academic Year 2024

Student's Signature

Advisor's Signature

Co-Advisor's Signature

Co-Advisor's Signature

ACKNOWLEDGEMENTS

This journey of my student life has been filled with rich memories and precious lessons. It taught me the meaning of hardship and perseverance, the need to balance life and rest. This thesis represents not only a proud milestone in my academic achievements but also a reminder to remain humble and prepare for the even longer voyage of life. Within this interlude of self-reflection, I wish to express my deepest gratitude to those who have illuminated and supported me all along the path.

First of all, I would like to express my sincere gratitude to Prof. Dr. Marcus Bleicher who has been an extraordinary figure in my academic life. During my time in Germany, You have been my kind academic guardian, reliable mentor, respectful professor, boss, and friend-much like a big tree holding my sky. I am grateful to all the opportunities you gave me to experience a bigger world either by my first hand experiences or all of your enriching stories. In addition to all the fun, You gave me discipline and guided me how to become a proper physicist. I remember the praises you gave, which I often felt unworthy of, but I aim to live up to your expectations. Despite the fact that I am still trying to answer email faster. Cheers.

As I reflect on every step up to this milestone, I have been and always under guidance and supervision of Assoc. Prof. Dr. Christoph Herold mentorship. I am happy and thankful for my choice in following your steps since my clueless bachelor years, a decision that has greatly shaping my path. You have provided me life-changing opportunities along with the supports to realize them. I am grateful for your teaching which has made me grow noticeably.

The starting point of this thesis has to be credited to my teacher at SUT, Assoc. Prof. Dr. Ayut Limphirat. I would never know and thank you enough on how much efforts you have put into realizing this special Cotutelle PhD program. I am grateful to your advice on both research and life. The introduction of me to Wanna and Götting family was a smaller gesture for you but it was really a big step that provided me friendships and a perfect environment to properly focus on this research.

Now I would like to devote a paragraph to my good friend Dr. Tom Reichert. My PhD life would not have been as progressive and complete without your inductive ambitious for your extraordinary PhD record. You have greatly help me get through this

endeavor. I appreciated all the drinks, struggles, and joys we shared as we traveled the world and grow together during our academic journey. I wish you a successful academic career, and as you, Amine, and I have said, “nothing could go wrong with us”.

Another name I have to mention and express my thanks to is Dr. Jan Steinhilber. You have always been my respectable mentor and the role model for what I imagine a proper researcher has to be. All of my physics questions seem to be solvable by you. I deeply appreciated your supports not only now but since the last 5 years when I first came to Germany. I remember all valuable discussions and advice you gave me as well as a good discussion about a fate of your chickens.

Special thanks to all wonderful friends in Germany, Amine Chabane, Dr. Gabriele Cocci, Jan Fotakis, Dr. Olga Soloveva, and Lisa, who never forgot to invite me to a party or have lunch together. We have had lunch and coffee breaks almost every day for those two years in Germany. My days at the University has been this lively was because of you guys.

I also have to extend my thanks to all good friends of mine from/in Thailand. Sometimes it could be hard to withstand the cold night in a new environment. Their support made me through this challenge. We stayed connected through daily calls, and they were always there to drink, share experiences and even help me with the cooking together.

Gratitude fills my heart as I thought of Götting family. They gave me a warm shelter, a place to call home with abundance food especially Thai food in Germany. I had a comfortable life there and could not be better without their hospitality.

I could not leave this page without mentioning our teachers and secretaries from both universities. At the School of Physics at SUT, I would like to express my courtesy to Aj. Yupeng, P' Yip, P' Noei, P' Jang, and AomAmm for all their support. At GU, my special thanks go to Birgit Rieger. Finally, I am deeply grateful for the support from DPST scholarship, Thailand Fundamental Funds, DAAD scholarship, FIAS peoples, and the supports from HGS-HIRe for FAIR.

Apiwit Kittiratpattana

CONTENTS

	Page
ABSTRACT IN THAI	I
ABSTRACT IN ENGLISH	III
ACKNOWLEDGEMENTS	V
CONTENTS	VII
LIST OF TABLES	X
LIST OF FIGURES	XI
LIST OF ABBREVIATIONS	XXII
CHAPTER	
I INTRODUCTION	1
II PROSPECTS OF HEAVY-ION COLLISIONS	6
2.1 Exploring the QCD Phase Diagram	6
2.1.1 The Development of Models and Equation of State	6
2.1.2 Beam Energy Scan and Low Energy Regime	13
2.2 Space-Time Evolution	15
III MODELLING HEAVY-ION COLLISIONS	18
3.1 Transport models	19
3.2 Boltzmann(Vlasov)-Uehling-Uhlenbeck (B(V)UU) approach	19
3.3 Ultra-relativistic Quantum Molecular Dynamics (UrQMD) model	24
3.3.1 Initialization	24
3.3.2 Propagation and Collision	26
3.3.3 (Hyper)nuclei Formation Routine	29
3.4 Hydrodynamics Models	30
3.5 Hybrid Models	32
IV EXPLORING THE SPACE-TIME STRUCTURE OF THE FIREBALL	36
4.1 (Anti)deuteron formation rate and source geometry	37
4.1.1 Mrówczyński Density Function	38
4.2 Energy Dependence of Formation Geometry	40
4.3 Validation with UrQMD	43
4.4 HBT Correlation	47

CONTENTS (Continued)

		Page
	4.4.1 Two-Particle Correlations	48
	4.5 Simulation set-ups and EoS	52
	4.6 Two-Pion HBT Analysis	54
	4.7 Effect of the EoS with Phase Transition	57
	4.8 Space-time Structure from HBT radii	58
V	REVIEWS ON (HYPER) (LIGHT) NUCLEI	64
	5.1 Role of (Hyper)Nuclei Formation	64
	5.1.1 Hypernuclei	68
	5.2 Cluster Formation Mechanisms	69
	5.2.1 Thermal productions	69
	5.2.2 Coalescence Model	72
	Simple Momentum Coalescence	73
	Analytic Coalescence Models	76
	Wigner's Function	78
	5.2.3 Dynamical Model	79
	5.2.4 Multifragmentation	82
VI	CORRECTING B_A COALESCENCE FACTOR	85
	6.1 Problems with B_A	86
	6.2 Reconstructing Primordial Protons and Neutrons	87
	6.2.1 Rapidity Distribution	87
	6.2.2 p_T Distribution	90
	6.2.3 Estimating B_2 and B_3	93
VII	INVESTIGATING CLUSTER PRODUCTION MECHANISMS	99
	7.1 Thermal vs Coalescence	99
	7.2 Isospin triggering	100
	7.2.1 Simple estimates	101
	7.3 Qualitative Estimates	103
	7.3.1 Freeze-out time distributions	104
	7.4 Light cluster yields versus isospin fluctuation	105

CONTENTS (Continued)

	Page
VIII RESULTS IN PION INDUCED REACTIONS	109
8.1 The needs and potential of small collision systems	109
8.2 Model Setup	112
8.3 Proton and Λ Baryon Production	113
8.4 (Light) Nuclei distributions	118
8.5 (Hyper) Nuclei distribution	123
8.6 Fragments of larger mass numbers	125
IX SUMMARY	130
REFERENCES	134
CURRICULUM VITAE	170

LIST OF TABLES

Table		Page
3.1	Table of Baryons.	28
3.2	Table of Mesons.	28
3.3	The numerical coalescence parameters of UrQMD v3.5.	30
6.1	The B_2 values calculated final state protons and both primordial protons and neutrons at $p_T/A = 0.0$ GeV at midrapidity $ y \leq 0.5$. The calculation is extracted from 0 — 10% central Au+Au collisions at kinetic beam energies from $E_{\text{beam}} = 0.3A$ to 40A GeV.	96
6.2	The B_3 values calculated final state protons and both primordial protons and neutrons at $p_T/A = 0.0$ GeV at midrapidity $ y \leq 0.5$. The calculation is extracted from 0 — 10% central Au+Au collisions at kinetic beam energies from $E_{\text{beam}} = 0.3A$ to 40A GeV.	96



LIST OF FIGURES

Figure		Page
2.1	The compilation of the predicted location of the QCD critical point from various models, mainly chiral models and lattice QCD (Stephanov, 2006). Black points represent chiral model predictions. Green points indicate lattice predictions. The two dashed lines are the slopes corresponding to $dT/d\mu_B^2$ of the transition line at $\mu_B = 0$. The red circles denote the freeze-out points for heavy ion collisions at corresponding center-of-mass energies in GeV per nucleon.	12
2.2	QCD diagram with BES program and various facilities (Collaboration, 2014).	14
2.3	Space-Time Evolution (Braun-Munzinger and Dönigus, 2019). . .	16
4.1	The schematic picture of the geometric coalescence model for (anti)deuteron formation if the two (anti)nucleons are close enough in phase-space. A_p and A_T are the incoming projectile and target nucleons and X represents the particles that carry the rest momenta of the system. (Left) The nucleon emission source is a whole spherical with radius r_0 . (Right) the survived antinucleons are emitted only on a spherical shell radius r_0 as the NN annihilations destroy most of the antinucleon at the center radius r_*	38
4.2	The antideuteron formation according to the source bulk radius r_0 with varying suppression radii r_*	41
4.3	The energy dependence coalescence parameters B_2 for deuterons (left) and \bar{B}_2 antideuterons (right) from various experiments ranging from $\sqrt{s_{NN}} = 4.7 - 200$ GeV. The black lines show the B_2 and \bar{B}_2 fits using the extracted radii r_0 and r_* according to the formation rate in Eq. (4.7)	41
4.4	The emission source radius r_0 of deuteron (solid black lines) and the suppression region of antideuteron source r_* (dash-dotted line) as a function of energy	42

LIST OF FIGURES (Continued)

Figure		Page
4.5	The normalised (anti)nucleon distribution in transverse plane r_T at $\sqrt{s_{NN}} = 11.5$ GeV (left panel) and $\sqrt{s_{NN}} = 200$ GeV (right panel). The black solid line represents the nucleon distribution and antinucleon distribution is depicted with the dotted line.	44
4.6	The energy dependence of the fitted (anti)nucleon source radii is illustrated. The solid circles represent the whole nucleon source radius r_0 . The extracted source radii of antinucleons are depicted with square symbols. The outer source radius of antinucleons r_0 is represented by the full symbols, while the inner source radius of the suppression region r_* is indicated by the open symbols.	45
4.7	The energy dependence of the r_*/r_0 ratio of antinucleon source from Mrówczyński coalescence model (red star symbol) and UrQMD simulation (blue square symbol) at central 0 — 10% Au+Au collisions.	46
4.8	The diagram of particle detection. Particle 1 and particle 2 are emitted, with a four-momentum p_1 and p_2 , at points a and b respectively. Then they are detected by detectors A and B. If the particles are identical, we also need to consider the cases where the particles propagate indistinguishably into the detectors as illustrated with the dashed lines.	48
4.9	The comparison of the density dependent potential V (a) and the pressure p (b) from different the CMF EoS scenarios. CMF_PT2 EoS and CMF_PT3 EoS both are incorporated with a phase transition as well as instability region indicated by local maximum and minimum. The simple CMF EoS corresponds to a smooth crossover transition (Li et al., 2023).	53

LIST OF FIGURES (Continued)

Figure		Page
4.10	<p>Comparison of k_T dependence of pion HBT radii showing the effect of Coulomb interactions. Panels (a), (b), and (c) display the R_0, R_S, and R_L radii, respectively, and panel (d) shows the ratio R_0/R_S of the π-source from central (0 — 10%) Au+Au collisions at $\sqrt{s_{NN}} = 2.4$ GeV. Red star symbols depict the results from the HADES experiments (Adamczewski-Musch et al., 2019). Black dotted lines indicate the UrQMD simulation results without Coulomb potential (w.o. Coul.), blue dashed lines show the UrQMD simulation results with Coulomb potential for baryons only (with Coul. (B)), and pink solid lines depict the UrQMD simulation with the full Coulomb potential for all hadrons (with Coul. (B+M)). . . .</p>	55
4.11	<p>The transverse momentum (k_T) dependence of the HBT radii, R_0 (left panels), R_S (middle panels), and R_L (right panels), for 0 — 10% central Au+Au collisions at $\sqrt{s_{NN}}$ ranging from 2.4 GeV (top panels) to 7.7 GeV (bottom panels). Experimental data are denoted by star symbols from HADES, E895, E866, and STAR collaborations (Lisa et al., 2000; Lisa et al., 2005; Adamczyk et al., 2015; Adamczewski-Musch et al., 2019; Adamczewski-Musch et al., 2020; Adam et al., 2021). The UrQMD simulations are represented by lines: the cascade mode (black line with square), hard EoS (blue line with circle), and soft EoS (pink line).</p>	56

LIST OF FIGURES (Continued)

Figure		Page
4.12	Comparison of the collision energy dependence of the (top panel) R_0/R_S ratio and (bottom panel) $R_0^2 - R_S^2$ for cascade (black line with squares) and various EoS models (hard EoS: blue line with circles, CMF EoS: green line, CMF_PT2 EoS: orange dotted line, CMF_PT3 EoS: pink dashed line) with available experimental data (Lisa et al., 2000; Lisa et al., 2005; Adamczyk et al., 2015; Adamczewski-Musch et al., 2019; Adamczewski-Musch et al., 2020; Adam et al., 2021).	61
4.13	The freeze-out time distribution of π^- from 0 — 10% Au+Au collisions with the different EoS; Cascade mode (solid black line), Hard EoS (solid blue line), CMF EoS (green dashed line), CMF_PT2 EoS (solid orange line), and CMF_PT3 EoS (pink dash-dotted line)	62
4.14	(a) The corresponding mean π^- emission time $\langle t \rangle$ and (b) transverse radii r_T at freeze-out as a function of collision energies calculated from different EoS.	63
5.1	The schematic for a particle production from a thermal model. A projectile A_p and a target nucleus A_T exchange energy and momentum upon collision. All particles X, p and n, are emitted directly from the fireball including the composited particle d. This hadronization occurs at chemical freeze-out. The figure is adopted from Ref. (Kapusta, 1980)	70
5.2	The comparison between thermal predictions and the measured (anti)nuclei production on the energy spectrum. The figure is adopted from Ref. (Dönigus, 2020)	72
5.3	The schematic for a particle production and cluster formation from a colliding projectile nucleus A_p and a target nucleus A_T . In the coalescence model, the free streaming neighbor of p and n pair after flying a certain distance will coalesce and form a deuteron outside of the fireball. The rest of the momentum is represented by X. This coalescence process happens at kinetic freeze-out. The figure is adopted from Ref. (Kapusta, 1980)	73

LIST OF FIGURES (Continued)

Figure		Page
5.4	The invariant cross section of π^- , K^- , \bar{p} and \bar{d} from Si+Al, Si+Cu, and Si+Au collisions. The solid-line represents the \bar{d} 's predicted by coalescence model. The measured \bar{d} and the instrumental upper limit are represented by the square open symbol at 6.1 GeV and down arrow symbols (Aoki et al., 1992).	77
5.5	The Comparison of the tp/d^2 ratio from two cluster formation mechanisms of thermal (dashed line) and simple coalescence model (solid line) with experimental data (symbols).	81
5.6	Different statistical ensembles used for describing the breakup of a nuclear system with partition f (Bondorf et al., 1995; Fai and Randrup, 1983; Gross, 1984).	83
6.1	Coalescence parameter B_A measured by experiments (Braun-Munzinger and Dönigus, 2019) and predicted by HBT (Adamczyk et al., 2015) as a function of center-of-mass energy $\sqrt{s_{NN}}$ [GeV].	86
6.2	Rapidity distribution comparison of protons and light nuclei in 0 – 10% Au+Au collisions at $E_{beam} = 1.23A$ GeV. Simulated primordial protons (red circles), simulated final state protons (red dashed lines), and reconstructed primordial protons (red solid lines) are contrasted alongside the rapidity distributions of deuterons (green diamonds), tritons (cyan crosses), and ^3He nuclei (yellow hexagons).	88
6.3	Rapidity distribution of simulated (symbols) and reconstructed (lines) proton and neutron at central Au+Au collisions $E_{beam} = 1.23A$ GeV. (Left panel) The comparison for the simulated and reconstructed primordial proton (red) and neutron (blue) rapidity based on Eq. (6.2) and Eq. (6.8). (Right panel) The comparison for the simulated and reconstructed final neutron rapidity based on Eq. (6.9).	91

LIST OF FIGURES (Continued)

Figure		Page
6.4	Invariant p_T spectra of d (green diamonds with dotted line), t (cyan pluses with dotted line), ^3He (yellow hexagons with dotted line), the primordial proton (full red circles) and neutron (full blue squares) from the simulations. While, the reconstructed primordial protons and neutrons are shown with solid red and solid blue lines respectively. The calculations are done at mid-rapidity in central Au+Au reactions at $E_{\text{beam}} = 1.23A \text{ GeV}$	92
6.5	(Left panel) The Rapidity distributions of the neutron/proton ratio (full black line), and the integrated $\Delta_{\text{iso}}^{\text{prim}}$ (dashed line). (Right panel) The transverse momentum distributions of the primordial neutron/proton ratio (full black line), and the integrated $\Delta_{\text{iso}}^{\text{prim}}$ (dashed line). Both from UrQMD for 0 — 10% central Au+Au reactions at $E_{\text{beam}} = 1.23A \text{ GeV}$	93
6.6	The scaled transverse momentum p_T/A -dependence of the coalescence parameter B_2 (left panel) and B_3 (right panel) calculated using the final state nucleons and reconstructed primordial nucleons from UrQMD for 0 — 10% central Au+Au reactions at $E_{\text{beam}} = 1.23A \text{ GeV}$	94

LIST OF FIGURES (Continued)

Figure		Page
6.7	<p>The figure caption describes the beam energy dependence of B_2 extracted at $p_T/A = 0$ GeV in mid-rapidity $y \leq 0.5$ for 0 — 10% central Au+Au collisions. Left panel: The dashed red line illustrates the original calculation of B_2 using the final state proton square, while the solid red line shows the corrected B_2 calculated by the product of reconstructed primordial protons and neutrons. Right panel: the original B_3 of tritons and ^3He, calculated from the final state proton cubic square, are depicted by the blue dashed line and green dotted line while the corrected B_3 of tritons and ^3He, using our reconstructed primordial protons and neutrons, are shown as the blue solid line and the green dash-dotted line, respectively. Experimental data (Wang et al., 1995; Ambrosini et al., 1998; Armstrong et al., 1999; Ahle et al., 1999; Barrette et al., 2000; Armstrong et al., 2000; Afanasiev et al., 2000; Bearden et al., 2002; Anticic et al., 2004; Anticic et al., 2016; Botvina et al., 2021) are denoted by symbols, while the dash-dotted black line represents the volume extracted from HBT results from STAR (Adamczyk et al., 2015).</p>	97
7.1	<p>The theoretical estimation of the deuteron d (pink full line), triton t (blue dashed line), and ^3He (orange dotted line) production according to the Eq. (7.6)- (7.8) for central Au+Au reactions as a function of ΔY_π.</p>	103
7.2	<p>Freeze-out time distribution of nucleons (full black line), pions (dashed black line), deuterons (dotted pink line), tritons (dotted blue line), and ^3He (dotted orange line).</p>	104
7.3	<p>Deuteron yield as a function of ΔY_π for Au+Au reactions. The UrQMD results are shown by red circles. The estimated yield, Eq. (7.7), is represented by the full red line. Left: Results at $\sqrt{s_{NN}} = 3$ GeV. Right: Results at $\sqrt{s_{NN}} = 7.7$ GeV.</p>	105

LIST OF FIGURES (Continued)

Figure		Page
7.4	<p>The ΔY_π dependent of triton (blue squares and dashed blue line) and ${}^3\text{He}$ (orange triangles and dotted orange line) yields. The UrQMD results are shown by symbols. The estimated yields, Eqs. (7.7) and (7.8), are represented by the lines. Left: Results at $\sqrt{s_{\text{NN}}} = 3$ GeV. Right: Results at $\sqrt{s_{\text{NN}}} = 7.7$ GeV</p>	106
7.5	<p>Distribution of cluster yields on the ΔY_π spectrum is normalized to unity at $\Delta Y_\pi = 39$. The symbols represent simulation results from various collision energies ranging from $E_{\text{lab}} = 1.23A$ GeV to $E_{\text{lab}} = 40A$ GeV in ultra-central Au+Au reactions from UrQMD. Left: Deuteron distribution. Right: Triton and ${}^3\text{He}$ distribution.</p>	107
8.1	<p>ALICE measurements in p + Pb (in red) and Pb + Pb collisions (Adam et al., 2016) (in blue) as a function of mean charged-particle multiplicity and the predictions from canonical statistical hadronization (excluded volume) (Vovchenko et al., 2018a) and coalescence models are shown (Sun et al., 2019). The figure is adopted from Ref. (Acharya et al., 2022)</p>	110

LIST OF FIGURES (Continued)

Figure		Page
8.2	<p>The transverse momentum (p_T) spectra of protons produced in minimum bias $\pi^- + C$ (left panel) and $\pi^- + C$ (right panel) collisions at various rapidity bins ($0 \leq y < 0.1$ to $0.9 \leq y < 1.0$) as measured by the UrQMD model (v3.5). The p_T spectra are represented by differential cross sections ($d^2\sigma/dp_T dy$) in units of $[\mu b / (\text{GeV}\Delta y)]$. The curves for each rapidity bin are consecutively multiplied by a factor of 10 from bottom to top for better visualization. Solid lines with symbols depict the UrQMD simulation results, while open symbols represent recent HADES experimental measurements (Yassine et al., 2023). The lower panel shows the relative deviation (percentage difference) between the UrQMD simulations and the corresponding experimental data for each rapidity bin.</p>	114
8.3	<p>The upper panel displays the transverse momentum (p_T) spectra of Λ hyperons produced in minimum bias $\pi^- + C$ (left) and $\pi^- + C$ (right) collisions at various rapidity bins ($0 \leq y < 0.15$ to $0.9 \leq y < 1.05$) as calculated by the UrQMD model (v3.5). The p_T spectra are represented by differential cross sections ($d^2\sigma/dp_T dy$) in units of $[\mu b / (\text{GeV}\Delta y)]$. The curves for each rapidity bin are consecutively multiplied by a factor of 100 for improved visualization (bottom to top). Solid lines with symbols depict the UrQMD simulations, while open symbols represent recent HADES experimental measurements (Yassine et al., 2023). The lower panel presents the relative deviation (percentage difference) between the UrQMD simulations and the corresponding experimental data for each rapidity bin</p>	115

LIST OF FIGURES (Continued)

Figure		Page
8.4	<p>The differential cross section with respect to the rapidity $d\sigma/dy$ [$\mu\text{b}/\Delta y$] of protons (red), Λ's (orange), and Ξ's (black) from minimum bias $\pi^- + \text{C}$ (left panel) and $\pi^- + \text{C}$ (right panel) collisions. The UrQMD results are shown as colored lines with symbols, while the open black symbols depict the recent HADES measurements (Yassine et al., 2023). The blue line with crosses shows the experimental fit function for the p_T extrapolation.</p>	117
8.5	<p>The transverse momentum differential cross section $d^2\sigma/dp_T dy$ in [$\mu\text{b}/(\text{GeV}\Delta y)$] of deuterons as a function of transverse momentum in different rapidity bins (from $0 \leq y < 0.1$ to $0.8 \leq y < 0.9$, the curves are successively multiplied by factors of 100 from bottom to top) for minimum bias $\pi^- + \text{C}$ (left panel) and $\pi^- + \text{C}$ (right panel) collisions from UrQMD.</p>	119
8.6	<p>The transverse momentum differential cross section $d^2\sigma/dp_T dy$ in [$\mu\text{b}/(\text{GeV}\Delta y)$] of tritons as a function of transverse momentum in different rapidity bins (from $0 \leq y < 0.1$ to $0.5 \leq y < 0.6$, the curves are successively multiplied by factors of 100 from bottom to top) for minimum bias $\pi^- + \text{C}$ (left panel) and $\pi^- + \text{C}$ (right panel) collisions from UrQMD.</p>	120
8.7	<p>The transverse momentum differential cross section $d^2\sigma/dp_T dy$ in [$\mu\text{b}/(\text{GeV}\Delta y)$] of ^3He as a function of transverse momentum in different rapidity bins (from $0 \leq y < 0.1$ to $0.5 \leq y < 0.6$, the curves are successively multiplied by factors of 100 from bottom to top) for minimum bias $\pi^- + \text{C}$ (left panel) and $\pi^- + \text{C}$ (right panel) collisions from UrQMD.</p>	121
8.8	<p>The rapidity differential cross section $d\sigma/dy$ in [$\mu\text{b}/\Delta y$] of deuterons (orange), tritons (green), ^3He (blue) and ^4He (red) as a function of the rapidity for minimum bias $\pi^- + \text{C}$ (left panel) and $\pi^- + \text{C}$ (right panel) collisions from UrQMD (v3.5) as denoted by dashed lines with symbols and from statistical multifragmentation model (SMM) as denoted by solid lines without symbols.</p>	122

LIST OF FIGURES (Continued)

Figure		Page
8.9	<p>The differential cross section with respect to transverse momentum $d^2\sigma/dp_T dy$ [$\mu\text{b}/(\text{GeV}\Delta y)$] of ${}^3\text{He}$ (blue line with squares) and $\text{N}\Xi$ (black triangles) from UrQMD results at mid-rapidity minimum bias $\pi^- + \text{C}$ (left panel) and $\pi^- + \text{W}$ (right panel) collisions. The dashed line indicates the extrapolated fit of $\text{N}\Xi$.</p>	123
8.10	<p>The differential cross section with respect to rapidity $d\sigma/dy$ [$\mu\text{b}/\Delta y$] of $\text{N}\Lambda$ (blue), $\text{NN}\Lambda$ (green), ${}^3_\Lambda\text{H}$ (red), ${}^4_\Lambda\text{H}$ (orange), ${}^4_\Lambda\text{He}$ (pink), and $\text{N}\Xi$ (black) from minimum bias $\pi^- + \text{C}$ (left panel) and $\pi^- + \text{W}$ (right panel). The UrQMD results are denoted by dashed lines with open symbols, while the results from the statistical multifragmentation model (SMM) are denoted by solid lines with full symbols.</p>	124
8.11	<p>The mass number distribution of the integrated cross section of light nuclei (full symbols: $Y=0$) and hypernuclei (single-strange as open symbols: $Y=1$) production with different charges Z (denoted by the color) from SMM analysis of the UrQMD data at minimum bias $\pi^- + \text{C}$ and $\pi^- + \text{C}$ collisions.</p>	126
8.12	<p>The comparison in the yield ratio of the hypertriton (${}^3_\Lambda\text{H}/(\Lambda + \Sigma^0)$) as a function of the mean charged particles multiplicity with various models. Our analysis for $\pi^- + \text{C}$ (green line) and $\pi^- + \text{C}$ (black line) is presented alongside data from p+Pb and Pb+Pb. The figure also includes predictions from two models: the thermal-statistical model denoted by CSM Thermal-FIST (dotted line) (Vovchenko et al., 2018a) and the previous UrQMD-hybrid coalescence model (coloured lines with symbols (Sun et al., 2019)). Finally, brown diamonds represent experimental measurements by the ALICE collaboration (Acharya et al., 2022).</p>	127

LIST OF ABBREVIATIONS

AGS	Alternating Gradient Synchrotron
ALICE	A Large Ion Collider Experiment
BNL	Brookhaven National Laboratory
BES	Beam Energy Scan
BUU	Boltzmann-Uehling-Uhlenbeck
CBM	Compressed Baryonic Matter
CMF	Chiral Mean Field
EoS	Equation of State
FAIR	Facility for Antiproton and Ion Research
FOPI	Forschungszentrum für Atomphysik und Institut für Nuklearphysik
GiBUU	Giessen Boltzmann-Uehling-Uhlenbeck
GSI	Gesellschaft für Schwerionenforschung
HADES	High Acceptance Di-Electron Spectrometer
HBT	Hanbury-Brown Twiss
LHC	Large Hadron Collider
PHSD	Parton-Hadron-String Dynamics
QCD	Quantum Chromodynamics
QGP	Quark Gluon Plasma
QMD	Quantum Molecular Dynamics
RHIC	Relativistic Heavy Ion Collider
SIS	Schwerionen Synchrotron
SMM	Statistical Multifragmentation Model
SHM	Statistical Hadronization Model
STAR	Solenoidal Tracker at RHIC
UrQMD	Ultra-relativistic Quantum Molecular Dynamics
VUU	Vlasov-Uehling-Uhlenbeck

CHAPTER I

INTRODUCTION

Heavy-ion collisions offer a unique testing ground for studying the properties of nuclear matter under various conditions. Advancements in theory and experiment over several decades have led more research areas to converge on a few, or perhaps even a single, fundamental truth about the universe. The acquired knowledge and interdependent knowledge are intertwined between various fields of physics research especially between nuclear physics and astrophysics. As various puzzles from astrophysics can be solved by testing on Earth within the heavy-ion collision facilities and the nuclear physics puzzles can also be tested with observable stellar objects, e.g., neutron stars and binary neutron mergers, dark matter, and others. This leads the heavy-ion collision facilities all over the world to move their focus toward the lower energy collisions, low temperature with extreme density, in order to probe various scenarios within the QCD phase diagram especially for the existence of the critical end point and the Equation of state (EoS) which is a direct connection between the nuclear properties and the compact stellar objects like neutron stars. The Beam Energy Scan (BES) program initiated by RHIC, and upcoming experiments GSI-FAIR and HADES that are joining the efforts, are particularly designed for low energy regimes.

During this PhD studies, our colleges and me have been investigated the dynamics of the heavy-ion collisions particularly focusing on its space-time dynamics ranging from the initial stage to the final stage of the heavy-ion collisions. Together, we have published the following papers:

1. Kittiratpattana, A., Reichert, T., Steinheimer, J., Herold, C., Lymphirat, A., Yan, Y., and Bleicher, M. (2022). Correcting the B_A coalescence factor at energies relevant for the GSI-HADES experiment and the RHIC Beam Energy Scan. *Phys. Rev. C*, 106(4):044905 (Kittiratpattana et al., 2022)
2. Reichert, T., Kittiratpattana, A., Li, P., Steinheimer, J., and Bleicher, M. (2023a). Probing system size dependence at high baryon density by systematic comparison of Ag+Ag and Au+Au reactions at 1.23A GeV. *J. Phys. G*, 50(2):025104 (Reichert et al., 2023a)

3. Li, P., Steinheimer, J., Reichert, T., Kittiratpattana, A., Bleicher, M., and Li, Q. (2023). Effects of a phase transition on two-pion interferometry in heavy ion collisions at $\sqrt{s_{NN}} = 2.4 - 7.7$ GeV. *Sci. China Phys. Mech. Astron.*, 66(3):232011 (Li et al., 2023)
4. Kittiratpattana, A., Reichert, T., Li, P., Lymphirat, A., Herold, C., Steinheimer, J., and Bleicher, M. (2023). Investigating the cluster production mechanism with isospin triggering: Thermal models versus coalescence models. *Phys. Rev. C*, 107(4):044911 (Kittiratpattana et al., 2023)
5. Reichert, T., Savchuk, O., Kittiratpattana, A., Li, P., Steinheimer, J., Gorenstein, M., and Bleicher, M. (2023b). Decoding the flow evolution in Au+Au reactions at 1.23A GeV using hadron flow correlations and dileptons. *Phys. Lett. B*, 841:137947 (Reichert et al., 2023b)
6. Kittiratpattana, A., Reichert, T., Buyukcizmeci, N., Botvina, A., Lymphirat, A., Herold, C., Steinheimer, J., and Bleicher, M. (2024). Production of nuclei and hypernuclei in pion-induced reactions near threshold energies. *Phys. Rev. C*, 109(4):044913 (Kittiratpattana et al., 2024)

However, the scope of this thesis will be on the exploration and demonstration of the dynamics of heavy-ion collisions, with a particular emphasis on the interplay and the utilization between (hyper)nuclei formation and space-time evolution of the created fireball, considering the various dependencies that influence them especially toward lower energies, e.g., the beam energy, EoS, formation mechanisms, stopping power, and system size. These studies are essential to the study of QCD matter, the critical behavior, and potentially to constrain the EoS. They are reported in the following papers:

- Kittiratpattana, A., Reichert, T., Steinheimer, J., Herold, C., Lymphirat, A., Yan, Y., and Bleicher, M. (2022). Correcting the B_A coalescence factor at energies relevant for the GSI-HADES experiment and the RHIC Beam Energy Scan. *Phys. Rev. C*, 106(4):044905 (Kittiratpattana et al., 2022)
- Li, P., Steinheimer, J., Reichert, T., Kittiratpattana, A., Bleicher, M., and Li, Q. (2023). Effects of a phase transition on two-pion interferometry in heavy ion

collisions at $\sqrt{s_{NN}} = 2.4 - 7.7$ GeV. *Sci. China Phys. Mech. Astron.*, 66(3):232011 (Li et al., 2023)

- Kittiratpattana, A., Reichert, T., Li, P., Lymphirat, A., Herold, C., Steinheimer, J., and Bleicher, M. (2023). Investigating the cluster production mechanism with isospin triggering: Thermal models versus coalescence models. *Phys. Rev. C*, 107(4):044911 (Kittiratpattana et al., 2023)
- Kittiratpattana, A., Reichert, T., Buyukcizmeci, N., Botvina, A., Lymphirat, A., Herold, C., Steinheimer, J., and Bleicher, M. (2024). Production of nuclei and hypernuclei in pion-induced reactions near threshold energies. *Phys. Rev. C*, 109(4):044913 (Kittiratpattana et al., 2024)

To achieve these goals, both theoretical and simulation models are indispensable because first principle QCD calculations are computationally too expensive. These models help us understand the origin of particle formations and the space-time evolution of the systems, as well as help us interpret experimental data. This thesis employs the UrQMD v3.5 transport model for event simulations and comparing the results with findings from our assumptions and/or other models. The importance on the understanding of space-time picture of the heavy-ion collisions and the development of theoretical models as well as other prospects are introduced and discussed in Chapter II. Chapter III focuses on developments and core assumptions of various simulation models.

Ch. IV points out our aims by demonstrating the utilization of the space-time structure of the fireball and the influences from the beam energies and the EoS. The space-time dynamics in the context of beam energies are explored based on the cluster formations in Sec. 4.1. The spatial geometric coalescence model is adopted and improved to estimate the (anti)deuteron productions and to extract the space-time structure of (anti)nucleon source. The (anti)nucleon source geometries will also be tested and confirmed with the UrQMD simulation. The extracted source geometries might help in revealing the presence of critical behavior on the beam energy spectrum and provide a proper explanation for the space-time structure of nucleon and antinucleon source geometries. Additionally, the space-time structure of the fireball is further investigated on various EoS with different phase transition scenarios from the standard UrQMD EoS to the chiral mean field EoS with and without phase transition. Sec. 4.4 will illustrate not only the energy-dependence but also the density-dependent nature

of the emission source geometry. The distinct critical behaviors from HBT radii and the UrQMD freeze-out time are expected and the corresponding critical density could be extracted.

The cluster formations, e.g. (anti)deuteron, from the previous chapter, have displayed some of their influences on the emission source structure which may potentially lead to the possible critical behavior of the fireball. As final stage observables, these clusters, in fact, can be also influenced by many more factors since the early stage ranging from the strangeness enhancement, the fluctuations, correlations, and initial collision geometries which all are as sensitive to the EoS and the critical behavior. They also have a direct implication for the astrophysics subjects like the neutron star structure, the early universe, and dark matter. Moreover, different assumptions on their formation mechanisms could also result in different outcomes and interpretations. Thus, all of these topics will be reviewed in detail in Ch. V.

Due to the maximum fluctuations and correlations of conserved quantities as well as the prolonging of the relaxation time, the critical behavior could be manifested by the cluster formations, particularly within the coalescence picture. The coalescence parameter reflects the emission volume with an inverse proportional relation. However, this volume is not the same as the (charged) volume from the thermal picture which scales monotonic exponentially with the beam energies. Instead, it is similar to the homogeneity volume of the HBT emission source. However, at low energies, the experimental data of B_2 and B_3 from various experiments indicate that this emission source volume behaves like the thermal volume which is unlikely. Ch. VI will address the discrepancy in coalescence parameter B_A measurements by proposing a corrected formula to account for primordial nucleons. The correction is expected to bring coalescence parameters to align with HBT predictions as a support the validity of our approach providing a consistent space-time picture.

To accurately estimate and interpret the final-stage cluster spectra from experiments, an understanding of their space-time origin and formation mechanisms is needed. There are tensions on the origin of these clusters from the two most common mechanisms, i.e., the thermal and coalescence model. A key distinction between them is the difference in space-time pictures of their occurrences. That is, the thermal model directly produces and emits clusters from the hot fireball at the chemical freeze-out together with all other particle species, while the coalescence model happens during the final stage of the collisions, kinetic freeze-out. Given our focus on the space-time

dynamics of collisions, we leverage this difference and aim to resolve this tension. In Ch. VII will demonstrate how these clusters experienced the isospin equilibration from the chemical freeze-out. The isospin exchange should lead to the fluctuations of the available nucleons to coalesce in the system. Due to this, the distinct maxima behaviors of clusters could be expected while the grand-canonical thermal model will average out all the fluctuation and only show constant thermal yields. This will be a clear indication that the clusters must be formed later at kinetic freeze-out with the coalescence picture.

The solutions for such debate can also be investigated at different collision systems via the hypernuclei formations. The coalescence models predict a stronger suppression on the system size-dependence of the hypertriton yield ratio ${}^3_{\Lambda}\text{H}/\Lambda$ when compared with the thermal model's. This raises the need for data at smaller system sizes. These data will not only help to pin down the cluster mechanisms between the thermal and coalescence models but also be crucial for the hypernuclei internal interactions which have a direct implication on constraining the neutrons star EoS. The investigation in Ch. VIII will provide another coalescence prediction for hypertriton yield ratio at even lower energies and smaller system sizes and point out the potential advantages of pion-induced reactions at HADES experiments for studying (hyper)nuclei formations. The UrQMD and the Statistical Multifragmentation Model (SMM) will be employed to show that (hyper)nuclei abundances in these reactions are comparable or could even be higher than those at high-energy facilities. Since the environments provided by the pion beam at HADES is conducive for (hyper)nuclei formation due to a stronger stopping power than other collision systems.

CHAPTER II

PROSPECTS OF HEAVY-ION COLLISIONS

The ultimate goal for nuclear physicists is to understand QCD matter and its governing Equation of State (EoS). In order to study this strongly interacting matter, we need sufficient energy to tear the nucleus apart, generating conditions where the “strong force” is dominant. Hence, we need heavy-ion collisions. In this chapter, we introduce the concepts and goals of heavy-ion collisions.

2.1 Exploring the QCD Phase Diagram

2.1.1 The Development of Models and Equation of State

Early theoretical prediction for a new state of nuclear matter was done in the 1970s by Ref. (Fritzsch et al., 1973; Freedman and McLerran, 1977; Shuryak, 1978; McLerran, 1986) regarding nuclear matter under extreme conditions leading to the so-called “Quark Gluon Plasma (QGP)”. Naturally, one expects an accompanying phase transition between two different states in the phase diagram. A type of transition is dictated by the order parameter or a relation between thermodynamic properties, e.g., pressure, energy density, chemical potential, and temperature. This relation is known as “Equation of State (EoS)”. Ref. (Cabibbo and Parisi, 1975) reported that there could be many kinds of orders of phase transitions in the QCD phase diagram. A smooth second-order phase transition or a crossover at high temperatures with low baryochemical potential is expected from the earlier theoretical calculation either by chiral model or lattice QCD (see below). Then there should be a first-order phase transition line with a critical end point where the thermodynamic changes are abruptly strong and even diverge. However, since then, there is still no clear experimental evidence to prove the existence of this critical point.

During this period, Ref. (Johnson, 1975) has proposed an empirical approach to explain the physical behaviors that could provide the EoS with the first-order phase transition as well as a critical end point. This model is called the MIT Bag Model.

Only until 1990s, the first principle non-perturbative QCD calculation could be successfully published. The approach is known as “lattice QCD”. It is based on the

discretizing the space-time grid, allowing for numerical simulation processes (Karsch, 2002; Fodor and Katz, 2002). After a decade, this approach has become one of the most basis for the simulation comparison due to its fundamental nature. The development of the lattice QCD is now focusing on extending its computational ability via complex numerical techniques for simulating the QCD matter at the larger chemical potential. Currently, the lattice QCD could provide the reliable EoS and confirm the smooth crossover phase transition at the region $\mu_B/T \leq \pi$ (no critical point has been found) (Allton et al., 2005; Aoki et al., 2006; Vovchenko et al., 2018b).

Another important theoretical development was the introduction of the chiral models (Brown and Rho, 1996; Berges and Rajagopal, 1999; Alford et al., 1999). The chiral model could also provide a similar physical description of the two major phases, the chiral symmetry restored phase and the chiral spontaneously breaking phase, which is comparable to the de-confinement phase at QGP conditions and the confinement phase at low temperature and baryochemical potential where quarks are bound into normal hadrons, respectively. Despite arising from the same origin, some simple chiral models provide only a first-order phase transition (Koch, 1997), while some models could suggest a critical end point. However, the specific details remain under investigation.

Aside from the theoretical developments, the advancement of heavy-ion collision facilities also plays an important role in nuclear physics. The very first announcement for the existence of QGP was presented by CERN Super Proton Synchrotron (SPS) with several collaborations in the 1990s (Heinz and Jacob, 2000). Since the first heavy-ion collision experiments from Bevalac to the Large Hadron Collider (LHC) at CERN, the data collected over the years are immersed and further confirms the existence of the QGP definitively with a multitude of observables, such as strangeness enhancement K/π , the J/Ψ suppression (Matsui and Satz, 1986; Wiedemann, 2010), the collective flow (Muller et al., 2012).

Despite massive evidence of the new phase of nuclear matter QGP, the exploration of the QCD phase diagram still remains being an active research (Collaboration, 2014) in order to study the physical behavior of the phase transition and locate the critical end point (if exists). Over the past decades with theoretical and experimental developments, there seem to be more than two phases of QCD matters, e.g., Color-Glass superconductor (CGC) phase at low temperature but very high baryochemical potential, as well as the connection between nuclear physics and the very dense/com-

pact stellar objects, like neutron stars, i.e., the EoS. Thus, future efforts will likely focus on the lower energies but extremely dense conditions for extracting the EoS as well as studying the critical behavior of the QCD matter undergoing the phase transition (as well as the critical point).

The equation of state describes the relation between the thermodynamic quantities. These quantities can be obtained from the partition function of any equilibrium system parametrized by the volume V , temperature T , and chemical potential μ . For instance, in the grand-canonical picture of monotonic gas we have,

$$Z(T, V, \mu) = \text{Tr} \left[\exp^{-\frac{(\hat{H} - \mu \hat{N})}{T}} \right], \quad (2.1)$$

$$\Omega(T, V, \mu) = -T \ln Z. \quad (2.2)$$

$Z(T, V, \mu)$ is the grand-canonical partition function with $\Omega(T, V, \mu)$ as a grand potential. Here \hat{H} and \hat{N} are the Hamiltonian operator and the number operator. The thermodynamic relations is

$$\Omega(T, V, \mu) = E - TS - \mu N, \quad (2.3)$$

$$d\Omega(T, V, \mu) = -SdT - pdV - Nd\mu, \quad (2.4)$$

where S is the average entropy. Oftentimes, the thermodynamic quantities are expressed in terms of density,

$$-P = \epsilon - Ts - \mu n, \quad (2.5)$$

$$dP = sdT + nd\mu, \quad (2.6)$$

$$d\epsilon = Tds + \mu dn. \quad (2.7)$$

The following relations are also useful:

$$\epsilon = \frac{T}{V} \left(\frac{\partial \ln Z}{\partial \ln T} + \frac{\partial \ln Z}{\partial \ln \mu} \right), \quad (2.8)$$

$$P = T \frac{\partial \ln Z}{\partial V}. \quad (2.9)$$

We now have all of the connections required to create the equation of state.

Non-interacting relativistic particles: The grand-canonical partition function

for non-interacting massive particles is given by,

$$Z(T, V, \mu) = \prod_k \left(\sum_{\sigma} e^{-\sigma(\epsilon(k)-\mu)/T} \right)^d = \prod_k \left(1 \pm e^{-(\epsilon(k)-\mu)/T} \right)^{\pm d}.$$

The partition function is expressed as the production of a single momentum state, which is a sum over all possible same occupying states, i.e., the occupation number σ . For bosons, they can take any state up to the infinite number $\sigma = 0, 1, 2, 3, \dots$, while fermions can only take the same state up to $\sigma = 0, 1$ due to Pauli's exclusion. The d is the degeneracy factor accounting for all possible spin states.

In an extreme case like the early universe QGP, we expect a very high temperature with $\mu \rightarrow 0$. Under these conditions, the system is approximately at the chiral limit, where the bare quarks are massless. The system can be described with massless Goldstone boson gas. The grand potential density or pressure of massless boson gas reads as,

$$P = \begin{cases} \text{for bosons;} \\ d \int \frac{d^3k}{(2\pi^3)} T \ln \left(1 - e^{-\epsilon(k)/T} \right) = d \frac{\pi^2}{90} T^4. \\ \text{for fermions;} \\ -d \int \frac{d^3k}{(2\pi^3)} T \ln \left(1 + e^{-\epsilon(k)/T} \right) = d \frac{7\pi^2}{890} T^4. \end{cases} \quad (2.10)$$

The degeneracy factor of pion arises from the isospin state; we have $d_{\pi} = 3$ (for both $N_f = 2$ or 3 (Yagi et al., 2005)). This description can be used to describe the system at LHC or ALICE energies, where the pion dominates the medium.

MIT Bag Model

The MIT Bag Model describes the confining of quarks inside the bag, forming a hadrons (Johnson, 1975; DeTar and Donoghue, 1983) where the strong force is described by the empirical bag pressure. At high temperatures and density, the pressure inside the hadron bag becomes very strong, leading the bag to expand and eventually break down. This breakdown is similar to the abrupt change nature of the first-order phase

transition, resulting in the hadron bag to de-confine and achieving the de-confinement state, or QGP phase.

Bag Model EoS: The nature of phase transition is dictated by the EoS. Here, the thermal properties of the non-interacting relativistic gases of QGP and pion are connected and serve as a governing EoS,

$$P_{\text{QGP}} = d_{\text{QGP}} \frac{\pi^2}{90} T^4 - B, \quad (2.11)$$

$$\epsilon_{\text{QGP}} = 3d_{\text{QGP}} \frac{\pi^2}{90} T^4 + B, \quad (2.12)$$

$$s_{\text{QGP}} = 4d_{\text{QGP}} \frac{\pi^2}{90} T^3. \quad (2.13)$$

B is the bag parameter whose purpose is similar to the binding energy, $d_{\text{QGP}}(d_q, d_g)$ is the effective degeneracy factor for quarks and gluons. The main feature of the bag model is the strong first order phase transition. In addition, we can use the bag model equation of state to extract the critical temperature for first-order phase transition using the boundary conditions, $P_{\text{H}}(T_c) = P_{\text{QGP}}(T_c)$.

Lattice QCD

One of the most important features of QCD is asymptotic freedom (Gross and Wilczek, 1973). While, the coupling constant between quarks and gluons in the normal hadron gas condition is very strong, leading to the quark confinement phase. However, when the energy and density of the system increase, the coupling constant between constituents becomes smaller. The quarks and gluons become asymptotically free inside a soup of QGP. The problem arises when one needs to describe the phase transition between these two phases for the EoS from the first principle QCD Lagrangian. Thus, the perturbative approach is not allowed in this case (Politzer, 1973). Furthermore, due to the many-interacting-body problems between the quarks, gluons, and bound state hadrons, the analytic solution for such dynamics is extremely computationally expensive and deemed almost impossible.

However, Ref. (Philipsen, 2006) suggests the numerical technique such that the field variables of the Lagrangian can be defined on a discrete space-time lattice. Despite still being computationally expensive, this method allows us to solve the QCD

Lagrangian through the first principle at assuming thermal equilibrium.

The EoS in lattice QCD can be derived from the grand canonical partition function,

$$Z = \int \mathcal{D}U \mathcal{D}\bar{\psi} \mathcal{D}\psi e^{(S_g - S_f)}. \quad (2.14)$$

where the integration is accounting over all U gauge fields (gluons) and $\bar{\psi}, \psi$ fermionic fields (quarks) within SU(3) matrices. S_g represents the gauge action while S_f the fermionic action as the system depends on both gauge and fermionic fields. The expectation values of an observable O can be obtained with

$$\langle O \rangle = \frac{1}{Z} \int \mathcal{D}U \mathcal{D}\bar{\psi} \mathcal{D}\psi O(U, \bar{\psi}, \psi) e^{S_g - S_f}. \quad (2.15)$$

These path integrals are evaluated on a discretized space-time grid using Monte Carlo techniques, i.e., choosing some quark-lattice-sites and gluon-link configurations randomly and evaluating the observables on these fields.

The lattice QCD results help to confirm that at the vanishing baryon chemical potential $\mu_B = 0$, the QCD transition is a crossover type (Aoki et al., 2006; Bazavov et al., 2012). Furthermore, at non-vanishing μ_B although the lattice QCD suffers from the “sign problem” (de Forcrand, 2009), it was reported that as far as lattice QCD can go in the QCD phase diagram, there is no expected critical point from $\mu_B > 0$ until $\mu_B/T \lesssim 3$ (Laermann and Philipsen, 2003; Schmidt, 2006; Bazavov et al., 2019; Borsanyi et al., 2020).

Chiral Model

The Nambu-Jona-Lasinio (NJL) models (Nambu and Jona-Lasinio, 1961; Vogl and Weise, 1991; Klevansky, 1992; Hatsuda and Kunihiro, 1994; Buballa, 2005) and other chiral models (Meisinger and Ogilvie, 1996; Koch, 1997; Meisinger et al., 2002; Meisinger et al., 2004; Fukushima, 2004; Mocsy et al., 2004; Ratti et al., 2006) are theoretical frameworks based on the chiral symmetry. Unlike lattice QCD, the chiral models are effective models aiming to describe the QCD Lagrangian. In the limit where bare quark masses are zero, $m_q \rightarrow 0$, QCD Lagrangian is invariant under the $SU(N_f)_L \times SU(N_f)_R \times U(1)_V$ group. However, due to the finite quark masses in nature, this chiral symmetry is explicitly or spontaneously broken already in vacuum, leading to the formation of a quark condensate and the emergence of pseudo-Goldstone bosons, such as pions (Koch, 1997).

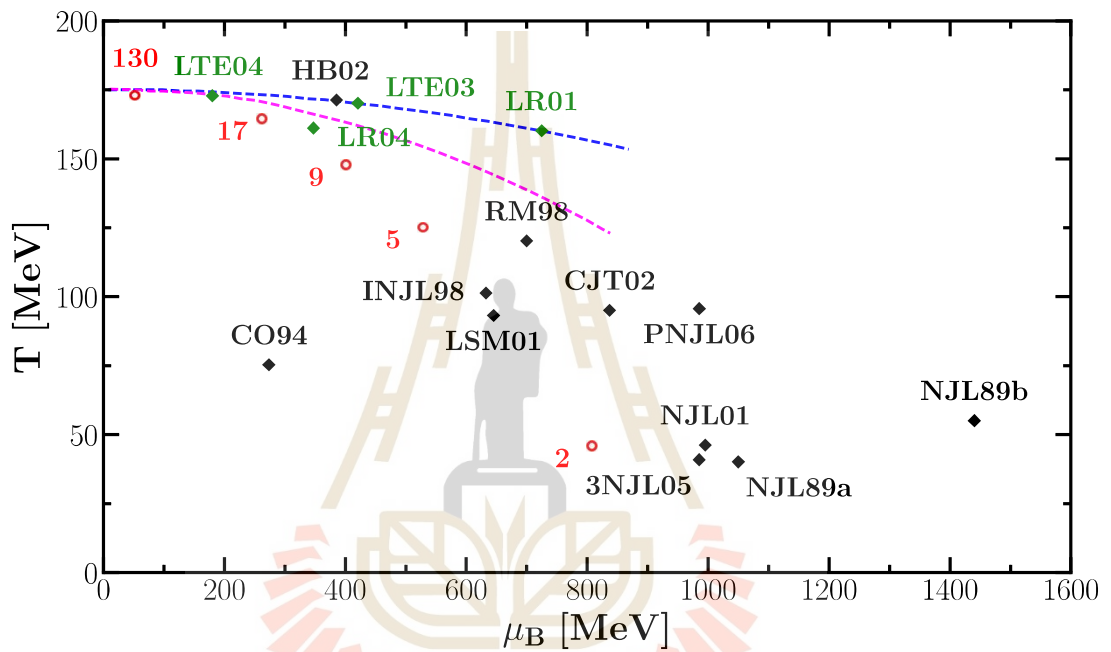


Figure 2.1 The compilation of the predicted location of the QCD critical point from various models, mainly chiral models and lattice QCD (Stephanov, 2006). Black points represent chiral model predictions. Green points indicate lattice predictions. The two dashed lines are the slopes corresponding to $dT/d\mu_B^2$ of the transition line at $\mu_B = 0$. The red circles denote the freeze-out points for heavy ion collisions at corresponding center-of-mass energies in GeV per nucleon.

The thermodynamical properties of the QCD from the chiral models are determined by the path integral of the effective action of the quark condensate field σ and π field. Various phase transition scenarios may be feasible via the chiral models, e.g., a purely crossover or first-order phase transition along with the critical end point.

However, as chiral models are quite model-dependent yet produce powerful predictions, they are typically used in conjunction with other models and experiments as a basis, e.g., implementing with lattice QCD (Borsanyi et al., 2020), or with the hydrodynamics models (Mishustin and Scavenius, 1999; Nahrgang et al., 2011; Herold et al., 2019).

Chiral EoS: The chiral model includes all the sets of baryons and the entire multiplets of scalar, pseudo-scalar, vector, and axial-vector mesons. The grand-canonical potential can then be expressed as

$$\begin{aligned} \Omega/V &= \mathcal{V}_{\text{meson}} - \mathcal{V}_{\text{vac}} \\ &- T \sum_{i \in B} \frac{\gamma_i}{(2\pi)^3} \int d^3k \left[\ln \left(1 + e^{-\frac{1}{T}[E_i^*(k) - \mu_i^*]} \right) \right] \\ &+ T \sum_{i \in M} \frac{\gamma_i}{(2\pi)^3} \int d^3k \left[\ln \left(1 + e^{-\frac{1}{T}[E_i^*(k) - \mu_i^*]} \right) \right]. \end{aligned} \quad (2.16)$$

where γ_B, γ_M are the baryonic and mesonic spin-isospin degeneracy factors and $E_{B,M}^*(k) = \sqrt{k^2 + m_{B,M}^{*2}}$ are the single baryon and meson particle energies. The effective baryon chemical potential μ_i^* includes the quark and strange quark chemical potentials. The term \mathcal{V}_{vac} is the vacuum energy. Here, we include the interaction between baryons and scalar mesons (BM), the vector mesons (\mathcal{L}_{vec}) and the scalar self-interactions \mathcal{L}_0 . The scalar meson interaction induces spontaneous symmetry breaking of the chiral symmetry (\mathcal{L}_{SB}). The effective mesonic potential can be written by $\mathcal{V}_{\text{meson}} = -\mathcal{L}_{\text{vec}} - \mathcal{L}_0 - \mathcal{L}_{\text{SB}}$. Figure 2.1 shows potential critical points have been reported according to chiral models and lattice calculations, where a detailed derivation of the chiral equation of state can be found in (Omana Kuttan et al., 2022; Steinheimer et al., 2022; Omana Kuttan et al., 2023).

2.1.2 Beam Energy Scan and Low Energy Regime

The Beam Energy Scan (BES) program (Collaboration, 2014; Luo, 2016; Bzdak et al., 2020) plays an important role in the QCD phase diagram exploration. Heavy-ion

will be collided at various energy ranges, scanning all over the QCD phase diagram, aiming to pinpoint the location of a critical point, if it exists. This critical point is expected to be located in the environments created by low- to intermediate-energy heavy-ion collisions. The corresponding trajectories in the QCD phase diagram are shown in Figure 2.2.

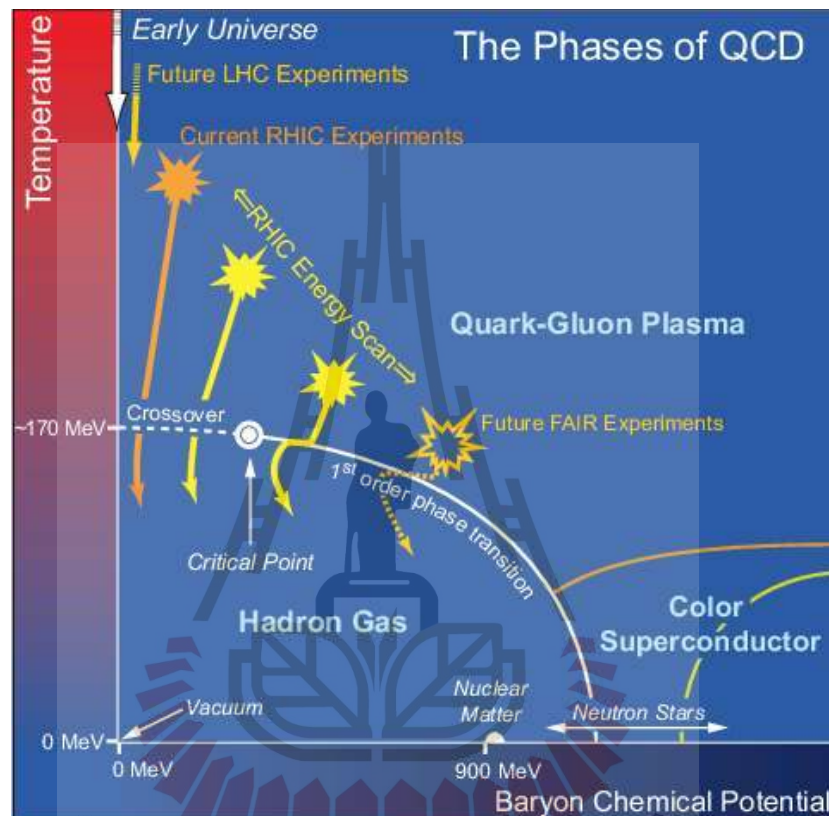


Figure 2.2 QCD diagram with BES program and various facilities (Collaboration, 2014).

- **Relativistic Heavy-ion Collider (RHIC):** The facility is originally designed for exploring the QCD at very high energies particularly searching for the existence of the new phases of QCD matter, QGP. After many updates, it now can provide a broader range of collision energies from 7.7 — 200 GeV. This allows RHIC to initiate the Beam Energy Scan (BES) program (Luo, 2016; Bzdak et al., 2020; Collaboration, 2014) which most of the heavy-ion collision facilities will collectively join with the aims for locating the critical point and extracting the EoS as well as new physics at extremely dense medium.
- **Future Facilities (FAIR and HADES):** The upcoming Facility for Antiproton and

Ion Research (FAIR) at GSI will also join the BES effort (Almaalol et al., 2022), offering a new dimension to the study. FAIR's energy and intensity (Friman et al., 2011; Ablyazimov et al., 2017; Durante et al., 2019; Bzdak et al., 2020) allow for a boarder range of physics study from nuclear physics to astrophysics. In terms of heavy-ion physics research, FAIR will extend the BES coverage to even lower energy ranges $\sqrt{s_{NN}} < 7.7$ GeV and more dense medium allowing to probe the critical behavior from first-order phase transition, the formation of rare probes like exotic nuclei and ultimately the EoS (for the neutron stars). HADES (High Acceptance Di-Electron Spectrometer) is also one of the facilities at GSI focusing on the low energy and dense medium similar to FAIR. It specializes in the study the rare probes such as dileptons and exotic nuclei. Dileptons are a powerful probe for the properties of the QCD matter at the early stage. While the (exotic) (hyper)nuclei serve as valuable basis for the EoS of neutron star conditions (Weber, 2005; Lattimer, 2021; Most et al., 2023). Furthermore, as we will discuss in Ch. VIII, the pion-induced reactions at HADES also provide a unique opportunity to study these rare probes at smaller system sizes.

2.2 Space-Time Evolution

One should note the critical importance of understanding the space-time picture of heavy-ion collisions and their evolution (Shuryak, 1978). To comprehend the physical signatures (observables) produced in these collisions, we need a detailed understanding of the medium's evolution after the impact until the particle free streaming into the detectors. Figure 2.3 depicts this sequence of events.

When the two Lorentz contracted heavy nuclei collide, a huge amount of energy and momentum exchange occurs. At the overlapping region, an extremely hot, dense, and chaotic system is created. This medium is hardly in any equilibrium since the change is strong and sudden. Numbers of theoretical models (Bravina et al., 1999; Mishra et al., 2008; Sorensen, 2010a; Sorensen, 2010b; Bally et al., 2022) is trying to describe this pre-equilibrium stage since realistic initial conditions are essential to any dynamical evolution. Nevertheless, a clear understanding is still a work in progress.

After some time, this initial chaos settles down, the system approaches a state of (local) thermal equilibrium allowing for the hydrodynamics description (Yagi et al., 2005). The matter at this stage is in the QGP state which exhibits properties

system, treating hadrons as relativistic gases (at chemical freeze-out). While some other models, like transport models (Wolter et al., 2022), treat the dynamics of individual hadron interactions at the microscopic picture.

The dynamics within each stage of this space-time evolution can be linked to the EoS as it dictates the expansion and cooling rate as well as the critical behavior of the system. However, the EoS alone could not directly imply a complete set of final stage observables. The influence from the initial stage has to be considered (Mishra et al., 2008; Sorensen, 2010a; Sorensen, 2010b; Bally et al., 2022) as well as the interplay between various factors during the evolution. These factors ultimately shape the final-state observables, e.g., collective flows (Ollitrault, 1992; Reichert et al., 2022), fluctuations (Skokov et al., 2013; Adare et al., 2016; Luo and Xu, 2017), and etc (Iancu, 2014; Vovchenko et al., 2020; Acharya et al., 2022).



CHAPTER III

MODELLING HEAVY-ION COLLISIONS

QCD, or Quantum Chromodynamics has limitations when it comes to describing the exact solution of quark and gluon dynamics and particle production within the heavy-ion collisions. For example, due to the asymptotic freedom (Gross and Wilczek, 1973) the perturbative QCD is not allowed and only feasible at higher energies (Politzer, 1973). In addition, in the heavy-ion collisions, the system needs to account for an enormous many-body problem and with different degrees of freedom at that, from parton to hadron. This makes the first-principle calculations practically impossible for a complete dynamical picture of the whole evolution.

However, one can still calculate these dynamics with an innovative approach like lattice QCD simulations (Borsanyi et al., 2014) for the non-perturbative QCD. These methods, however, have their own limitations in terms of computational complexity and reliable results are currently limited to relatively low net-baryon densities, $\mu_B/T \leq \pi$ (Allton et al., 2005; Aoki et al., 2006; de Forcrand and Philipsen, 2010; Bazavov et al., 2012; Vovchenko et al., 2018b; Philipsen, 2021). Hence, theoretical models are required for further development in terms of empirical models and/or phenomenological approaches.

Especially with the hunts for the critical point and the Equation of State (EoS) toward lower energy heavy-ion collisions, these studies are driven forces for even more rigorous improvement of these models. One of the alternative approaches, to describe the many-body behavior of the Quark-Gluon Plasma (QGP) and/or the hadronic interactions in heavy-ion collisions, is to look into the kinetic theory. This leads to the development of both transport models and hydrodynamics models.

Transport models rely on a microscopic description, treating each hadron individually via interactions and scattering processes. Hydrodynamics models, on the other hand, adopt a macroscopic viewpoint, treating the whole system as a fluid characterized by bulk properties like pressure, temperature, and density profile as well as transport coefficients. The EoS plays an important role in dictating the dynamics based on the relationship between these thermodynamic quantities. Both approaches have their own advantages and limitations.

In this chapter, we briefly review transport models with a special focus on the Ultra-relativistic transport model (UrQMD) and the hybrid model which combine the hydrodynamical description at the earlier state with the transport model by following the explanation in Ref. (Bratskovkaya, 2019a; Bratskovkaya, 2019b; Xu, 2019; Wolter et al., 2022; Sorensen et al., 2024).

3.1 Transport models

Every transport model for heavy-ion collisions begins with the kinetic theory that describes the time evolution of the N-body phase-space distribution function ρ by N-body Hamiltonian. Derived from the conservation law of the phase-space density $\frac{d\rho}{dt} = 0$, we can get the continuity equation or namely the Liouville equation reads as,

$$\frac{\partial \rho}{\partial t} = \{H, \rho\}. \quad (3.1)$$

This equation describes the free streaming of a single or N-body density according to the Hamiltonian H with $\{\cdot\}$ is the Poisson bracket. However, the dynamics in the heavy-ion collisions are far more complex, not only we have a huge multiplicity of the different particle species but they can also interact quantum mechanically, e.g. elastic collisions, inelastic collisions, and decays. Defining this N-body phase-space density is challenging and their interactions will appear as a gain and loss term for the phase-space density. Thus we need to derive the equation of motion that incorporate these quantum effects and express them in terms of quantum operators.

3.2 Boltzmann(Vlasov)-Uehling-Uhlenbeck (B(V)UU) approach

We begin our derivation with the N-body non-relativistic Schrödinger's equation describing the total wavefunction $\Psi(1, \dots, N; t)$ with the Hamiltonian operator $H_N(1, \dots, N; t)$ of N-particles,

$$i\hbar \frac{\partial}{\partial t} \Psi_N(1, \dots, N; t) = H_N(1, \dots, N; t) \Psi_N(1, \dots, N; t) \quad (3.2)$$

By introducing the N-particle density matrix from the product of N-body wavefunctions, $\rho_N(1, \dots, N; 1', \dots, N'; t, t') = \Psi_N^*(1, \dots, N; t) \Psi_N(1, \dots, N; t')$, we can write Eq. 3.2 and its conjugate equation in the density matrix formalism, i.e., $i\hbar \frac{\partial}{\partial t} \rho_N = H_N \rho_N$

and $-i\hbar \frac{\partial}{\partial t'} \rho_N = H'_N \rho_N$. If we subtract the former with the latter equations and assume that $t = t'$, we finally arrive at the von-Neumann equation,

$$i\hbar \frac{\partial}{\partial t} \rho_N - [H_N, \rho_N] = 0. \quad (3.3)$$

However, the determination of the N-body density as well as calculating the equation of motion for each particle is impractical. We need to reduce the N-body density matrix down to the desirable level. By taking the trace over particle $n + 1^{\text{th}}$ to N^{th} of ρ_N , the n-body density is realized $\rho_n = \frac{1}{(N-n)!} \text{Tr}_{n+1, \dots, N} (\rho_N)$. This reduced density matrix method leads to the BBGKY (Bogoliubov-Born-Green-Kirkwood-Yvon) hierarchy (Boercker and Dufty, 1979). This hierarchy provide a set of coupled equations to recursively determine the dynamics of the reduced n-body density matrices using the (n+1)-body density. The BBGKY hierarchy reads,

$$i\hbar \frac{\partial}{\partial t} \rho_n - \left[\sum_i^n H_i^0, \rho_n \right] = \left[\sum_{i < j}^{n-1} V_{ij}, \rho_n \right] + \text{Tr}_{n+1} \left(\left[\sum_{i=1}^n V_{i(n+1)}, \rho_{n+1} \right] \right). \quad (3.4)$$

H_i^0 is the Hamiltonian of free n-particles (propagate within an external field). The second term represents the mutual interactions between particle i^{th} and others in the system. The third term is accounting for the correlations controlled by another (n+1)-particle.

The first two levels for the hierarchy equations read as,

$$i\hbar \frac{\partial}{\partial t} \rho_1 - [H_1^0, \rho_1] = \text{Tr}_2 ([V_{12}, \rho_2]) \quad (3.5)$$

$$i\hbar \frac{\partial}{\partial t} \rho_2 - [H_1^0 + H_2^0, \rho_2] = [V_{12}, \rho_2] + \text{Tr}_3 ([V_{12} + V_{13}, \rho_3]) \quad (3.6)$$

The calculation of the 2-body density matrix ρ_2 in the last term of Eq. 3.5 will be evaluated by the next hierarchy ($n = 2$) in Eq. 3.6 which in turn also needs 3-body density ρ_3 from the next hierarchy, and so on. However, one can do some approximation to truncate the 2- or 3-body density down to the product of single-particle densities and close the set of equations. The different truncation schemes will lead to the different single-density equations of motions as shown in Ref. (Aichelin, 1991)

Time-Dependent Hartree-Fock (TDHF) approach: For instance, the Time-

Dependent Hartree-Fock (TDHF) approach for simple two-body density truncation which is limited to the effective in-medium mean field interactions. The 2-body density can be reduced into a product of antisymmetric product of single-particle density (fermion),

$$\rho_2(1, 2; 1', 2'; t) \approx A_{12}\rho_1(1, 1'; t)\rho_1(2, 2'; t),$$

where A_{ij} is the permutation operator. By substitute this back to Eq. 3.5, we obtain,

$$\begin{aligned} i\hbar\frac{\partial}{\partial t}\rho_1(1, 1'; t) &= [T_1^0 - T_{1'}^0]\rho_1(1, 1'; t) + [V_1^0 - V_{1'}^0]\rho_1(1, 1'; t) \\ &= \text{Tr}_2 \left([V_{12}^F A_{12} - V_{1'2'}^F A_{1'2'}] \right) \rho_1(1, 1'; t)\rho_1(2, 2'; t) \end{aligned} \quad (3.7)$$

From the formula, a single-particle i^{th} dynamics within TDHF approximation can be understood as a single-particle propagation with the kinetic T_i^0 under a direct influence within the medium (external fields and/or other nucleons). This interaction is determined from a self-generated local mean-field potential called Hartree term V_i^0 or V_i^H . Finally, a time-dependent exchange or non-local mean-field potential, called Fock potential V_i^F , accounts for the Pauli principle.

In order to draw any further meaningful interpretation from the density matrix ρ , we need to derive the proper phase-space distribution function $f(\vec{r}, \vec{p})$. Hence, we will perform the Wigner transformation which is a Fourier transform on a single-particle wavefunction or single-particle density matrix (Hillery et al., 1984) with new variable $\vec{s} \equiv \vec{x}_1 - \vec{x}'_1$ and $\vec{r} \equiv (\vec{x}_1 + \vec{x}'_1)/2$ which reads,

$$f(\vec{r}, \vec{p}, t) = \int d^3s \exp\left(\frac{-i\vec{p} \cdot \vec{s}}{\hbar}\right) \rho(\vec{r} + \vec{s}/2, \vec{r} - \vec{s}/2) \quad (3.8)$$

For simplicity, we will determine the phase-space distribution from TDHF approach within the diluted gas limit, i.e., neglecting the Fock time-dependent exchange term.

Under the Wigner transformation, Eq. 3.7 becomes,

$$\begin{aligned}
& i\hbar \frac{\partial}{\partial t} \int d^3s \exp\left(\frac{-i\vec{p} \cdot \vec{s}}{\hbar}\right) \rho(\vec{r} + \vec{s}/2, \vec{r} - \vec{s}/2) \\
&= \frac{\hbar^2}{2m} \int d^3s \exp\left(\frac{-i\vec{p} \cdot \vec{s}}{\hbar}\right) [\nabla_{\vec{r}+\vec{s}/2}^2 - \nabla_{\vec{r}-\vec{s}/2}^2] \rho(\vec{r} + \vec{s}/2, \vec{r} - \vec{s}/2) \\
&+ \int d^3s \exp\left(\frac{-i\vec{p} \cdot \vec{s}}{\hbar}\right) [v^0(\vec{r} + \vec{s}/2) - v^0(\vec{r} - \vec{s}/2)] \rho(\vec{r} + \vec{s}/2, \vec{r} - \vec{s}/2)
\end{aligned} \tag{3.9}$$

Then we can simplify the second term with $[\nabla_{\vec{r}+\vec{s}/2}^2 - \nabla_{\vec{r}-\vec{s}/2}^2] = 2\vec{\nabla}_r \cdot \vec{\nabla}_s$, and the third term by the Taylor expansion around $\vec{s} \rightarrow 0$ of self-consistent mean-field potentials $\lim_{\vec{s} \rightarrow 0} [v^0(\vec{r} + \vec{s}/2) - v^0(\vec{r} - \vec{s}/2)] \approx s\vec{\nabla}_r v^0 = s\vec{\nabla}_r U$. Finally, The Vlasov equation is obtained,

$$\frac{\partial f}{\partial t} + \frac{\vec{p}}{m} \cdot \vec{\nabla}_r f + \vec{\nabla}_r U \cdot \vec{\nabla}_p f = 0. \tag{3.10}$$

The equation describes a free propagation of a single-particle phase-space distribution $f(\vec{r}, \vec{p})$ in the self-generated Hartree mean-field potential U or U_H . The right hand side of the Vlasov equation can be non-zero, if we introduce the quantum effect corrections, e.g., Fock exchange potential or the collision term $\left(\frac{\partial f}{\partial t}\right)_{\text{coll}}$.

Vlasov-Uehling-Uhlenbeck (VUU) approach: If one wants to include the potential from the realistic interaction between particles instead of the effective mean-field potential. We need to evaluate the dynamics of a single-particle from, at least, a truncation of the 3-body density matrices. The coupling term with a second particle is responsible for the collision with the first particle. While the third particle will generate an external field to correlate with the first two particles. However, this requires lengthy mathematics calculations where one needs to discuss not only the reduction of the density but also the calculation that arises from the trace terms, e.g., Pauli-blocking and G-matrix, which is not really inline with our focus in this thesis. Hence, we will only discuss how to derive the VUU equation with the collision term from the 2-body level density or second hierarchy of the BBGKY equation $n = 2$.

The 2-body density can be reduced into single-particle densities while non-zero two-body correlations are still kept into account. The 2-body density matrix be-

comes,

$$\rho_2(1, 2; 1', 2'; t) \approx A_{12}\rho_1(1, 1'; t)\rho_1(2, 2'; t) + c_2(1, 2; 1', 2'; t).$$

Substitute this reduced density into the BBGKY second hierarchy Eq. 3.6, we get a similar result to the TDHF approach with an additional trace term of c_{12} ,

$$\overbrace{i\hbar\frac{\partial}{\partial t}\rho_1(1, 1'; t) - [H_1^0 - H_{1'}]\rho_1(1, 1'; t)}^{\text{TDHF-Vlasov}} = \underbrace{\text{Tr}_2([V_{12} - V_{1'2'}])}_{\text{Collision term + Pauli exchange}} c_2(1, 2; 1', 2'; t) \quad (3.11)$$

Finally, we perform the Wigner transformation to express the equation in terms of physical phase-space distribution. This equation of motion is called “VUU” or “BUU” equation;

$$\frac{\partial f}{\partial t} + \frac{\vec{p}}{m}\vec{\nabla}_r f - \vec{\nabla}_r U \cdot \vec{\nabla}_p f = I_{\text{coll}}[f_1, \dots, f_N]. \quad (3.12)$$

The left hand side is equivalent to the Vlasov equation describing the free propagation within the mean-field where U is a self-consistent potential. On the right hand side, I_{coll} represents the collision integral arising from the trace term with the correlation matrix density. This term is connected to the transition rates from various contributed collision processes which reads,

$$I_{\text{coll}} = \frac{1}{(2\pi)^3} \int d^3\vec{p}_2 d^3\vec{p}_3 d\Omega |V_{12}| \left(\frac{d\sigma}{d\Omega} \right)_{12 \rightarrow 34} \delta^3(\vec{p}_1 + \vec{p}_2 - \vec{p}_3 - \vec{p}_4) \times \underbrace{[f_3 f_4 (1 - f_1)(1 - f_2)]}_{\text{Gain term: } 3+4 \rightarrow 1+2} - \underbrace{[f_1 f_2 (1 - f_3)(1 - f_4)]}_{\text{Loss term: } 1+2 \rightarrow 3+4}. \quad (3.13)$$

Several BUU-based transport models have been developed to simulate heavy-ion collisions, e.g., GiBUU (The Giessen BUU model) (Buss et al., 2012), PHSD (The Parton-Hadron-String Dynamics model) which includes both hadronic and partonic degree of freedom (Linnyk et al., 2016), and SMASH (The Simulating Many Accelerated Strongly-interacting Hadrons model) (Weil et al., 2016). In BUU transport models, the phase-space distribution function is often represented using test particles (Wong, 1982). This method discretizes the continuous distribution function into a large number of test

particles, each representing a small fraction of the system:

$$f_i(r, p, t) \sim \frac{1}{N_{tp}} \sum_i g(r - r_i(t))g(p - p_i(t)) \quad (3.14)$$

Here, N_{tp} is the number of the test particles and the g is the sharp function, e.g., the delta function. These test particles are generated for every time step and averaged over all events. Also, the mean-field potential is also updated according to the one-body test particles. However, this method reduces the ability to generate realistic 2-body correlations in each time step as well as the event-by-event fluctuations. These issues are, however, not a problem with the QMD approach which we will discuss later.

3.3 Ultra-relativistic Quantum Molecular Dynamics (UrQMD) model

In contrast to BUU models, Quantum Molecular Dynamics (QMD) approaches simulate the system using classical equations of motion for quasi-particles (Aichelin, 1991). Instead of using the test particles, each particle is represented as a Gaussian wave packet (Ono et al., 1992a), and their dynamics are governed by mutual 2-body interactions through effective potentials and realistic binary particle collisions. Thus the QMD approach (Hartnack et al., 1989; Ono et al., 1992a; Bass et al., 1998; Bleicher et al., 1999; Nara et al., 2000; Aichelin et al., 2020) could directly provide many-body correlations and fluctuations. It has recently extended its capabilities to describe larger clusters and even hyperclusters. In this thesis, we utilize the latest version of the UrQMD transport model (UrQMD v3.5). The UrQMD will be briefly introduced in this section.

3.3.1 Initialization

QMD approach initializes the particles with the explicit N-body nuclear wavefunction which can be approximated with a simple product of single-particle wavefunction, $\Psi(\vec{r}; t) = \prod_i^N \psi_i(\vec{r}, \vec{r}_i; t)$. Note that, in UrQMD, we can neglect the Slater determination for the antisymmetrization from the Pauli in exchange for the computational time. However, the nature of the two-body correlation will arise from the effective Pauli potential which will be discussed below. However, a few QMD models attempt to initialize with real antisymmetric wavefunction, e.g., Antisymmetrized Molecular Dynamics (AMD) model (Ono et al., 1992b) and the Fermionic Molecular Dynamics

(FMD) model (Feldmeier, 1990). In UrQMD, the single-particle wavefunction is assumed as a Gaussian wave packet,

$$\psi_i(\vec{r}, \vec{r}_i; t) = \left(\frac{1}{2\pi L} \right)^{4/3} \exp \left[-\frac{(\vec{r} - \vec{r}_i(t))^2}{4L} - i\vec{p}_i(t) \cdot \vec{r} \right]. \quad (3.15)$$

L is the width of the Gaussian wave packet in coordinate space. Then, we apply the Wigner transform in a similar fashion from Eq. 3.8. The phase-space density of particle i^{th} reads,

$$f_i(\vec{r}, \vec{p}; t) = \left(\frac{1}{\pi\hbar} \right)^3 \exp \left[-\frac{(\vec{r} - \vec{r}_i(t))^2}{2L} - 2L(\vec{p} - \vec{p}_i(t)) \right]. \quad (3.16)$$

The equation of motion in the QMD approach is derived from the Euler-Lagrange. The generalized Lagrangian function is given by,

$$\mathcal{L} = \int d^3 r_1 \dots d^3 r_N \Psi^* \left(-i \frac{\partial}{\partial t} - H \right) \Psi, \quad (3.17)$$

$$\mathcal{L} = \left(\frac{d\vec{r}_i}{dt} \cdot \vec{p}_i - T_i - \sum_j \langle V_{ij}^{\text{tot}} \rangle - \frac{3}{8mL} \right). \quad (3.18)$$

The N -body Hamiltonian is defined as $H = \sum_i T_i + \sum_{j \neq i} V_{ij}^{\text{tot}}$ where the kinetic energy and the total potential energy of the particle i^{th} are T_i and V_{ij}^{tot} with $\langle V_{ij}^{\text{tot}} \rangle = \int d^3 r_j d^3 p_j \int d^3 r'_j d^3 p'_j f_j(\vec{r}, \vec{p}) V_{ij} f_j(\vec{r}', \vec{p}')$. The total 2-body interactions involved

in the propagation are the following:

$$V^{\text{Skyrme}} = \alpha \left(\frac{\rho}{\rho_0} \right) + \beta \left(\frac{\rho}{\rho_0} \right)^\gamma, \quad (3.19)$$

$$V^{\text{Yukawa}} = C_{\text{yuk}} \frac{\exp(-\mu|\vec{r}_i - \vec{r}_j|)}{|\vec{r}_i - \vec{r}_j|}, \quad (3.20)$$

$$V^{\text{Coul}} = \frac{Z_i Z_j e^2}{|\vec{r}_i - \vec{r}_j|}, \quad (3.21)$$

$$V^{\text{MD}} = t_4 \ln [t_5 (\vec{p}_i - \vec{p}_j)^2 + 1] \delta(\vec{r}_i - \vec{r}_j), \quad (3.22)$$

$$V^{\text{Pauli}} = \frac{C_{\text{pauli}}}{(q_0 p_0)^3} \exp \left[-\frac{(\vec{r}_i - \vec{r}_j)^2}{2q_0^2} - \frac{(\vec{p}_i - \vec{p}_j)^2}{2p_0^2} \right]. \quad (3.23)$$

Already from here, one can see the difference between the QMD and BUU for the treatment of the 2-body (and 3-body) interactions. In QMD, they appear as effective potential replacing the real part of the transition matrix from the collision term. The local short-range V^{Skyrme} and long-range V^{Yukawa} potentials are responsible for the nucleon-nucleon interaction in the nucleus. The parameters α , β , γ are fixed to mimic the proper binding energy and the compressibility ruling the stiffness of the density-dependent equation of state, e.g., soft EoS and hard EoS. The parameter C_{yuk} is necessary to ensure the nuclear surface properties and its fluctuations. The Coulomb potential V^{Coul} is straightforward and does not need further explanation. The Momentum-Dependent potential V^{MD} is a small correction for more repulsive nuclear interactions leading to a small adjustment for the Skyrme's parameters and the stiffness of the equation of state. Finally, The Pauli potential is parametrized to prevent fermions from occupying the same phase-space cell. The last two potentials, although optional, are important in order to investigate the nuclear properties at low energies where the two-body or three-body correlations become strong, e.g., collective flow (Steinheimer et al., 2018; Steinheimer et al., 2022) and fluctuations (Ye et al., 2020).

3.3.2 Propagation and Collision

The propagation of all particles is also based on the non-relativistic Boltzmann or BUU equations similar to Eq. 3.12 where the time evolution of the momentum and

coordinate of particle i^{th} is evaluated by the Euler—Lagrange equations,

$$\frac{d\vec{r}_i}{dt} = \frac{\partial \langle H \rangle}{\partial \vec{p}_i}, \quad (3.24)$$

$$\frac{d\vec{p}_i}{dt} = -\frac{\partial \langle H \rangle}{\partial \vec{r}_i}. \quad (3.25)$$

However, unlike the BUU approach, UrQMD does not operate with the phase-space density or test particles but real microscopic n -body (classical-)particles of 70 baryon- and 39 meson-species (Table 3.1 and 3.2) and their antiparticles. Hence, the scattering process in the collision (source) term between hadrons will be triggered based on a geometrical interpretation of elastic and inelastic cross-sections. The collision will occur once the relative distance between two particles is below $d \leq \sqrt{\sigma_{\text{tot}}/\pi}$.

Furthermore, while two-body or three-body interactions in the BUU approach are calculated together in the collision term I_{coll} . It requires tedious calculation for both the real and imaginary parts of the transition matrix (or the Bruckner g -matrix). However, in the UrQMD approach, these interactions are expressed in terms of effective potentials replacing the real part of the transition matrix and leaving only the imaginary part in the collision terms. The imaginary part of scattering amplitude is modeled via binary elastic and inelastic collisions and fitted with the experimental data.

Baryon-Baryon scattering: The cross-section of the BB-scattering is given by,

$$\sigma_{\text{tot}}^{\text{BB}}(\sqrt{s}) \propto (2S_1 + 1)(2S_2 + 1) \frac{\langle p_{3,4} \rangle 1}{\langle p_{1,2} \rangle s} |\mathcal{M}(m_3, m_4)|^2, \quad (3.26)$$

where S_i is the spin of particle i^{th} . The matrix element $|\mathcal{M}(m_3, m_4)|$ will be taken in a general form with an adjustable free parameter to fit with the experiments. Or if the out-going particles are resonances, the matrix element will be written according to the mass distributions of Breit-Wigner form and fit with the decay width and branching ratio from PDG.

Meson scattering: The scattering processes for the meson are mostly reso-

Table 3.1 Table of Baryons.

N	Δ	Λ	Σ	Ξ	Ω
N ₉₃₈	Δ_{1232}	Λ_{1116}	Σ_{1192}	Ξ_{1317}	Ω_{1672}
N ₁₄₄₀	Δ_{1600}	Λ_{1405}	Σ_{1385}	Ξ_{1530}	
N ₁₅₂₀	Δ_{1620}	Λ_{1520}	Σ_{1660}	Ξ_{1690}	
N ₁₅₃₅	Δ_{1700}	Λ_{1600}	Σ_{1670}	Ξ_{1820}	
N ₁₆₅₀	Δ_{1900}	Λ_{1670}	Σ_{1750}	Ξ_{1950}	
N ₁₆₇₅	Δ_{1905}	Λ_{1800}	Σ_{1775}	Ξ_{2025}	
N ₁₆₈₀	Δ_{1910}	Λ_{1810}	Σ_{1915}		
N ₁₇₀₀	Δ_{1920}	Λ_{1820}	Σ_{1940}		
N ₁₇₁₀	Δ_{1930}	Λ_{1830}	Σ_{2030}		
N ₁₇₂₀	Δ_{1950}	Λ_{1890}			
N ₁₉₀₀		Λ_{2100}			
N ₁₉₉₀		Λ_{2110}			
N ₂₀₈₀					
N ₂₁₉₀					
N ₂₂₀₀					
N ₂₂₅₀					

Table 3.2 Table of Mesons.

0^{0-}	1^{--}	0^{++}	1^{++}
π	ρ	a_0	a_1
K	K^*	K_0^*	K_1^*
η	ω	f_0	f_1
η'	ϕ	f_0^*	f_1^*
1^{+-}	2^{++}	$(1^{--})^*$	$(1^{--})^*$
b_1	a_2	ρ_{1450}	ρ_{1700}
K_1	K_2^*	K_{1410}^*	K_{1680}^*
h_1	f_2	ω_{1420}	ω_{1662}
h_1'	f_2'	ϕ_{1680}	ϕ_{1900}

nance scattering. For example, the total cross-section for MB-scattering reads,

$$\sigma_{\text{tot}}^{\text{MB}}(\sqrt{s}) = \sum_{R=\Delta, N^*} \langle j_B, m_B, j_M, m_M | | j_R, M_R \rangle \frac{2S_R + 1}{(2S_B + 1)(2S_M + 1)} \times \frac{\pi}{p_{\text{cm}}^2} \frac{\Gamma_{R \rightarrow \text{MB}} \Gamma_{\text{tot}}}{(M_R - \sqrt{s})^2 + \Gamma^2/4} \quad (3.27)$$

where the decay width and branching ratio are obtained from the PDG data. However, for the unknown cross-sections, e.g., $\bar{B}B$, B^*B , YN , M^*B^* , M^*M^* , these processes will be obtained via detailed balance (Goulianos, 1983) or the Additive Quark Model (AQM) re-scaling (Danielewicz and Bertsch, 1991). For example,

$$\sigma_{\text{tot}}^{\text{MM}}(\sqrt{s} > 1.7 \text{ GeV}) = \sigma_{\text{tot}}^{\pi p}(\sqrt{s}) \frac{\sigma_{\text{AQM}}^{\text{MM}}}{\sigma_{\text{AQM}}^{\pi p}}. \quad (3.28)$$

One also should be noted that the particle productions are not only subjected to the scattering processes or cross-section calculations. The string excitation, fragmentation, and coalescence routines are also embedded to the current version of the UrQMD v3.5. The detailed implementations for the string excitation and the fragmentation can be found in Ref. (Andersson et al., 1983). While the coalescence routine will be discussed here.

3.3.3 (Hyper)nuclei Formation Routine

Another remarkable update of the UrQMD v3.5 is a coalescence routine for the (hyper)cluster formations. The coalescence model states that if two or more constituent particles are close enough in phase-space, they will coalesce and form into a cluster (see Ch. V for more details). Within UrQMD v3.5, the coalescence model is applied numerically using a method known as box coalescence.

For each pair of nucleons and/or hyperons, the relative distance in their center of mass frame is calculated. If their relative distance $\Delta x = |\mathbf{x}_{n,1} - \mathbf{x}_{n,2}|$ is less than $\Delta x_{\text{max},nn}$ and their relative momentum $\Delta p = |\mathbf{p}_{n,1} - \mathbf{p}_{n,2}|$ is less than $\Delta p_{\text{max},nn}$, and if the spin-isospin coupling probabilities are satisfied, a two-body state will form with combined momentum $\mathbf{p}_{nn} = \mathbf{p}_{n,1} + \mathbf{p}_{n,2}$ and position $\mathbf{x}_{nn} = (\mathbf{x}_{n,1} + \mathbf{x}_{n,2})/2$.

The procedure is then extended to form three-body cluster states. The relative distance within their local rest frame $\Delta x = |\mathbf{x}_{nn,12} - \mathbf{x}_{n,3}|$ must be

less than $\Delta x_{\max, \text{nnn}}$, and the relative momentum $\Delta p = |\mathbf{p}_{n,12} - \mathbf{p}_{n,3}|$ must be less than $\Delta p_{\max, \text{nnn}}$. If these conditions are met and the appropriate spin-isospin probabilities are satisfied, a three-body cluster will form with combined momentum $\mathbf{p}_{\text{nnn}} = \mathbf{p}_{n,12} + \mathbf{p}_{n,3}$ and position $\mathbf{x}_{\text{nnn}} = (\mathbf{x}_{n,1} + \mathbf{x}_{n,2} + \mathbf{x}_{n,3})/3$.

The criteria for forming these clusters are listed in Table ??, where Δx_{\max} and Δp_{\max} are determined based on iterative fits to cluster multiplicity data from various experiments (see Ref. (Hillmann et al., 2018; Sombun et al., 2019) for light nuclei and Ref. (Reichert et al., 2023c; Reichert et al., 2023d) for hypernuclei).

Table 3.3 The numerical coalescence parameters of UrQMD v3.5.

Particle	Δx [fm]	Δp [GeV/c]	spin-isospin
d	4.0	0.25	3/8
t, ${}^3\text{He}$	3.5	0.32	1/12
${}^4\text{He}$	3.5	0.41	1/12
$\text{N}\Xi$	9.5	0.15	3/8
${}^3\Lambda\text{H}$	9.5	0.15	1/12

In conclusion, due to the realistic n-body treatments of the UrQMD, the coalescence model will also register two-body correlation effects throughout the evolution allowing us to better capture the fluctuations, the correlations, and cluster formation (which may relate to the critical behavior) than other transport approaches. All these aspects are inline with our following investigations, thus we will use UrQMD v3.5 as our basis for the event simulations.

3.4 Hydrodynamics Models

The hydrodynamics model offers a comprehensive framework for simulating the dynamics of heavy-ion collisions, providing insights into the evolution of the quark-gluon plasma (QGP). One of the key advantages of hydrodynamic models is the explicit description of the thermodynamic properties of the medium, allowing for a more accurate incorporation of the equation of state (EoS).

The conservation laws of energy-momentum and baryon density form the

foundation of hydrodynamic models, expressed by the following equations:

$$\begin{aligned}\partial_\mu T^{\mu\nu} &= 0, & (\text{Energy-Momentum Conservation}) \\ \partial_\mu N^\mu &= 0, & (\text{Baryon Four-Current Conservation})\end{aligned}$$

Here, $T^{\mu\nu}$ represents the energy-momentum tensor, and N^μ denotes the baryon four-current. These quantities can be expressed in terms of the fluid's four-velocity u^μ and the thermodynamic state in the local rest frame of the fluid, described by the energy density ϵ , the pressure p , and the baryon density n :

$$T^{\mu\nu} = (\epsilon + p)u^\mu u^\nu - pg^{\mu\nu}, \quad N^\mu = nu^\mu. \quad (3.29)$$

In addition to the hydrodynamic equations, a specific EoS, $p = p(\epsilon, n)$, is required to close these coupling equations.

The standard relativistic hydrodynamics model treats the medium from the collision as a single fluid (Belenkij and Landau, 1955; Amsden et al., 1975; Wong et al., 1975; Csernai et al., 1980; Mishustin et al., 1987; Rischke, 1999; Spieles and Bleicher, 2020). However, this simple approach has its limitations, particularly in heavy-ion collisions where the conditions are far from equilibrium (Noronha-Hostler et al., 2016). One of the major shortcomings of the single fluid model is the assumption of instantaneous thermalization and infinite stopping power, which leads to unrealistically rapid thermal equilibration and excessive energy densities.

To address these issues, three-fluid hydrodynamics models have been proposed (Mishustin et al., 1989; Katscher et al., 1993; Brachmann et al., 1997; Ivanov et al., 2006; Batyuk et al., 2016; Cimerman et al., 2023). These models aim to parametrize the projectile, target, and fireball as separate fluids within the system. This three-fluid approach allows for a more realistic initialization and handling of the hydrodynamic expansion stage of the collisions. Each fluid component can permeate and exchange energy-momentum appropriately, overcoming the limitations of the single-fluid model. The basic equations of relativistic hydrodynamics for the three-fluid model involve the conservation of energy-momentum and baryon current for each fluid i :

$$\partial_\mu T_i^{\mu\nu} = F_i^\nu, \quad \partial_\mu j_i^\mu = S_i \quad (i = 1, 2, 3)$$

where the source terms F_i^ν and S_i account for the energy-momentum and baryon charge

exchange between the fluids. The total conservation equations obey $\sum_i F_i^\nu = 0$ and $\sum_i S_i = 0$. These source terms include frictional forces arising from the relative motion between fluids, where viscosity could enter the equations (Busza et al., 2018), influencing the flow dynamics and leading to the development of shear and bulk viscosity effects.

Hydrodynamic models, as macroscopic descriptions, primarily provide macroscopic observables or bulk properties of heavy-ion collisions, such as thermodynamic properties that may not be directly measured, like particle spectra. To translate these thermodynamic quantities into experimental observables, the freeze-out condition must be defined, marking the transition where particles free stream to the detectors.

Defining the freeze-out condition within hydrodynamic models is not straightforward and requires certain assumptions to describe hadronization. The “particlization” approach, which is adopted from the Cooper-Frye approach, occurs when the local thermodynamic properties (energy density) of the medium at the freeze-out hypersurface fall below a certain threshold. At this point, the fluid elements convert into hadrons, which subsequently stream freely to the detectors.

However, the criteria for freeze-out are debatable and model-dependent. This has led to a newly novel approach suggesting a continuous freeze-out during the evolution instead of a snapshot of the hypersurface at the end of the calculation (Grassi et al., 1996; Hung and Shuryak, 1998; Akkelin et al., 2008; Knoll, 2009).

Another approach is the hybrid model, where the hydrodynamic model is integrated into the early stage of a microscopic transport model, often referred to as an afterburner. This method provides the realistic initial stage and the possible phase transition from QGP where the partons dominate the system to a hadronic phase as well as realistic dynamics and kinetic freeze-out during and after the hadronic phase, e.g., resonances, decays, and re-scattering.

3.5 Hybrid Models

Describing the hadronic freeze-out and extracting secondary particle spectra presents a challenge for hydrodynamic models. The application of the Cooper-Frye equation (Cooper and Frye, 1974) is commonly used for this purpose, where the transition from the fluid to free hadrons occurs instantaneously on a hypersurface of equal local energy density.

Pure microscopic models, such as transport models, excel at describing the hadronic phase of heavy-ion collisions, effectively capturing the non-equilibrium dynamics and individual particle interactions. However, they struggle to accurately describe the QGP or partonic phase and capture the effects of a phase transition in the thermodynamical perspective which is important for the EoS studies.

Conversely, macroscopic hydrodynamic models are adept at describing the QGP phase and the collective flow at the early stage of the collisions, assuming local thermal equilibrium and using EoS to describe the system's evolution. Yet, they fall short in describing the hadronic phase, particularly the freeze-out process and subsequent particle interactions, due to their reliance on equilibrium assumptions.

The hybrid model aims to combine the strengths of both microscopic transport models and macroscopic hydrodynamic models. By integrating these approaches, hybrid models provide a comprehensive description of the entire evolution of a heavy-ion collision, from the initial QGP phase to the final hadronic interactions. In this section, we will briefly introduce the implementation based on the UrQMD hybrid approach (Steinheimer et al., 2008; Steinheimer et al., 2012).

The UrQMD hybrid model incorporates the hydrodynamic evolution of the QGP phase allowing for a more accurate depiction of the transition from (local) equilibrium hydro phase to non-equilibrium hadronic phases. The implementation steps are the following:

- **Initial State:** The hydrodynamic evolution begins after the two Lorentz-contracted nuclei have passed through each other, triggering the thermalization. The energy and momentum of the participants are mapped into hydrodynamic quantities serving as initial conditions (Petersen et al., 2008). The initial geometry is typically based on the Glauber model.
- **Hydrodynamic Evolution and EoS:** A (3+1)-dimensional ideal hydrodynamic evolution is assumed for the early stage collision, where the system is thermalized. The chosen EoS guides the fluid's evolution, determining how the system transitions from QGP to hadronic matter.
- **Final State - Particlization:** The change from the hydrodynamic to transport phase occurs through particlization, where hydrodynamic parameters are converted to hadron distributions using the Cooper-Frye procedure (Cooper and Frye, 1974). Finally, these particles and their interactions, e.g., scattering and

resonance decays, are simulated within the UrQMD transport algorithm until freeze-out.

In addition to the UrQMD hybrid model, several other hybrid models have been developed, integrating various transport and hydrodynamic approaches:

- Integrated UrQMD 3.3 (Petersen et al., 2008)
- Hadronic Dissipative Effects (Hirano et al., 2006)
- 3-D Hydro + Cascade Model at RHIC (Nonaka and Bass, 2006)
- NeXSpheRIO (Hama et al., 2008)
- EPOS+Hydro+UrQMD at LHC (Werner et al., 2010)
- MUSIC@RHIC and LHC (Schenke et al., 2011)

As mentioned before, particlization in pure hydrodynamics is akin to freeze-out, where particle spectra are generated from the final stage of the hydrodynamic evolution. However, in the hybrid model, particlization refers to the mapping of hydrodynamic quantities to particle distributions for the transport model. It is important to note that particlization is neither the hadronization process nor freeze-out but rather a practice for transitioning between two frameworks while maintaining consistent initial and freeze-out conditions.

The particlization is implemented numerically with a Monte Carlo based on the Cooper-Frye equation:

$$E \frac{dN}{dp^3} = \int d\sigma_\mu p^\mu f(x, p) \approx \sum_\sigma \Delta\sigma_\mu p^\mu f(x, p), \quad (3.30)$$

where σ_μ is a hypersurface element of hydrodynamics. The challenge lies in determining both the location and the normal direction of these surface elements. In Eq. (3.30), $f(x, p)$ represents the momentum distribution of hadrons inside the fluid. The assumptions about the fluid are directly reflected in the particle distribution

function. For near-equilibrium fluids, allowing for dissipation (viscous hydrodynamics), $f(x, p)$ reads:

$$f(x, p) = f_{F/B}(x, p) + \delta f \left(c_s^{(\text{shear})}, c_s^{(\text{bulk})} \right) . \quad (3.31)$$

This function is simply the density distribution of a fermion/boson gas, $f_{F/B}(x, p)$, plus terms representing shear and/or bulk viscosities, c_s (from dissipating non-equilibrium effects).



CHAPTER IV

EXPLORING THE SPACE-TIME STRUCTURE OF THE FIREBALL

As already emphasized in Ch. II, understanding the dynamical space-time picture of the heavy-ion collisions is important for interpreting the final stage observables from experimental data for EoS and the critical behavior studies.

We will begin this chapter by demonstrating the influence on the cluster formations, particularly the simplest cluster deuteron and antideuteron, from the freeze-out geometry of the fireball. We explore the fireball geometry across beam energy spectra to investigate the possible critical behavior on the source volume. Then UrQMD transport model will be employed to validate our findings.

Later on, we further our fireball volume investigation by studying the fireball space-time geometries from the effects of various phase transition scenarios, i.e., from different EoS using the HBT radii. The HBT radii are equivalent to the interpretation of the emission source for these clusters and they are related to the expansion time.

Overall, in this Ch. IV we present comprehensive studies on the space-time structure of the fireball from various beam energies and various EoS using the cluster formations and HBT radii.

Clusters are final stage observables and one of the most direct probes for such studies. Clusters are composed particles of nucleons. Their formations are sensitive to critical phenomena due to the fact that their constituents, nucleons, are subjected to baryon conservation. At the critical point, it is well known that all conserved quantities will diverge at chemical freeze-out. This leads to the divergence of the correlation length, fluctuation, and susceptibilities of the conserved quantities. The divergence of correlation length and fluctuation of the nucleons will influence the formation of the clusters at the kinetic freeze-out. These divergences are also related to the compression and expansion of the source volume, fireball.

However, these physical interpretations could only be manifested and investigated with the proper choice of formation mechanisms. The coalescence model states that if two or more nucleons are close enough in phase-space, they will coalesce and form a cluster at the very last stage of collisions, kinetic freeze-out (for more

details, see Ch. V). This physical description, on the space-time localization of the coalescence model, makes it suitable for our following studies. It allows us to investigate their emission sources and constituent density profiles and the all influences before their emission at kinetic freeze-out.

Back in 1992, the deviations from the simple approach were reported with the failure to predict antideuteron yield in Si+Au collisions at AGS (Aoki et al., 1992), where the measured antideuteron invariant cross section is suppressed by 5-10 times compared to the deuteron's. Since the simple coalescence dictates the cluster formation mainly by a single coalescence parameter B_2 , the formation of deuterons and antideuterons are expected to yield similar amount. This inconsistency leads to the development of the phase-space coalescence approach.

The failure to describe the suppression of antideuterons was attributed to the dependency of deuteron (Sato and Yazaki, 1981; Remler, 1981; Mrowczynski, 1987; Lyuboshits, 1988; Danielewicz and Schuck, 1992; Mrowczynski, 1992) and antideuteron (Mrowczynski, 1990; Dover et al., 1991; Leupold and Heinz, 1994) formation rates to the emission-source geometries in nuclear collisions. Then S. Mrówczyński proposed the geometrical space-time formation rate to address the phase-space coalescence model (Mrowczynski, 1993).

His approach assumed that antinucleons are emitted from the outer shell of the source due to a high probability of nucleon-antinucleon annihilation in the central baryon-rich region, while nucleons are emitted from the entire volume. Despite assuming spherical symmetry, this model successfully described experimental data from Si+Au collisions at $E_{\text{lab}} = 14.6A$ GeV (Aoki et al., 1992).

In the next section, we will apply the antideuteron and deuteron formation by Mrówczyński coalescence approach to reconstruct and explore the size of the emission source, assuming spherically symmetric (anti)nucleon source functions and call this approach “Mrówczyński coalescence model”.

4.1 (Anti)deuteron formation rate and source geometry

The original Mrówczyński coalescence model (Mrowczynski, 1993) purposed that the shape of the antinucleons source has to be reconsidered as well as suggesting an analytic formula to get rid of the un-measurable constant parameter p_0 . The (anti)deuteron distributions and (anti)nucleon distributions can then be formulated according to the tunable space-time parameter which can be related to the collision

system's initial conditions.

4.1.1 Mrówczyński Density Function

The main assumption of this approach is that the produced antinucleons located close to the center of the collision have a substantial probability to experience secondary interactions and annihilation in the baryonic rich environment. Antinucleons produced on the closer to the surface, on the other hand, have a higher chance to escape the fireball and proceed to coalescence. Nucleons are emitted from the whole source or fireball volume. From the above picture, we can impose and modify different geometries on the antinucleon and nucleon sources which can help us addressing the difference formation rates.

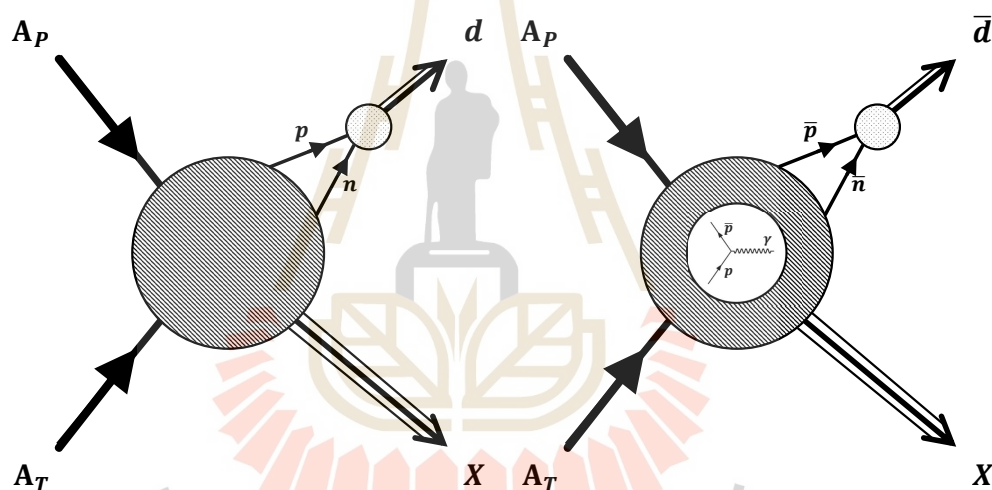


Figure 4.1 The schematic picture of the geometric coalescence model for (anti)deuteron formation if the two (anti)nucleons are close enough in phase-space. A_P and A_T are the incoming projectile and target nucleons and X represents the particles that carry the rest momenta of the system. (Left) The nucleon emission source is a whole spherical with radius r_0 . (Right) the survived antinucleons are emitted only on a spherical shell radius r_0 as the $N\bar{N}$ annihilations destroy most of the antinucleon at the center radius r_* .

The simple coalescence model describes the formation of clusters assuming that a pair of final-state (anti-)nucleons carrying similar momenta can coalesce to form a deuteron or an antideuteron with total momentum P . The invariant differential production cross sections for deuterons (d) and nucleons (p) and accordingly for

antideuterons and antinucleons are related by

$$E \frac{d^3 \sigma_d}{dP^3} = B_2 \left(\frac{E}{2} \frac{d^3 \sigma_p}{d(P/2)^3} \right)^2, \quad (4.1)$$

where (E, \vec{P}) and $(E/2, \vec{P}/2)$ denote the deuteron and nucleon 4-momenta and σ_{inel} is the total inelastic cross section. The coalescence parameter B_2 can be measured in experiments and is usually used to infer the volume of the source size. Then, Mrówczyński coalescence states that the formation rate is related to this coalescence parameter via $\mathcal{A} = \frac{m}{2} B_2$, with m denoting the nucleon mass. The formation rate \mathcal{A} is calculated as

$$\mathcal{A} = \frac{3}{4} (2\pi)^3 \int \int d^3 r_1 d^3 r_2 \mathcal{D}(\vec{r}_1) \mathcal{D}(\vec{r}_2) |\Psi_d(\vec{r}_1, \vec{r}_2)|^2, \quad (4.2)$$

where the bulk nucleon source $\mathcal{D}(\vec{r}_i)$ describes the probability of finding one nucleon at a given point \vec{r}_i in kinetic freeze-out fireball (volume emission) and $\Psi_d(\vec{r}_1, \vec{r}_2)$ denotes the deuteron wavefunction. The emitted nucleons are assumed to be uncorrelated.

Figure 4.1 shows the emission regions for (anti)nucleons, the nucleon source is distributed over the whole fireball, while the antinucleons are suppressed near the center of the whole volume. This leads to a surface-like to shell-like emission source for antinucleon's. The nucleon source function $\mathcal{D}(\vec{r})$ is parametrized by a normalized Gaussian (Mrowczynski, 1993),

$$\mathcal{D}(\vec{r}_i) = \frac{\exp(-\vec{r}_i^2/2r_0^2)}{(2\pi)^{3/2} r_0^3}, \quad (4.3)$$

with r_0 given by the mean radius squared $\langle r^2 \rangle = 3r_0^2$. The normalized antinucleon source function $\bar{\mathcal{D}}(\vec{r})$ contains a second Gaussian of width r_* that effectively cuts out the central region reads as

$$\bar{\mathcal{D}}(\vec{r}_i) = \frac{\exp(-\vec{r}_i^2/2r_0^2) - \exp(-\vec{r}_i^2/2r_*^2)}{(2\pi)^{3/2} (r_0^3 - r_*^3)}. \quad (4.4)$$

It is useful to simplify our analysis into the center of mass frame coordinates, $\vec{P} = \vec{p}_1 + \vec{p}_2$, $\vec{R} = \frac{1}{2} (\vec{r}_1 + \vec{r}_2)$ with relative motions, $\vec{p} = \frac{1}{2} (\vec{p}_1 - \vec{p}_2)$, $\vec{r} = \vec{r}_1 - \vec{r}_2$.

The deuteron wavefunction then factorizes to

$$\Psi_d(\vec{r}_1, \vec{r}_2) = \exp(i\vec{P}\cdot\vec{R})\phi_d(\vec{r}), \quad (4.5)$$

The Hulthén wavefunction reads

$$\phi_d(\vec{r}) = \left(\frac{\alpha\beta(\alpha + \beta)}{2\pi(\alpha - \beta)^2} \right)^{1/2} \frac{\exp(-\alpha r) - \exp(-\beta r)}{r}, \quad (4.6)$$

with parameters $\alpha = 0.23 \text{ fm}^{-1}$ and $\beta = 1.61 \text{ fm}^{-1}$ (Hodgson et al., 1997). The formation rate \mathcal{A} in relative coordinates then reads,

$$\mathcal{A} \equiv \frac{3}{4}(2\pi)^3 \int d^3r \mathcal{D}_r(\vec{r}) |\phi_d(\vec{r})|^2, \quad (4.7)$$

where the nucleon source function is

$$\mathcal{D}_r(\vec{r}) = \frac{1}{(4\pi)^{3/2} r_0^{3/2}} \exp(-r^2/4r_0^2), \quad (4.8)$$

and the antinucleon source function is

$$\overline{\mathcal{D}}_r(\vec{r}) = \frac{r_0^3 e^{-\frac{r^2}{4r_0^2}} + r_*^3 e^{-\frac{r^2}{4r_*^2}} - \frac{2^{\frac{5}{2}} r_0^3 r_*^3}{(r_0^2 + r_*^2)^{3/2}} e^{-\frac{r^2}{2(r_0^2 + r_*^2)}}}{(4\pi)^{3/2} (r_0^3 + r_*^3)^2}. \quad (4.9)$$

The antideuteron formation rate $\overline{\mathcal{A}}$ as function of r_0 is depicted in Figure 4.2. When the suppression region $r_* = 0 \text{ fm}$, the antideuteron formation rate is identical to the deuteron formation rate. As the size of the suppression region r_* increases at the same source size r_0 , the antideuteron formation rate decreases. This decrease is attributed to the thinning of the antideuteron emission shell as the suppression region expands.

4.2 Energy Dependence of Formation Geometry

To extract the energy-dependent geometries of the antideuteron and deuteron sources, we first determine the deuteron emission source radius r_0 by fitting the coalescence parameter B_2 from various experiments, as it is proportional to

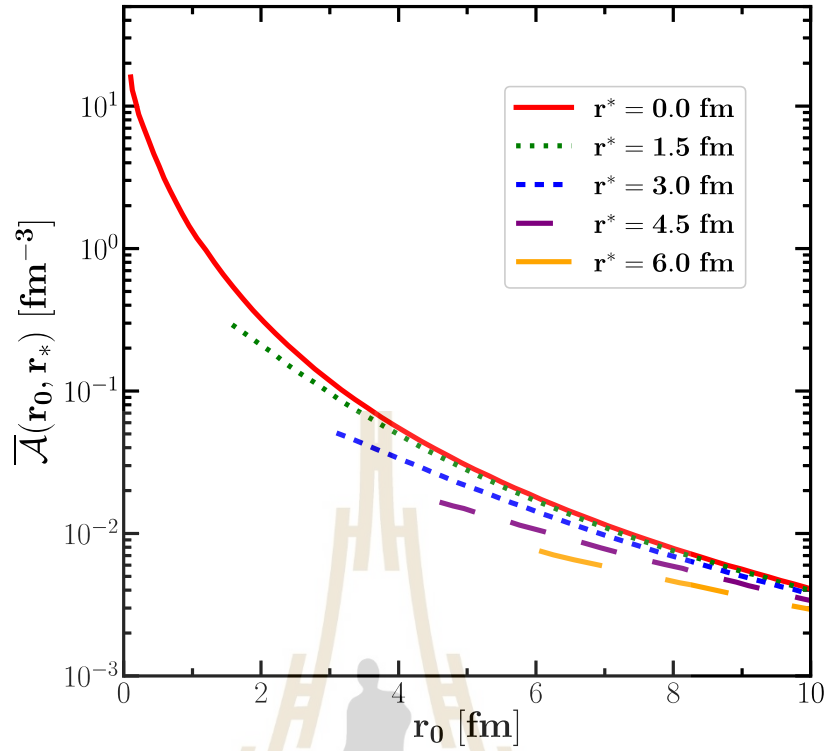


Figure 4.2 The antideuteron formation according to the source bulk radius r_0 with varying suppression radii r_* .

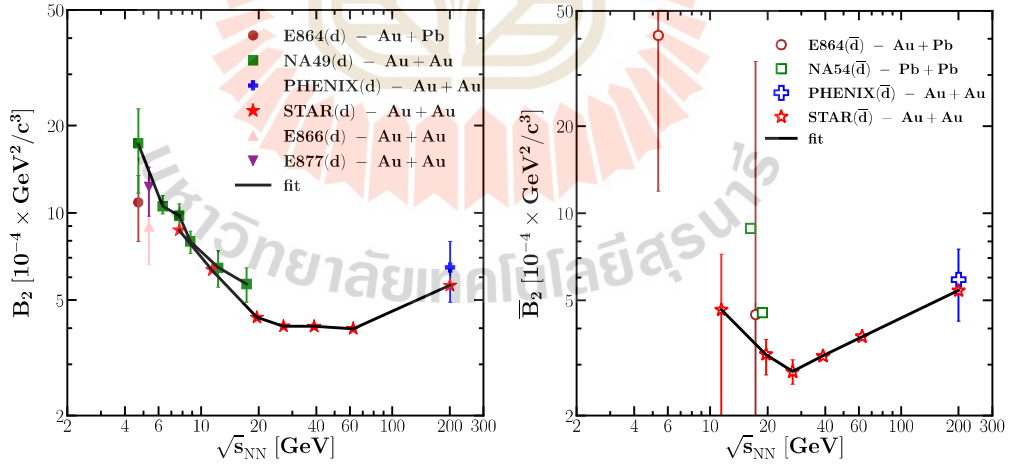


Figure 4.3 The energy dependence coalescence parameters B_2 for deuterons (left) and \bar{B}_2 antideuterons (right) from various experiments ranging from $\sqrt{s_{NN}} = 4.7 - 200$ GeV. The black lines show the B_2 and \bar{B}_2 fits using the extracted radii r_0 and r_* according to the formation rate in Eq. (4.7)

the deuteron formation rate $\mathcal{A}(\vec{r}, r_0)$. The fit results for experiments such as NA49 and STAR are illustrated in Figure 4.3 (left) as black lines. Next, we extract the suppression region of the antideuteron source r_* by fitting the antideuteron coalescence parameters $\overline{B}_2 \propto \overline{\mathcal{A}}(\vec{r}, r_0, r_*)$ to the experiments shown in Figure 4.3 (left). We assume that both deuteron and antideuteron share the same emission source radius r_0 . This process allows us to characterize both the emission source r_0 and the suppression region r_* , providing insights into the energy dependence of formation geometries.

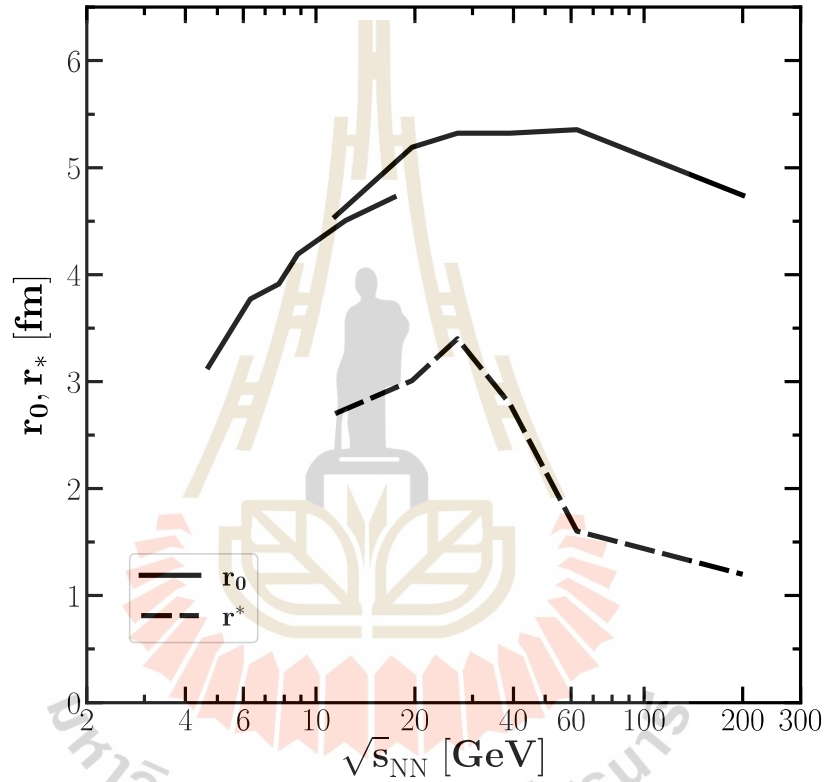


Figure 4.4 The emission source radius r_0 of deuteron (solid black lines) and the suppression region of antideuteron source r_* (dash-dotted line) as a function of energy

The energy dependence of the extracted source radii is presented in Figure 4.4. The deuteron emission source and also the antideuteron outer radius r_0 (solid black lines) exhibit rapid growth with increasing center-of-mass energy below $\sqrt{s_{NN}} = 20$ GeV. The extracted radii r_0 from NA49 and STAR experiments show good agreement with a smooth connection with respect to the center-of-mass energy. However, the growth is suppressed and declines after reaching a maximum at $\sqrt{s_{NN}} = 63$ GeV. The flattening and subsequent decrease in B_2 and r_0 for energies $\sqrt{s_{NN}} \geq 20$ GeV contradict the assumption that a volume of the emission source, i.e.,

a fireball, increases with energy. This phenomenon may be attributed to flow effects, as reported in Ref. (Gaebel et al., 2021).

Regarding the annihilation region, i.e., the inner radius r_* (depicted as a dash-dotted line), it similarly exhibits an increase at low energies followed by a drop after reaching a maximum at $\sqrt{s_{NN}} = 27$ GeV. This trend might suggest a nutcracker-like shell structure in this energy regime, as speculated by Ref. (Shuryak, 1999). The decrease in the inner radius implies that antideuterons have a higher probability of survival inside the fireball. This can be explained by the dominance of pions over nucleons in the fireball at this energy regime, significantly reducing the annihilation cross section of $N\bar{N}$.

4.3 Validation with UrQMD

For theoretical validation of the source geometries, we conducted simulations using the Ultrarelativistic Quantum Molecular Dynamics (UrQMD) transport model. Serving as a realistic microscopic simulation, UrQMD tracks the propagation of each hadron's 4-coordinates and 4-momenta from the initial collisions until the last collisions at kinetic freeze-out, accounting for all re-scatterings, annihilations, and decays. To confirm our interpretations of the nucleon and antinucleon source geometries and extract the corresponding parameters, we simulate 0 — 10% central Au+Au collisions at various collision energies ranging from $\sqrt{s_{NN}} = 7.7$ to 200 GeV. The nucleon and antinucleon distributions are examined in the transverse plane r_T given by $\frac{1}{r_T} \frac{dN}{dr_T}$, where $r_T = \sqrt{r_x^2 + r_y^2}$, the normalization by $1/r_T$ accounting for a cylindrical geometry at mid-rapidity. The expression of the (anti)nucleon distribution is

We present examples of the normalized transverse distribution r_T of (anti)nucleons at $\sqrt{s_{NN}} = 11.5$ and 200 GeV in Figure 4.5. In the case of $\sqrt{s_{NN}} = 11.5$ (left panel), within the range $r_T \leq 5$ fm, nucleons experience a slight suppression around 5% below the maximum. Conversely, the suppression of antinucleons is notably stronger, amounting to around 80%.

At the higher energy of $\sqrt{s_{NN}} = 200$ GeV (the right panel), both nucleons and antinucleons exhibit comparable suppression levels, approximately 60 — 70% at the core of the sources. This indicates that, across different energy regimes, both antinucleons and nucleons experience some kind of suppression at the core. For the nucleons, this is due to the increased production of other particles at the core of the fireball, particularly pions, which become dominant at higher energies. However, the degree of antinucleon suppression reflects nucleon-antinucleon annihilation. At high

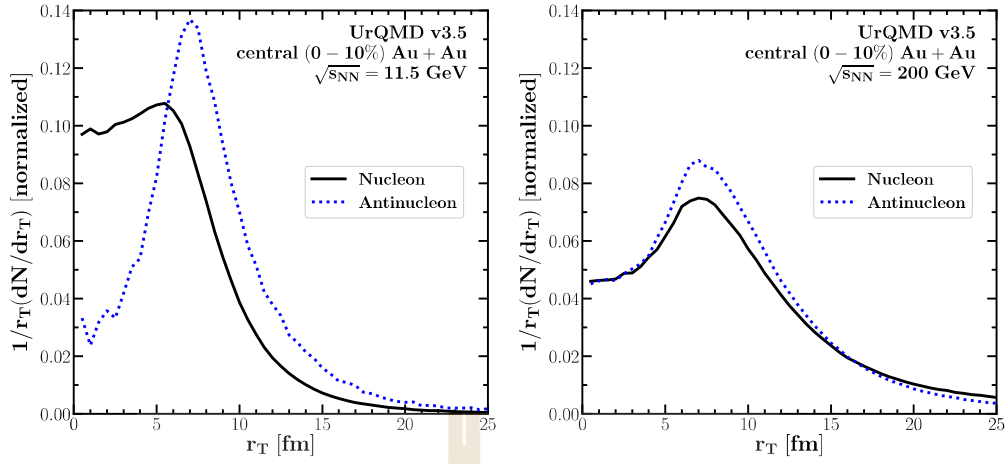


Figure 4.5 The normalised (anti)nucleon distribution in transverse plane r_T at $\sqrt{s_{NN}} = 11.5$ GeV (left panel) and $\sqrt{s_{NN}} = 200$ GeV (right panel). The black solid line represents the nucleon distribution and antinucleon distribution is depicted with the dotted line.

energies, the annihilation probability is reduced because the nucleon distribution is scarcer compared to lower energies reducing the suppression of antinucleons at the core.

After analyzing the quantitative distributions of both nucleon and antinucleon sources, we can extract the source geometries by fitting the nucleon and antinucleon distributions with Gaussian source functions $\mathcal{D}(r_0)$ and $\overline{\mathcal{D}}(r_0, r_*)$, respectively. We assume a simple non-suppressed source function for the nucleons. Additionally, the outer source radii of nucleons and antinucleons are assumed to be independent and fitted separately.

The extracted freeze-out geometries of (anti)nucleons shown in Figure 4.6 support the idea that nucleon-antinucleon annihilation is suppressed due to the pion enhancement at high energy, as evidenced by the drop in the inner radius r_* (open blue squares) with increasing energy. Furthermore, we observe that all the extracted radii exhibit a monotonic behavior with energy. This is in contrast to the sources extracted from the Mrówczyński coalescence model fitted with experimental data, which exhibit local maxima for both the shared r_0 and r_* of the antinucleon source. This might be attributed to using the cascade mode in UrQMD which lacks critical behavior as the EoS is turned off. The sizes of the nucleon source radius r_0 (full black circles) are comparable to the sizes of the antinucleon source's outer radius r_0 (full blue squares). This supports

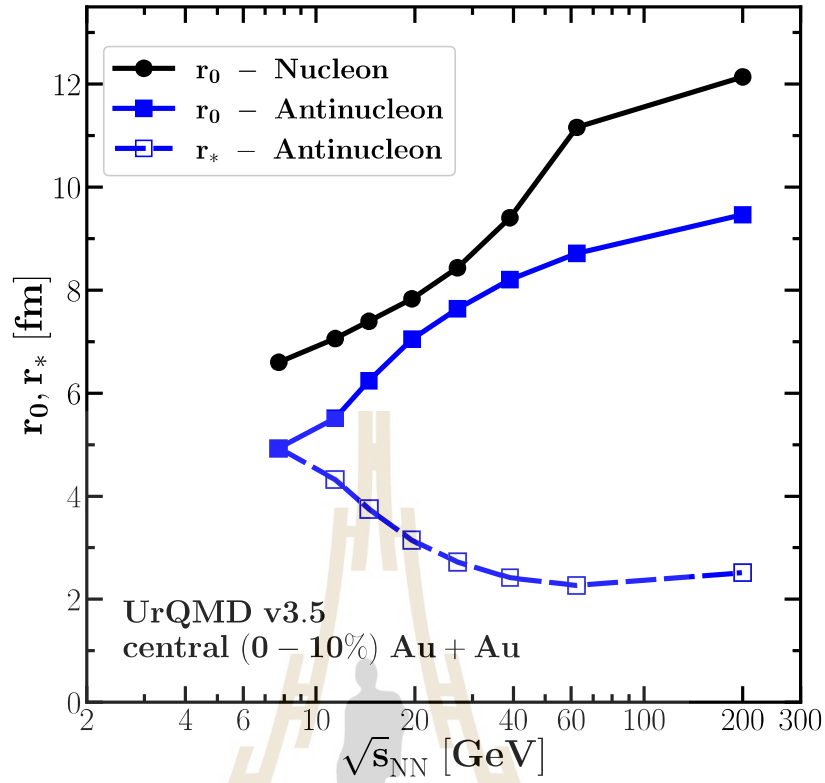


Figure 4.6 The energy dependence of the fitted (anti)nucleon source radii is illustrated. The solid circles represent the whole nucleon source radius r_0 . The extracted source radii of antinucleons are depicted with square symbols. The outer source radius of antinucleons r_0 is represented by the full symbols, while the inner source radius of the suppression region r_* is indicated by the open symbols.

our previous assumption that the antinucleon source shares the same source as nucleons, or at least, is very close around $r_0 \simeq 5 - 12$ fm. Although this value is twice that of the Mrówczyński nucleon source, it is understandable as in UrQMD, the (anti)nucleons gradually freeze out, while the Mrówczyński model assumes instantaneous emission.

In light of these differences, the qualitative comparison of the antinucleon source from two different approaches is undertaken by examining the r_*/r_0 ratio in Figure 4.7. It is expected that the r_*/r_0 ratio will approach or reach unity at the lowest energy, indicating complete suppression of antinucleon emission. While the results from the Mrówczyński coalescence model (red star symbol) cannot fully support this notion due to the lack of available experimental data at low energy $\sqrt{s_{NN}} < 10$ GeV, the ratio from UrQMD simulations (blue square symbol) does indeed converge to unity at $\sqrt{s_{NN}} = 7.7$ GeV. Furthermore, the overall trends from both approaches align well, as

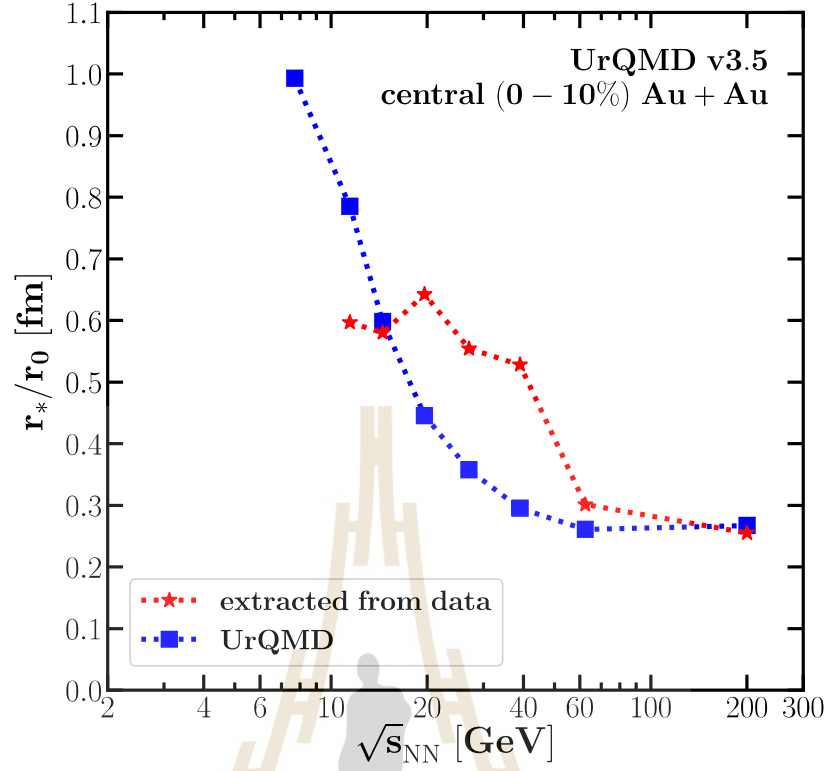


Figure 4.7 The energy dependence of the r_*/r_0 ratio of antinucleon source from Mrówczyński coalescence model (red star symbol) and UrQMD simulation (blue square symbol) at central 0 – 10% Au+Au collisions.

the ratios decrease with increasing energy, supporting the idea of reduced suppression from nucleon-antinucleon annihilation due to the dominance of pion enhancement in the fireball at high energy.

In conclusion, we have presented the Mrówczyński coalescence model which assumes an annihilation region inside the antinucleon source and extracted the (anti)nucleon source radii of r_0 and r_* by fitting the (anti)deuteron formation rate with available experimental data of B_2 and \overline{B}_2 from NA49 to STAR. Comparison with UrQMD supports the idea of suppression inside the core especially for the antinucleons at low energy. For high energy, the nucleon-antinucleon annihilation is suppressed due to the pions dominating the fireball as seen by the transverse distribution and the drop of r_* . Finally, the comparison of r_*/r_0 shows that both models share the same trend as UrQMD's ratio starts at unity at low energy as expected and both ratios decrease with energy. The disappearance of the local maximum of the ratio in UrQMD is attributed by the fact that we employ the cascade mode in UrQMD, so there is no critical behavior

from the change of the EoS. It would be interesting to test our model and the effects of the EoS within UrQMD in the future when experimental data at lower energies becomes available.

So far, we have demonstrated the interplay between the cluster formations and source volume which is crucial for understanding the QCD matter revolving around the critical point and first-order phase transition. The result has hinted at the possibility of critical behavior in the fireball volume measured by the coalescence parameter $B_2(\overline{B_2})$, contrasting with results from the (cascade) UrQMD model.

To deepen our understanding on the effects on the source volume from a phase transition, particularly at low energies, we turn to HBT interferometry (Lacey, 2015; Bluhm et al., 2020), specifically focusing on pion intensity (Pratt, 1986). HBT offers various unique observables sensitive to the first order phase transition, allowing us to probe the critical behavior of the (emission) source volume via the space-time structure and momentum correlations (Ackermann et al., 2003; Csorgo et al., 2006).

The investigations into the effects of the EoS on HBT interferometry within different models are mostly limited to high energies (Pratt, 1986; Bertsch et al., 1988; Ma et al., 2006). Moreover, at high beam energies, other observables like fluctuations haven't exhibited the anticipated behavior indicative of a phase transition. These intensify the debate surrounding the existence of the critical point.

The following section aims to study the interplay between phase transitions and HBT source volumes, with different phase transition scenarios or EOS toward lower energies.

4.4 HBT Correlation

The principle of HBT interferometry proposed by R. Hanbury-Brown and R. Q. Twiss in 1954 (Brown and Twiss, 1956) has become a useful tool in the study of the space-time geometry of the emission sources in astronomy (Hanbury Brown and Twiss, 1956), and nuclear and particle physics (Goldhaber et al., 1960; Csorgo, 2006).

The main difference between the HBT interference and the conventional Michelson interferometry is that the latter one is based on the superposition of two amplitudes. The interference pattern is predicted simply by the path difference between two sources as a function of relative angle. In contrast, the HBT interference occurs by correlating two wave intensities which can also result in intensity distributions as a function of the relative angle between the detectors. Thus, HBT interferometry

can also be understood as intensity interferometry (Wiedemann and Heinz, 1999).

4.4.1 Two-Particle Correlations

The effect of HBT correlations is strongly related to the flow (Dinh et al., 2000; Retiere and Lisa, 2004; Lisa et al., 2005) which can be used to hint at a phase transition (Speies and Bleicher, 2020). Various species of particle waves are emitted from the created fireball. Let us consider the particles emitted from the source according to a density distribution $\rho(r)$. The source is parametrized at the later stage of the collision where the source distribution is at the kinetic freeze-out stage. The correlation function C is defined as a ratio of the correlation intensity I_{AB} from detector A and detector B divided by the individual intensity from detector A and B, I_A and I_B , i.e., $C = I_{AB} / (I_A \cdot I_B)$.

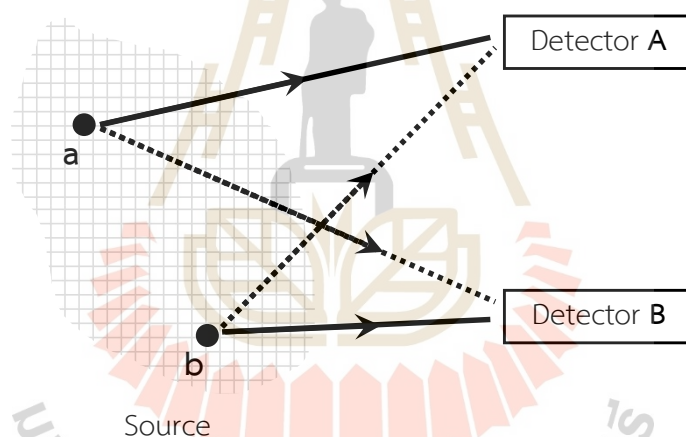


Figure 4.8 The diagram of particle detection. Particle 1 and particle 2 are emitted, with a four-momentum p_1 and p_2 , at points a and b respectively. Then they are detected by detectors A and B. If the particles are identical, we also need to consider the cases where the particles propagate indistinguishably into the detectors as illustrated with the dashed lines.

According to Figure 4.8, we can measure the correlation function by the density ratio of two-particle coincident event divided by the single particle event in phase-

space. The correlation function now reads,

$$c(\vec{k}, \vec{q}) = \frac{(d^6N/d\vec{p}_1 d\vec{p}_2)}{(dN^3/d\vec{p}_1) \cdot (dN^3/d\vec{p}_2)} = \mathcal{N} \frac{P(p_1, p_2)}{P(p_1) \cdot P(p_2)}, \quad (4.10)$$

where the relative and average momentum of the two particles are denoted by $\vec{q} = (\vec{p}_1 - \vec{p}_2)$ with $q_0 = E_1 - E_2$ and $\vec{k} = \frac{1}{2}(\vec{p}_1 + \vec{p}_2)$ with $k_0 = E_0 = \sqrt{m^2 + \vec{k}^2}$. Here, $P(p_i)$ is the probability of a single particle carrying four-momentum p_i , \mathcal{N} is a normalization factor between $P(p_1, p_2)$, the probability of the coincident event with particle 1 having four-momentum p_1 and particle 2 having four-momentum p_2 , and the product of two $P(p_i)$, the probability of an uncorrelated single particle event. We have

$$P(p_1, p_2) = \int_{\text{source}} S(x_1, p_1) S(x_2, p_2) |\phi(q, r)|^2 d^4x_1 d^4x_2, \quad (4.11)$$

where $\phi(q, r)$ is the probability amplitude for detecting two particles described with by relative four-momentum $q = p_1 - p_2$, $k = \frac{1}{2}(p_1 + p_2)$ and space-time point $r = (x_1 - x_2)$, $R = \frac{1}{2}(x_1 + x_2)$, one from point a with p_1 in detector A and one from point b with p_2 in detector B. However, since the particles of interest are identical, we cannot determine which particle is registered by A or B. So, we need to consider the exchange of two particles as a linear combination,

$$\phi(p_1, p_2) = \frac{1}{\sqrt{2}} (\phi_{12} \pm \phi_{21}). \quad (4.12)$$

Here, $\phi_{12}(\phi_{21})$ represents the case where particle 1(2) from point a is detected in A(B) and particle 2(1) from point b in B(A). For bosons, we have a symmetric configuration (plus-sign). For fermions, we have an anti-symmetric configuration, thus a minus sign.

If a single emitted particle is described by a plane wave as a free particle, we have

$$\begin{aligned} \phi_{12} &= e^{ip_1 \cdot x_1} \cdot e^{ip_2 \cdot x_2}, \\ \phi_{21} &= e^{ip_2 \cdot x_1} \cdot e^{ip_1 \cdot x_2}, \end{aligned}$$

where the space-time coordinates of positions a and b are denoted x_1 and x_2 , respec-

tively. Now Eq. (4.11) becomes,

$$\begin{aligned}
 P(\mathbf{q}, r) &= \int_{\text{source}} \mathcal{S}(\mathbf{r}) \mathcal{S}^*(\mathbf{r}) d^4 r d^4 r \\
 &\quad \pm \int_{\text{source}} \mathcal{S}(\mathbf{r}) e^{i\mathbf{q}\cdot\mathbf{r}} d^4 r \mathcal{S}(\mathbf{r}) e^{-i\mathbf{q}\cdot\mathbf{r}} d^4 r \\
 &= |\mathcal{F}[\mathcal{S}(0)]|^2 \pm |\mathcal{F}[\mathcal{S}(\mathbf{q})]|^2, \tag{4.13}
 \end{aligned}$$

with a smoothness approximation coupled with the on-shell momentum, we can use $S(R - \frac{r}{2}, k - \frac{q}{2}) S(R + \frac{r}{2}, k + \frac{q}{2}) \simeq S(r, k) S(r, k)$, and define $\mathcal{S}(\mathbf{r}) \equiv S(\mathbf{r}) e^{i\mathbf{q}\cdot\mathbf{r}}$. For the single-particle probability, we have $P(p_i) = \int_{\text{source}} S(x_i) e^{i\mathbf{p}_i \cdot \mathbf{x}_i} d^4 x = \mathcal{F}[R(0)]$. Substituting into the correlation function (Eq. (4.10)), we finally end up with,

$$c(\vec{k}, \vec{q}) = 1 \pm \frac{|\mathcal{F}[\mathcal{S}(\mathbf{q})]|^2}{|\mathcal{F}[\mathcal{S}(0)]|^2}. \tag{4.14}$$

Here, we can clearly see the relation between the correlation and the source density distribution. The mass-shell constraint is $\mathbf{k}\cdot\mathbf{q} = 0$ and it is convenient to consider the system in the co-moving frame of the particle pair. Thus in this particle pair rest frame, the time structure of the relative source and correlation function are integrated out, i.e., $S(\vec{q}, \vec{r})$ and $C(\vec{k}, \vec{q})$. We assume a certain source function $S(\vec{q}, \vec{r})$ for the fireball and fit the result with experimental data. In this way, we can get a general idea of the size and the lifetime (Kopylov and Podgoretsky, 1972) of the emission source created by the collisions (Shuryak, 1973).

A different choice of source distribution will give us a different interpretation of the freeze-out formation. The most common parametrization for the source is the Gaussian distributions, $S(\vec{r}, t) \propto \exp(-\vec{r}^2/2R^2)$, resulting in a correlation function $C(\vec{k}, \vec{q})$ given by,

$$c(\vec{k}, \vec{q}) = 1 \pm \lambda \cdot \text{Re} \exp\left(-\frac{1}{2} \mathbf{q}^2 R^2\right). \tag{4.15}$$

The factor λ is called ‘‘chaoticity’’ or ‘‘incoherent factor’’ and added as a free parameter for a better fitting to the data (Adams et al., 2005; Adhikary et al., 2023; Weiner, 2000; Kincses et al., 2020). So far, we have discussed only the simplest example of the two-particle correlations. The correlation functions can be parametrized by various

formulae depending on the origin of correlations between considered particles.

Ref. (Chapman et al., 1995a) has shown in detail that one can assume an expanding source parametrized alternative to the Gaussian (Bertsch et al., 1988; Boal et al., 1990; Sarabura et al., 1992; Abbott et al., 1992; Seyboth et al., 1992; Chapman et al., 1995b; Roland, 1994; Heinz et al., 2002) by Yano-Koonin-Podgoretsky (Yano and Koonin, 1978) and Heinz (Chapman et al., 1995a) which is appropriate to explicitly take into account a collective cylindrical expansion, the correlation due to quantum statistics can be parametrized in terms of the components of q :

$$C(q_L, q_O, q_S) = 1 + \exp\left(-R_L^2 q_L^2 - R_O^2 q_O^2 - R_S^2 q_S^2 - 2R_{OL}^2 q_{OL}^2\right), \quad (4.16)$$

where q_i is the relative momentum of a particle pair in longitudinal q_L , outward q_O and sideward q_S directions, and R_i are the HBT radii in the same direction as defined for q_i . An advantage of using this coordinate system is that the outward radius R_O reflects the space-time structure of the source. The sideward radius R_S is separated from the temporal structure and measures a bare spatial extension. The observation of a pronounced difference of these two radii on the transverse plane, i.e., $R_O^2 - R_S^2$ or R_O/R_S , is expected to provide a hadronic signature for the realization of the new state of matter* (Chapman et al., 1995a; Ackermann et al., 2003; Heinz and Kolb, 2002; Retiere and Lisa, 2004; Kolb and Heinz, 2004; Lisa et al., 2005; Shen and Heinz, 2012). Once the quark-gluon plasma is formed, one expects that the time evolution of the system becomes slower in the phase transition (or possibly, a crossover) regime, which reflects in the long lifetime of the hadron source, and possibly a prolonged emission time.

In the above considerations, the electromagnetic interactions between charged hadrons were neglected. Namely, the quantum-statistical correlation functions discussed so far were obtained with the plane-wave assumption for the wavefunction. In the following, these will be denoted by $C_0(\vec{q}, \vec{k})$.

If the final-state electromagnetic interactions are also taken into account, the correlation function has to be calculated not via the interference of plane waves, but via the interference of solutions of the two-particle Schrödinger equation with a Coulomb-potential, describing the final state electromagnetic interactions. The ratio of these two correlation functions is called the Coulomb correction (Csorgo et al., 2004):

* Note that it has been shown in Ref. (Chapman et al., 1995a) that the interpretation for $R_O^2 - R_S^2 \propto \Delta t_{\text{emission}}$ is highly model dependent. However, only within the fixed frame, such an assumption is justified.

In order to extract the quantum-statistical effects, the counter-acting influence of the Coulomb repulsion as well as the dilution by misidentified pairs must be taken into account, while the effect of the strong interaction can be neglected (Csorgo et al., 2004; Kincses et al., 2020). This leads to the ansatz:

$$C = N \left[(1 - \lambda) + \lambda K_C(q_{inv}, R_{inv}) \cdot C_2(\vec{q}, \vec{k}) \right] \quad (4.17)$$

where λ denotes the purity of the pairs, K_C represents the Coulomb repulsion factor, and $C(q)$ is the correlation from quantum statistics parameterized by the source function. For pions, the Coulomb correction can be approximately determined from the experimental correlation function for unlike-sign pairs (Boal et al., 1990; Bowler, 1991; Baym and Braun-Munzinger, 1996), which is dominated by the Coulomb interaction and receives no contribution from Bose-Einstein correlation.

The factor $K_C(q_{inv}, R_{inv})$ describes the Coulomb interaction. It is determined as (Sinyukov et al., 1998; Csorgo, 2008; Rogochaya, 2017),

$$K = \frac{C(QS + \text{Coulomb})}{C(QS)} \quad (4.18)$$

4.5 Simulation set-ups and EoS

We use the latest version of the UrQMD transport model (UrQMD v3.5) to generate the freeze-out scenarios within heavy-ion collisions operated in various EoS modes and use the “correlation after-burner” (CRAB v3.0 β) program (Pratt, 2000) to explore the results via pion intensity interferometry.

The study will first employ three default modes within UrQMD as baseline for comparing the results from different equations of state with different types of phase transitions: I) The cascade mode is primarily used for simulating high-energy collisions where the interactions between hadrons are predominantly binary scattering and the effects of nuclear potentials become less significant compared to lower energies. Thus, in cascade mode, nuclear potentials are turned off, and interactions occur solely through binary scattering based on available cross-sections. II) The soft EoS mode is used to refer to the system with more substantial compression and less stiffening of the matter created in heavy-ion collisions. Soft EoS modes are often employed to study collisions at lower energies, where the system may spend more time in a dense, hot state before

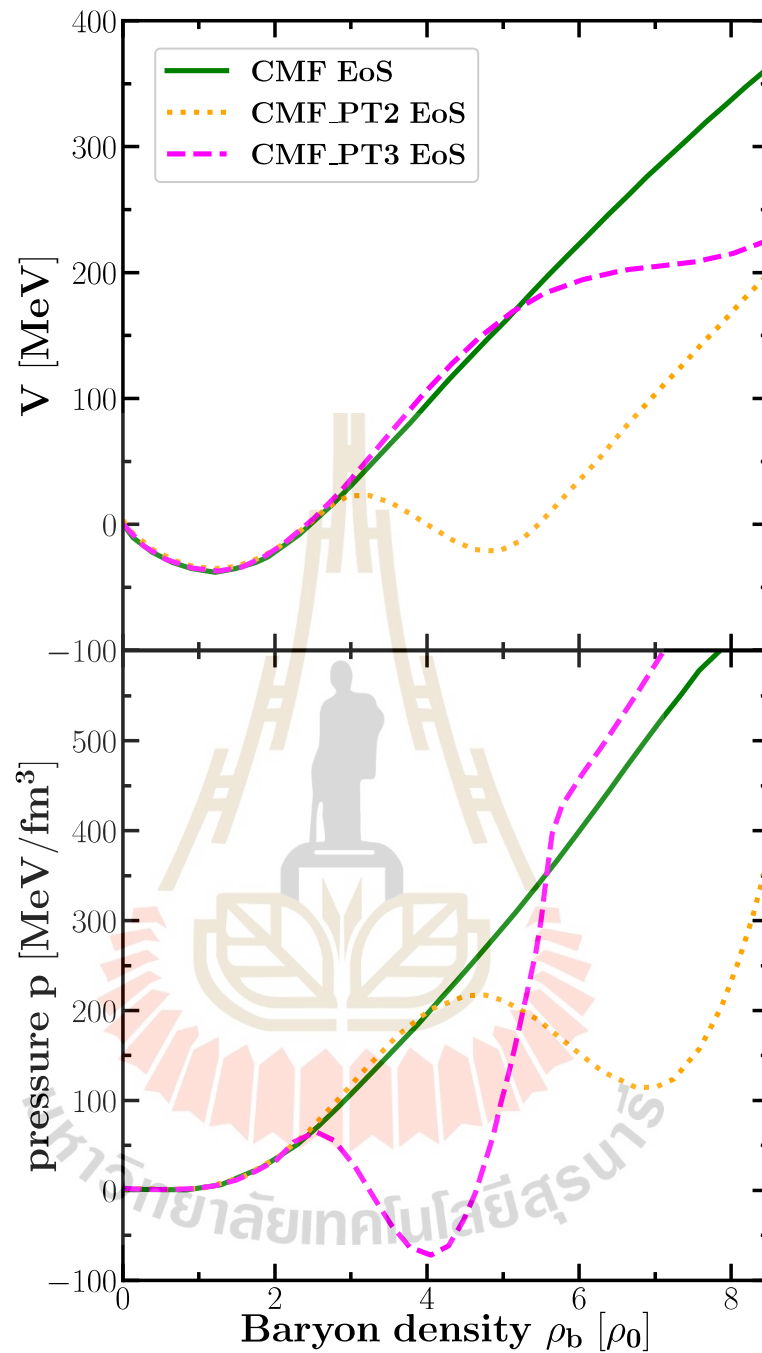


Figure 4.9 The comparison of the density dependent potential V (a) and the pressure p (b) from different the CMF EoS scenarios. CMF_PT2 EoS and CMF_PT3 EoS both are incorporated with a phase transition as well as instability region indicated by local maximum and minimum. The simple CMF EoS corresponds to a smooth crossover transition (Li et al., 2023).

expanding and cooling. The softer interactions can lead to more substantial collective flow patterns, allowing researchers to investigate the transition from the initial dense phase to the final state hadrons. At the phase transition, the system is expected to be at the softest point. III) The hard Skyrme EoS represents a scenario with less compression and more rapid expansion of the matter created in heavy-ion collisions and is often used for simulating collisions at higher energies. While this may initially suppress collective flow, the higher temperatures and densities reached in collisions at higher energies can still induce significant flow effects.

Then, we extend our investigation by adopting EoS based on chiral mean field (CMF) models (Machleidt and Entem, 2011; Omana Kuttan et al., 2022) with different phase transition scenarios to demonstrate how distinct EoS and phase transitions manifest in pion interferometry. The successful integration of CMF in the UrQMD model is done by calculating the density-dependence mean field potential energy V from the CMF model's energy per baryon as demonstrated in Figure 4.9 and also in detail in Ref. (Motornenko et al., 2020; Omana Kuttan et al., 2022).

To explore the effects of various EoS with and without different phase transition scenarios, we feed the obtained pion freeze-out phase-space coordinates at the last interactions (either collisions and decay) from UrQMD calculations to the “correlation after-burner” (CRAB v3.0 β) program (Pratt, 2000), provided by S. Pratt.

4.6 Two-Pion HBT Analysis

To begin our analysis, we want to rule out other influences or effects that could affect the final results. The Coulomb interaction could microscopically alter hadron trajectories and influences the spatial and momentum correlations at freeze-out, ultimately impacting the collective behavior of the system on the macroscopic level. Consequently, the inclusion or neglect of Coulomb interactions in HBT calculations can lead to differences in the extracted HBT radii and, thus, affect interpretations of the system size and dynamics.

Figure 4.10 compares the transverse momentum dependence (k_T) of HBT radii in central 0 — 10% Au+Au collisions at $\sqrt{s_{NN}} = 2.4$ GeV for different Coulomb interaction scenarios with the hard EoS. The analysis focuses on negative pion pairs with a pair-rapidity cut at $|y_{\pi\pi}| < 0.35$, defined as $y_{\pi\pi} = \frac{1}{2} \ln \frac{(E_1 + E_2 + p_{1,L} + p_{2,L})}{(E_1 + E_2 - p_{1,L} - p_{2,L})}$, where E_i and $p_{i,L}$ represent the energies and longitudinal momenta of each pion, respectively. This configuration aligns with the experimental data.

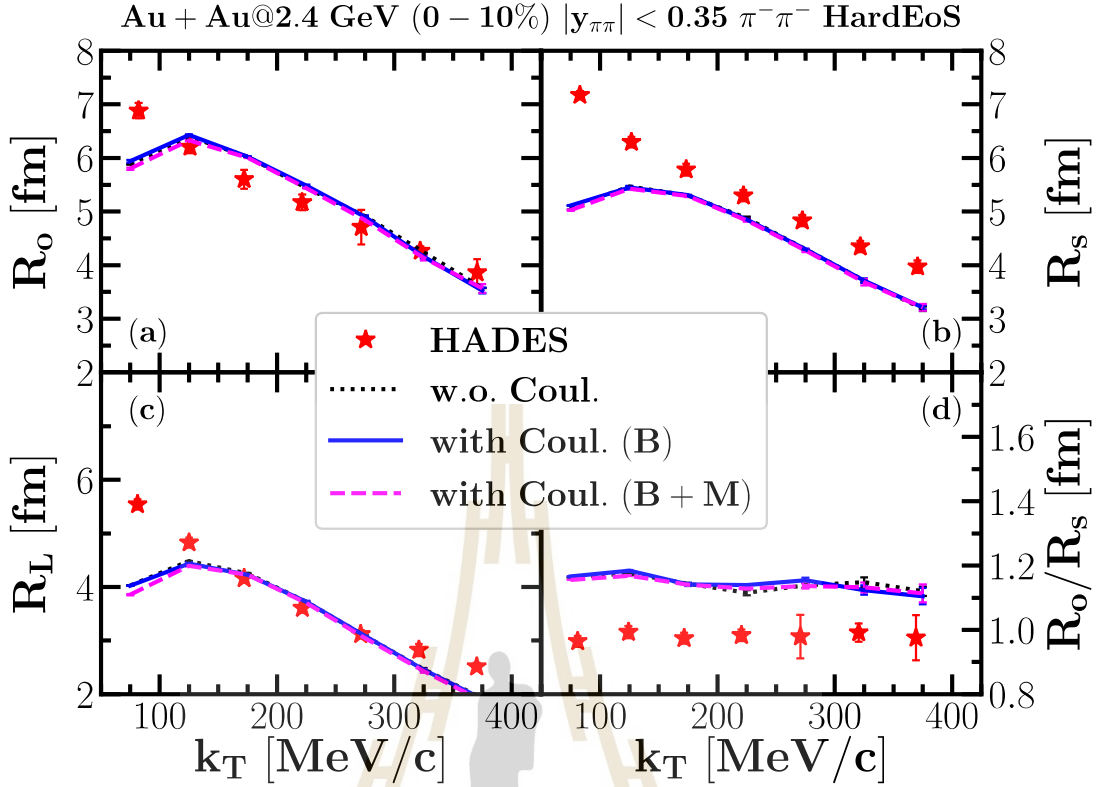


Figure 4.10 Comparison of k_T dependence of pion HBT radii showing the effect of Coulomb interactions. Panels (a), (b), and (c) display the R_0 , R_s , and R_L radii, respectively, and panel (d) shows the ratio R_0/R_s of the π -source from central (0 – 10%) Au+Au collisions at $\sqrt{s_{NN}} = 2.4$ GeV. Red star symbols depict the results from the HADES experiments (Adamczewski-Musch et al., 2019). Black dotted lines indicate the UrQMD simulation results without Coulomb potential (w.o. Coul.), blue dashed lines show the UrQMD simulation results with Coulomb potential for baryons only (with Coul. (B)), and pink solid lines depict the UrQMD simulation with the full Coulomb potential for all hadrons (with Coul. (B+M)).

At high transverse momenta ($k_T > 100$ MeV/c), all simulation scenarios can reproduce the data reasonably well, except for a slight underestimation of R_s . This underestimation leads to a higher R_0/R_s ratio compared to the measured values. Furthermore, it is clear that the impact of the Coulomb potential from both scenarios (blue dashed lines and pink solid lines) is negligible when compared to the Coulomb-free interaction (black dotted line).

Therefore, the subsequent discussion will omit the Coulomb effect on the

HBT radii. The following results will more or less come from purely nuclear potential, i.e., the choice of EoS and the phase transition.

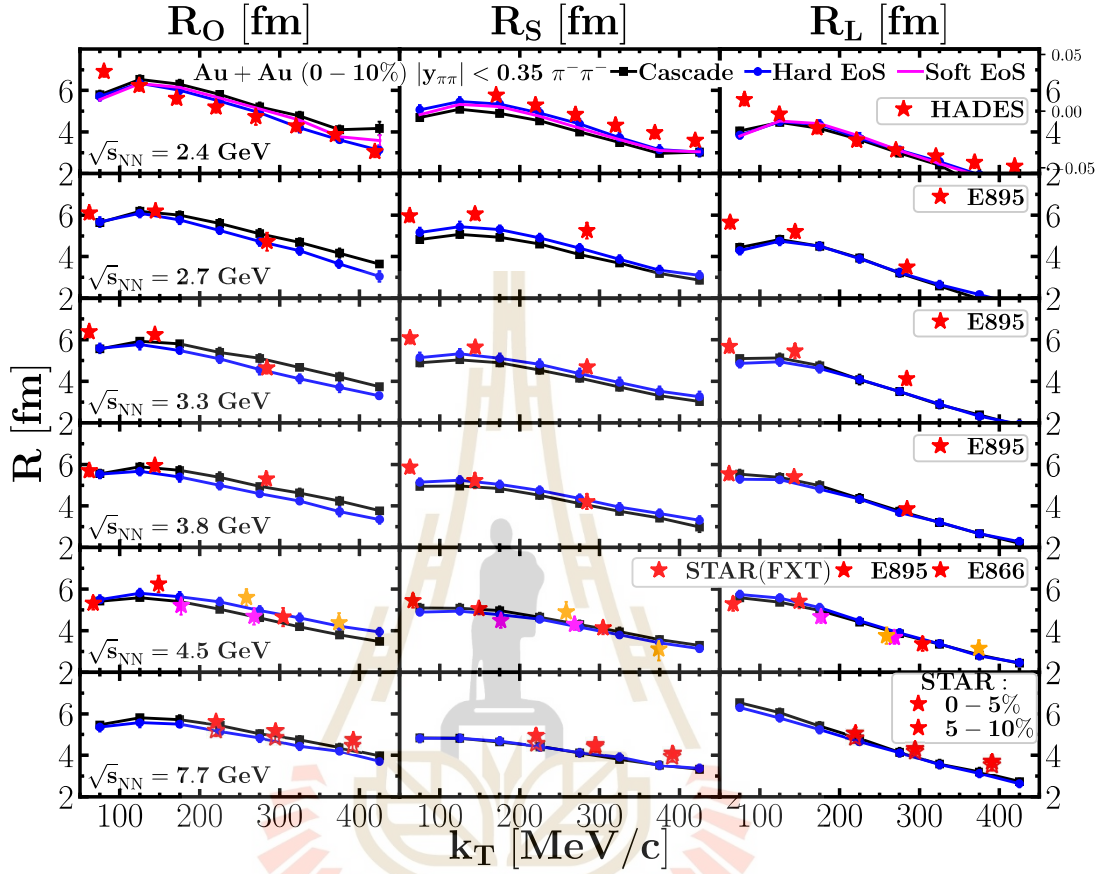


Figure 4.11 The transverse momentum (k_T) dependence of the HBT radii, R_O (left panels), R_S (middle panels), and R_L (right panels), for 0 — 10% central Au+Au collisions at $\sqrt{s_{NN}}$ ranging from 2.4 GeV (top panels) to 7.7 GeV (bottom panels). Experimental data are denoted by star symbols from HADES, E895, E866, and STAR collaborations (Lisa et al., 2000; Lisa et al., 2005; Adamczyk et al., 2015; Adamczewski-Musch et al., 2019; Adamczewski-Musch et al., 2020; Adam et al., 2021). The UrQMD simulations are represented by lines: the cascade mode (black line with square), hard EoS (blue line with circle), and soft EoS (solid pink line).

The influence of the density dependence of the nuclear potential on HBT radii is explored in Figure 4.11. The UrQMD model simulations are depicted for three scenarios: cascade mode (black line with square), hard EoS (blue line with circle), and soft EoS (solid pink line) are compared with experimental data (star symbols) (Lisa et al., 2000; Lisa et al., 2005; Adamczyk et al., 2015; Adamczewski-Musch et al., 2019; Adamczewski-

Musch et al., 2020; Adam et al., 2021) as a function of transverse momentum (k_T) within the same collision system and rapidity configuration mentioned above.

A clear impact of the nuclear potential is evident when comparing the colored lines (with nuclear potential) to the black line with squares (without nuclear potential) across the entire k_T range. This effect is particularly pronounced at lower center-of-mass energies. The hard EoS (blue line with circle) generally leads to a decrease in R_0 values and an increase in R_S compared to the cascade mode (black line with squares). This behavior results in a better description of the experimental data (star symbols) observed for most collision energies. The soft EoS (solid pink line) exhibits qualitatively similar trends to the hard EoS, hence we present the results only for $\sqrt{s_{NN}} = 2.4$ GeV for the sake of brevity.

An interesting observation is seen at $\sqrt{s_{NN}} = 4.5$ GeV, where the hard EoS predicts a higher R_0 than the cascade mode, unlike at other energies. This finding suggests a potential non-monotonic behavior in the difference between R_0 and R_S , which may not necessarily be indicative of a critical point associated with a phase transition. To gain a deeper understanding of these observations, the next section will focus on a detailed analysis of the R_0 and R_S difference across various nuclear potential scenarios, including those incorporating and excluding a phase transition.

4.7 Effect of the EoS with Phase Transition

As discussed earlier, the expected non-monotonic behavior in the R_0 and R_S difference remains ambiguous (Pratt, 2009). It's unclear whether this arises from critical behavior near the phase transition or solely from the effects of a strong repulsive potential (hard EoS). This ambiguity is further amplified by the large error bars associated with the experimental data at the relevant energy ($\sqrt{s_{NN}} = 4.5$ GeV) where the actual trend might even be a smooth increase rather than a peak (Lacey, 2015; Adamczyk et al., 2015; Adamczewski-Musch et al., 2019).

Therefore, to gain deeper insights, we explore the difference between R_0 and R_S , quantified by R_0/R_S and $R_0^2 - R_S^2$, as a function of center-of-mass energy ($\sqrt{s_{NN}}$) for various nuclear potential scenarios. These results are then compared with available experimental data, as illustrated in Figure 4.12. The R_0 and R_S values are chosen at $k_T = 275 \pm 25$ MeV/c in central (0 — 10%) Au+Au collisions with a pair-rapidity cut of $|y_{\pi\pi}| < 0.35$.

Based on our previous observations, nuclear potentials without a phase tran-

sition tend to decrease R_O and increase R_S . This explains the behavior of the hard EoS (blue line with circle) and the nuclear density dependent CMF EoS (green line), where both result in suppression of R_O/R_S and $R_O^2 - R_S^2$ compared to the cascade mode (black squares). At these energies, the hard EoS and CMF EoS potentials exhibit similar strength as the nuclear density reaches around $\rho_b/\rho_0 \leq 5$. This similarity in terms of repulsive strength results in the earlier pion emission, as aligned with the relation $\Delta\tau^2 \propto 1/(R_O^2 - R_S^2)$. Consequently, the non-monotonic behavior observed around $\sqrt{s_{NN}} \approx 4.5$ GeV in Figure 4.11 is not attributable solely to a rise in R_O from the hard EoS.

We can now shift our focus to the effects of a phase transition in the results from the CMF EoS with critical behavior representing the phase transition at $\rho_b/\rho_0 \approx 4$ and $\rho_b/\rho_0 \approx 5$ (CMF_PT2 EoS with orange dotted line and CMF_PT3 EoS with pink dashed line). At the lowest energy ($\sqrt{s_{NN}} = 2.4$ GeV), the results from all CMF EoS scenarios are similar to the ones from the hard EoS. However, as the energy increases, CMF_PT2 EoS (orange dotted line) gradually approaches the cascade scenario, reaching a maximum around $\sqrt{s_{NN}} \approx 4$ GeV. This reflects the softening of the nuclear potential due to the critical behavior from the phase transition. In contrast, CMF_PT3 EoS (pink dashed line) remains consistent with the default CMF EoS (green line) across all energies. This suggests that the nuclear density in this energy range never reaches the critical regime implied by CMF_PT3 EoS, i.e., $\rho_b/\rho_0 \approx 4 - 5$.

In conclusion, our findings indicate that HBT radii are sensitive to the EoS. CMF_PT2 suggests that critical behavior is expected around a nuclear density of $\rho_b \approx 4 - 5\rho_0$, as it best describes the experimental data at $\sqrt{s_{NN}} \approx 4$ GeV.

4.8 Space-time Structure from HBT radii

Now we continue with the discussion of the negative pion π^- emission time. The critical behavior at the phase transition may result in a softening of the EoS, leading to longer emission times. This can be interpreted in terms of the HBT radii, where $R_O^2 - R_S^2 \propto \Delta\tau_{\text{emission}}^2$ (for non-flow volume). To assess how different assumptions about the EoS affect the freeze-out time distribution, we present this comparison for various collision energies ranging from $\sqrt{s_{NN}} = 2.4 - 7.7$ GeV in Figure 4.13.

At $\sqrt{s_{NN}} = 2.4$ GeV, all the freeze-out time distributions with different EoS (colored lines) are nearly identical, except for the cascade mode (solid black line), where most pions freeze out around $t \approx 15$ fm/c. This uniformity occurs because, at

this energy, the density-dependent nuclear potentials are nearly the same.

As we move towards higher energies, the freeze-out distribution for the CMF_PT2 EoS (solid orange line) approaches that of the cascade mode, while the distributions for the other EoS remain almost identical for the rest of the energy range, with slight deviations at $\sqrt{s_{\text{NN}}} = 7.7$ GeV. Here, the freeze-out times for CMF EoS (green dashed line) and CMF_PT3 are extended similarly, while the hard EoS (solid blue line) exhibits the shortest emission times.

The corresponding mean freeze-out times $\langle t \rangle$ and transverse radii $r_{\text{T}} = \sqrt{r_x^2 + r_y^2}$ of π^- are then illustrated in Figure 4.14 as functions of collision energy $\sqrt{s_{\text{NN}}}$. In panel (a), the mean freeze-out time $\langle t \rangle$ exhibits a minimum at $\sqrt{s_{\text{NN}}} \approx 4$ GeV for all calculations. The similar behaviors of increasing freeze-out time $\langle t \rangle$ at higher energies of all EoS scenarios may be attributed to resonance decay, with string excitation overcoming fragmentation. The emission time from a hard EoS (coloured line) is prolonged over the entire energy range.

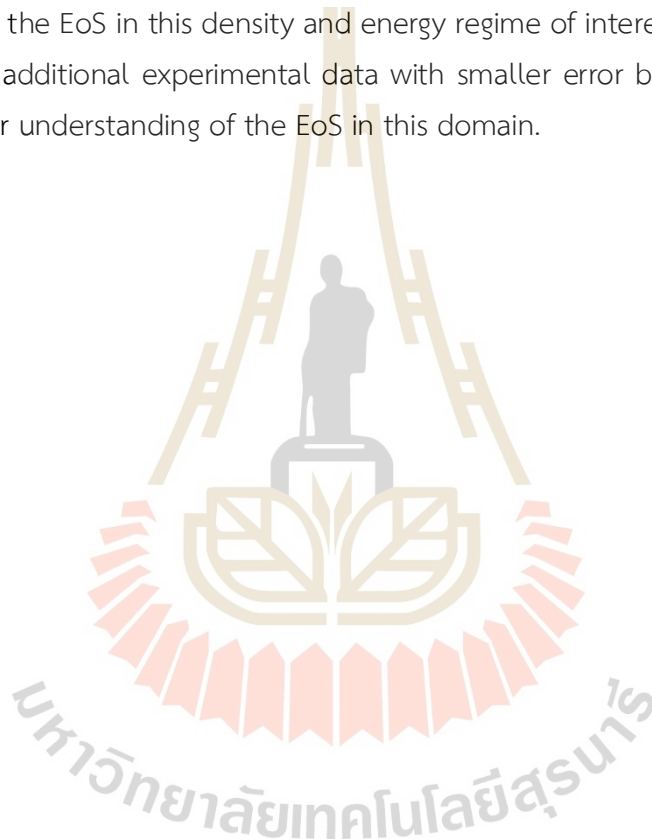
Furthermore, we observe a consistent increase in transverse radii r_{T} in panel (b), in line with the assumption of an expanding charged volume. The transverse radii r_{T} from the EoS scenarios with strong repulsive potentials (colored lines) result in consistently larger r_{T} compared to the cascade mode (solid black line), suggesting a stronger system expansion due to higher pressure. We observe an interesting behavior of the transverse radii from the CMF_PT2 EoS (orange dotted line), where it remains relatively constant and approaches the cascade mode (solid black line).

In summary, we investigate the sensitivity of HBT radii to different Equations of State (EoS) using UrQMD simulations of central (0 – 10%) Au+Au collisions at collision energies ranging from $\sqrt{s_{\text{NN}}} = 2.4 - 7.7$ GeV. We explicitly demonstrated that the inclusion of nuclear potential, independent of Coulomb interactions, significantly impacts HBT radii (contrast to (Li et al., 2006)). We found that incorporating a hard EoS, either with or without a phase transition, leads to a better description of the experimental data for the R_0 and R_S differences of the HBT radii (R_0/R_S and $R_0^2 - R_S^2$). The results obtained with the CMF_PT2 EoS exhibit a softening of the nuclear potential around $\sqrt{s_{\text{NN}}} \approx 4$ GeV due to the critical behavior, providing an even better agreement with the data compared to other EoS scenarios. This suggests that the nuclear density in this energy range falls within the region of $\rho_{\text{B}} \lesssim 4 - 5\rho_0$ and likely doesn't exceed these values, as the CMF_PT3 EoS doesn't exhibit any critical behavior.

Finally, we investigated the emission time, represented by the freeze-out

time distribution of negative pions π^- . Interestingly, all EoS scenarios, including the cascade mode (without any EoS), display a minimum emission time at $\sqrt{s_{NN}} \approx 4$ GeV. As expected, the freeze-out time distribution from the CMF_PT2 EoS shows a distinct behavior, with a prolonged freeze-out time approaching the cascade mode. This finding, coupled with the observation of nearly constant transverse radii until $\sqrt{s_{NN}} \approx 4$ GeV, strongly suggests a critical behavior involving a longer relaxation time associated with the softening of the nuclear EoS during the phase transition.

These results demonstrate the potential of using HBT radii as a direct probe to investigate the EoS in this density and energy regime of interest. Future studies can benefit from additional experimental data with smaller error bars to further validate and refine our understanding of the EoS in this domain.



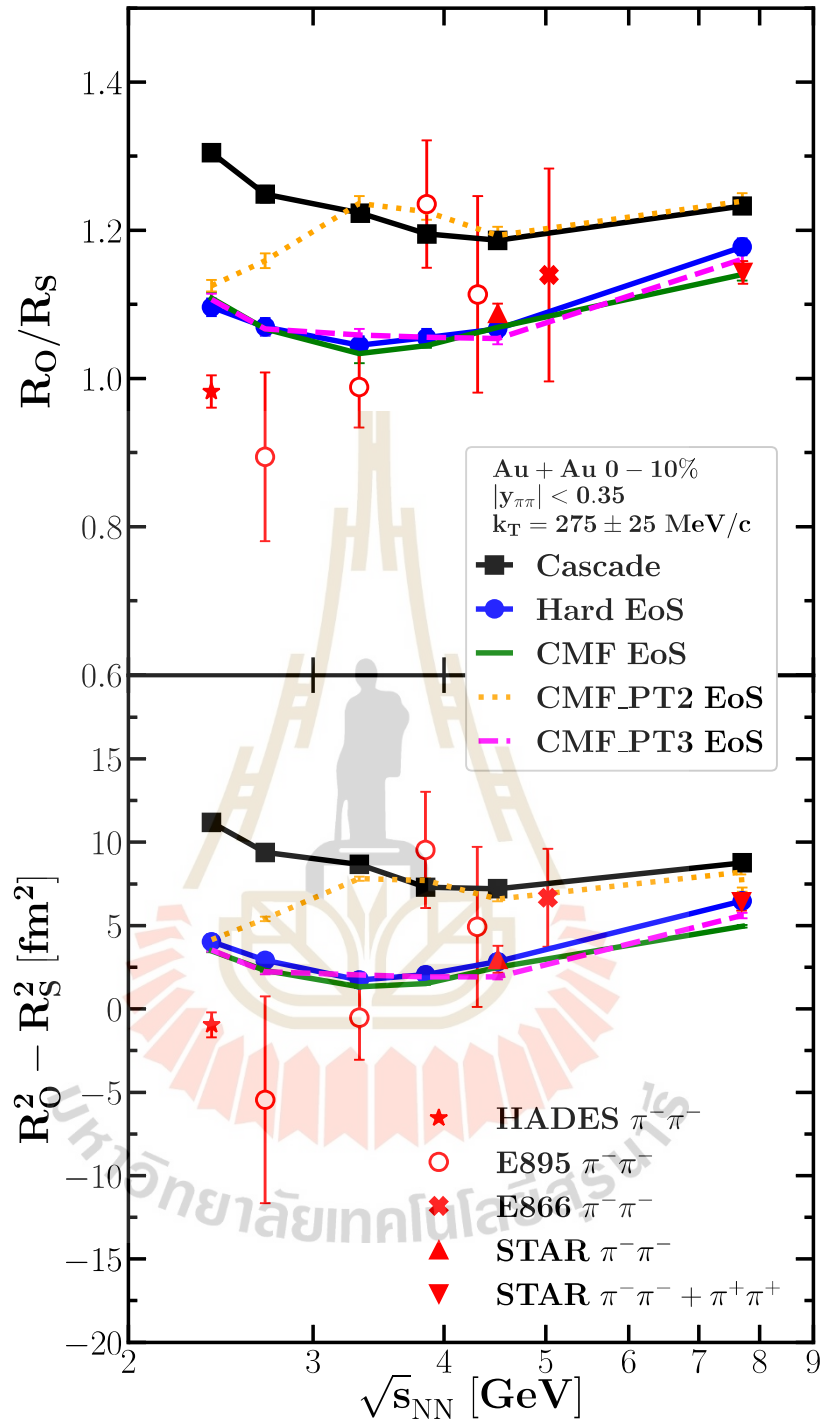


Figure 4.12 Comparison of the collision energy dependence of the (top panel) R_0/R_5 ratio and (bottom panel) $R_0^2 - R_5^2$ for cascade (black line with squares) and various EoS models (hard EoS: blue line with circles, CMF EoS: green line, CMF_PT2 EoS: orange dotted line, CMF_PT3 EoS: pink dashed line) with available experimental data (Lisa et al., 2000; Lisa et al., 2005; Adamczyk et al., 2015; Adamczewski-Musch et al., 2019; Adamczewski-Musch et al., 2020; Adam et al., 2021).

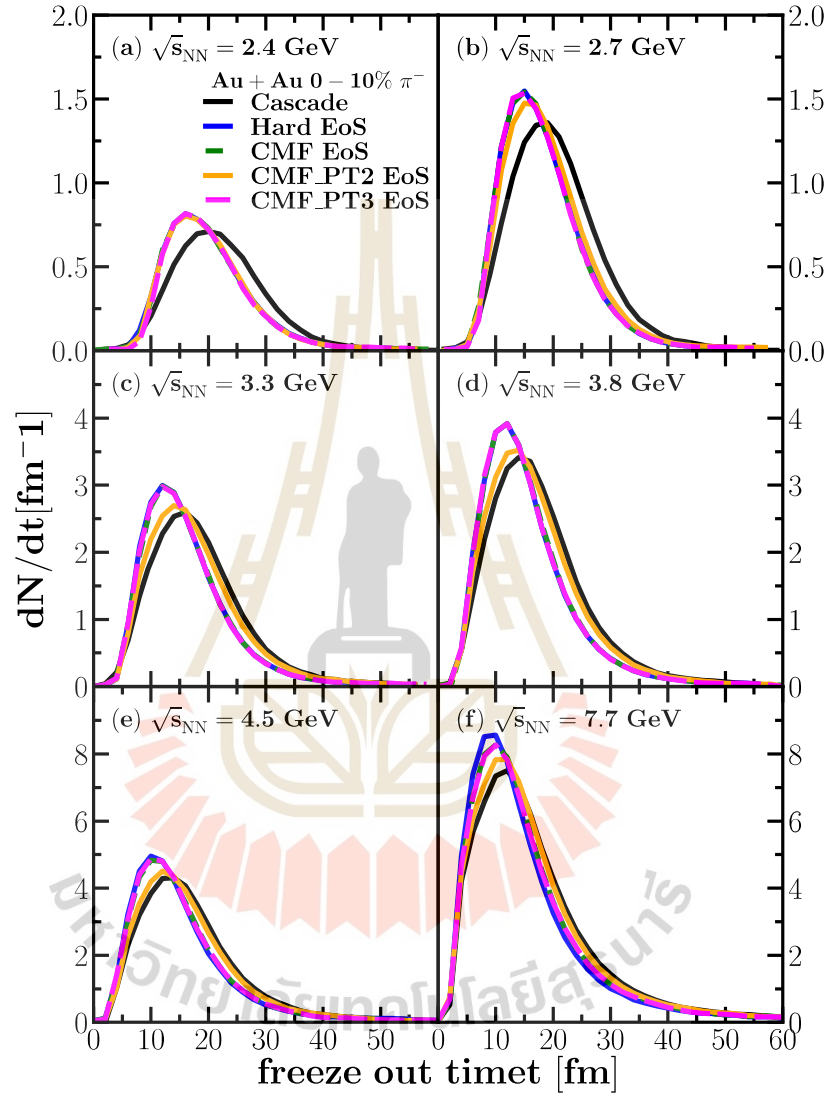


Figure 4.13 The freeze-out time distribution of π^- from 0 — 10% Au+Au collisions with the different EoS; Cascade mode (solid black line), Hard EoS (solid blue line), CMF EoS (green dashed line), CMF_PT2 EoS (solid orange line), and CMF_PT3 EoS (pink dash-dotted line)

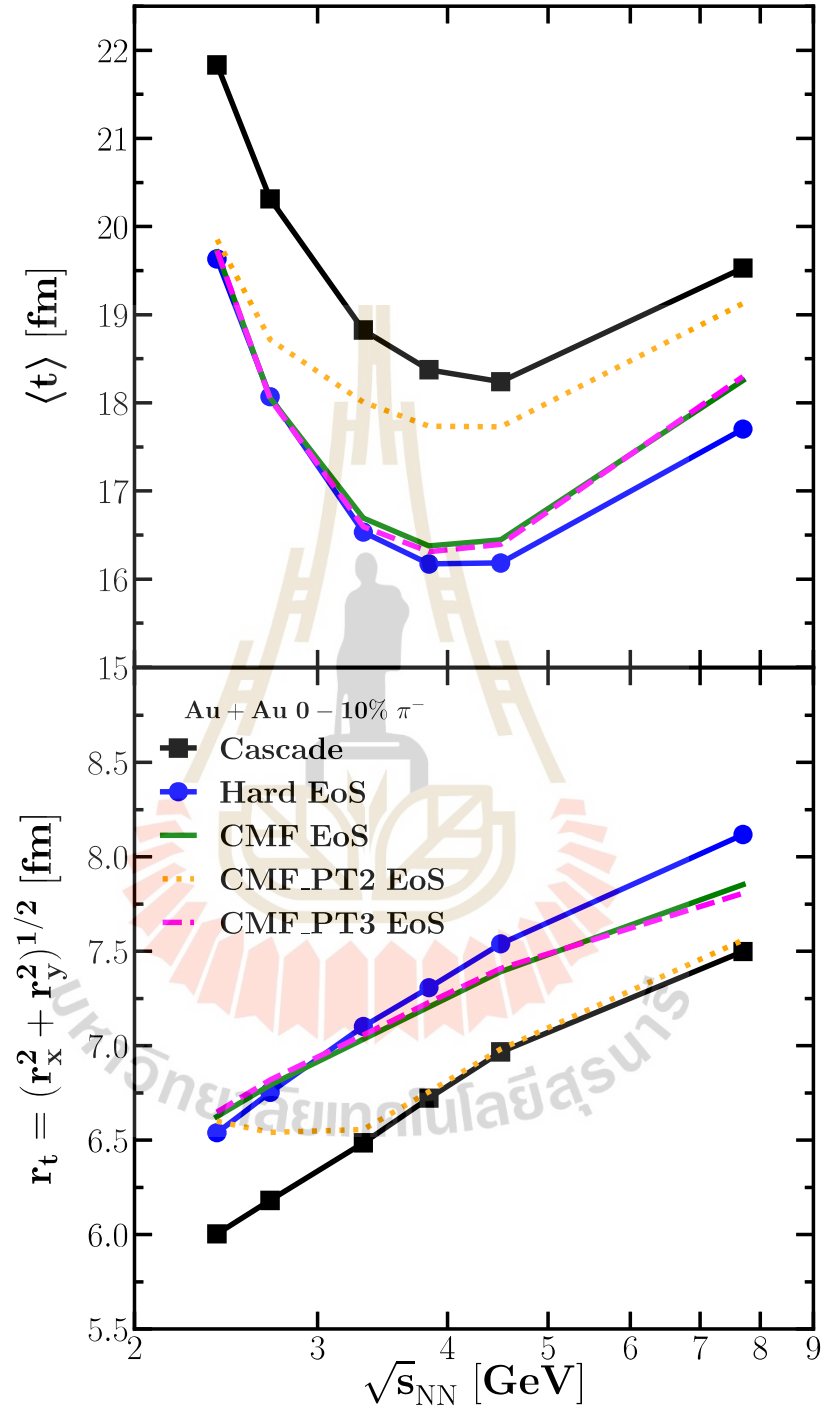


Figure 4.14 (a) The corresponding mean π^- emission time $\langle t \rangle$ and (b) transverse radii r_t at freeze-out as a function of collision energies calculated from different EoS.

CHAPTER V

REVIEWS ON (HYPER) (LIGHT) NUCLEI

The previous chapter has already pointed out that cluster formations are important for critical phenomena of the medium and the EoS studies. Also, the tension between formation mechanisms arises due to the different space-time pictures in the heavy-ion collisions. In this chapter, we will review on the cluster formations ranging from the normal nuclei to the hypernuclei by discussing their roles in various studies and the available formation mechanisms on the markets.

5.1 Role of (Hyper)Nuclei Formation

Nuclei or clusters, such as deuteron, triton, and Helium-3, are the bound state of two or more nucleons. The studies of these particles are crucial for a broad range of physics from the nuclear physics (Knoll et al., 1982; Sun et al., 2017; Zhu et al., 2015; Oh and Ko, 2007) to the astrophysics (Hagedorn, 1960; Butler and Pearson, 1961; Carlson et al., 2014; Hou et al., 2017; Most et al., 2023).

In the context of the heavy-ion collisions, they are important probes for the critical behavior and the EoS due to their sensitivity to the medium (Andronic et al., 2011; Blaschke et al., 2020; Knoll et al., 1982; Hagedorn et al., 2012; Yang et al., 1984). This is attributed to the nature of the bound state and the final stage observables. They can be reflective to the various medium effects from the early to final stage of the collisions. For example, beam energy and initial geometries can lead to the different temperatures and densities affecting the cluster formations at the final stage (Csernai and Kapusta, 1986; Hagedorn et al., 2012). The correlations and fluctuations of the baryon at the critical point also lead to change in their multiplicities (Knoll et al., 1982; Bertsch and Cugnon, 1981; Oliinychenko, 2021).

In the context of astrophysics and cosmology, these clusters, particularly the light nuclei, play a critical role in understanding the early universe (Yang et al., 1984) providing a strong support on the most famous cosmological models, i.e., Big Bang models (Alpher and Herman, 1948; Yang et al., 1984; Malaney and Mathews, 1993; Pospelov and Pradler, 2010). Also it has been postulated that the antideuterons in space could

be used to trace and investigate the candidate and nature of dark matter (Korsmeier et al., 2018; Bellini, 2022; Fuke et al., 2005; Ibarra and Wild, 2013; Aguilar et al., 2016).

However, the research on these clusters has been recently highlighted again due to the fact that their fundamental structures and formations could serve as a basis for studying hypernuclei (Cho et al., 2017; Andronic et al., 2018; Braun-Munzinger and Dönigus, 2019). The hypernuclei are the bound state between nucleons with a least one strange baryon called hyperon. These hypernuclei could extend our understanding of the QCD matter in both nuclear physics and astrophysics aspects as well.

Furthermore, since the strangeness is only produced from the early stage of the collisions, these hypernuclei also carry information at the very initial stage of the collisions. They are also subjected to the correlations and fluctuations of the medium due to their bound state nature. Particularly, the goal for investigating the hypernuclei in the nuclear medium is to understand their internal structures and interactions. However, at high collision energies, these hypernuclei are very rare making their experimental data situations very limited.

This motivates most of the heavy-ion collision facilities to design lower energies collision to enhance the strangeness productions in the nuclear medium (Schaffner-Bielich and Gal, 2000; Andronic et al., 2011). These created environments correspond to the neutron stars and binary neutron star mergers. The presence of hyperons in these compact stellar objects can influence the neutron star EoS (Balberg et al., 1999; Chatterjee and Vidaña, 2016; Oertel et al., 2016) through hyperon-nucleon interactions (Nagels et al., 1977; Nagels et al., 1979; Shinmura et al., 1984; Fujiwara et al., 1996a; Fujiwara et al., 1996b; Nemura et al., 2000; Hildenbrand and Hammer, 2019) and ultimately affecting the maximum mass and radius of these stellar objects (Bombaci, 2017; Özel and Freire, 2016; Lattimer, 2021). This suggests that the hypernuclei could also serve as sensitive probes for the EoS especially around neutron star density.

The investigation on their internal interactions are also important to their formation mechanisms. One could argue that these normal nuclei and hypernuclei are formed from the same mechanism. The investigation on the formation mechanism from the normal nuclei could also be crucial to understand the nature of the hyperon interactions.

The following sections will delve deeper into these highlighted topics, exploring the detailed mechanisms and implications of (hyper)nuclei studies in various physical contexts (for more detailed reviews Ref. (Dönigus, 2020)).

Big Bang Nucleosynthesis

Big Bang Nucleosynthesis (BBN) is one of the eras of the early universe where a larger amount of light atomic nuclei are continuously created. It was postulated to happen a few minutes after the Big Bang (Alpher and Herman, 1948; Malaney and Mathews, 1993). Originally, while the universe was cooling down, many light nuclei could be formed but hot universe with energetic nucleons, also destroyed them continuously. Only until the universe is cool enough such that it allows deuterons to survive. This is one of the most important threshold in the BBN, the so-called “deuteron bottleneck”. A large amount of light nuclei can be produced with these deuterons as their constituent in which inducing an enormous nuclear chain reaction to form other heavier nuclei (Pospelov and Pradler, 2010).

Interestingly, most of the abundance of deuterium observed in the universe today is accounted from the BBN era. By investigating the primordial deuteron yields from the coalescence model along with the constraints on the density and composition of baryonic matter in the early universe from the cosmic microwave background, we can obtain the most valuable evidence for supporting the BBN model (Alpher and Herman, 1948; Yang et al., 1984; Pospelov and Pradler, 2010).

Furthermore, the same argument can also be applied to the heavy-ion collisions. The cluster formation from the thermal model provides a contradict picture with the deuteron bottle neck argument leading to the so-called “snow ball in hell” where these loosely bound clusters are directly emitted from the hot fireball at the chemical freeze-out with temperature $T_{\text{chem}} \geq 100$ MeV. However, in this thesis, we will eventually point out that the coalescence model could provide more consistent pictures between the emission source geometries, BBN, and other arguments like isospin fluctuations.

Potential Signal of the Critical point

When the medium reaches the critical point, it induces a significant change to the thermodynamics properties leading to the divergence of the correlation length, susceptibility, and fluctuations particularly in conserved quantities like baryon number, electric charge, or strangeness. The fluctuation of these conserved observables has been extensively studied both theoretically and experimentally through event-by-event fluctuations and correlations (Sun et al., 2017; Stephanov et al., 1999; Stephanov, 2009; Skokov et al., 2013; Luo and Xu, 2017; Mrówczyński and Słor, 2020).

Measurements from the Beam Energy Scan (BES) program by the STAR Collaboration have reported clear deviations from unity or shown a non-monotonic behavior in the energy-dependence of event-by-event fluctuations, such as fourth-order fluctuations ($\kappa\sigma^2$) of the net-proton number, which could indicate a critical behavior (Adamczyk et al., 2014). This critical behavior manifests in various final state observables, including $\eta/s \propto d/p$ (Andronic et al., 2009; Braun-Munzinger and Dönigus, 2019; Andronic et al., 2017), and the slope of harmonic flows of light clusters (Hartnack et al., 1994). These observations are sensitive to the correlations and fluctuations near the critical point.

Moreover, due to the fact that the constituent nucleons are subjected to the baryon conservation, the critical fluctuations and the correlation length will be reflected by the relative densities between nuclei and nucleons at kinetic freeze-out in heavy-ion collisions, e.g., $\mathcal{O}(d/p)$, $\mathcal{O}(tp/d)$ and $\mathcal{O}(p^3\text{He}/d)$. These ratios are expected to reflect pure contributions from proton-neutron correlations and baryon fluctuations (Oliinychenko, 2021; Liu et al., 2020).

Relation to Dark Matter

The estimated ratio of, e.g., d/p abundances aligns reasonably well with the observable number of baryons in the universe today (Yang et al., 1984; Hou et al., 2017). This implies that there isn't a significant unseen source for baryons. However, the observations also suggest that a large quantity of matter is necessary to explain the gravitational behavior of galaxies and their halos, at least 10 times the mean density of the visible baryons (Aguilar et al., 2016). Thus, this indicates that this missing mass is not made of ordinary matter, but the so-called dark matter.

The AMS experiment aims to measure the flux of antinuclei in space (Fuke et al., 2005; Ibarra and Wild, 2013; Aguilar et al., 2016). It has been postulated that dark matter annihilation could produce the $\bar{N}\bar{N}$ which then potentially form the antinuclei (Carlson et al., 2014; Korsmeier et al., 2018; Bellini, 2022; Šerkšnytė et al., 2022) where the formation rates of these antinuclei are theoretically estimated by the coalescence model that is also applied in heavy-ion collisions (Nagle et al., 1994; Bleicher et al., 1995; Abelev et al., 2010; Zhu et al., 2015; Chen et al., 2018).

Understanding the correct mechanism for cluster formation from heavy-ion collisions might help us provide the correct estimated production rate of these antinuclei.

5.1.1 Hypernuclei

One of the important aspects for cluster studies in heavy-ion collisions is the role of strange quarks and strange hadrons in the medium. These strange quarks are only produced after the medium reaches the QGP stage and only after the hadronization passes, their bound states are then allowed to form. From this point, one can foresee that the hypernuclei could be influenced by various factors such as strong interactions, decays, fluctuations, and re-scattering throughout the evolution. However, these final stage observables can also be seen as information carrier from the early stages of the QGP (Koch et al., 1986; Soff et al., 1999).

Despite significant theoretical advancements and the fact that available models could already accurately estimate hyperon and hypernuclei behaviors and spectra, several topics remain open for investigation (Rufa et al., 1990; Gibson and Hungerford, 1995).

One of such topics is the hypertriton structure and its dependence on system size (Acharya et al., 2022). Measurements of the hypertriton lifetime, which is close to that of Λ hyperons, suggest a structure consisting of a deuteron core and a loosely bound Λ (Juric et al., 1973; Abelev et al., 2010; Adam et al., 2016; Dönigus, 2020; Andronic et al., 2018). Understanding the correct hypertriton structure requires a consistent wavefunction, and interactions between its constituents, such as ΛN or ΛNN interactions and even $\Lambda\Lambda N$ interactions (Nagels et al., 1977; Nagels et al., 1979; Shinmura et al., 1984; Fujiwara et al., 1996a; Fujiwara et al., 1996b; Nemura et al., 2000).

The main challenge in understanding hyperon-nucleon interactions is the lack of experimental data. Thus for the current trend for most facilities will focus on these hypernuclei studies especially toward the lower energy regime (lower temperature but higher density) where hypernuclei yields are expected to be enhanced and the environments are suitable for studying their internal interactions through correlations (Bertsch and Cugnon, 1981; Lisa et al., 2005; Mihaylov et al., 2018; Acharya et al., 2019). Future facilities like FAIR, PANDA, and HADES will conduct research with particular interest in this regime for hypernuclei physics (Pochodzalla, 2005; Ablyazimov et al., 2017; Gal et al., 2016; Almaalol et al., 2022) aiming to investigate their structure, the underlying internal interactions such as hyperon-nucleon and hyperon-hyperon interactions, and the weak decays of these objects.

These hypernuclei structure and internal interaction studies have direct implications to the neutron stars EoS (Huth et al., 2022). Since the attractive and repulsive

nature of these interactions will influence the balance of the Fermi pressure. Inside the neutron stars, it is expected the presence of hyperons and hypernuclei. However, the inclusion from their contributions from various models result in a strong softening of the EoS (Balberg et al., 1999; Chatterjee and Vidaña, 2016; Oertel et al., 2016). The maximum masses in these cases could never reach the observed neutron stars masses of around $2M_{\odot}$ (Biswas, 2021). While the pure neutron star model exhibits a too stiff EoS leading to the always larger possible masses for pure neutron stars. Thus, a comprehensive understanding of the effects of hypernuclei and their constituent hyperons is also crucial for understanding the properties of matter under extreme conditions, not only in heavy-ion collisions but also in contexts such as the early universe (Rafelski and Yang, 2022) and the cores of neutron stars (Özel and Freire, 2016; Lattimer, 2021).

5.2 Cluster Formation Mechanisms

To accurately predict the yield of nuclei formation, understanding the underlying mechanisms responsible for this process is important. In this section, we will introduce the most successful and well-known mechanisms for nuclei formation. Despite their successes, each model has its own interpretations, leading to debates over which mechanism is realized in nature.

5.2.1 Thermal productions

Thermodynamic models have been extensively used to study the macroscopic properties of strongly interacting matter over a broad range of energies. These statistical thermal models are applicable when the system has reached its equilibrium. In the sense of heavy-ion collisions, this equilibrium refers to the stage of chemical freeze-out (Andronic, 2014; Cleymans et al., 2006). In this section, we will introduce the setup of the model for nuclei production by following the explanation presented by Ref. (Kapusta, 1980; Vovchenko and Stoecker, 2019) and discuss some drawbacks (see also Ref. (Mrowczynski, 2017)).

The basic idea of the thermal model is to treat each particle species as a non-interacting gas. The schematics for the thermal model is shown in Figure 5.1.

Inside the fireball, all kinds of particles (hadrons and clusters) can form. The nuclei are treated, like other particles, as free particles inside a volume V_{chem} characterized by temperature T_{chem} and chemical potential $\mu_{\text{chem},i}$. The distribution of particle i

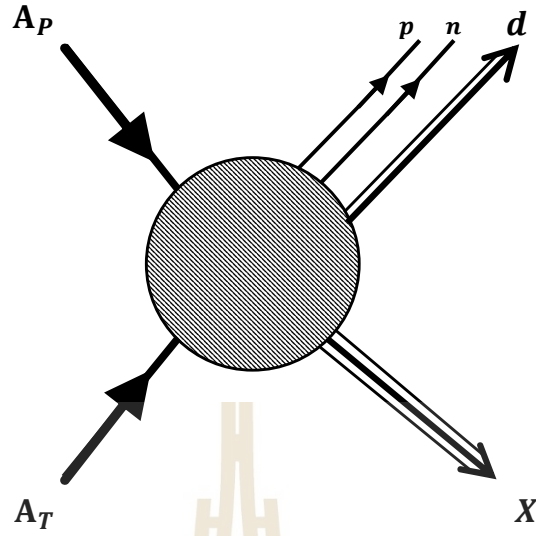


Figure 5.1 The schematic for a particle production from a thermal model. A projectile A_P and a target nucleus A_T exchange energy and momentum upon collision. All particles X , p and n , are emitted directly from the fireball including the composited particle d . This hadronization occurs at chemical freeze-out. The figure is adopted from Ref. (Kapusta, 1980)

can be described as:

$$\frac{d^3N_i}{dp_i} = \frac{(2S_i + 1)}{(2\pi)^3} V \left[\exp \left(\frac{(p_i^2 + m_i^2)^{1/2} - \mu_i}{T} \right) \pm 1 \right]^{-1}, \quad (5.1)$$

where S_i is the spin multiplicity of the particle, and \pm depends on whether the particle is a fermion or boson.

The particle distribution function can then be rewritten in terms of the Milne momentum coordinates, while the spatial coordinates are integrated and yield the three-volume V . It is also possible to introduce Milne-coordinates for coordinate space $(t, x, y, z) \rightarrow (\eta, r_T, \tau, \theta)$,

$$\frac{d^3N}{dm_T dy d\phi} = \frac{gV}{(2\pi)^3} m_T \frac{1}{e^{\beta(E-\mu)} \pm 1} \quad (5.2)$$

$$= \frac{gV}{(2\pi)^3} \frac{m_T^2 \cosh(y)}{e^{\beta(m_T \cosh(y) - \mu)} \pm 1} \quad (5.3)$$

If the bulk evolution is symmetric with respect to ϕ , one can integrate over the azimuthal angle and obtain the particle distribution as a function of y and m_T :

$$\frac{d^2N}{dm_T dy} = \frac{gV}{(2\pi)^2} \frac{m_T^2 \cosh(y)}{e^{\beta(m_T \cosh(y) - \mu)} \pm 1} \quad (5.4)$$

From here on one can calculate the transverse momentum spectrum of a given particle species or the rapidity distribution. Moreover, integration over y and m_T yields the total number of particles.

$$N = \frac{gV}{(2\pi)^2} \int_{-\infty}^{\infty} dy \int_m^{\infty} dm_T \frac{m_T^2 \cosh(y)}{e^{\beta(m_T \cosh(y) - \mu)} \pm 1} \quad (5.5)$$

The thermal description can provide a good estimate for normal hadron productions, see figure 5.2. However, the estimated (anti)cluster or hypernuclei yields are usually poor (on the logarithmic scale). Nevertheless, a simple thermal model can still give us a lot of insight on the particle productions from a very wide spectrum ranging from SPS to RHIC energies without any need to introduce more parameters (Andronic et al., 2010).

Various extensions of the ideal gas picture have been discussed mostly within the excluded volume (Rischke et al., 1991; Yen et al., 1997; Yen and Gorenstein, 1999), where the effects of repulsive hadronic interactions at short distances are introduced. Another extension is the quantum van der Waals model (Vovchenko et al., 2015; Vovchenko et al., 2017a; Vovchenko et al., 2017b), which allows to include both the repulsive and attractive interactions between hadrons. Recently, repulsive interactions have received renewed interest in the context of lattice QCD data on fluctuations of conserved charges. In addition, the fugacity free parameters sometimes are introduced and used to describe how the presence of particles deviates from ideal gas behavior due to interactions (Koch et al., 1986; Rafelski, 1991; Letessier and Rafelski, 1999). A modified pressure term accounts for the chemical potential and reflects the departure from equilibrium conditions. Especially for hypernuclei, there is a strong enhancement visible at low energies that can be understood as an interplay of the medium T , μ_i , and canonical effects. This is of particular interest for low energy facilities where collisions occur at chemical potential, like the upcoming FAIR facility (Friman et al., 2011; Ablyazimov et al., 2017; Durante et al., 2019; Bzdak et al., 2020).

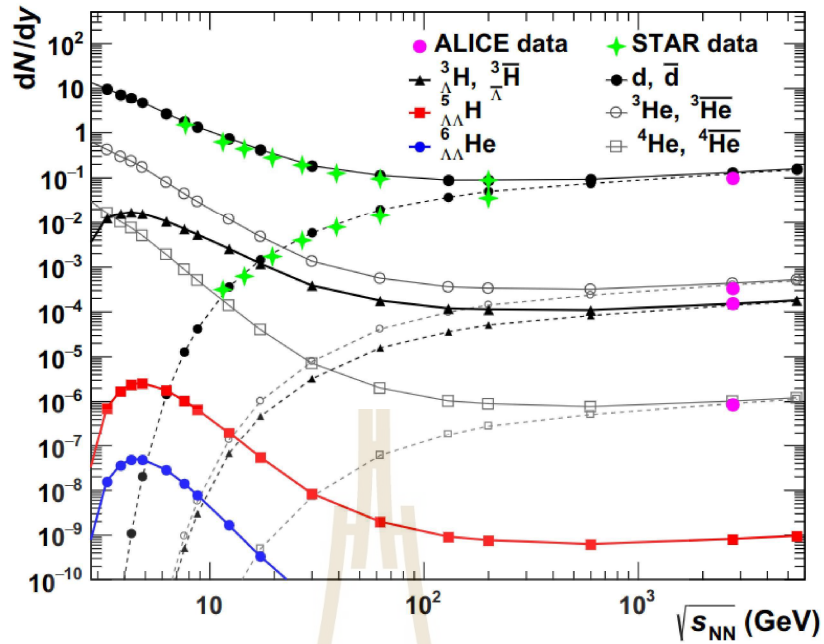


Figure 5.2 The comparison between thermal predictions and the measured (anti)nuclei production on the energy spectrum. The figure is adopted from Ref. (Dönigus, 2020)

Despite its simplicity and successful predictions of cluster yields, the thermal prescription ultimately assumes the formation of nuclei directly from the chemical freeze-out stage with $T_{\text{chem}} \approx 150$ MeV which is much larger than the binding energies of all (hyper)nuclei, thus raising the questions which mechanisms are realized in nature.

In contrast to the thermal model, the coalescence assumes that light (anti)nuclei are produced at a later stage, i.e., the kinetic freeze-out (Braun-Munzinger and Dönigus, 2019; Mrówczyński and Stoń, 2020).

5.2.2 Coalescence Model

The coalescence model assumes that light nuclei are formed by the coalescence of nucleons and other light clusters that are sufficiently close in coordinate and momentum space. The coalescence probability depends on the momentum and separation of the nucleons or clusters.

The model describes the formation of composited particles in the late stage of the collision - first, all resonances decay into nucleons, then nucleons coalesce into nuclei at the freeze-out stage. There are many types of coalescence models (Hagedorn, 1960; Butler and Pearson, 1963; Bond et al., 1977; Csernai and Kapusta, 1986; Sato and

Yazaki, 1981; Hillery et al., 1984; Danielewicz and Schuck, 1992; Mrowczynski, 1992; Kittiratpattana et al., 2020). The model states that a pair of final-state (anti)nucleons that are carrying similar momenta can coalesce to form a deuteron or an anti-deuteron with total momentum \mathbf{P} as shown in figure 5.3. The nucleus-nucleus collision creates a fireball which emits protons, neutrons, and many other particles out. In the case where an emitted proton and neutron have similar momenta, they will be localized and formed into a deuteron. Different formulations for the coalescence rate are possible. In this section, we will discuss the problems with the simple coalescence model and present the more considerate treatment for the model.

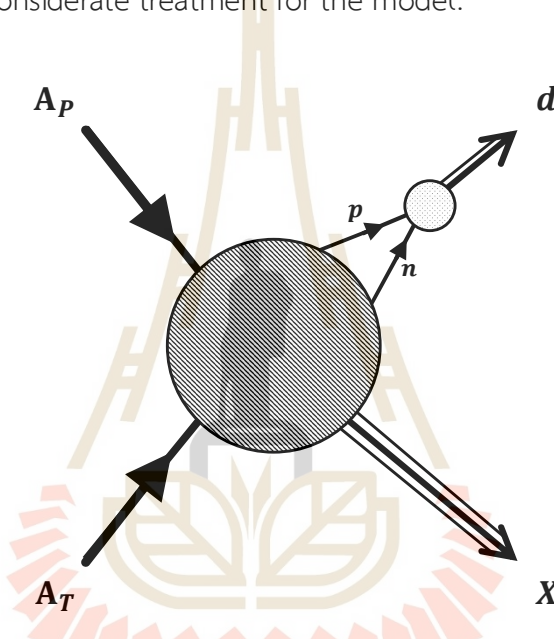


Figure 5.3 The schematic for a particle production and cluster formation from a colliding projectile nucleus A_P and a target nucleus A_T . In the coalescence model, the free streaming neighbor of p and n pair after flying a certain distance will coalesce and form a deuteron outside of the fireball. The rest of the momentum is represented by X . This coalescence process happens at kinetic freeze-out. The figure is adopted from Ref. (Kapusta, 1980)

Simple Momentum Coalescence

The coalescence model for relativistic nuclear collisions was developed from the physical insight provided by proton-nucleus collisions by Butler and Pearson (Butler and Pearson, 1963). Then, Ref. (Schwarzschild and Zupancic, 1963) pointed out that, independent of the detailed production mechanism, the deuteron density d^3N_d/dP^3

should be proportional to the square of the proton density $(d^3N_p/d\mathbf{p}^3)^2$. The coefficient may be momentum dependent and could be made dependent on the space-time details of the mechanism.

The derivation of the coalescence model for deuterons goes as follows. Let $d^3N_p/d\mathbf{p}^3$ be the invariant momentum space density for nucleons before coalescence into deuterons. We assume that protons and neutrons have equal densities but the formulas can be generalized to include the non-equal cases. The probability of finding one nucleon with momentum p_0 is density times the volume of momentum sphere averaging by the mean of nucleon multiplicity.

$$P = \frac{1}{M} \frac{4\pi}{3} p_0^3 \gamma \frac{d^3N_p}{d\mathbf{p}^3} \quad (5.6)$$

where M is the mean nucleon multiplicity. The purely statistical probability for finding two nucleons in the case where $M \ll 1$ and $MP \gg 1$ of this sphere is

$$P_M(2) = \binom{M}{2} P^2 (1 - P)^{M-2} \quad (5.7)$$

$$\frac{4\pi}{3} p_0^3 \gamma \frac{d^3N_d}{d\mathbf{P}^3} = \frac{M^2}{2} \left(\frac{1}{M} \frac{4\pi}{3} p_0^3 \gamma \frac{d^3N_p}{d\mathbf{p}^3} \right)^2 \quad (5.8)$$

$$\gamma \frac{d^3N_d}{d\mathbf{P}^3} = \frac{1}{2} \frac{4\pi}{3} p_0^3 \left(\gamma \frac{d^3N_p}{d\mathbf{p}^3} \right)^2 \quad (5.9)$$

If we consider the spin (triplets and singlet) and isospin (triplets and singlet) combinations, we obtain,

$$\gamma \frac{d^3N_d}{d\mathbf{P}^3} = 8 \frac{3}{4} \frac{4\pi}{3} p_0^3 \left(\gamma \frac{d^3N_p}{d\mathbf{p}^3} \right)^2 \quad (5.10)$$

again with deuteron momentum $\mathbf{P} = \mathbf{p}_1 + \mathbf{p}_2$ and assuming that these nucleons approximately carry the same momenta $\mathbf{p}_1 = \mathbf{p}_2 = \mathbf{p}$. From here, one can express that whenever two nucleons with correct spin-isospin states are within a momentum sphere with radius p_0 of each other then they will coalesce and form a deuteron. However, it is more common to express the density in the form of the Lorentz invariant.

Thus the coalescence model is usually written as,

$$E \left(\frac{d^3 \sigma_d}{dP^3} \right) = B_2 \left(\frac{E d^3 \sigma_p}{2 dp^3} \right)^2, \quad (5.11)$$

assuming the equality of proton and neutron cross sections. E is the energy of the deuteron where the nucleons are assumed to be $E/2$. B_2 is a well-known coalescence parameter which is used and measured by most experiments related to the coalescence model. Still, B_2 also contains the proportionality to the unknown p_0 . However, the physical interpretation of radius p_0 is still questionable (Butler and Pearson, 1963; Schwarzschild and Zupancic, 1963; Gutbrod et al., 1976; Bond et al., 1977; Sato and Yazaki, 1981; Gyulassy et al., 1983; Csernai and Kapusta, 1986; Mrowczynski, 1990). Because this parameter could not be expressed with any dependencies on the collision initial conditions, e.g., the target/projectile size, beam energy, impact parameter etc. However, based on this proportionality, a similar relation between p_0 and the volume V from the thermal model can be drawn,

$$\frac{d^3 N_d}{dP^3} = \frac{3 (2\pi)^3}{4 V} \frac{d^3 N_p}{dp_1^3} \frac{d^3 N_n}{dp_2^3}. \quad (5.12)$$

The weighting factor of $3/4$ averages the spin multiplicity per nucleon-nucleon bound state. In Lorentz invariant density form, this is:

$$\left(\gamma \frac{d^3 N_d}{dp^3} \right) = 8 \frac{3 (2\pi)^3}{4 V} \frac{1}{\gamma} \left(\gamma \frac{d^3 N_p}{dp^3} \right)^2. \quad (5.13)$$

Comparing this the Eq. (5.10) with the thermal model Eq. (5.13), we get the relation with p_0 ,

$$\frac{4}{3} \frac{p_0^3}{\pi} = \frac{1 (2\pi)^3}{\gamma V} \quad (5.14)$$

According to this naive relation, p_0 seems to be inversely proportional to the thermal volume V and the Lorentz factor γ . One can see that p_0 can now be understood as the coalescence parameter B_A which is expected to have a direct connection with the volume as $B_A \propto \left(\frac{1}{V} \right)^{A-1}$. However, the interpretations of the volume from the thermal model and the coalescence model are not the same. The latter one refers to the volume of homogeneity of the emission source which is in line with the volume from

HBT interferometry (Kapusta, 1980; Ackermann et al., 2003; Csorgo et al., 2006).

Because of its simplicity, this model fails to describe the antideuteron invariant yield at Si+Au in the AGS experiment E802 (Aoki et al., 1992). Figure 5.4 shows the invariant cross section of the negative charged particles, i.e., π^- , K^- , \bar{p} , and antideuterons \bar{d} . The anticipated cross section ratio of antideuteron to antiproton squared according to the coalescence model is actually 5 — 10 times smaller than the ratio obtained from normal deuteron.

The coalescence model can be upgraded with more explicit descriptions of the phase-space correlation which can incorporate quantum mechanical considerations. An approach for a better description of the antinuclei yields has been suggested by (Mrowczynski, 1993) which we have adopted in this studies the in previous chapter Ch. IV.

Analytic Coalescence Models

The simple coalescence model does not provide any insights into the dynamics of nucleon clustering. It does not predict a numerical value for the coalescence parameter p_0 in Eq. (5.10) or how coalescence parameters depend on system size, centrality or beam energy. Moreover, it does not allow one to extract useful information of nuclear matter properties. Therefore, there was a clear need for a dynamical basis for the coalescence model.

These models generally are based on based on the density matrix of the source (Feynman, 2018; Shuryak and Torres-Rincon, 2020) or the equivalent Wigner function formalism (Hillery et al., 1984), where the quantum effects are incorporated inside the wavefunction calculated with and without potential. In this approach, the coalescence yield is governed by the wavefunction of the state formed by coalescence, typically approximated by a Gaussian function or Hulthén wavefunction (with Yukawa potential) (Zhaba, 2017).

This approach allows us to study the coalescence parameter and cluster yields and to estimate their structure and their underlying interaction (for example ΛN in hypertriton) from different factors (Nagels et al., 1977; Nagels et al., 1979; Shinmura et al., 1984; Fujiwara et al., 1996a; Fujiwara et al., 1996b; Nemura et al., 2000).

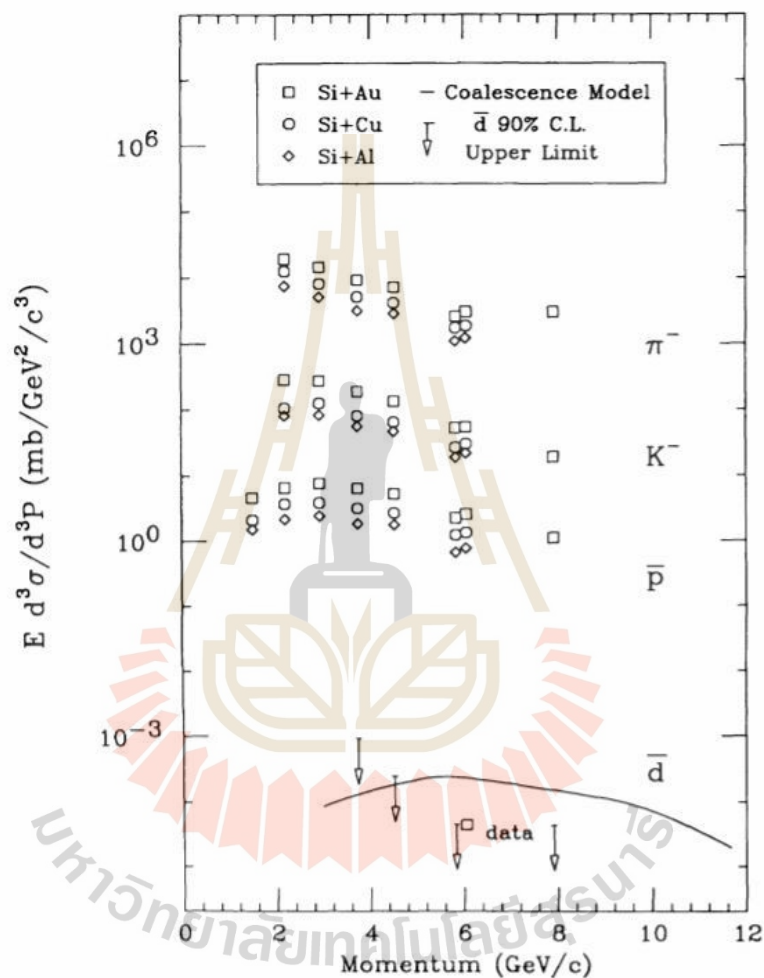


Figure 5.4 The invariant cross section of π^- , K^- , \bar{p} and \bar{d} from Si+Al, Si+Cu, and Si+Au collisions. The solid-line represents the \bar{d} 's predicted by coalescence model. The measured \bar{d} and the instrumental upper limit are represented by the square open symbol at 6.1 GeV and down arrow symbols (Aoki et al., 1992).

Wigner's Function

According to the rules of statistical quantum mechanics, the number of created deuterons with momentum \vec{P}_d is given by projecting the deuteron density matrix onto the two-nucleon density matrix ρ_d in the fireball at freeze-out:

$$\frac{d^3 N_d}{d\vec{P}_d} \propto \int d^3 \vec{x}_1 d^3 \vec{x}_2 d^3 \vec{x}'_1 d^3 \vec{x}'_2 \rho_d(\vec{x}_1, \vec{x}_2; \vec{x}'_1, \vec{x}'_2) \times \rho_{pn}(\vec{x}_1, \vec{x}_2; \vec{x}'_1, \vec{x}'_2) \quad (5.15)$$

The two-nucleon spatial density matrix ρ_{pn} in the fireball is not known and has to be approximated. We assume that at freeze-out the nucleons are uncorrelated, i.e., $\rho_{pn}(\vec{x}_1, \vec{x}_2; \vec{x}'_1, \vec{x}'_2) \approx \rho_p(\vec{x}_1, \vec{x}'_1) \rho_n(\vec{x}_2, \vec{x}'_2)$. In order to translate a single particle density matrix into phase-space density representation, the Wigner transformation is needed with new relative coordinates $\vec{r} \equiv (\vec{x}_i + \vec{x}'_i)/2$ and $\vec{R} = \vec{x}_i - \vec{x}'_i$,

$$f_i(\vec{r}_i, \vec{p}_i) = \int d^3 \vec{R}_i \exp(i\vec{p}_i \cdot \vec{R}_i) \rho_i(\vec{r}_i + \vec{R}_i/2, \vec{r}_i - \vec{R}_i/2), \quad (5.16)$$

where $f_i(\vec{r}_i, \vec{p}_i)$ is the single-particle Wigner function. This is also applicable to the density matrix of the deuteron. The Wigner transformation of clusters are usually expressed within the wavefunction form since we can calculate and impose physical structure on the wavefunction. We have,

$$\mathcal{W}_d = \int d^3 \vec{R} \Psi_d\left(\vec{r} + \frac{\vec{R}}{2}\right) \Psi_d^*\left(\vec{r} - \frac{\vec{R}}{2}\right) \exp(-i\vec{p} \cdot \vec{R}), \quad (5.17)$$

where $\Psi(\vec{r})$ is the cluster wavefunction, i.e., deuteron wavefunction or a relative wavefunction of the constituents.

With all of these ingredients, we now can formulate the cluster yields of mass A in the expression of the overlapping nucleons phase-space functions $f_i(\vec{r}_i, \vec{p}_i)$ with the probability of the reaction determined by Wigner transformation of the cluster matrix:

$$N_A = g_A \int \left[\prod_i^A d^3 \vec{r}_i d^3 \vec{p}_i f_i(\vec{r}_i, \vec{p}_i) \right] \mathcal{W}_A(\vec{r}, \vec{p}), \quad (5.18)$$

where $\mathcal{W}_A(\vec{r}, \vec{p})$ is the so-called Wigner transformation function and g_A is the spin-isospin degeneracy. Typically the relative wavefunction or cluster wavefunction $\Psi(\vec{r})_A$ is usually assumed to be the spherical harmonic-oscillator wavefunction which leads to the expression of:

$$\mathcal{W}_A(\vec{r}, \vec{q}) = 8^{A-1} \exp \left[- \sum_{i=1}^A \left(\frac{\vec{R}_i^2}{\sigma_i^2} + \sigma_i^2 \vec{q}_i^2 \right) \right], \quad (5.19)$$

The parameter σ_i is associated with the root-mean-square (rms) radius of coalesced nuclei.

Besides this simple Wigner's transformation, one can also apply the same idea, adopted from density matrix considerations, with different assumptions as, e.g., suggested by S. Mrówczyński which not only assumes a simple Gaussian model but also uses the more realistic Hulthén wavefunction (well described at low energies, but does not impact on the final results much). We will discuss this model in more detail in Ch.IV.

5.2.3 Dynamical Model

To consider dynamical effects for cluster productions, we generally integrate cluster formation into the event generators, mostly the transport models and/or hydrodynamical models.

UrQMD + Box Coalescence

The coalescence model is integrated into UrQMD with the concept of box coalescence, i.e., the phase-space coordinates (positions and momenta) of all nucleons are extracted at kinetic freeze-out, a criterion is then established to determine if nucleons are close enough in phase space to form a nucleus. This involves both spatial and momentum proximity criteria ΔR and ΔP .

The distance between nucleons is evaluated in the center of mass frame of the nucleons considered for coalescence. This process is repeated iteratively for all nucleons in the system, ensuring that all possible clusters are identified. The final step involves the spin-isospin projection probability to a pair of these proximity nucleons.

In this study, we will use and discuss about this hybrid approach often and in more detailed in the following sections.

PHQMD + MST

In the Quantum Molecular Dynamics (QMD) approach (specifically the PHQMD realization (Aichelin et al., 2020)), nucleons interact through both potentials and collisions. The potential between nucleons is attractive around nuclear ground state densities, and thus, at the end of a heavy-ion reaction, nucleons tend to stay together and form clusters. To identify these clusters, a Minimum Spanning Tree (MST) procedure (Aichelin, 1991) is applied, described as follows:

In the MST algorithm, only coordinate space information is used to identify clusters. A nucleon is considered part of a cluster if its spatial distance to any other nucleon is less than $r_0 = 4$ fm in the local rest frame of the cluster. The distance is calculated by a Lorentz transformation from the computational frame to the local rest frame, and the cut-off distance is chosen according to the range of the potential in PHQMD. Nucleons more distant than the cut-off distance are assumed not to be bound by the attractive nuclear interaction of that specific cluster.

The main advantage of the MST method is that it allows the identification of clusters at any time during the system's evolution. While the coalescence mechanism combines nucleons into deuterons at the kinetic freeze-out hypersurface, the MST method identifies clusters dynamically as the clusters are created by potential interactions at different stages of the evolution.

SMASH + Nucleon/Pion Catalyses

While coalescence and thermal models offer valuable frameworks for understanding cluster formation, recent developments suggest a more nuanced picture. Here, we discuss the SMASH (Simulating Many Accelerated Strongly-interacting Hadrons) transport model and its potential to capture the complexity of deuteron production.

Similar to the URQMD model, SMASH (Weil et al., 2016) simulates heavy-ion collisions by accounting for various interaction types based on the mean-field BUU numerical code. However, SMASH also includes multiple reactions like three-body collisions (Staudenmaier et al., 2021). It also directly calculates or fits inelastic cross sections, incorporating the detailed balance relationship between deuteron creation and destruction reactions. Recent advancements in SMASH include a stochastic collision implementation coupled with a hydrodynamic afterburner, allowing for the calculation of these multiple reactions.

As highlighted in Ref. (Oliinychenko, 2021; Liu et al., 2020), observed deuteron

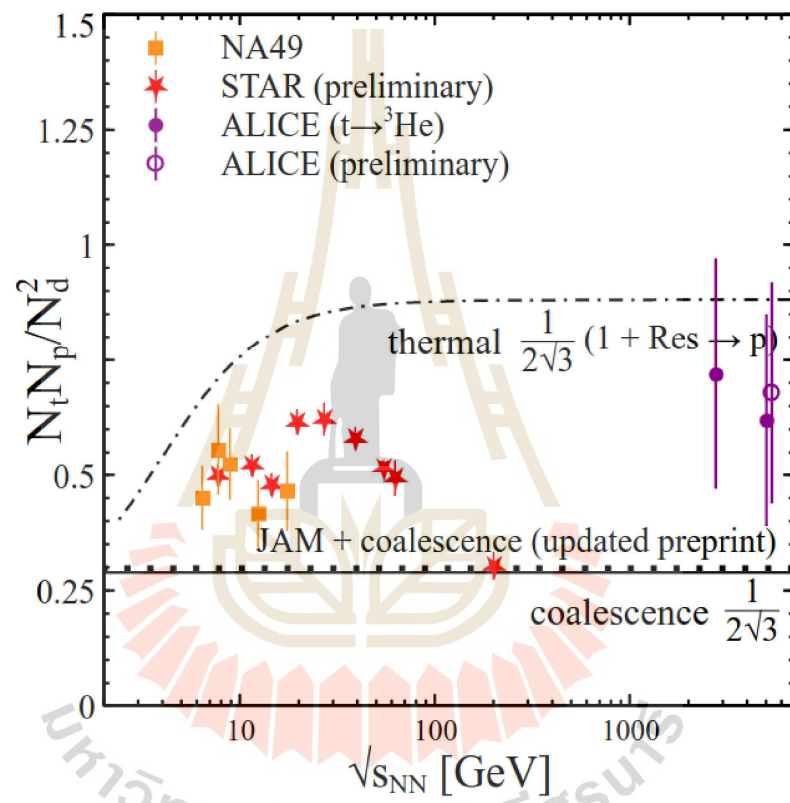
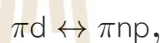


Figure 5.5 The Comparison of the tp/d^2 ratio from two cluster formation mechanisms of thermal (dashed line) and simple coalescence model (solid line) with experimental data (symbols).

production might not be solely explained by either coalescence or thermal models. The thermal model suggests cluster formation directly at the chemical freeze-out stage, alongside resonances and decays. In contrast, the coalescence model proposes cluster formation at the later kinetic freeze-out, with constituent nucleons influenced by resonances and decays only at final state.

Figure 5.5 illustrates how experimental data for the tp/d^2 ratio falls somewhere between the predictions of these two models. This suggests that cluster formation likely involves a combination of mechanisms working together.

The formation and disintegration of deuterons is catalyzed by reactions involving pions or nucleons, such as:



Additionally, rate reactions for these particle-deuteron interactions are included in the model. Studies suggest that $Nd \leftrightarrow Nnp$ dominates at lower beam energies (4 — 5 GeV), while $\pi d \leftrightarrow \pi np$ becomes more significant at higher energies (7.7 GeV).

SMASH's nucleon/pion catalysis model suggests that deuterons, often described as “snowballs in hell” within the thermal model analogy, do not simply survive from the chemical freeze-out ($T_{\text{chem}} \approx 150$ MeV) to the kinetic freeze-out. Instead, they are likely continuously disintegrated and re-created at similar rates, maintaining a state of relative equilibrium with the surrounding nucleons (Oliinychenko et al., 2021).

5.2.4 Multifragmentation

The multifragmentation model (Bondorf et al., 1995) describes the breakup of a highly excited nucleus into smaller fragments, i.e., (light)(hyper)nuclei, based on their mass A and charge Z . It can be viewed as a liquid-gas phase transition analogy applied to excited nuclear matter (Barz et al., 1986).

The excitation energy involved in the heavy-ion collisions is typically ranging between $\epsilon^* \simeq 1 - 10$ MeV/nucleon. At low excitation energies $\epsilon^* \approx 1$ MeV/nucleon, the nuclear system can be fully described with the liquid-drop model as the baryon density is then close to the saturation density $\rho_0 \approx 0.15$ fm³. When the system

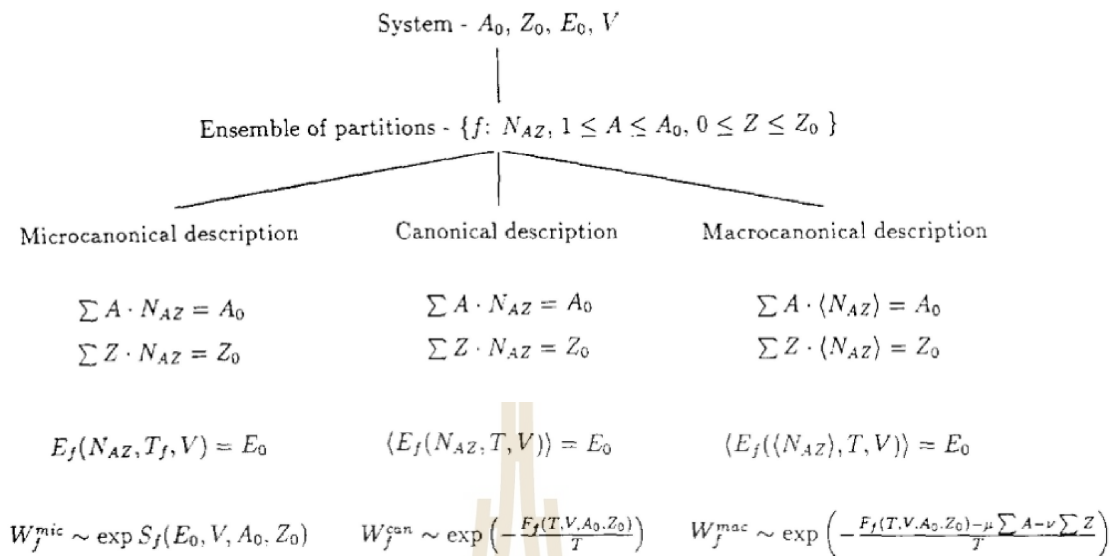


Figure 5.6 Different statistical ensembles used for describing the breakup of a nuclear system with partition f (Bondorf et al., 1995; Fai and Randrup, 1983; Gross, 1984).

reaches higher excitation energies, the baryon density becomes smaller $\rho < \rho_0$, the nuclear system can be excited and realized as a droplet as described by the liquid-drop model (if $\rho \lesssim \rho_0/2$). At this stage, attractive nuclear force dominates and favoring clusterization, leading to so-called pre-fragments. Finally, when the excitation energy is high enough $\epsilon^* \simeq 5 - 8$ MeV/nucleon, i.e., higher than most total binding energies of (light) nuclei, the compound (excited) nuclei begin to loosen as long-range Coulomb repulsion becomes important. In the excited nuclear system, the primary fragments cannot hold together anymore and evaporation-like decay mechanisms occur, resulting in the explosive break-up. This process could occur multiple times reducing the excitation energies of the fragments and emitting multiple fragments, a process known as multifragmentation.

Considering a large ensemble of final fragments and assuming local equilibrium with constraints from nuclear configurations and Coulomb energies, we can describe multifragmentation statistically. Figure 5.6 illustrates different statistical ensembles used for describing the breakup of the nuclear system, all conserving total mass (A_0), charge (Z_0), and energy (E_0).

The total energy of a fragment partition (f) can be expressed as:

$$E_f(T, V) = E_f^{\text{tr}}(T, V) + \sum_{(A,Z)} E_{(A,Z)}(T, V) + E_0^C(V) \quad (5.20)$$

The first term (E_f^{tr}) describes the translational and rotational motion of fragments. The second term accounts for the internal excitation energy and clusterization energy of individual fragments (A, Z). The third term (E_0^C) represents the total Coulomb energy.

The final fragment multiplicities can be determined by considering the system at thermal equilibrium, where the number of microscopic states leading to a specific partition is governed by its entropy (S_f).

The multifragmentation process can be visualized in three stages: (I) The initial non-equilibrium stage, this stage leads to the production of an intermediate highly-excited nuclear system. It is important to note that there is no clear or unified model to describe the initial non-equilibrium stage. Additionally, the final multiplicity of the fragment nuclei is highly sensitive to the initial conditions. (II) Fragment formation and breakup: Breakup of the system into separate fragments through a complex interplay of nuclear and Coulomb forces. (III) Coulomb Propagation and de-excitation: Hot fragments interact via Coulomb repulsion and undergo de-excitation through various mechanisms.

Since the initial non-equilibrium stage lacks a complete theoretical description, a hybrid modeling approach is often employed. This combines dynamical models (e.g., transport models like UrQMD) to describe the initial stages (system size, participants, energy density) with statistical multifragmentation models to describe fragment formation at later stages when the system approaches equilibrium. The implementation of such hybrid models will be discussed in Chapter VIII.

CHAPTER VI

CORRECTING B_A COALESCENCE FACTOR

Our previous focuses have been on understanding the mechanisms and outcomes of cluster formation, particularly emphasizing the fireball geometry and the space-time picture. We found that the extracted (anti)nucleon source geometries, by fitting the experimental data on B_2 and \overline{B}_2 coalescence parameters, reveals a local maximum around $\sqrt{s_{NN}} = 27$ GeV. This source volume contradicts the conventional belief that the source volume grows with charged particle yields.

It is well-known and also mentioned before in Ch. V that the yield ratio of deuterons to nucleon square inversely scales with the volume $d/p^2 \propto 1/V$. In the thermal model, this volume corresponds to the volume of the thermal source, while the coalescence model suggests it corresponds to the spatial source where the clusters coalesce. Quantitatively, the relation between the density of nucleons N_p or N_n and the final cluster yield N_A based on the coalescence model is,

$$E_A \frac{d^3 N_A}{dp_A^3} = B_A \left(E_p \frac{d^3 N_p}{dp_p^3} \right)^Z \left(E_p \frac{d^3 N_n}{dp_n^3} \right)^N. \quad (6.1)$$

Here, $A = N + Z$ is the mass number of the produced nuclei. The coalescence parameter B_A is proportional to $(1/V)^{A-1}$. As mentioned above, the final values and the interpretation of the volume are model dependent (Butler and Pearson, 1963; Schwarzschild and Zupancic, 1963; Gutbrod et al., 1976; Bond et al., 1977; Sato and Yazaki, 1981; Gyulassy et al., 1983; Csernai and Kapusta, 1986; Mrowczynski, 1990). In the coalescence model, this volume is akin to the region of homogeneity interpreted by Hanbury-Brown-Twiss (HBT) analyses (Kapusta, 1980). This prompts further exploration to ascertain the compatibility between the coalescence volume and the HBT volume through the B_A values.

The comparison between experimental data of the coalescence factor B_A and predictions by HBT is illustrated in Figure 6.1. The HBT data (represented by the black dash-dotted line) aligns well with experimental data at high energies $E_{\text{beam}} > 10A$ GeV (Adamczyk et al., 2015). However, discrepancies emerge at lower

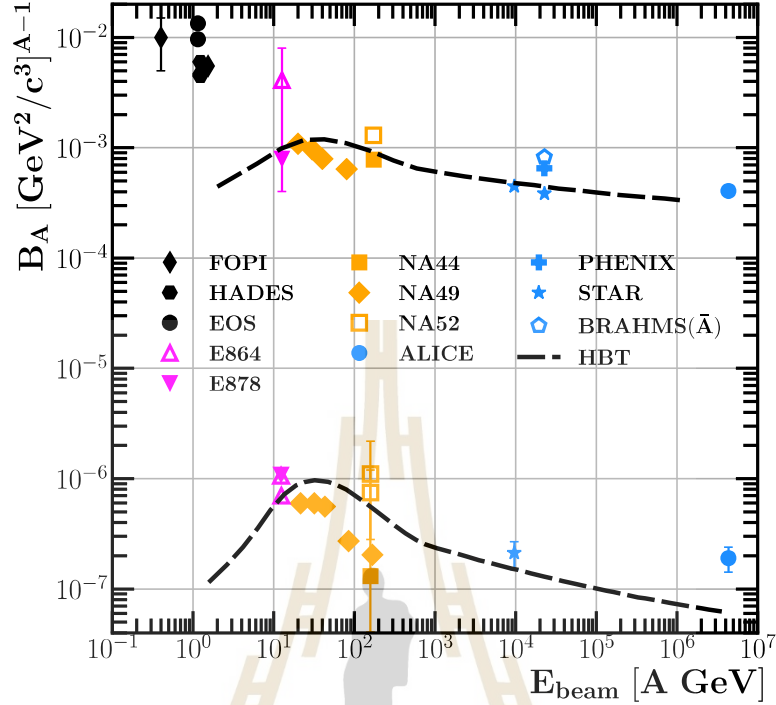


Figure 6.1 Coalescence parameter B_A measured by experiments (Braun-Munzinger and Dönigus, 2019) and predicted by HBT (Adamczyk et al., 2015) as a function of center-of-mass energy $\sqrt{s_{NN}}$ [GeV].

energies $E_{\text{beam}} \leq 10A$ GeV, raising questions as experimental measurements exhibit a notable spike in B_2 values, whereas the HBT prediction decreases.

In this chapter, our objective is to investigate and demonstrate that the observed discrepancy can be effectively addressed and resolved through a proper correction of the measured data. By implementing these corrections and testing with UrQMD simulations, we aim to not only solve the discrepancies at low collision energies but also enable the prediction of B_3 for the entire energy range under consideration.

6.1 Problems with B_A

We begin by addressing the issues with the measurements of B_2 as outlined in Eq. (6.1): First, the equation requires measurement of the neutron density, yet in practice, the estimated neutrons are obtained by assuming an equal number of neu-

trons and protons. Second, the measured protons typically represent the final-stage protons, which is justifiable only at high energies where cluster yields are significantly smaller than the square of final-stage protons.

At lower energies, however, the protons and neutrons in Eq. (6.1) are meant to be the primordial ones before coalescence, not the final-stage ones. At these energies, not only is there an enhancement in cluster production, but other clusters are also produced at mid-rapidity, drawing from the primordial protons and neutrons. This leads to a discrepancy of almost 40% compared to the final-stage nucleon contents, rendering the assumption of final-stage protons and neutrons unjustified. Additionally, the unequal distribution of protons to neutrons due to isospin equilibration further invalidates the assumption of equal nucleon distribution at low energies, as discussed in Ch. VII. Below we will investigate how to obtain the proper B_A for the experiments and present how do these effects affect the final results from the measurements.

6.2 Reconstructing Primordial Protons and Neutrons

6.2.1 Rapidity Distribution

We begin by illustrating the distinction between the final state protons typically measured by the experiments and the primordial protons before coalescence obtained from the simulations. To quantify these effects, we simulate the Au+Au 0 — 10% central collisions at $E_{\text{beam}} = 1.23A$ GeV using the UrQMD transport model, reflecting conditions attainable in current HADES experiments. As discussed above, at such low energy, the fraction of (light) clusters relative to the final state nucleons is substantial.

Figure 6.2 clearly illustrates the difference between the simulated primordial protons N_p^{prim} (red circles) and the final state protons N_p^{final} (red dashed line) in rapidity yields, with the final state protons accounting for only approximately 60% of the overall primordial protons before coalescence. This discrepancy arises because a portion of primordial protons is bound into light clusters. Based on this idea, we can estimate the primordial protons reconstructed from the measured final state protons by

$$\frac{dN_p^{\text{prim(reco)}}}{dy} = \frac{dN_p^{\text{final}}}{dy} + \sum_c^{\text{clusters}} Z_c \frac{dN_c^{\text{final}}}{dy}. \quad (6.2)$$

Here, the reconstructed primordial proton distribution $dN_p^{\text{prim(reco)}}/dy$ is estimated by

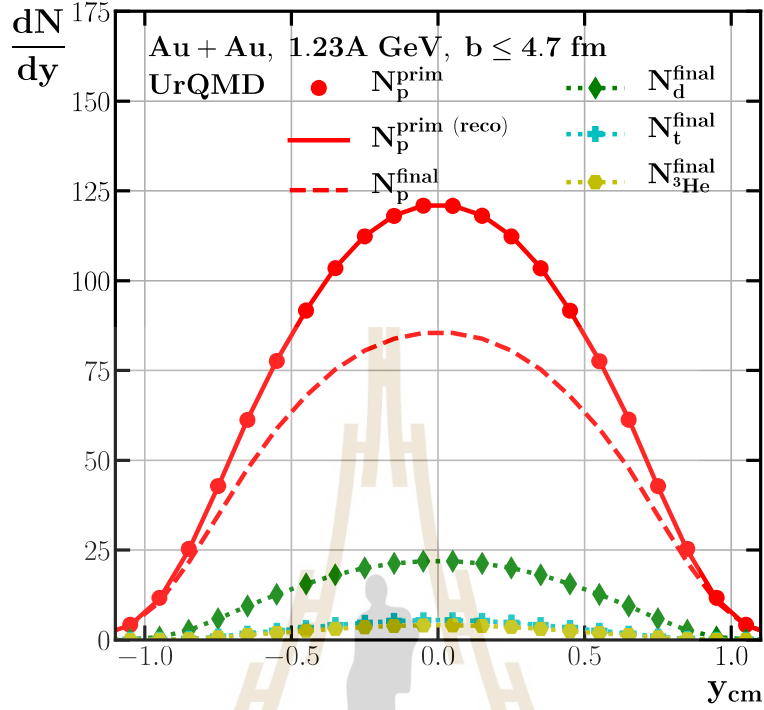


Figure 6.2 Rapidity distribution comparison of protons and light nuclei in 0 — 10% Au+Au collisions at $E_{\text{beam}} = 1.23A$ GeV. Simulated primordial protons (red circles), simulated final state protons (red dashed lines), and reconstructed primordial protons (red solid lines) are contrasted alongside the rapidity distributions of deuterons (green diamonds), tritons (cyan crosses), and ^3He nuclei (yellow hexagons).

adding all the final state proton contents, comprising the free final state protons dN_p^{final}/dy , along with the clusters dN_c^{final}/dy , where Z_c represents the proton number of the clusters c . The estimated reconstructed primordial proton distribution is depicted in Figure 6.2 as a red solid line, illustrating its high accuracy in describing the primordial proton distribution.

Similarly, a comparable approach as in Eq. (6.2) can be employed to estimate the primordial neutron numbers, given by

$$\frac{dN_n^{\text{prim(reco)}}}{dy} = \frac{dN_n^{\text{final}}}{dy} + \sum_c^{\text{clusters}} N_c \frac{dN_c^{\text{final}}}{dy}, \quad (6.3)$$

where N_c is the neutron number of cluster c . However, unlike protons, we lack experimental data on both the primordial and the final state neutron distributions. In order to estimate the final state neutrons, we consider the isospin configuration and the isospin exchange of the system. Initially the isospin contents are from two gold nuclei $2N_{Au}/2Z_{Au} = 1.49$. After the collision, isospin begins to exchange and equilibrate toward the final stage of the collision. The charged pions are emitted from the resonance decays carrying the isospin. The isospin exchange, transforming a primordial proton to a final stage neutron, produces a positively charged pion π^+ . On the other hand, the production of a negatively charged pion π^- represents the isospin exchange of a primordial neutron transformed into a final state proton. This implies that the integrated number of primordial protons and neutrons at given fixed participants A_{part} can be written as

$$N_p^{prim(reco)} = \frac{2Z_{Au}}{2A_{Au}} A_{part} + (N_{\pi^-} - N_{\pi^+}), \quad (6.4)$$

$$N_n^{prim(reco)} = \frac{2N_{Au}}{2A_{Au}} A_{part} - (N_{\pi^-} - N_{\pi^+}) \quad (6.5)$$

The first terms from both equations account for the isospin fraction from the gold nuclei to the participant numbers, i.e., estimated N_p^{part} and N_n^{part} . The second term subtracts and adds the primordial protons and neutrons from the final stage charged pions.

The participant numbers A_{part} cannot be measured directly. However, we can infer the number via $A_{part} = N_p^{part} + N_n^{part}$. Assuming the same isospin content ratio for the participants and the initial two gold nuclei which are well justify within the central collisions, we have $N_n^{part} \simeq \frac{2N_{Au}}{2Z_{Au}} N_p^{part*}$. The number of participating protons can be calculated and measured via $N_p^{part} = N_p^{prim} - (N_{\pi^-} - N_{\pi^+})$. So, The participant numbers can be expressed in all measurable observables as

$$A_{part} = \left(N_p^{prim} - \Delta\pi \right) \times \left(\frac{2N_{Au}}{2Z_{Au}} \right), \quad (6.6)$$

*The UrQMD simulations give us the $\langle N_n^{part} \rangle = 2N_{Au} - \langle N_n^{spec} \rangle = 143.61$ and $\langle N_n^{part} \rangle = 2N_{Au} - \langle N_n^{spec} \rangle = 213.99$ which is $N_n^{part} \simeq \frac{2N_{Au}}{2Z_{Au}} N_p^{part} = 214.51$.

with $\Delta\pi \equiv (N_{\pi^-} - N_{\pi^+})$. Inserting this into Eq. (6.4) and Eq. (6.5), we finally obtain,

$$N_n^{\text{prim(reco)}} = N_p^{\text{prim(reco)}} \frac{\left(N_p^{\text{prim}} - \Delta\pi\right) \left(\frac{2N_{Au}}{2Z_{Au}} + 1\right) \frac{2N_{Au}}{2A_{Au}} - \Delta\pi}{\underbrace{\left(N_p^{\text{prim}} - \Delta\pi\right) \left(\frac{2N_{Au}}{2Z_{Au}} + 1\right) \frac{2N_{Au}}{2A_{Au}} + \Delta\pi}_{\equiv \Delta_{iso}^{\text{prim}}}}. \quad (6.7)$$

The factor $\Delta_{iso}^{\text{prim}}$ denotes the isospin ratio of the primordial state estimated from the integrated numbers in 4π . Now the reconstructed primordial neutron distribution Eq. (6.3) can now be expressed via the measured rapidity distributions of protons and clusters and the integrated number of charged pions $\Delta\pi$ in 4π . The primordial neutron rapidity distribution is then given by,

$$\frac{dN_n^{\text{prim(reco)}}}{dy} = \left(\frac{dN_p^{\text{final}}}{dy} + \sum_c^{\text{clusters}} Z_c \frac{dN_c^{\text{final}}}{dy} \right) \Delta_{iso}^{\text{prim}}. \quad (6.8)$$

Finally, the reconstructed final state neutron rapidity distribution reads

$$\frac{dN_n^{\text{final(reco)}}}{dy} = \left(\frac{dN_p^{\text{final}}}{dy} + \sum_c^{\text{clusters}} Z_c \frac{dN_c^{\text{final}}}{dy} \right) \Delta_{iso}^{\text{prim}} - \left(\sum_c^{\text{clusters}} N_c \frac{dN_c^{\text{final}}}{dy} \right). \quad (6.9)$$

The comparison of the UrQMD simulated neutron rapidity distributions with our reconstructions is depicted in Figure 6.3. We observe that the reconstructed neutron distributions from Eq. (6.8) (blue dashed line) and Eq. (6.9) (blue dotted line) match the results from simulations (blue squares), validating our proposed reconstruction method. Furthermore, we can observe that the neutron densities exceed the proton densities around $\simeq 1.3 - 1.5$ for both primordial and final states.

6.2.2 p_T Distribution

Proceeding from our successful testing of the reconstruction methods for estimating the differential rapidity distributions of primordial and final state neutrons and protons, we can now extend our analysis to the transverse momentum p_T distribution which is crucial for determining the coalescence parameter B_A . We follow the same procedure as for the rapidity distribution, but additionally scale the transverse momentum

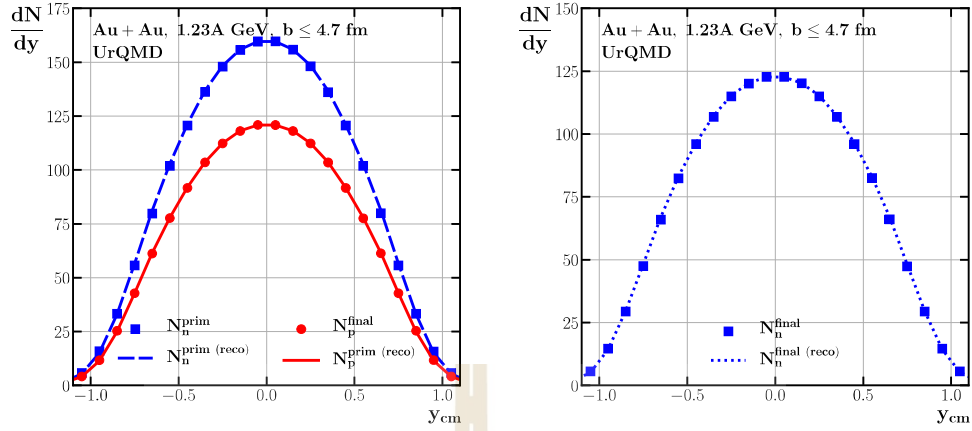


Figure 6.3 Rapidity distribution of simulated (symbols) and reconstructed (lines) proton and neutron at central Au+Au collisions $E_{\text{beam}} = 1.23A$ GeV. (Left panel) The comparison for the simulated and reconstructed primordial proton (red) and neutron (blue) rapidity based on Eq. (6.2) and Eq. (6.8). (Right panel) The comparison for the simulated and reconstructed final neutron rapidity based on Eq. (6.9).

of the clusters by their respective mass number, p_T/A . The reconstructed primordial proton and neutron transverse momentum distribution reads

$$\frac{1}{p_T} \frac{dN_p^{\text{prim(reco)}}}{dp_T} = \frac{1}{p_T} \frac{dN_p^{\text{final}}}{dp_T} + \sum_c^{\text{clusters}} Z_c \frac{1}{p_T/A} \frac{dN_c^{\text{final}}}{dp_T/A}, \quad (6.10)$$

$$\frac{1}{p_T} \frac{dN_n^{\text{prim(reco)}}}{dp_T} = \frac{1}{p_T} \frac{dN_n^{\text{final}}}{dp_T} + \sum_c^{\text{clusters}} N_c \frac{1}{p_T/A} \frac{dN_c^{\text{final}}}{dp_T/A}. \quad (6.11)$$

Figure 6.4 illustrates the invariant transverse momentum distributions of light clusters from our simulations, including deuterons (d: green diamonds), tritons (t: blue crosses), and ^3He (yellow hexagons), represented by dotted lines. Additionally, comparisons are made between simulated primordial neutrons (blue squares), protons (red circles), and the reconstructed primordial neutrons (dash-dotted lines) and protons (red solid line) at 0 — 10% central Au+Au collisions $E_{\text{beam}} = 1.23A$ GeV mid-rapidity, all at the same transverse momentum p_T/A . The calculations accurately depict both the reconstructed primordial protons and neutrons compared to their simulated counterparts. Additionally, the neutron density is higher than the proton density across the

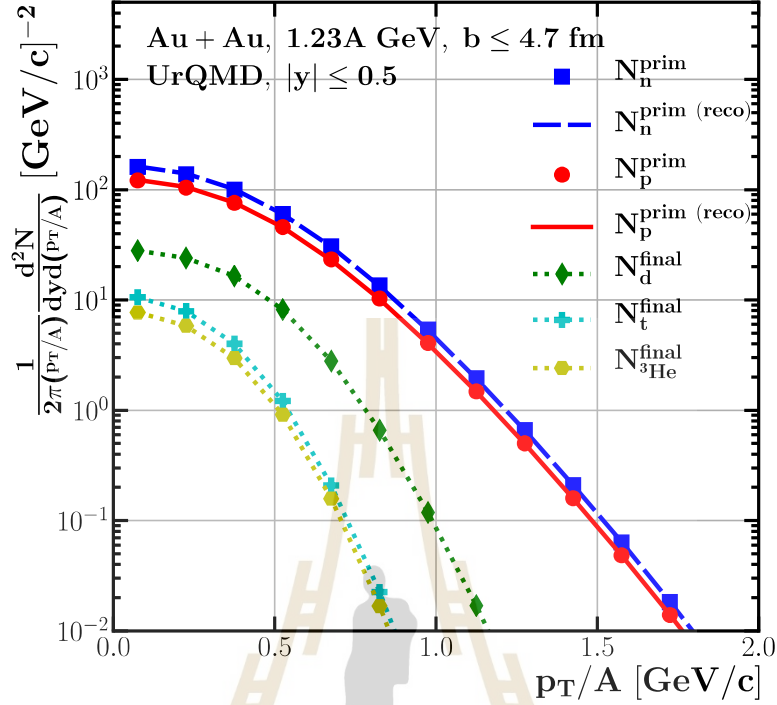


Figure 6.4 Invariant p_T spectra of d (green diamonds with dotted line), t (cyan pluses with dotted line), ^3He (yellow hexagons with dotted line), the primordial proton (full red circles) and neutron (full blue squares) from the simulations. While, the reconstructed primordial protons and neutrons are shown with solid red and solid blue lines respectively. The calculations are done at mid-rapidity in central Au+Au reactions at $E_{\text{beam}} = 1.23A \text{ GeV}$

entire transverse momentum range, consistent with the initial isospin asymmetry of the gold nuclei. This results in a higher abundance of tritons compared to ^3He nuclei in the coalescence spectra as expected.

We now discuss and clarify the use of the rapidity and p_T independence of $\Delta_{\text{ISO}}^{\text{prim}}$ from Eq. (6.7) for reconstructing primordial protons and neutrons with the 4π -integrated $\Delta\pi$. The pion rapidity and p_T distributions differ from those of participating nucleons. For instance, pion distributions are typically broader in rapidity due to their lower mass. Moreover, in p_T spectra, pions tend to have lower p_T values compared to nucleons. Consequently, applying a p_T -dependent correction would lead to increasingly severe corrections as p_T increases. Therefore, $\Delta_{\text{ISO}}^{\text{prim}}$ cannot be evaluated differ-

entially in rapidity and scaled transverse momentum p_T since it is also experimentally challenging to associate the rapidity and p_T bin of emitted pions with the corresponding primordial nucleons from their respective spectra. Figure 6.5 supports our approach and justifies the use of a constant $\Delta_{\text{iso}}^{\text{prim}}$ by demonstrating that $\Delta_{\text{iso}}^{\text{prim}}$ remains nearly constant across rapidity (left panel) and transverse momentum distributions p_T/A (right panel).

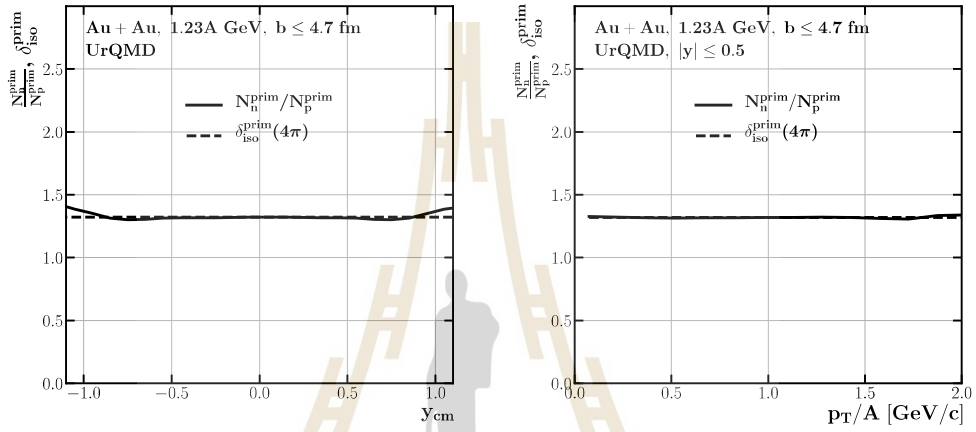


Figure 6.5 (Left panel) The Rapidity distributions of the neutron/proton ratio (full black line), and the integrated $\Delta_{\text{iso}}^{\text{prim}}$ (dashed line). (Right panel) The transverse momentum distributions of the primordial neutron/proton ratio (full black line), and the integrated $\Delta_{\text{iso}}^{\text{prim}}$ (dashed line). Both from UrQMD for 0 — 10% central Au+Au reactions at $E_{\text{beam}} = 1.23A$ GeV

6.2.3 Estimating B_2 and B_3

We finally can test the impact of the invariant distribution of the (reconstructed) primordial protons and neutrons as a function of transverse momentum per nucleon p_T/A on the coalescence parameter B_A (Eq. (6.1)),

$$B_A = \left(\frac{1}{2\pi(p_T/A)} \frac{d^2 N_A}{dyd(p_T/A)} \right) / \left(\frac{1}{2\pi p_T} \frac{d^2 N_p}{dyd(p_T)} \right)^Z \cdot \left(\frac{1}{2\pi p_T} \frac{d^2 N_n}{dyd(p_T)} \right)^N. \quad (6.12)$$

Figure 6.6 illustrates the dependence of the coalescence parameters B_2 (left panel) and B_3 (right panel) on the scaled transverse momentum p_T/A .

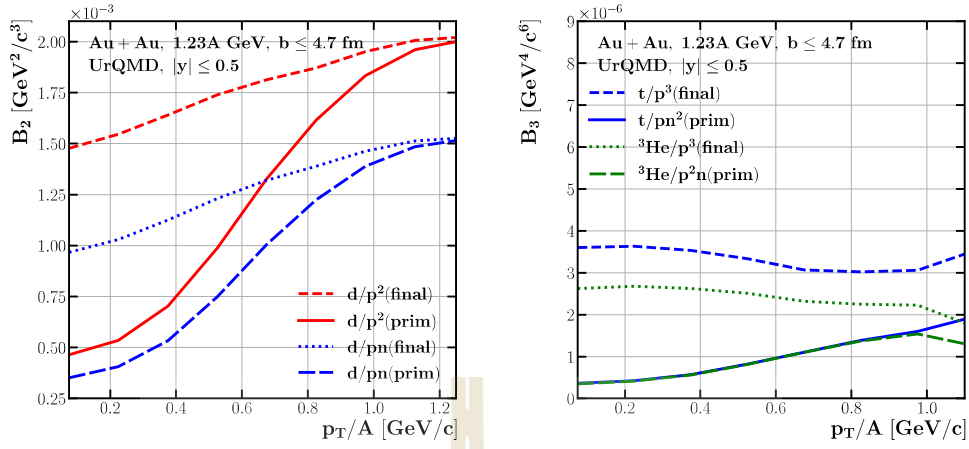


Figure 6.6 The scaled transverse momentum p_T/A -dependence of the coalescence parameter B_2 (left panel) and B_3 (right panel) calculated using the final state nucleons and reconstructed primordial nucleons from UrQMD for 0 — 10% central Au+Au reactions at $E_{\text{beam}} = 1.23A$ GeV

First, considering the impact of using final state neutrons for calculating the coalescence parameter, the original B_2 obtained by the final state proton squared ratio $d/p^2(\text{final})$ (red dashed line) already overestimates B_2 calculated with the product of final state protons and neutrons $d/pn(\text{final})$ (blue dotted line) by a factor ≈ 1.5 across the entire range of p_T/A . This p_T -independent scaling is attributed to the isospin asymmetry from the initial stage, aligning with the expected values from the initial isospin of gold nuclei $N_{\text{Au}}/Z_{\text{Au}} = 1.49$ and the primordial isospin factor $\Delta_{\text{iso}}^{\text{prim}} = 1.32$.

Second, upon changing from final state to primordial nucleons, B_2 calculated with the reconstructed primordial protons $d/p^2(\text{prim})$ (red solid line) noticeably suppresses the original $B_2 \propto d/p^2(\text{final})$ (red dashed line) across the entire p_T spectrum, with a maximum suppression factor of approximately 3 at $p_T/A \simeq 0$, gradually decreasing to unity for $p_T/A > 1.0$. This arises because clusters are more likely to coalesce at lower p_T/A than at higher p_T/A (see Figure 6.4), resulting in similar numbers of final and primordial protons and neutrons.

With the complete correction of the coalescence parameter calculated using the product of primordial protons and neutrons $d/pn(\text{prim})$ (blue dash-dotted line), it is evident that this correction further suppresses B_2 calculated using primordial proton square (red solid line) by a factor of 1.2 — 1.5, and around 4 times at p_T/A when compared to the original B_2 (red dashed line).

Similarly, in Figure 6.6 (right panel), the correction impacts on the original B_3 of tritons and ${}^3\text{He}$ calculated using the final state proton cubic square, i.e., t/p^3 (blue dashed line) and ${}^3\text{He}$ (green dotted line), are shown. The total corrections of B_3 tritons using primordial proton and neutrons squared (blue solid line) suppress their original B_3 (blue dashed line) by a factor of 7, while the corrected B_3 of ${}^3\text{He}$ using the primordial neutron and proton squared (green dash-dotted line) is suppressed by approximately 5 times its original B_3 value (green dotted line). Interestingly, the original values of B_3 for tritons (blue dashed line) and ${}^3\text{He}$ (green dotted line) are initially separated by an isospin factor of 1.2 — 1.5. However, after the correction, both become identical for $p_T/A \leq 1.0$.

Finally, we arrive at our main objective of investigating the energy dependence of the coalescence parameter B_A and its comparison with experimental data (Wang et al., 1995; Ambrosini et al., 1998; Armstrong et al., 1999; Ahle et al., 1999; Barrette et al., 2000; Armstrong et al., 2000; Afanasiev et al., 2000; Bearden et al., 2002; Anticic et al., 2004; Anticic et al., 2016; Botvina et al., 2021). The representing coalescence parameter B_A is chosen at $p_T/A = 0$ [GeV/c] for each beam energy as we follow the HADES approach. Figure 6.7 shows our analyses of B_2 (left panel) and B_3 (right panel) from the original calculations and the corrected version comparing with the experimental data depicted by the symbols and the result from the HBT (Adamczyk et al., 2015) shown as a black dash-dotted line.

In the left panel, the original B_2 calculated by the final state proton square (red dashed line) increases after $E_{\text{beam}} \leq 10\text{A GeV}$, consistent with FOPI and HADES experiments (black symbols). However, the corrected B_2 from our reconstructed primordial protons and neutrons (red solid line) aligns with the prediction from the HBT volume, decreasing with the energy for $E_{\text{beam}} \leq 10\text{A GeV}$. The values of B_2 are summarized in Table 6.1

The same trend is evident in the calculation of B_3 in the right panel. The original B_3 values for both triton and ${}^3\text{He}$ (blue dashed line and green dotted line) obtained from the final state cubed proton number increase at lower beam energies, where the discrepancy in their isospin asymmetry by a factor of 1.2 — 1.5 becomes more noticeable. This discrepancy arises because at lower energies, the system struggles to equilibrate the isospin due to time constraints and limited pion production for isospin exchange. In contrast, the corrected versions of B_3 for triton and ${}^3\text{He}$ exhibit almost identical behavior, decreasing with energy in qualitative agreement with the HBT predic-

Table 6.1 The B_2 values calculated final state protons and both primordial protons and neutrons at $p_T/A = 0.0$ GeV at midrapidity $|y| \leq 0.5$. The calculation is extracted from 0 — 10% central Au+Au collisions at kinetic beam energies from $E_{\text{beam}} = 0.3A$ to 40A GeV.

$E_{\text{beam}} [A \text{ GeV}]$	$B_2 [\times 10^{-4} \text{ GeV}^2 / \text{c}^3]$	
	d/p_{final}^2	$d/p_{\text{prim}} n_{\text{prim}}$
0.3	14.44	0.70
0.5	15.31	1.10
1.23	14.77	3.52
1.93	13.44	5.00
11.45	9.34	6.88
20	8.39	6.71
30	7.72	6.46
40	7.22	6.21

Table 6.2 The B_3 values calculated final state protons and both primordial protons and neutrons at $p_T/A = 0.0$ GeV at midrapidity $|y| \leq 0.5$. The calculation is extracted from 0 — 10% central Au+Au collisions at kinetic beam energies from $E_{\text{beam}} = 0.3A$ to 40A GeV.

$E_{\text{beam}} [A \text{ GeV}]$	$B_3^t [\times 10^{-7} \text{ GeV}^4 / \text{c}^6]$		$B_3^{\text{He}} [\times 10^{-7} \text{ GeV}^4 / \text{c}^6]$	
	t/p_{final}^3	$t/p_{\text{prim}} n_{\text{prim}}^2$	${}^3\text{He}/p_{\text{final}}^3$	${}^3\text{He}/p_{\text{prim}}^2 n_{\text{prim}}$
0.3	82.75	0.73	61.17	0.80
0.5	72.93	1.16	50.16	1.16
1.23	36.00	3.64	26.24	3.50
1.93	23.35	4.72	18.25	4.63
11.45	7.94	4.78	7.29	4.83
20	6.22	4.29	5.79	4.22
30	5.25	3.91	4.83	3.81
40	4.58	3.56	4.18	3.41

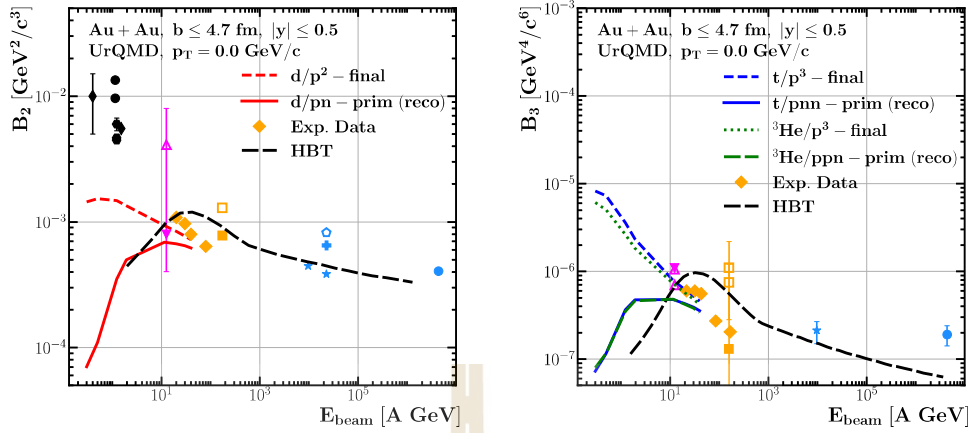


Figure 6.7 The figure caption describes the beam energy dependence of B_2 extracted at $p_T/A = 0$ GeV in mid-rapidity $|y| \leq 0.5$ for 0 – 10% central Au+Au collisions. Left panel: The dashed red line illustrates the original calculation of B_2 using the final state proton square, while the solid red line shows the corrected B_2 calculated by the product of reconstructed primordial protons and neutrons. Right panel: the original B_3 of tritons and ^3He , calculated from the final state proton cubic square, are depicted by the blue dashed line and green dotted line while the corrected B_3 of tritons and ^3He , using our reconstructed primordial protons and neutrons, are shown as the blue solid line and the green dash-dotted line, respectively. Experimental data (Wang et al., 1995; Ambrosini et al., 1998; Armstrong et al., 1999; Ahle et al., 1999; Barrette et al., 2000; Armstrong et al., 2000; Afanasiev et al., 2000; Bearden et al., 2002; Anticic et al., 2004; Anticic et al., 2016; Botvina et al., 2021) are denoted by symbols, while the dash-dotted black line represents the volume extracted from HBT results from STAR (Adamczyk et al., 2015).

tion. In this case, the splitting in isospin is already canceled out within each individual B_3 value, as mentioned above. The values of B_3 are summarized in Table 6.2.

In conclusion, we have investigated the discrepancy of the energy dependence of the coalescence parameters B_A between direct data from experiments and the prediction from HBT. Although the interpretation of $B_A \propto (1/V)^{A-1}$ is well-known and widely accepted, problems occur in its application. In the experiment, the measured B_A grows with decreasing energy. At first glance, this makes sense since the volume should also drop with energy if the cluster productions are not zero. However, the measurements of B_A not only estimate the number of neutrons from protons but

also use the final state protons in the calculations. However, we show that the coalescence parameter B_A , in fact, requires the primordial protons and neutrons as they are the main ingredients for the cluster before coalescence, i.e., the B_A is based on the probability with which the nucleons are drawn from the primordial state, not the final state. Thus, we obtain a method to acquire/reconstruct the primordial protons and neutrons from the final state observables and a corrected B_A . As expected, our calculation of the energy dependence of both B_2 and B_3 explains this discrepancy as supported by the HBT predictions.



CHAPTER VII

INVESTIGATING CLUSTER PRODUCTION MECHANISMS

7.1 Thermal vs Coalescence

(Hyper)(Light)Nuclei have been highlighted as crucial tools for investigating the medium properties and serving as a basis for studying the EoS around neutron star density regimes. In the Ch. IV, we have explored and discussed the roles of the source geometry and the cluster formations in the context of space-time exploration. We further emphasized on the different space-time pictures of various formation mechanisms in Ch. V especially two common approaches, i.e., the thermal model and the coalescence model. Despite the fact that their underlying physics assumptions differ significantly, there is no clear evidence to determine which mechanisms are really responsible for the cluster formation as both models result in similar estimated particle yields across a broad spectrum of collision energies.

The thermal model describes the particle production through the thermodynamic properties of the fireball, i.e., temperature and chemical potential, and typically within the grand canonical ensemble. It presumes that particle yields are fixed after the medium is fully thermalized at chemical freeze-out, thus implying that all particles form at a fixed temperature $T_{\text{chem}} \gtrsim 70$ MeV and corresponding chemical potential $\mu_{B,\text{chem}}(T)$ (Andronic et al., 2018). This raises questions about the survival of light clusters like the deuteron, with a binding energy of just a few MeV, in such an environment and contrasts with the deuteron bottleneck concept in Big Bang Nucleosynthesis (Pospelov and Pradler, 2010), where cluster formation requires cooling to match deuteron binding energies. Despite these challenges, the thermal model remains widely used to estimate particle yields (Vovchenko et al., 2020), even as it is difficult to incorporate dependencies like wavefunctions which are crucial at lower energies where the internal structure of clusters matters (Juric et al., 1973; Abelev et al., 2010; Adam et al., 2016; Dönigus, 2013; Andronic et al., 2018; Blaschke et al., 2020).

On the other hand, although the coalescence model is also based on statistical mechanics, it is closer in spirit to the microcanonical ensemble, allowing for the study of medium dynamics. Here, coalescence occurs at the kinetic freeze-out;

if two or more free nucleons, after their final collisions and decays, are close enough in phase-space, they will form a cluster. Typically, the temperature and volume of the source size are smaller than in the thermal model making it possible for the clusters to survive. In contrast to the thermal model's limitations, the coalescence model can accommodate various other factors and dynamical considerations. Distinguishing between thermal and coalescence methods for cluster production becomes crucial.

In this chapter, we use these distinctions to investigate which mechanism is realized in nature for cluster formation in heavy-ion collisions. In the thermal model, occurring at chemical freeze-out, all hadrons, including clusters and resonances, are generated at the same time before undergoing any decay processes. Consequently, the final yields of clusters may not experience any fluctuations due to the stochastic nature of the decays or uncorrelated. Conversely, the coalescence model operates at kinetic freeze-out, occurring after all resonances have decayed, potentially allowing for the effects of event-by-event fluctuations from resonance decays to influence the final yields.

In our study, we specifically consider isospin fluctuations. Although the thermal model adheres to conservation laws, it typically employs grand canonical ensembles* (Cleymans and Satz, 1993; Becattini et al., 1998; Florkowski et al., 2002; Cleymans et al., 2006; Andronic et al., 2011; Petráň et al., 2013; Vovchenko et al., 2016; Andronic et al., 2019). This implies that while the thermal model can indeed capture isospin fluctuations, it can only provide averaged values derived from these fluctuations (Vovchenko and Stoecker, 2019). Therefore, we will examine if there is any correlation between isospin fluctuations and light cluster yields in the coalescence approach, knowing that the thermal model will always yield uncorrelated results.

7.2 Isospin triggering

Due to isospin conservation, the number (density) of nucleons is correlated with the emitted charged pions at the kinetic freeze-out through Δ decays (Reichert et al., 2019; Reichert et al., 2021). While other charged particles, e.g. kaons, also carry isospin, the freeze-out nucleons and charged pions are still the dominant species at all

* Even for the canonical ensemble (Vovchenko et al., 2018a), the total baryon number and isospin are also fixed (for a $b = 0$ collision they are identical to the initial state). The light nuclei, e.g., deuterons with isospin zero, are therefore not correlated with the pion isospin fluctuations. The main driver of pion isospin fluctuations are resonance decays after the fixing of the deuteron (and other cluster) numbers

energies. The correlation arises from the isospin content exchanges via,

$$\begin{aligned} p_{\text{part}} &\rightarrow n_{\text{fr}} + \pi^+ \\ n_{\text{part}} &\rightarrow p_{\text{fr}} + \pi^-, \end{aligned}$$

where p_{part} and n_{part} represent participating protons and nucleons, respectively, while p_{fr} and n_{fr} denote protons and nucleons at kinetic freeze-out. It's important to note that we assume a fixed volume where the participants $A_{\text{part}} = N_{\text{Au}} + Z_{\text{Au}}$ and the isospin ratio $N_{\text{part}}/Z_{\text{part}} = N_{\text{Au}}/Z_{\text{Au}}$ do not fluctuate to demonstrate a clear isospin fluctuation effect (Kittiratpattana et al., 2022). With this assumption, we can estimate the number of light clusters using coalescence models.

To illustrate our argument, consider an initial scenario with head on Au+Au collisions with $p_{\text{part}} = 2 \times Z_{\text{Au}} = 2 \times 79 = 158$ participating protons. If we trigger on an extreme event with 158 emitted π^+ and zero π^- , we would have a pure $n_{\text{fr}} = 158$ medium at kinetic freeze-out. According to the coalescence model, the probability of forming other light nuclei should vanish in this scenario. Conversely, if we trigger on an event with pure π^- and p_{fr} , there should be no light nuclei present. Therefore, we can deduce that the yields of light nuclei can be expressed in terms of the relative difference in charged pion yields $\Delta Y_{\pi} \equiv (Y_{\pi^-} - Y_{\pi^+})$ which should exhibit a distinct maximum.

In summary, the presence of a local maximum in the deuteron yield at a fixed (or tightly constrained) A_{part} as a function of ΔY_{π} serves as a distinguishing factor between thermal deuteron production and the coalescence approach. Additionally, we will also study higher mass clusters to validate this scenario.

7.2.1 Simple estimates

The simple coalescence model states that,

$$d = \tilde{B}_2 \cdot n_{\text{fr}} \cdot p_{\text{fr}}, \quad (7.1)$$

$$t = \tilde{B}_3 \cdot n_{\text{fr}}^2 \cdot p_{\text{fr}}, \quad (7.2)$$

$${}^3\text{He} = \tilde{B}_3 \cdot n_{\text{fr}} \cdot p_{\text{fr}}^2 \quad (7.3)$$

From the previous discussion, the total number of neutrons at kinetic freeze-out, denoted as n_{fr} , is determined by the sum of initial neutrons from the nuclei, $2N_{\text{Au}}$, added

to the number of π^- responsible for newly produced neutrons, and then subtracted by the number of π^+ responsible for converting initial participant neutrons into protons at kinetic freeze-out. Similarly, the total number of protons at kinetic freeze-out, denoted as p_{fr} , can be expressed similarly. We write n_{fr} and p_{fr} in terms of the relative difference in charged pions ΔY_{π} ,

$$n_{\text{fr}} = 2N_{\text{Au}} - \Delta Y_{\pi} , \quad (7.4)$$

$$p_{\text{fr}} = 2Z_{\text{Au}} + \Delta Y_{\pi} . \quad (7.5)$$

Then, we can estimate the yields of light clusters based on the coalescence model, which is expressed as:

$$d = \tilde{B}_2 \cdot (2N_{\text{Au}} - \Delta Y_{\pi}) \cdot (2Z_{\text{Au}} + \Delta Y_{\pi}) \quad (7.6)$$

$$t = \tilde{B}_3 \cdot (2N_{\text{Au}} - \Delta Y_{\pi})^2 \cdot (2Z_{\text{Au}} + \Delta Y_{\pi}) \quad (7.7)$$

$${}^3\text{He} = \tilde{B}_3 \cdot (2N_{\text{Au}} - \Delta Y_{\pi}) \cdot (2Z_{\text{Au}} + \Delta Y_{\pi})^2 , \quad (7.8)$$

where \tilde{B}_A is a coalescence factor from (Kittiratpattana et al., 2022) which has been discussed already in Ch. VI.

The results from Eq. (7.6)-(7.8) are shown in Fig. 7.1. The estimated yields of deuterons (d) are represented by the solid pink line, tritons (t) by the blue dashed line, and 3-Helium (${}^3\text{He}$) by the orange dotted line. As anticipated, all three show a distinct maximum with respect to the ΔY_{π} triggering. The local maximum of deuterons occurs at $\Delta Y_{\pi} = 39$. This arises from the fact that deuterons, consisting of one proton and one neutron, will have the highest probability to form when the medium is dominated by an equal number of protons and neutrons at kinetic freeze-out, i.e., $\Delta Y_{\pi} = N_{\text{Au}} - Z_{\text{Au}} = 39$.

For the tritons and ${}^3\text{He}$, their respective local maxima at $\Delta Y_{\pi} = \frac{1}{3}(2N_{\text{Au}} - 4Z_{\text{Au}}) = -\frac{80}{3}$ for tritons and $\Delta Y_{\pi} = \frac{1}{3}(4N_{\text{Au}} - 2Z_{\text{Au}}) = \frac{314}{3}$. Additionally, at $\Delta Y_{\pi} = 39$, where the proton and neutron content in the medium are evenly distributed coupled with the symmetry between tritons and ${}^3\text{He}$, we expect their yields to be equal.

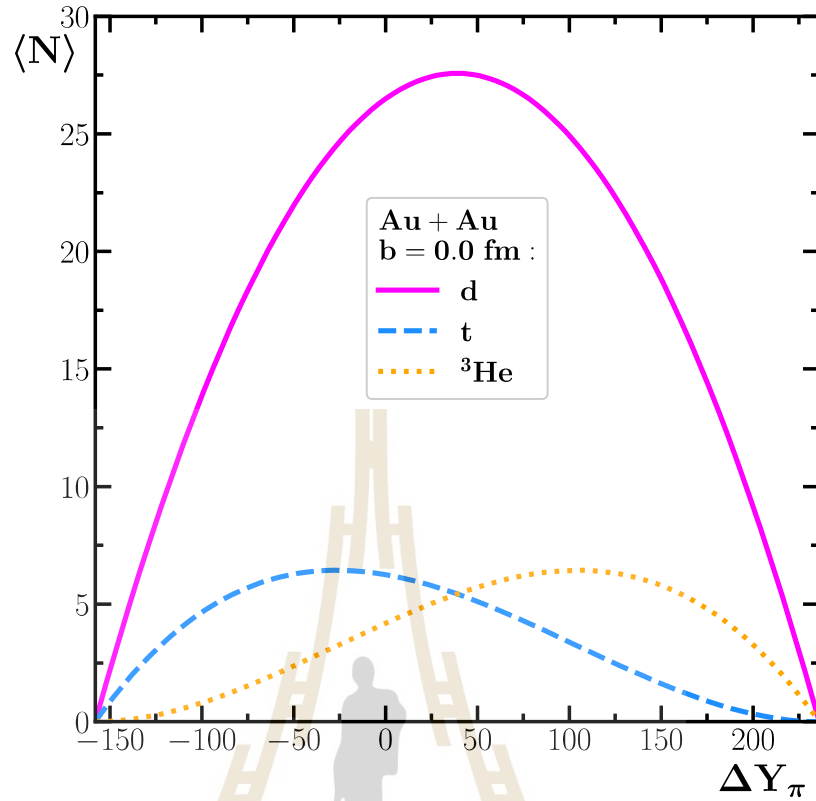


Figure 7.1 The theoretical estimation of the deuteron d (pink full line), triton t (blue dashed line), and ${}^3\text{He}$ (orange dotted line) production according to the Eq. (7.6)- (7.8) for central Au+Au reactions as a function of ΔY_π .

7.3 Qualitative Estimates

For the simplified theoretical model estimates, we assumed that the number of participants as well as their isospin N/Z ratio do not fluctuate, i.e., a fixed volume and $N/Z = N_{\text{Au}}/Z_{\text{Au}}$ for the estimation of the deuteron (and higher mass cluster) yields. However, this is not the case for a realistic situation. Thus, in this section, we will test our toy model with a detailed microscopic simulation of the UrQMD model which does not have such assumptions (even at the most central collisions). The results show nearly the same behavior as our simplified toy model.

In UrQMD model (Bass et al., 1998; Bleicher et al., 1999; Bleicher and Bratkovskaya, 2022) version v3.5, light clusters are produced by phase space coalescence from nucleons at kinetic freeze-out (see also (Sombun et al., 2019; Hillmann et al., 2022; Kireyeu et al., 2022) for details).

We focus on central Au+Au collisions with a center-of-mass energy range of $\sqrt{s_{NN}} = 3 - 8$ GeV, optimal for testing our concept, as pions and participating nucleons are strongly correlated, with their numbers being nearly equal or at least in the same order of magnitude. Moreover, at this energy range, both pions and nucleons dominate the medium, and when the isospin is (or is trying to become) equilibrated, the effects of isospin fluctuations on pions and nucleon numbers are more apparent than at higher energies. Although, at higher energies, the net charged pion fluctuations are stronger, it is compensated by the lesser deuteron yields and less correlation with the nucleons, as various hadrons also participate in the isospin exchange.

7.3.1 Freeze-out time distributions

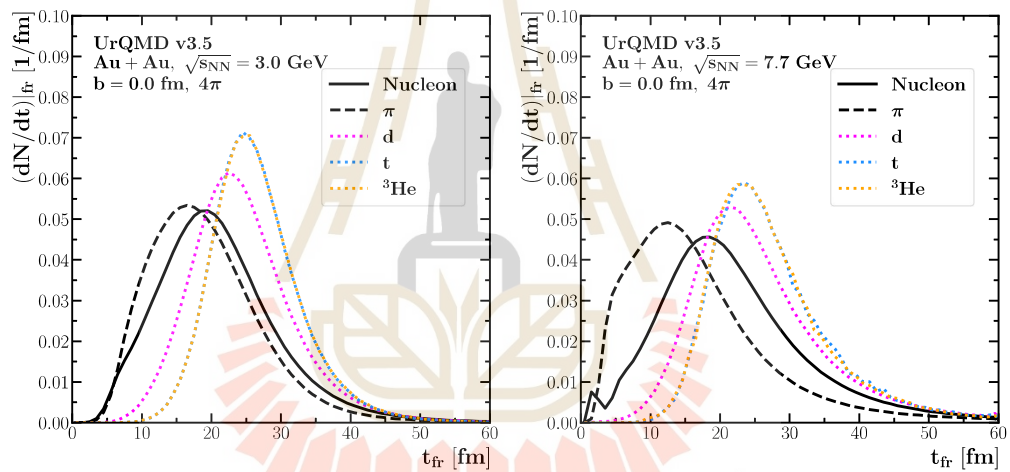


Figure 7.2 Freeze-out time distribution of nucleons (full black line), pions (dashed black line), deuterons (dotted pink line), tritons (dotted blue line), and ^3He (dotted orange line).

To begin and illustrate the idea, Fig. 7.2 shows the normalized freeze-out time distribution of the nucleons (solid black line), pions (dashed black line), deuterons d (dotted pink line), tritons t (dotted blue line) and 3-Helium ^3He (dotted orange line) in very central Au+Au collisions at $\sqrt{s_{NN}} = 3$ GeV (left panel) and at $\sqrt{s_{NN}} = 7.7$ GeV (right panel).

It is evident that light nuclei freeze-out after the pions have decoupled from the system, i.e., after isospin equilibration, as expected. Therefore, isospin fluctuations can indeed influence cluster formation. Although at both energies pions appear to decouple shortly before nucleons, this process is faster at higher energies ($\sqrt{s_{NN}} =$

7.7 GeV). This is due to the fact that, unlike our toy model, in the more realistic scenarios simulated by UrQMD, other hadrons can still be emitted together with the nucleons after the pions have decoupled. However, the overall assumption still holds true, as pions decouple before the clusters.

7.4 Light cluster yields versus isospin fluctuation

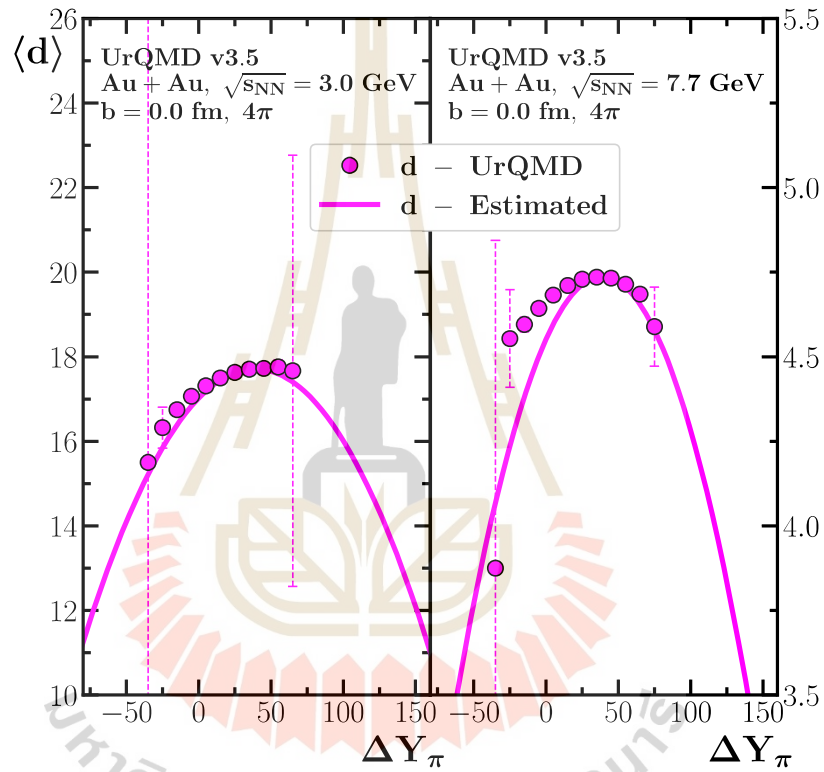


Figure 7.3 Deuteron yield as a function of ΔY_π for Au+Au reactions. The UrQMD results are shown by red circles. The estimated yield, Eq. (7.7), is represented by the full red line. Left: Results at $\sqrt{s_{NN}} = 3$ GeV. Right: Results at $\sqrt{s_{NN}} = 7.7$ GeV.

Finally, we contrast the estimated deuteron yields from the toy model with deuteron yields obtained from UrQMD simulations as a function of relative charged pion difference ΔY_π . The comparison at $\sqrt{s_{NN}} = 3.0$ GeV is depicted in Fig. 7.3 (left panel), and at $\sqrt{s_{NN}} = 7.7$ GeV in Fig. 7.3 (right panel). We clearly observe a local maximum in the deuteron yields at both energies around $\Delta Y_\pi = 39$, consistent with the expectation from the toy model.

The same comparison on light clusters with $A = 3$ is done and shown

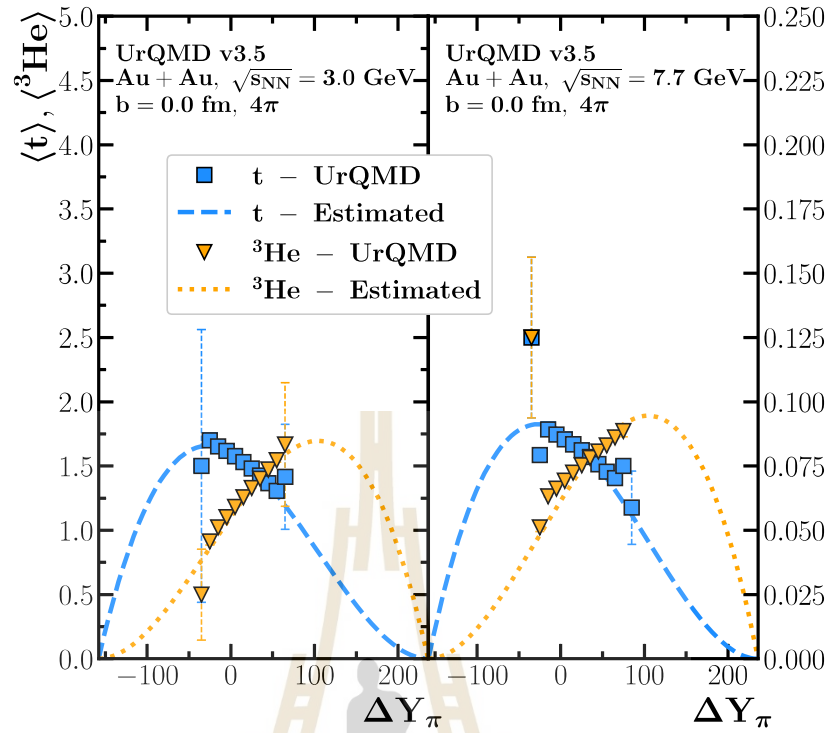


Figure 7.4 The ΔY_π dependent of triton (blue squares and dashed blue line) and ${}^3\text{He}$ (orange triangles and dotted orange line) yields. The UrQMD results are shown by symbols. The estimated yields, Eqs. (7.7) and (7.8), are represented by the lines. Left: Results at $\sqrt{s_{\text{NN}}} = 3$ GeV. Right: Results at $\sqrt{s_{\text{NN}}} = 7.7$ GeV

in Fig. 7.4, depicting the simulated triton (blue crosses) and ${}^3\text{He}$ (orange triangles) yields from UrQMD at $\sqrt{s_{\text{NN}}} = 3$ GeV (left panel) and $\sqrt{s_{\text{NN}}} = 7.7$ GeV (right panel) with the corresponding estimated yields from the toy model represented by the blue dashed and orange dotted line, respectively. We observe that both the UrQMD simulated tritons and ${}^3\text{He}$ at both energies follow the estimated yields. Especially at $\sqrt{s_{\text{NN}}} = 3.0$ GeV, where the tritons exhibit the maximum yield at $\Delta Y_\pi = -26.67$, we observe a close resemblance between UrQMD and estimated values.

Finally, we provide the energy dependence of the cluster yields as a function of ΔY_π from $E_{\text{lab}} = 1.23A - 40A$ GeV. the cluster yields are normalized by their respective yields at $\Delta Y_\pi = 39$. We can clearly observe that the local maxima of the deuteron yields and the $A = 3$ clusters are present and independent of the beam energy.

Also, some deviation from the UrQMD simulation to the toy model is observed as the distributions of light nuclei become broader along with the energies. This

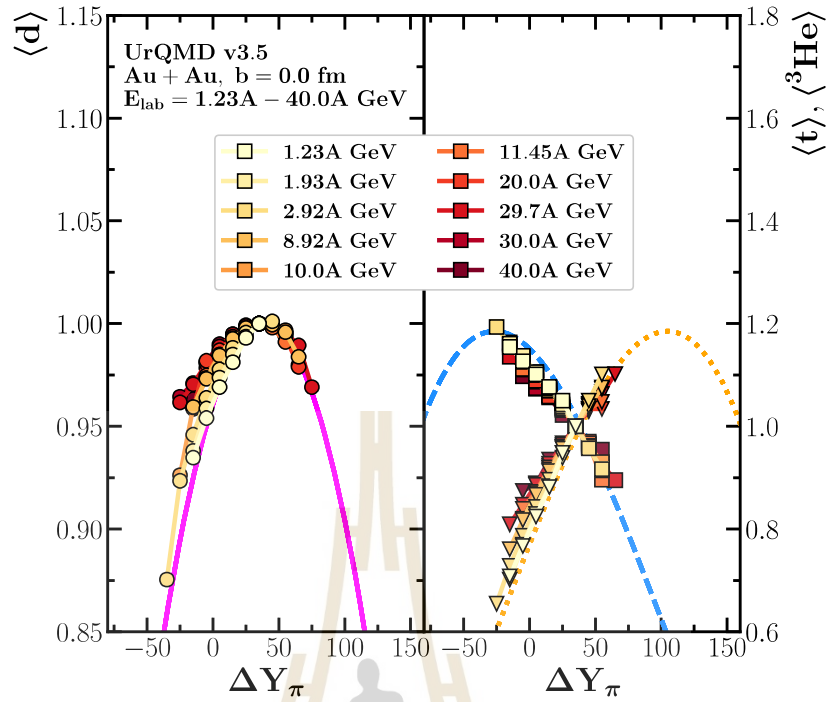


Figure 7.5 Distribution of cluster yields on the ΔY_π spectrum is normalized to unity at $\Delta Y_\pi = 39$. The symbols represent simulation results from various collision energies ranging from $E_{\text{lab}} = 1.23A$ GeV to $E_{\text{lab}} = 40A$ GeV in ultra-central Au+Au reactions from UrQMD. Left: Deuteron distribution. Right: Triton and ${}^3\text{He}$ distribution.

deviation can be attributed to the fact that in the toy model, isospin equilibration is assumed only between pions and nucleons. In a realistic scenario, some isospin is also carried by other hadron species such as charged kaons, Σ , etc.

We conclude our chapter with the observation that the coalescence model exhibits an energy-independent local maxima in cluster yields, e.g., the deuteron yields at $\Delta Y_\pi = 39$ (for Au+Au reactions). This distinct dependence on the isospin triggering allows us to potentially resolve tensions between the thermal model and the coalescence model. Since the thermal model usually uses grand canonical ensembles, it does not show any dependence of the cluster yield on ΔY_π . This is because the isospin fluctuations occur before kinetic freeze-out inducing the correlation between cluster yields and the emitted charged pions (and nucleons). In the thermal model, all hadron yields are generated or emitted simultaneously at the chemical freeze-out. Consequently, the cluster yields from the thermal model do not correlate with any isospin fluctuations, or at most, have been accounted for only on an averaged basis.

Our studies indicate that the cluster formation is governed by coalescence at the kinetic freeze-out rather than a direct emission from the chemical freeze-out by thermal productions. This approach can be measured in any ultra-central Au+Au collision facilities at $\sqrt{s_{NN}} = 3 - 8$ GeV.



CHAPTER VIII

RESULTS IN PION INDUCED REACTIONS

The previous chapters present extensive studies on the space-time geometry of the source volume and the cluster formations across the broad range of collision energies and EoS in heavy-ion collisions. We proposed the usage of space-time consideration, particularly the isospin exchange at chemical freeze-out as a tool to distinguish between thermal and coalescence models. However, we can extend our investigation beyond heavy-ion collisions at low energies as there is also a pressing need for investigations of smaller systems. Since the yield of hypertriton, for instance, demonstrates a system size dependence (Acharya et al., 2022), leading to another tension between the thermal and coalescence models. Furthermore, the hypertriton's potential use as a constraint for the coalescence parameter, hypernuclei structure, and neutron star EoS underscore the significance of probing smaller systems. In this chapter, we aim to provide supports for the realization of the coalescence mechanism as well as the theoretical predictions and insights for future experiments at smaller systems, particularly pion-induced reactions.

8.1 The needs and potential of small collision systems

The interest in the low energy regime is circulating around the cluster formations (Vovchenko et al., 2020), including the quest for dark matter (Hou et al., 2017; Korsmeier et al., 2018; Doetinchem et al., 2020; Hornung, 2021; Šerkšnytė et al., 2022), the extraction of the Equation of State (EoS) for neutron stars (Capano et al., 2020; Tolos and Fabbietti, 2020; Vidaña, 2018), and the essential interplay between theoretical predictions and experimental measurements. One of the main ingredients for the EoS of neutron stars is the understanding of Λ N-interactions, and even Λ NN-interactions, as hyperons and hypernuclei are expected to be presented at the core of neutron stars (Nagels et al., 1977; Nagels et al., 1979; Shinmura et al., 1984; Fujiwara et al., 1996a; Fujiwara et al., 1996b; Nemura et al., 2000; Hildenbrand and Hammer, 2019).

Exploring these interactions can be achieved through diverse methods, including the study of correlation functions and the direct examination of bound state

formation, such as the hypertriton ${}^3_{\Lambda}\text{H}$ made of a deuteron core with a weakly bound Λ (Juric et al., 1973; Abelev et al., 2010; Adam et al., 2016; Dönigus, 2013; Andronic et al., 2018). This state possesses a very small Λ separation energy, typically in the range of a few hundred keV (Davis, 2005; Adam et al., 2020), resulting in a wide wavefunction extending up to approximately 10 fm in radius (Braun-Munzinger and Dönigus, 2019). Notably, the size of the ${}^3_{\Lambda}\text{H}$ wavefunction may be associated with the constraint of the coalescence parameter and the underlying ΛN interaction for the neutron star EoS (Nagels et al., 1977; Nagels et al., 1979; Shinmura et al., 1984; Fujiwara et al., 1996a; Fujiwara et al., 1996b; Nemura et al., 2000; Hildenbrand and Hammer, 2019).

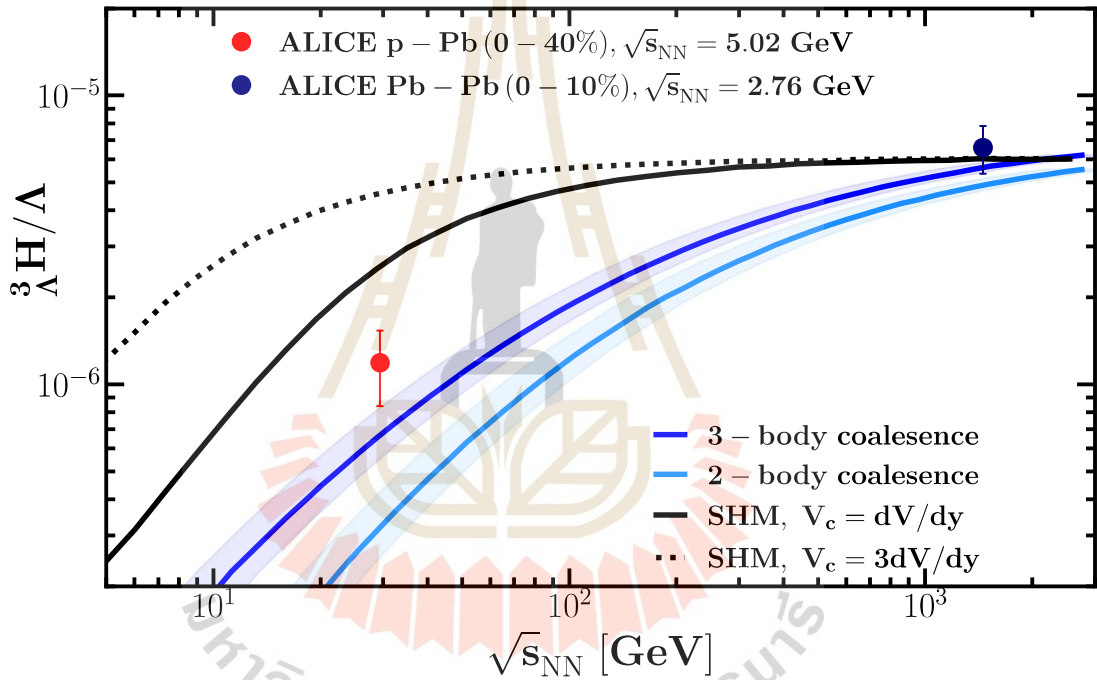


Figure 8.1 ALICE measurements in $p + \text{Pb}$ (in red) and $\text{Pb} + \text{Pb}$ collisions (Adam et al., 2016) (in blue) as a function of mean charged-particle multiplicity and the predictions from canonical statistical hadronization (excluded volume) (Vovchenko et al., 2018a) and coalescence models are shown (Sun et al., 2019). The figure is adopted from Ref. (Acharya et al., 2022)

The recently published data by the ALICE experiment (Acharya et al., 2022), Fig. 8.1, of the system size dependence of ${}^3_{\Lambda}\text{H}$ production for small collision systems in $p+p$ and $p+\text{Pb}$ shows that the predictions from the coalescence mechanism suppress the ${}^3_{\Lambda}\text{H}/\Lambda$ yield compared to the results from the thermal model. The result is compared with the prediction from the canonical SHM (Vovchenko et al., 2018a), which

assumes exact conservation of baryon number, strangeness, and electric charge across a correlation volume V_c . The SHM predictions are computed using a fixed chemical freeze-out temperature of $T_{\text{chem}} = 155$ MeV and two correlation volumes extending across one unit ($V_c = dV/dy$), and three units ($V_c = 3dV/dy$) of rapidity (Vovchenko et al., 2018a). The size of the correlation volume governs the influence of exact quantum number conservation, with smaller values leading to a stronger suppression of conserved charges and $V_c \rightarrow \infty$ leading to the grand canonical ensemble. The results seem to favor the 2-body coalescence model (d-core and weakly bound Λ). However, toward smaller systems, due to the limited available data, we cannot pin-point whether the hypertriton yield ratio will tend toward the thermal model prediction or the 2-body or 3-body coalescence model, thus changing the interpretation of its size and wavefunction. This again emphasizes the importance on the understanding of the cluster mechanisms and low energy studies.

Nevertheless, the new availability of secondary pion beams at the HADES experiment (Agakishiev et al., 2009) in Darmstadt, Germany, may provide a unique opportunity to study hadron and dilepton production in $\pi + A$ interactions with a momentum of 1.7 GeV on carbon (C) and tungsten (W) targets allowing to investigate normal clusters and hypernuclei production in small systems and at low energies.

Particle production of, e.g., Λ in $p + A$ reactions results in a large forward momentum of the created particle, therefore reducing the chance for hypernuclei production (within the coalescence picture). Thus, hypernuclei will be produced outside of the nucleus. In contrast to that, pion reactions $\pi + A$ have several advantages for cluster studies. The pion induced reaction proceeds via the excitation of a baryonic resonance, $\pi^- + n \rightarrow \Delta^{*,-}$ or $\Delta^- + p \rightarrow \Delta^{*,0}$ or N^* , with a typical mass up to 2 GeV. The baryon resonance (moving forward with respect to the target system) then decays after approx. 1-2 fm/c mostly into $\pi + N$ (leading to the production of protons and neutrons in the forward direction) and may also lead to the production of Λ and even Ξ via the decays $\Lambda + K$ and $\Xi \rightarrow KK$, respectively (Steinheimer et al., 2017). However, the pion projectile has a larger stopping power compared to the proton beam, the production of nucleons/hyperons must be richer around the target region than the forward rapidity. Thus, one can expect the enhancement of the hypernuclei formation within the target and this allow for larger hypernuclei $A \gg 3$ as Λ or Ξ inside the nucleus may slow down allowing for binding or multifragmentation into a hypernucleus. The deceleration of the hyperon will of course depend on the size of the target nucleus

and is more pronounced in the bigger tungsten than in the carbon target. Thus, the pion beam measurements at HADES provide a promising environment to explore the properties of the (${}^3_{\Lambda}\text{H}$) in small systems.

To demonstrate our arguments above and discuss the potential use of the pion beam experiment at HADES (Adamczewski-Musch et al., 2017; Yassine et al., 2023), we perform the first baseline predictions for the production of non-strange and strange clusters in $\pi^- + \text{C}$ and $\pi^- + \text{C}$ collisions.

To this aim, we will employ the UrQMD v3.5 with box coalescence model which has been successfully describe the production of non-strange light nuclei, i.e deuterons, tritons, helium, and strange hypertriton and further strange clusters which have not yet been measured (Gaebel et al., 2021; Hillmann et al., 2022; Reichert et al., 2023c; Reichert et al., 2023d) and then compare the results with the statistical multifragmentation approach which allows to produce (hyper)nuclei with large mass numbers relative to the system size (Botvina et al., 2021; Buyukcizmeci et al., 2020; Botvina et al., 2022; Buyukcizmeci et al., 2023).

8.2 Model Setup

For this study, we use the transport model UrQMD v3.5. For this analysis, the simulations are conducted in cascade mode, with potentials turned off. As a QMD-type simulation, UrQMD tracks all n-particle correlations during system evolution, preserving the collision history with detailed space-time and 4-momentum information for all particles. This data is then input into a numerical coalescence model and the Statistical Multifragmentation Model (SMM) (Bondorf et al., 1995) to compute cluster production.

All the following results are obtained by simulating 146 million and 41 million events of minimum bias $\pi^- + \text{C}$ and $\pi^- + \text{C}$ collisions, respectively. We define minimum bias collisions for $\pi^- + \text{C}$ with an impact parameter range of $0 < b < 2.5$ fm, excluding events without any interaction, and use a total cross section of $\sigma_{\text{tot}}^{\pi^- + \text{C}} = 196.35$ mb for normalization. For $\pi^- + \text{C}$, we use an impact parameter range of $0 < b < 6.5$ fm, also excluding non-interacting events, with a total cross section of $\sigma_{\text{tot}}^{\pi^- + \text{C}} = 1327.32$ mb.

All calculations are done in the target rest frame (laboratory frame in the HADES experiment) and the rapidity y refers to this frame, i.e. $y_{\text{target}} = 0$. To compare with the experimental data, free Λ hyperons always include the Σ^0 hyperons, as the Σ^0 decays into a Λ and can not be distinguished by the experiment. However, the coales-

cence and multifragmentation routines consider only initial Λ hyperons, since Σ^0 hyperons decay further away due to their comparatively long lifetime and do not significantly contribute to the hypertriton production. Protons in the simulation do not include feed down from the Λ decays. The units used for $d^2\sigma/dp_T dy$ are $[\mu\text{b}/(\text{GeV}\Delta y)]$, and for $d\sigma/dy$ are $[\mu\text{b}/\Delta y]$ chosen in line with the HADES measurements (Yassine et al., 2023).

The coalescence results are evaluated at the kinetic freeze-out, while the SMM uses input from UrQMD at a fixed time in this analysis. Furthermore, all particles, as well as spectators in UrQMD, are included in the statistical multifragmentation approach. The coalescence parameter in the SMM model has been set to $v_c = 0.22$ as this value has been shown to provide good results (Botvina et al., 2015; Buyukcizmeci et al., 2020; Botvina et al., 2021).

8.3 Proton and Λ Baryon Production

We begin our exploration by investigating the double differential transverse momentum spectra of cluster constituents, i.e., protons and Λ hyperons.

In Fig. 8.2 (upper panel), we illustrate the double differential cross section $d^2\sigma/dp_T dy$ in $[\mu\text{b}/(\text{GeV}\Delta y)]$ for protons against transverse momentum across various rapidity bins (ranging from $0 \leq y < 0.1$ to $0.9 \leq y < 1.0$). For clarity, the curves are progressively scaled by factors of 10 from bottom to top. The left panel shows results for minimum bias $\pi^- + \text{C}$ collisions, while the right panel shows results for minimum bias $\pi^- + \text{C}$ collisions, from UrQMD (v3.5) simulations. Solid lines with symbols depict the simulated data, while open symbols represent recent HADES measurements (Yassine et al., 2023). Additionally, a dotted line denotes the exponential fit, parameterized by the yield integral and slope parameter as $\sim C(y) p_T \sqrt{p_T^2 + m_0^2} \exp\left[-\frac{\sqrt{p_T^2 + m_0^2}}{T(y)}\right]$, consistent with the HADES analysis (Yassine et al., 2023). The fitting to the simulation data is done within the same p_T acceptance as the HADES setup, i.e., $p_T \geq 0.4$ [GeV] and is displayed only for the rapidity bin $0 \leq y < 0.1$. Fig. 8.2 (lower panel) illustrates the relative deviation between the UrQMD simulations and the experimental data.

The simulation results demonstrate both quantitative and qualitative agreement between UrQMD model calculations of the differential cross section for protons and experimental data (open symbols) (Yassine et al., 2023) for both collision systems and across all forward rapidity bins, as well as a good match of the slope parameters between our simulations and the measured data. Notably, as anticipated, we observe

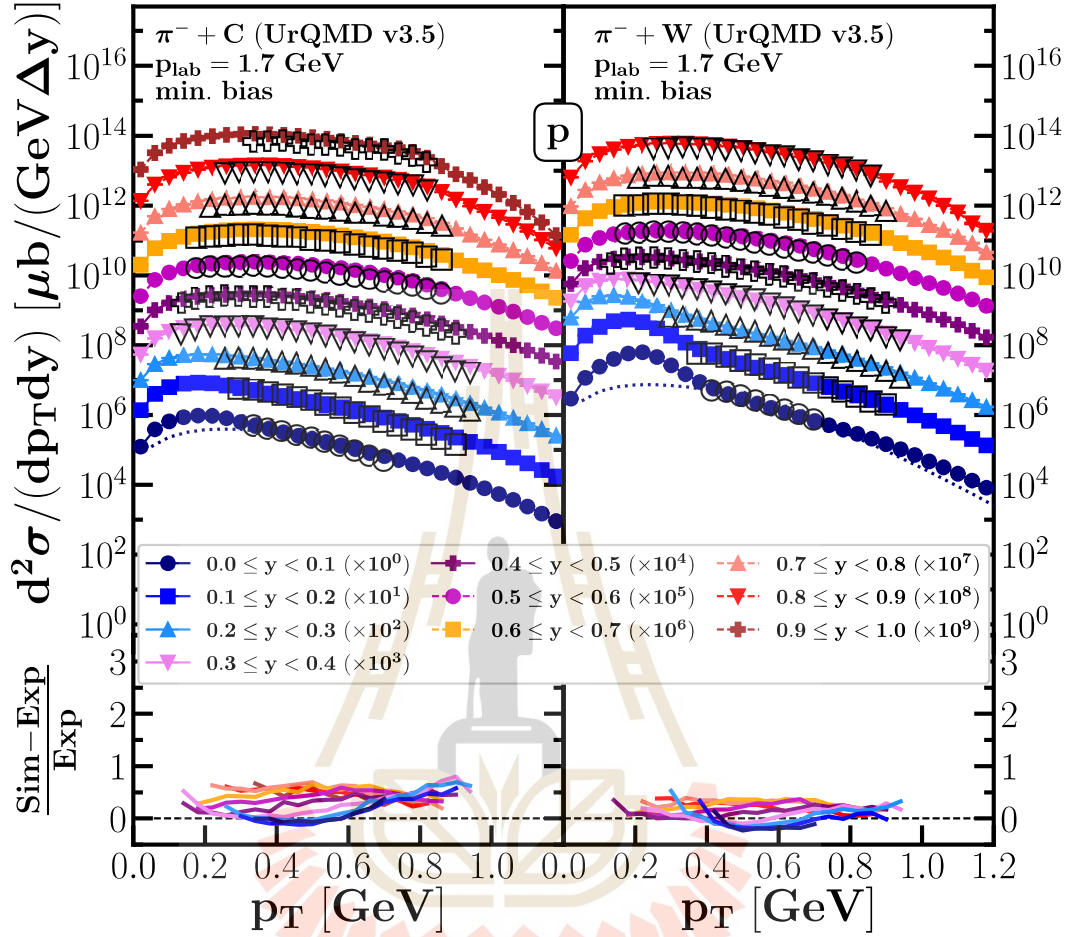


Figure 8.2 The transverse momentum (p_T) spectra of protons produced in minimum bias $\pi^- + C$ (left panel) and $\pi^- + W$ (right panel) collisions at various rapidity bins ($0 \leq y < 0.1$ to $0.9 \leq y < 1.0$) as measured by the UrQMD model (v3.5). The p_T spectra are represented by differential cross sections ($d^2\sigma/dp_T dy$) in units of $[\mu\text{b}/(\text{GeV}\Delta y)]$. The curves for each rapidity bin are consecutively multiplied by a factor of 10 from bottom to top for better visualization. Solid lines with symbols depict the UrQMD simulation results, while open symbols represent recent HADES experimental measurements (Yassine et al., 2023). The lower panel shows the relative deviation (percentage difference) between the UrQMD simulations and the corresponding experimental data for each rapidity bin.

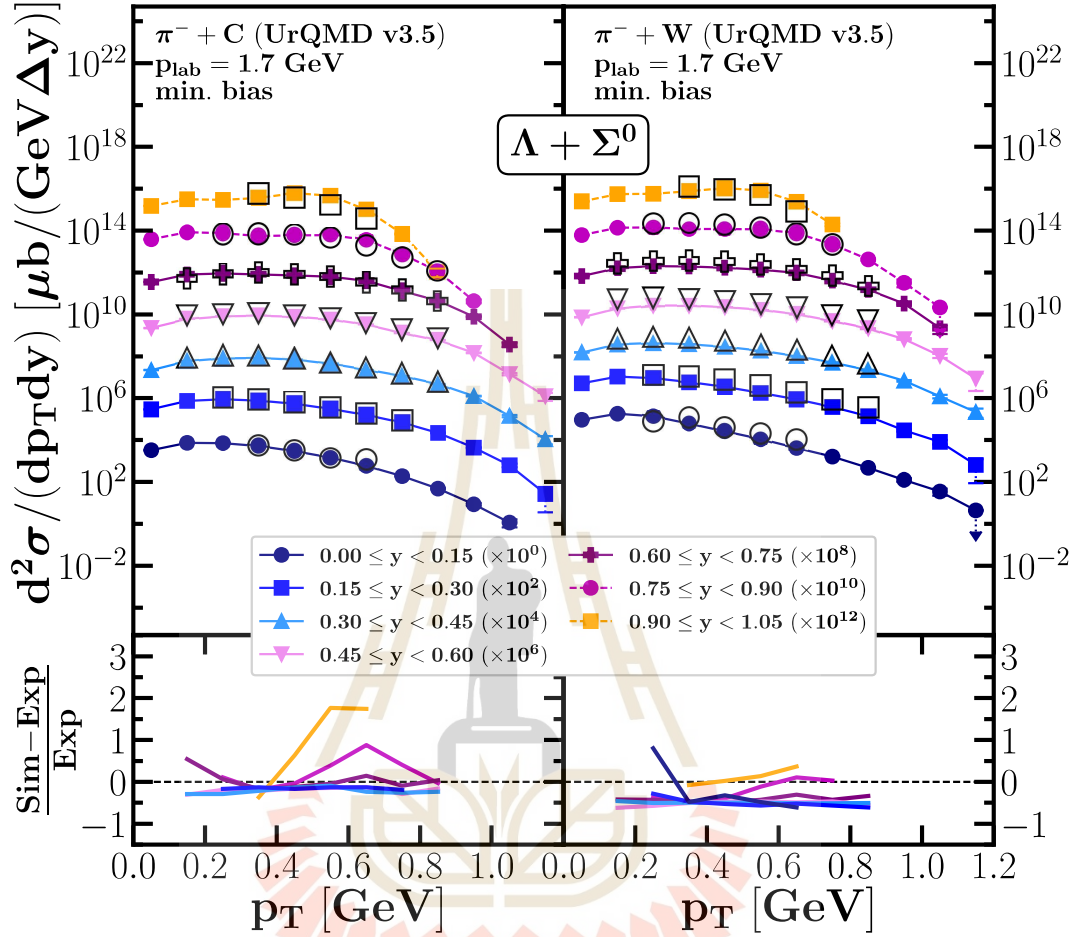


Figure 8.3 The upper panel displays the transverse momentum (p_T) spectra of Λ hyperons produced in minimum bias $\pi^- + C$ (left) and $\pi^- + W$ (right) collisions at various rapidity bins ($0 \leq y < 0.15$ to $0.9 \leq y < 1.05$) as calculated by the UrQMD model (v3.5). The p_T spectra are represented by differential cross sections ($d^2\sigma/dp_T dy$) in units of $[\mu b / (\text{GeV} \Delta y)]$. The curves for each rapidity bin are consecutively multiplied by a factor of 100 for improved visualization (bottom to top). Solid lines with symbols depict the UrQMD simulations, while open symbols represent recent HADES experimental measurements (Yassine et al., 2023). The lower panel presents the relative deviation (percentage difference) between the UrQMD simulations and the corresponding experimental data for each rapidity bin

a greater proton abundance at small transverse momenta p_T in the UrQMD simulation compared to the interpolation predicted via the exponential fit function, especially at low rapidity. This arises due to limitations in the phase space coverage of the HADES detector, preventing direct observation of these residue-free protons at transverse momenta $p_T < 0.4$ GeV around zero rapidity. This effect is evident for both systems and becomes more pronounced with increasing system size. In the subsequent section, we will demonstrate how typical extrapolation results in slight deviations in rapidity densities near $y \approx 0$.

Figure 8.2 (lower panels) presents the relative differences in p_T spectra between the UrQMD (v3.5) simulation and the HADES experimental data (Yassine et al., 2023) for protons. These differences remain below 1 across the p_T range and all rapidity bins. In the carbon system, the deviations become stronger with increasing momentum and further rapidity bin. Conversely, in the tungsten system, the deviations indicate less dependence on both p_T and rapidity.

Fig. 8.3 (upper panel) shows the transverse momentum double differential cross section $d^2\sigma/dp_T dy$ of Λ 's as a function of transverse momentum in different rapidity bins (from $0 \leq y < 0.15$ to $0.9 \leq y < 1.05$). The curves are scaled by factors of 100 from bottom to top for clarity. The results from minimum bias $\pi^- + C$ and $\pi^- + C$ collisions from UrQMD (v3.5) are presented in the left and right panels, respectively. The solid lines with symbols show the calculations and the open symbols represent the HADES measurements (Yassine et al., 2023). The relative deviation between the UrQMD simulations and experimental data is shown in the lower panel.

Similarly, the UrQMD simulations agree well with the data across the transverse momentum range in all rapidity bins. They reproduce the sharp drop-off behavior at high p_T values, a result of the limited available collision energy.

We are now able to discuss the slight deviation from using the extrapolated rapidity distribution from the exponential fit. In Fig. 8.4, we present the comparison of rapidity differential cross section spectra $d\sigma/dy$ in $[\mu b/\Delta y]$ of simulated protons and extrapolated protons as well as the rapidity distribution of Λ 's. The left panel displays the results from minimum bias $\pi^- + C$ collisions, while the right panel displays those from minimum bias $\pi^- + C$ collisions.

Unlike experimental approaches that rely on extrapolations from integrated transverse momentum spectra, UrQMD simulations can directly calculate particle rapidity distributions. Our results demonstrate that the extrapolated free protons obtained

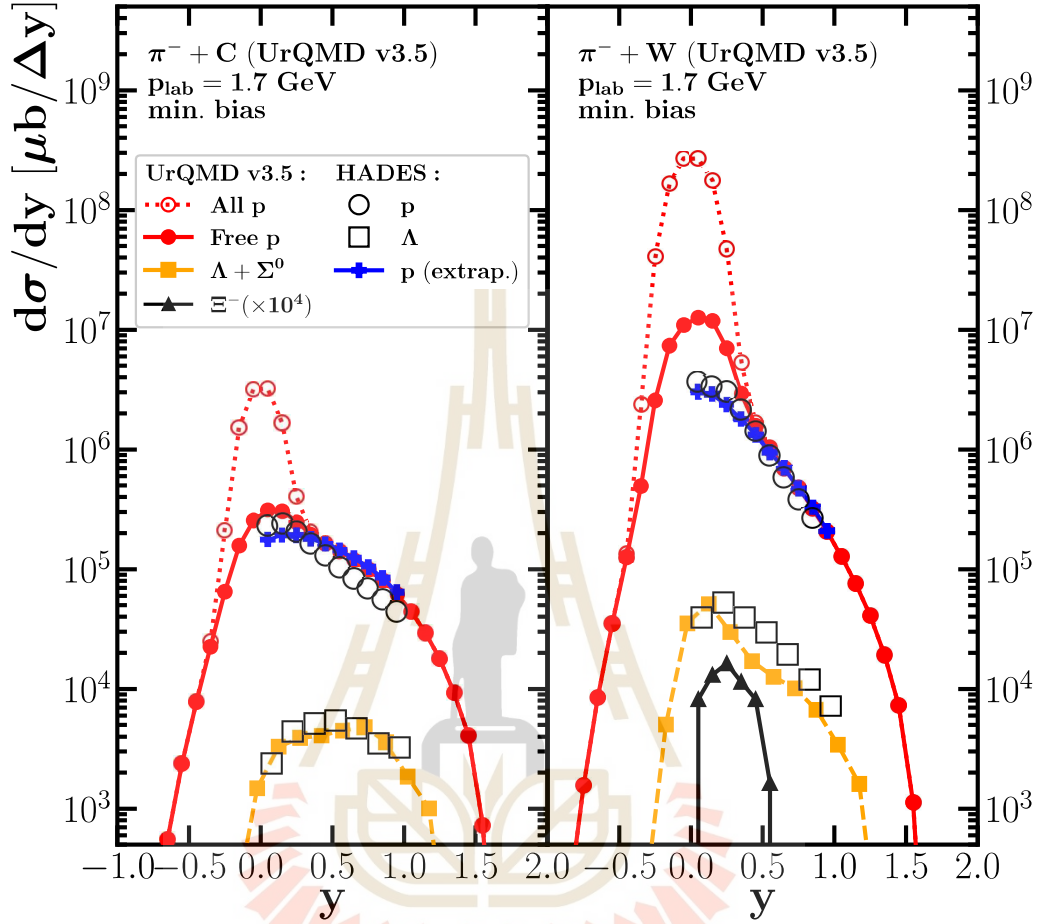


Figure 8.4 The differential cross section with respect to the rapidity $d\sigma/dy [\mu\text{b}/\Delta y]$ of protons (red), Λ 's (orange), and Ξ 's (black) from minimum bias $\pi^- + \text{C}$ (left panel) and $\pi^- + \text{W}$ (right panel) collisions. The UrQMD results are shown as colored lines with symbols, while the open black symbols depict the recent HADES measurements (Yassine et al., 2023). The blue line with crosses shows the experimental fit function for the p_T extrapolation.

from the exponential fit (solid blue line with crosses) generally agree with the HADES data (open circles) across the measurable rapidity range. However, as mentioned earlier, there are notable limitations to this approach.

Specifically, the current exponential fit function could not account for residue free protons residing near zero rapidity (target region). These protons are unde-

tectable by the HADES experiment due to its limited coverage at nearly zero rapidity ($p_T < 0.4$ GeV/c). The UrQMD simulations (solid red line with circles) clearly capture this effect, demonstrating a higher density of free protons around zero rapidity despite agreeing well with the exponential fit from both experimental data and simulations in the forward rapidity region. This limitation of the exponential fit extends to all protons, not just the free ones. In the target region, there are not only residue free protons but also bound protons within clusters, as depicted by the red dashed line with open circles. Additionally, the larger target nucleus, with stronger stopping power, further amplifies the presence of all protons (bounded and free protons) at zero rapidity.

The UrQMD model demonstrates its capability by successfully reproducing the measured Λ rapidity distributions (orange line with squares) in both $\pi^- + C$ and $\pi^- + C$ collision systems. This achievement indicates that the model can describe the multiplicity and general trend of Λ hyperons.

Furthermore, we also present the production of Ξ hyperons (black line with triangles), particularly in the $\pi^- + C$ system. This finding, combined with the successful description of proton and Λ production, suggests that these low-energy, small-system collisions hold promise for studying clusters and the possibility of exploring the formation of multi-strange hyperclusters, without the need for an anti-proton beam.

8.4 (Light) Nuclei distributions

Building upon the successful validation of the UrQMD model in describing the production of protons, Λ 's, and even Ξ 's (constituents of most (hyper)nuclei), we are now well-positioned to delve into the investigation of cluster and hypernuclei formation within these collision systems.

Figure 8.5 shows the transverse momentum (p_T) spectra of deuterons produced in minimum bias $\pi^- + C$ (left panel) and $\pi^- + C$ (right panel) collisions at various rapidity bins ($0 \leq y < 0.1$ to $0.8 \leq y < 0.9$) as simulated by the UrQMD model. The p_T spectra are represented by differential cross sections ($d^2\sigma/dp_T dy$) in units of $[\mu\text{b}/(\text{GeV}\Delta y)]$. The curves for each rapidity bin are consecutively multiplied by factors of 100 (bottom to top) for improved visualization. Similar plots for tritons (Figure 8.6) and ${}^3\text{He}$ (Figure 8.7) show the production of these light clusters across different rapidity bins ($0 \leq y < 0.1$ to $0.5 \leq y < 0.6$) in both collision systems.

The observed p_T spectra for deuterons, tritons, and ${}^3\text{He}$ show a substantial amount of light cluster production, particularly in the target rapidity region ($y \simeq 0$ with

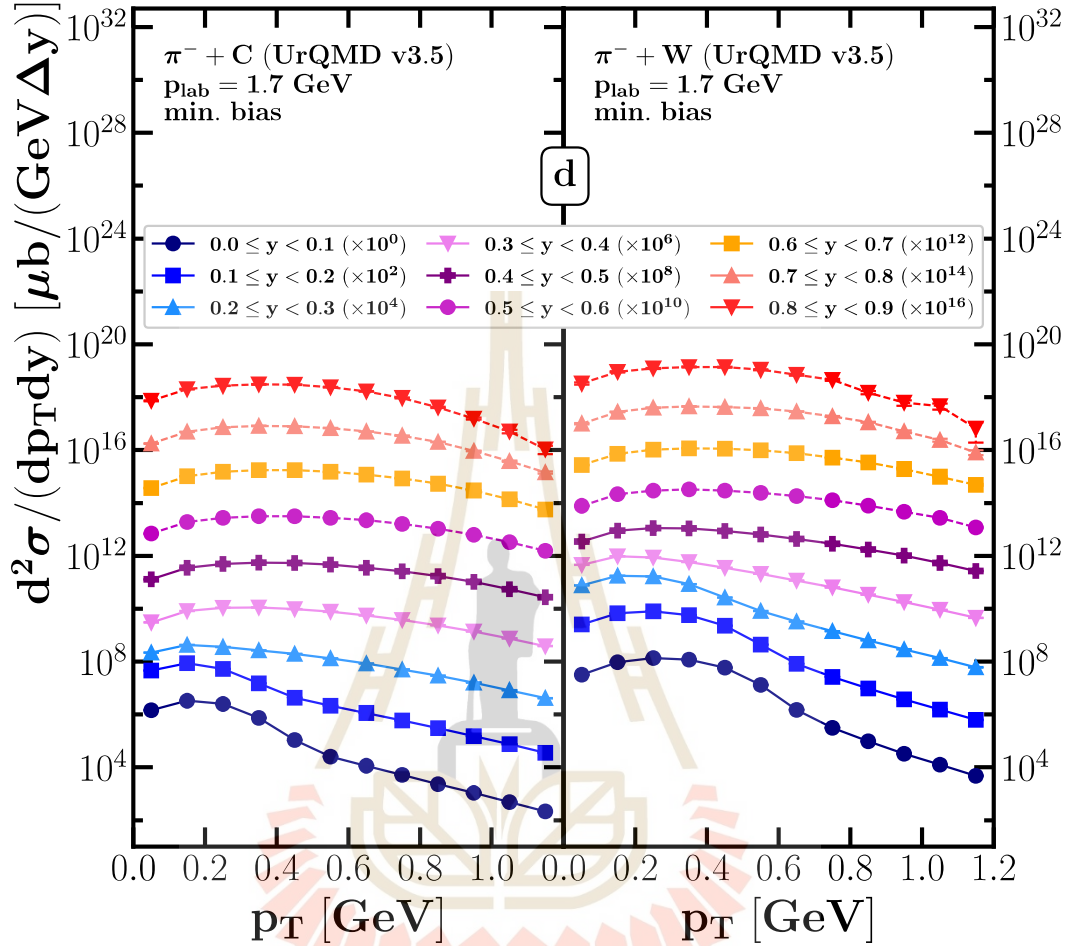


Figure 8.5 The transverse momentum differential cross section $d^2\sigma/dp_T dy$ in $[\mu\text{b}/(\text{GeV}\Delta y)]$ of deuterons as a function of transverse momentum in different rapidity bins (from $0 \leq y < 0.1$ to $0.8 \leq y < 0.9$, the curves are successively multiplied by factors of 100 from bottom to top) for minimum bias $\pi^- + \text{C}$ (left panel) and $\pi^- + \text{W}$ (right panel) collisions from UrQMD.

low p_T) similar to the transverse momentum of protons. This effect is present in all light nuclei p_T spectra due to the mentioned effect of protons sitting inside the target. This finding suggests that the UrQMD model can effectively describe the formation of these clusters in $\pi^- + \text{C}$ and $\pi^- + \text{C}$ collisions.

Figure 8.8 presents the rapidity dependence of cluster yields. It shows the rapidity differential cross sections ($d\sigma/dy$) in $[\mu\text{b}/\Delta y]$ for deuterons (orange), tritons

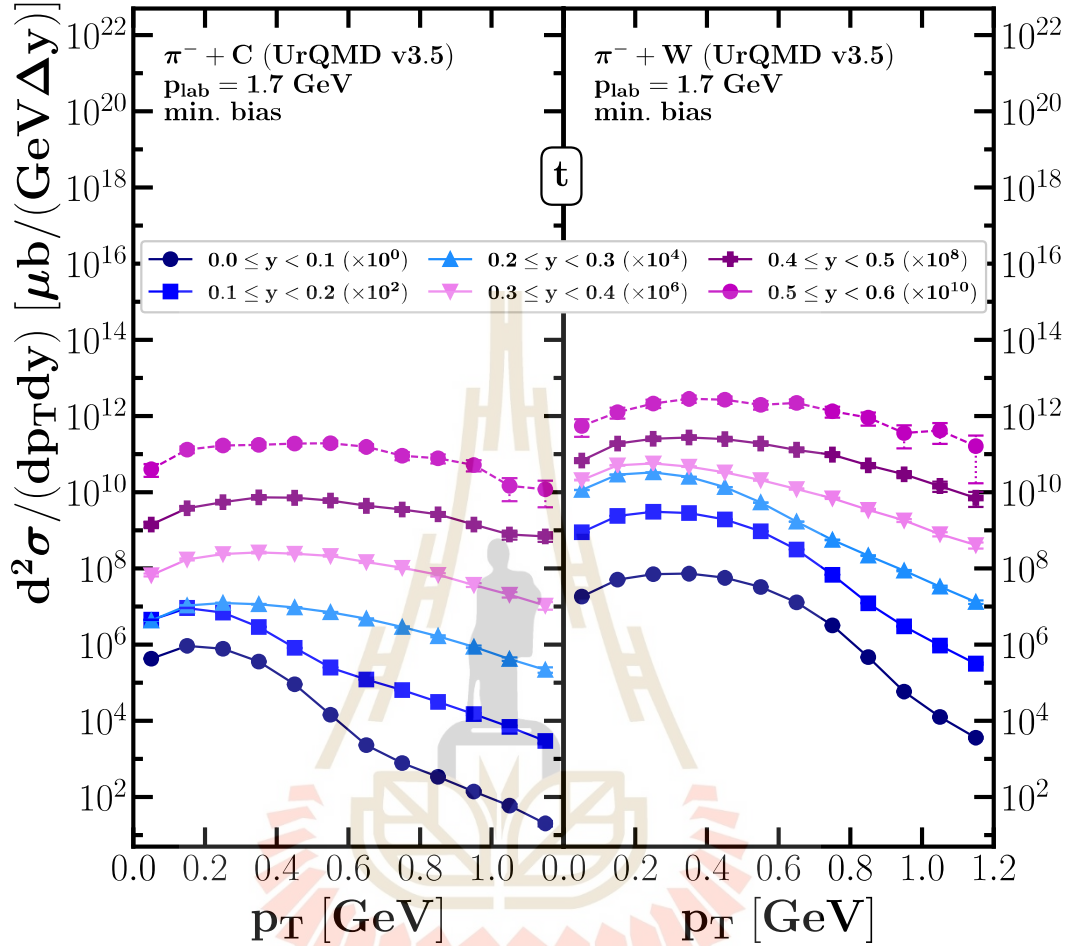


Figure 8.6 The transverse momentum differential cross section $d^2\sigma/dp_T dy$ in $[\mu\text{b}/(\text{GeV}\Delta y)]$ of tritons as a function of transverse momentum in different rapidity bins (from $0 \leq y < 0.1$ to $0.5 \leq y < 0.6$, the curves are successively multiplied by factors of 100 from bottom to top) for minimum bias $\pi^- + \text{C}$ (left panel) and $\pi^- + \text{C}$ (right panel) collisions from UrQMD.

(green), ^3He (blue), and ^4He (red) as a function of rapidity for both $\pi^- + \text{C}$ and $\pi^- + \text{C}$ collision systems. The UrQMD coalescence model results are depicted by dashed lines with open symbols, while the yields from the Statistical Multifragmentation Model (SMM) are represented by solid lines without symbols.

The overall light cluster multiplicities from both models show good agree-

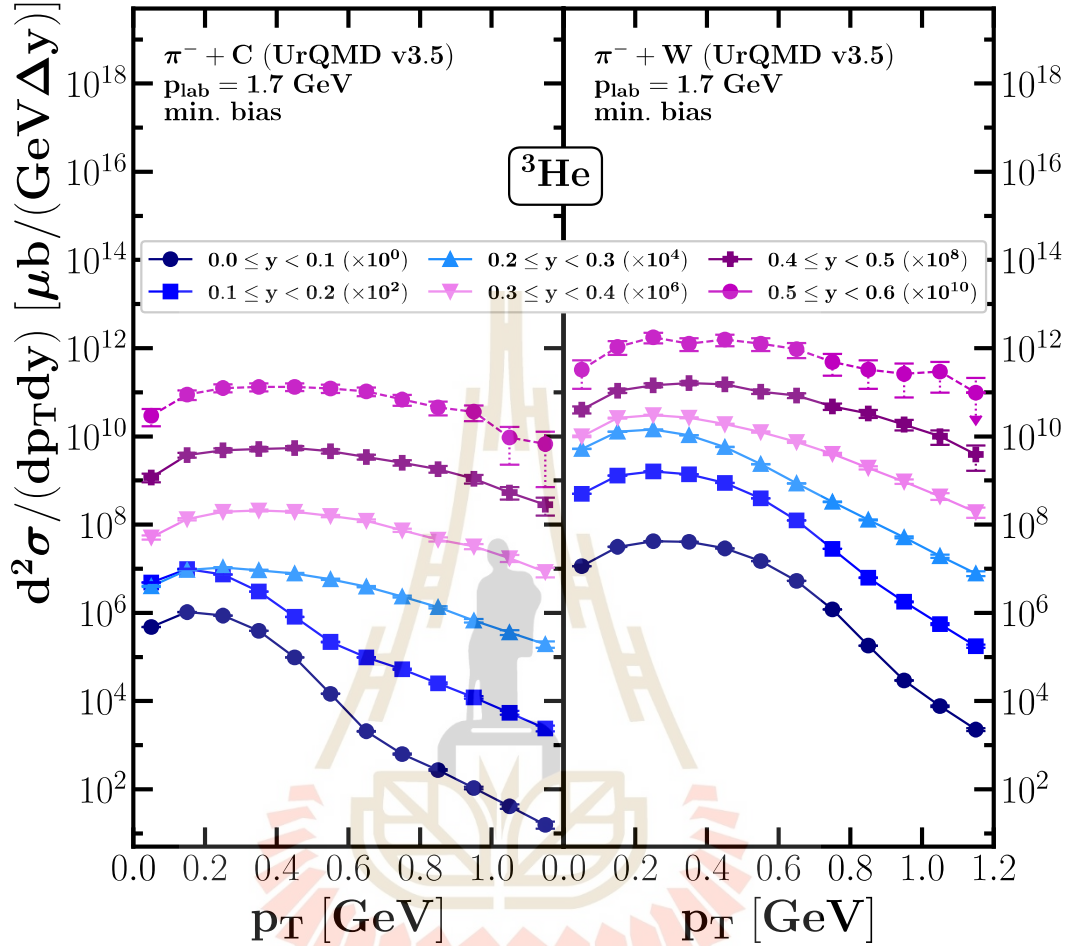


Figure 8.7 The transverse momentum differential cross section $d^2\sigma/dp_T dy$ in $[\mu\text{b}/(\text{GeV}\Delta y)]$ of ${}^3\text{He}$ as a function of transverse momentum in different rapidity bins (from $0 \leq y < 0.1$ to $0.5 \leq y < 0.6$, the curves are successively multiplied by factors of 100 from bottom to top) for minimum bias $\pi^- + \text{C}$ (left panel) and $\pi^- + \text{C}$ (right panel) collisions from UrQMD.

ment, with a factor of two difference between ${}^4\text{He}$ multiplicities. As expected, the cluster yields (shown in Figure 8.8) peak around zero rapidity, indicating that most clusters form in the target region where protons (nucleons) are abundant. Interestingly, both systems exhibit a protrusion in the deuteron distributions towards forward rapidity, particularly pronounced in the smaller carbon system. This suggests that the

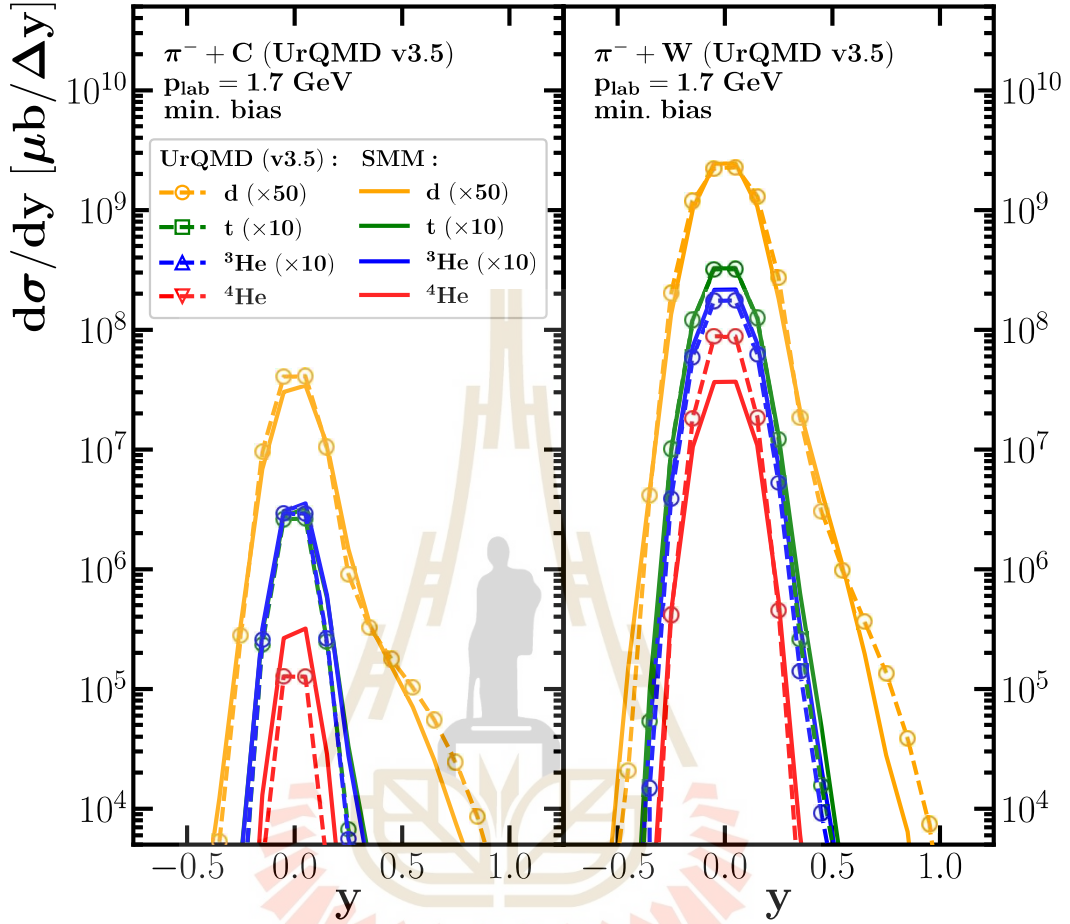


Figure 8.8 The rapidity differential cross section $d\sigma/dy$ in $[\mu\text{b}/\Delta y]$ of deuterons (orange), tritons (green), ^3He (blue) and ^4He (red) as a function of the rapidity for minimum bias $\pi^- + \text{C}$ (left panel) and $\pi^- + \text{W}$ (right panel) collisions from UrQMD (v3.5) as denoted by dashed lines with symbols and from statistical multifragmentation model (SMM) as denoted by solid lines without symbols.

incident pions could occasionally eject only a few nucleons out of the target.

The tungsten target ($\pi^- + \text{C}$) shows a more symmetrical deuteron distribution compared to the carbon target ($\pi^- + \text{C}$). This can be explained by the concept of stopping power. The larger size and higher stopping power of the tungsten nucleus lead to more frequent coalescence and/or multifragmentation around the target region. This, in turn, enhances and broadens the rapidity distributions for all clusters in the $\pi^- + \text{C}$

system compared to $\pi^- + C$ washing out the protrusion effect in deuteron distribution.

8.5 (Hyper) Nuclei distribution

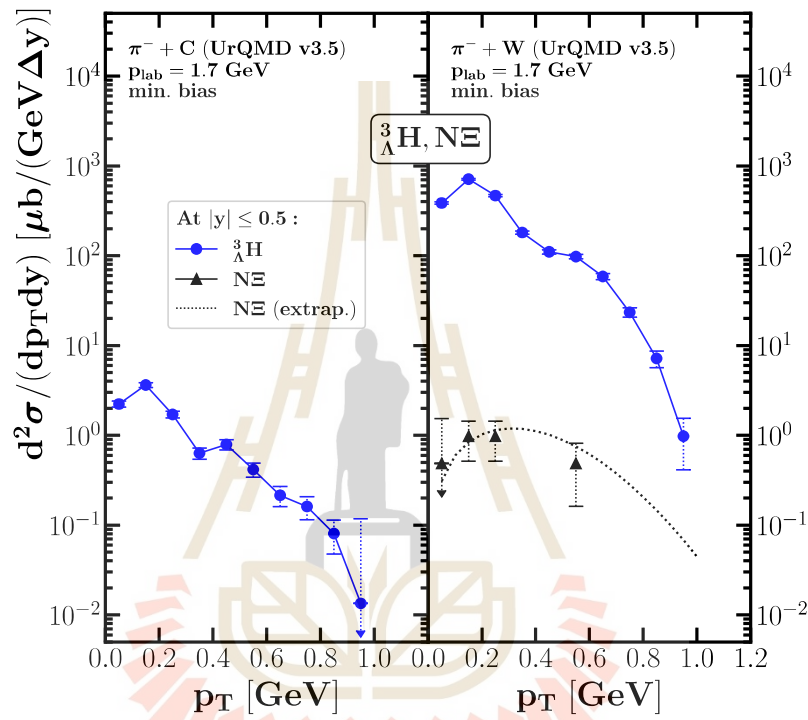


Figure 8.9 The differential cross section with respect to transverse momentum $d^2\sigma/dp_T dy$ [$\mu\text{b}/(\text{GeV}\Delta y)$] of ${}^3\text{He}$ (blue line with squares) and $N\Xi$ (black triangles) from UrQMD results at mid-rapidity minimum bias $\pi^- + C$ (left panel) and $\pi^- + W$ (right panel) collisions. The dashed line indicates the extrapolated fit of $N\Xi$.

Finally, we come to the most intriguing aspect of this study discussing about the potential production of hypernuclei. Here, we focus on the hypertriton (${}^3_{\Lambda}\text{H}$) and $N\Xi$ hypernuclei.

Figure 8.9 presents the predicted transverse momentum spectra of the hypertriton ${}^3_{\Lambda}\text{H}$ (blue line with circles) and anticipated $N\Xi$ clusters from UrQMD model simulations and its corresponding extrapolated fit (black triangles and dotted line respectively). The spectra show the production rates as a function of the transverse momentum (p_T) for minimum bias $\pi^- + C$ and $\pi^- + C$ collisions at mid-rapidity

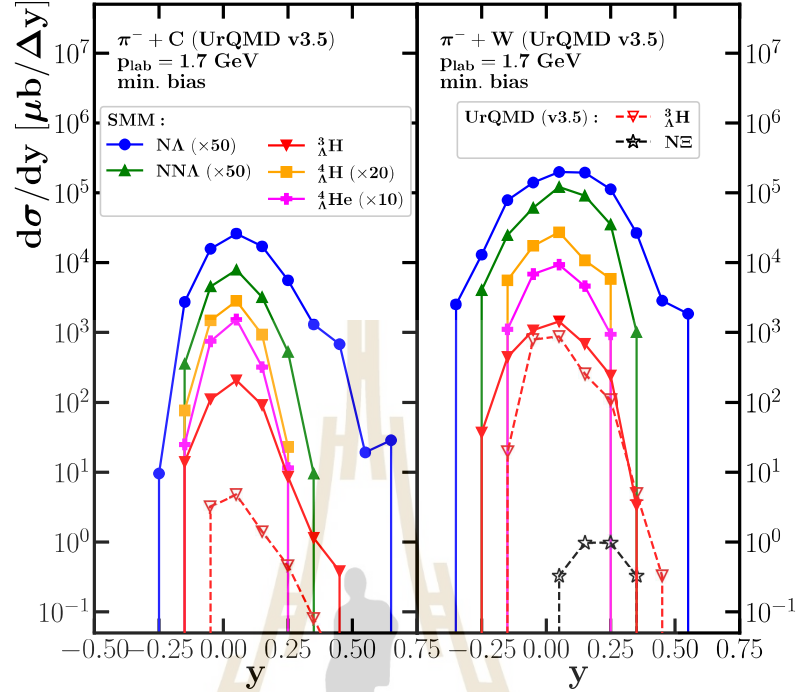


Figure 8.10 The differential cross section with respect to rapidity $d\sigma/dy [\mu\text{b}/\Delta y]$ of $N\Lambda$ (blue), NNA (green), ${}^3_{\Lambda}\text{H}$ (red), ${}^4_{\Lambda}\text{H}$ (orange), ${}^4_{\Lambda}\text{He}$ (pink), and $N\Xi$ (black) from minimum bias $\pi^- + \text{C}$ (left panel) and $\pi^- + \text{W}$ (right panel). The UrQMD results are denoted by dashed lines with open symbols, while the results from the statistical multifragmentation model (SMM) are denoted by solid lines with full symbols.

($|y| \leq 0.5$). The significant production of ${}^3_{\Lambda}\text{H}$ suggests a high probability of detection with momenta accessible by the HADES experiment. The production and measurement of $N\Xi$ clusters might also be achievable.

Figure 8.10 shows the predicted rapidity distributions of various hypernuclei from $A = 2 - 4$ in SMM (solid lines and filled symbols) models contrasting with UrQMD results (dashed lines and open symbols).

The ${}^3_{\Lambda}\text{H}$ production cross section peaks around the target rapidity region, indicating formation primarily within the target nucleus. The yield is higher and more symmetric in the $\pi^- + \text{C}$ system compared to $\pi^- + \text{W}$. This is attributed to the fact that the tungsten system produces more hyperons and has a higher stopping power, effectively increasing the probability of hypernuclei formation.

In addition, the protrusion effect is also observed in the hypernuclei yield with $A \leq 3$ from both models, i.e., $N\Lambda$ (blue line with circles), $NN\Lambda$ (green line with up triangles), and ${}^3_\Lambda\text{H}$ (SMM: red line with down triangles, UrQMD: red dashed line with down triangles). As discussed before, the incoming pions could knock out only a few nucleons toward the forward rapidity region. The agreement between UrQMD and SMM models for light cluster and hypertriton formation is good for the larger tungsten system. However, a factor of 10 difference exists for the smaller carbon system, given a potential lower and upper bound of error in hypertriton production estimates.

Quantifying these predictions, the expected yield is on the order of 10^{-3} hypertritons and 10^{-6} $N\Xi$ per event in these collisions. This translates to approximately 10^5 and 10^2 detectable ${}^3_\Lambda\text{H}$ and $N\Xi$ from the entire data set of the HADES collaboration (10^8 recorded events per system) reported in Ref. (Yassine et al., 2023). This large number allows for detailed studies and measurements of the hypertriton and potentially $N\Xi$.

8.6 Fragments of larger mass numbers

To conclude our analysis, we present a compilation of estimated total abundances for normal nuclei and hypernuclei, ranging from light elements up to oxygen (mass number $A = 16$). These estimates aim to quantify the production rates of various nuclei following pion beam collisions with carbon ($\pi^- + \text{C}$) and tungsten ($\pi^- + \text{C}$) targets at an incident momentum of $p_{\text{lab}} = 1.7 \text{ GeV}/c$.

Figure 8.11 showcases the integrated cross section for light nuclei (full symbols) and hypernuclei (single strange hyperon $Y = 1$, open symbols) as a function of their mass number (A). The data is further categorized by the charge (Z) of the nuclei, represented by different colors. The results are obtained from a SMM analysis of UrQMD (v3.5) simulation data for minimum bias $\pi^- + \text{C}$ (left panel) and $\pi^- + \text{C}$ (right panel) collisions.

The figure reveals that the abundance of both light clusters and hypernuclei follows an approximately exponential decrease with increasing mass numbers. This aligns with observations from light nuclei production at RHIC (Agakishiev et al., 2011). Despite the decline, the integrated production cross sections might still be sufficient for signal detection by the HADES collaboration or in future pion-beam experiments with higher beam luminosity.

Notably, the translated yields from the cross section for normal nuclei and

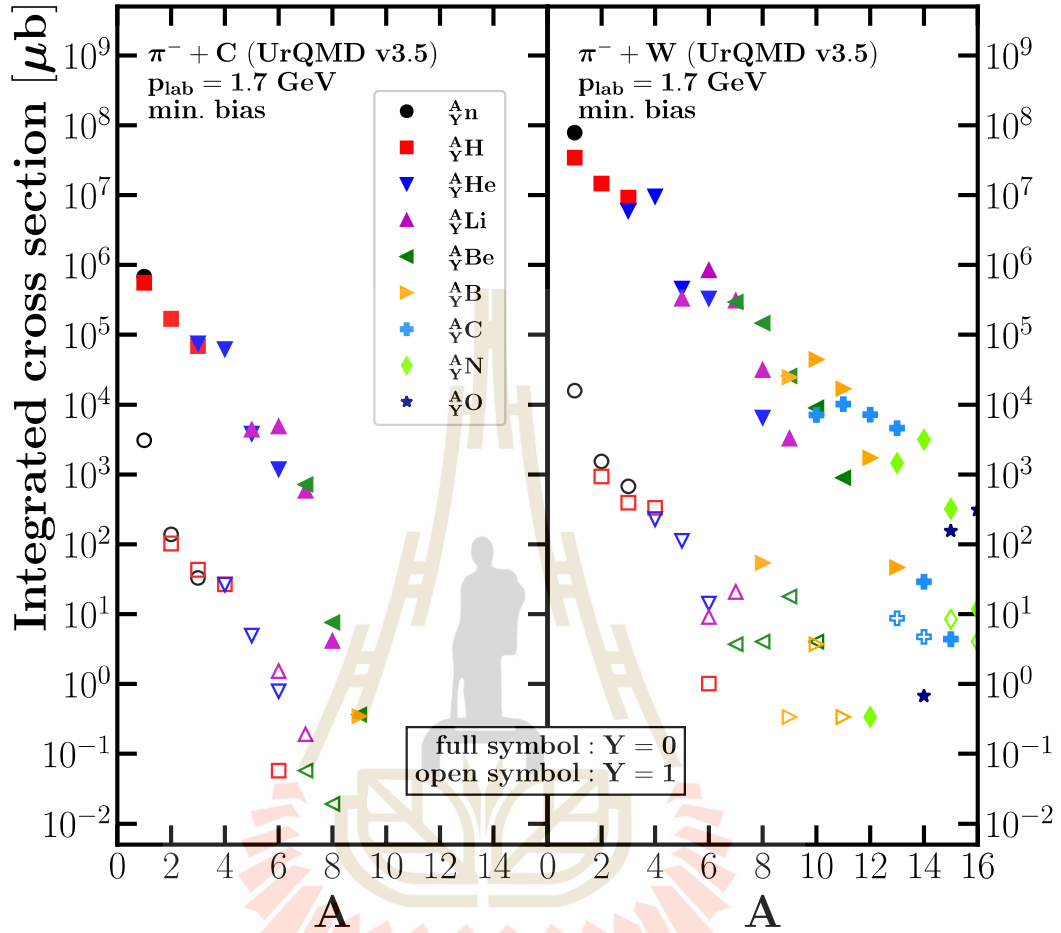


Figure 8.11 The mass number distribution of the integrated cross section of light nuclei (full symbols: $Y=0$) and hypernuclei (single-strange as open symbols: $Y=1$) production with different charges Z (denoted by the color) from SMM analysis of the UrQMD data at minimum bias $\pi^- + C$ and $\pi^- + C$ collisions.

hypernuclei remain at the level of 10^{-4} to 1 and 10^{-6} to 10^{-3} per event, respectively. This paves the way for the first-ever exploration of normal clusters and hypernuclei with mass $A > 4$ in pion beam collision experiments.

Furthermore, as reported by the HADES collaboration Ref. (Ardid et al., 1999), their pion beam can reach momenta of up to 2.5 GeV. This higher beam energy is expected to significantly increase the production cross sections, potentially enabling

the study of Ξ -hypernuclei as well. This opens an exciting opportunity to explore aspects of hypermatter physics within the HADES $\pi + A$ program, potentially mirroring some of the objectives envisioned for the PANDA experiment.

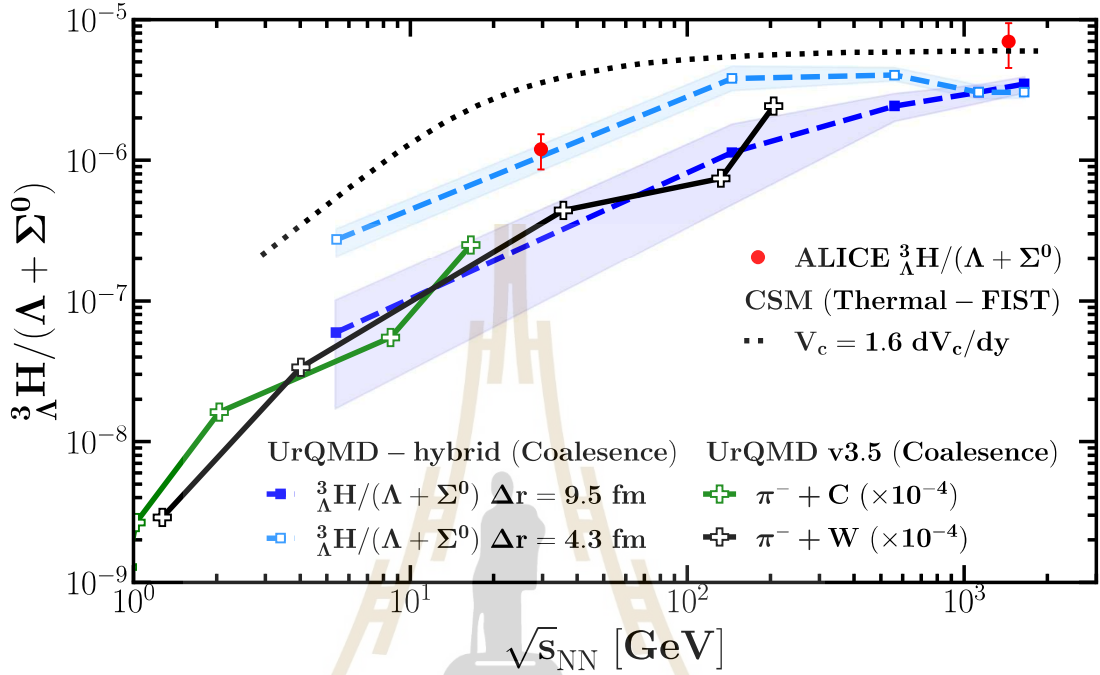


Figure 8.12 The comparison in the yield ratio of the hypertriton (${}^3_{\Lambda}\text{H}/(\Lambda + \Sigma^0)$) as a function of the mean charged particles multiplicity with various models. Our analysis for $\pi^- + \text{C}$ (green line) and $\pi^- + \text{C}$ (black line) is presented alongside data from p+Pb and Pb+Pb. The figure also includes predictions from two models: the thermal-statistical model denoted by CSM Thermal-FIST (dotted line) (Vovchenko et al., 2018a) and the previous UrQMD-hybrid coalescence model (coloured lines with symbols) (Sun et al., 2019)). Finally, brown diamonds represent experimental measurements by the ALICE collaboration (Acharya et al., 2022).

The integrated yields of hypertritons (${}^3_{\Lambda}\text{H}$) and $(\Lambda + \Sigma^0)$ hyperons allow for an analysis of the dependence on collision system size. Centrality classes are approximated by the proton multiplicities. Figure 8.12 presents the results.

The analysis aligns well with previous findings from the UrQMD-hybrid coalescence model (coloured line with squares) for larger systems, exhibiting a suppression of hypertriton yield ratio towards smaller systems. This $\pi^- + A$ study indeed enables predictions for the yield ratio behavior at even lower system sizes. Interestingly, for smaller systems ($dN_{\text{ch}}/d\eta < 10$), the hypertriton yield ratio from π^- -reactions shows

an even stronger suppression compared to the thermal model (dotted line), which fails to capture this effect even at the p+Pb volume. While the p+Pb experimental data agrees with the moderate suppression predicted by the coalescence parameter $\Delta r = 4.3$ fm, i.e., smaller hypertriton wavefunction, the overall trend supports the coalescence model's formation mechanism.

However, our predictions suggest a larger hypertriton wavefunction with a coalescence parameter of $\Delta r = 9.5$ fm. This indicates a potentially more extended wavefunction due to a loosely bound d-core with the Λ hyperon. Future HADES experiments with higher precision could validate these predictions and provide further insight on the formation mechanism.

This chapter explores the formation of clusters and hypernuclei in $\pi^- + A$ at the HADES experiment. Studying these collisions offers a unique opportunity allowing us to investigate cluster formation in regimes where there is limited experimental data, particularly for smaller systems.

The first step involved validating our simulation model. We employed the UrQMD model to simulate $\pi^- + C$ and $\pi^- + C$ at momentum of $p_{\text{lab}} = 1.7$ GeV/c. The simulated results, including the transverse momentum and rapidity distribution of protons and Λ 's, show good agreement with experimental data from the HADES experiment. However, we identified a limitation in HADES acceptance to capture low p_T protons near the target region. This suggests a need for adjustments to the exponential function used.

We then proceed to investigate the production of deuterons, tritons, ^3He , and ^4He nuclei. We compare two different theoretical approaches between the coalescence model and the Statistical Multifragmentation Model (SMM). Both approaches successfully reproduced the observed spectra of light clusters, with good agreement in their rapidity distributions. Interestingly, both models also show a protrusion in the distribution of deuterons towards forward rapidity. This suggests that incoming pions only knock a few nucleons out of the target nucleus. Furthermore, the larger tungsten target system results in broader rapidity distributions for all clusters compared to the carbon target. This can be attributed to the stronger stopping power of tungsten, which leads to a higher probability of binding and multifragmentation at kinetic freeze-out.

Building upon the success with light nuclei, we investigated the production of hypernuclei. Similar to light clusters, hypernuclei with a mass number $A < 3$ displayed a protrusion towards forward rapidity as well as broader rapidity distributions for all

hypernuclei in the tungsten system. We then estimated the total abundances for all clusters, including both normal nuclei and hypernuclei up to oxygen mass. These estimates suggest that the yields are sufficiently high to be detectable by the HADES collaboration.

Finally, we explored potential avenues for future research and investigated the system size dependence of hypernuclei. Our analysis of the yield ratio of hypertriton as a function of charged multiplicity revealed a strong suppression in $\pi^- + A$ collisions compared to the thermal model. This finding supports the coalescence model with a larger hypertriton wavefunction (coalescence parameter $\Delta r = 9.5$ fm).

In conclusion, this chapter highlights the potential of using pion-nucleus collisions at low energies and smaller system sizes to study cluster formation and hypernuclei production. The good agreement between simulations and experimental data paves the way for further exploration of hypermatter physics using the HADES pion-induced program. We propose that using a higher momentum pion beam in the HADES setup could enable studies of the production of Ξ hyperons via the decay of a resonance state (Steinheimer and Bleicher, 2016). This approach might also allow for the investigation of the formation of double- Λ hypernuclei.

CHAPTER IX

SUMMARY

In this thesis, we emphasize the importance of the understanding of the space-time picture of heavy-ion collision dynamics (as highlighted in Ch. II) which is helpful for the search of a potential critical point and constraining the EoS for neutron stars. These two topics are some of the main efforts for most of the future facilities, especially the BES program and GSI-FAIR and HADES. Various theoretical and simulation models are important tools for describing the physics and properties of the medium. Ch. III provides a brief introduction of transport, hydrodynamics, and hybrid models. The corresponding assumptions and advantages of these models are covered. For a microscopic treatment with realistic correlations and fluctuations, we adopt the UrQMD v3.5 transport model for event simulations and for the whole thesis.

The space-time structure of the fireball is explored by demonstrating the interplay between the coalescence parameter B_2 and the (anti)nucleon source geometries in Sec. 4.1 of Ch. IV. By adopting the Mrówczyński's spatial coalescence model, we investigate the (anti)deuteron production and extract the (anti)nucleon source radii r_0 and r_* by fitting the (anti)deuteron formation rate with the available coalescence parameter data B_2 and \bar{B}_2 from NA49 to STAR. The simulations from the cascade UrQMD v3.5 transport model show agreement with our (anti)nucleon source geometries, in which the antinucleon source suffers from the $N\bar{N}$ -annihilation at the center. The comparison of r_0/r_* from both models shares a similar trend. However, the r_0/r_* from our model exhibits a sign for critical behavior from the observed local maxima of both antinucleon source radii at $\sqrt{s_{NN}} = 27$ GeV. This finding also indicates that the (anti)nucleon emission source V_{source} of the coalescence model is not the same as the thermal (charged) volume V_{chem} , which always scales with the collision energy. This motivates us to further investigate and compare the effects of different critical behaviors on the emission source.

Since the interpretation of extracted (anti)nucleon sources is similar to the HBT source volume, we utilize two-pion HBT interferometry to study the source volume in Sec. 4.4, particularly the effects of different EoS with and without phase transition for the neutron star-like medium, i.e., HADES to STAR energies. We begin our investiga-

tion by showing that the impact from the Coulomb potential is minimal and negligible around these energies, where the strong interaction is dominant. The simulation results from the CMF_PT2 EoS are the only EoS that exhibits critical behavior from the phase transition, where the nuclear density for the phase transition to occur in this energy range is around $\rho_B/\rho_0 \leq 4 - 5$. The emission time distribution from the UrQMD v3.5 transport model further supports this critical behavior of CMF_PT2 by extending the freeze-out time distribution of the π^- toward the cascade's at higher energies. This indicates that the HBT radii are sensitive and can be used to test and constrain the EoS.

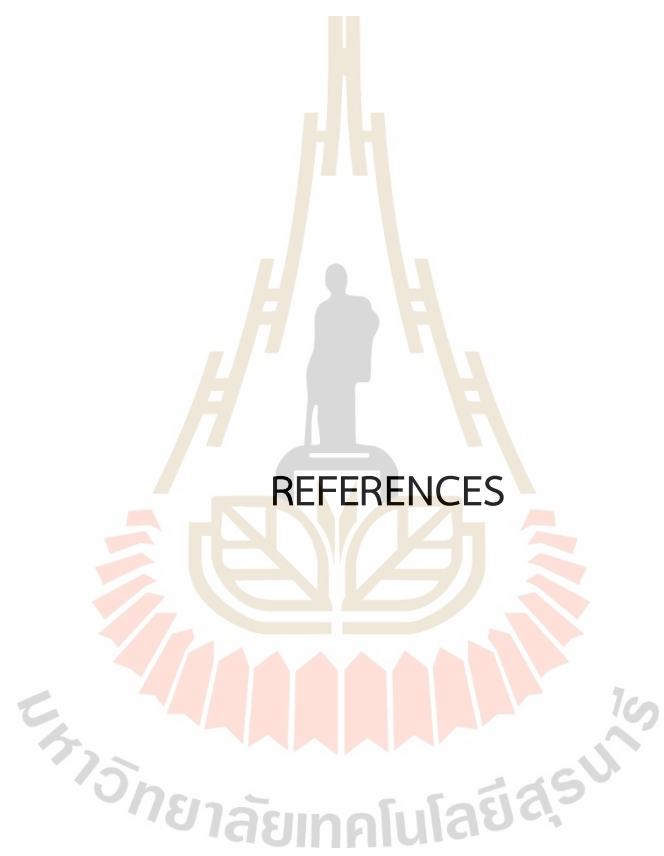
The space-time structure of emission sources is usually related to the coalescence parameters which are measured by either the HBT method or the cluster yields. However, in order to correctly estimate cluster formations and interpret the experimental data, we need to have a clear understanding of their origins and their implications to the whole space-time dynamics of the collisions. Ch. V details various possible cluster formation mechanisms and also highlights hypernuclei formation which shares a similar basis with normal cluster formation.

We continue our discussion on the emission source volume toward even lower collision energies. It is well known and has been clarified in this thesis how the coalescence parameter is inversely proportional to the emission source $B_A \propto (1/V)^{A-1}$, which is again equivalent to the volume of homogeneity of the HBT volume. However, the HBT prediction drops at lower energies, showing a discrepancy with the increasing B_A from the experiments. To solve this disagreement, we demonstrate in Ch. VI that the measurements of B_A from all experimental facilities are obtained from the estimated final state neutrons, e.g., $B_2 \simeq d/p_{\text{final}}^2$, which is justified only at high energies. We propose to make adjustments to B_A measurements by calculating the correct distributions of primordial protons and neutrons, e.g., $B_2 \simeq d/(\rho n)_{\text{prim}}$. By validating our formula with the simulated events from the UrQMD v3.5 transport model, our corrected B_A indeed aligns with the emission volume predicted by the HBT method, providing a consistent picture of the emission source.

One of the most debated concepts in cluster formation is which mechanism is realized in nature, especially the controversial interpretation of cluster formation within the thermal model. In Ch. VII, we propose an approach, based on the different distinct space-time pictures, to distinguish between the thermal (chemical freeze-out) and coalescence (kinetic freeze-out) model in order to solve this tension. By using the isospin triggering $\Delta Y_\pi = (Y_{\pi^-} - Y_{\pi^+})$, the results from the UrQMD v3.5 transport

model agree with our theoretical estimates as the simulated deuterons, tritons, and ${}^3\text{He}$ all show their maxima indicating the ΔY_π -dependent. This is a clear illustration that the coalescence mechanism, which occurs at the kinetic freeze-out, is sensitive to the isospin fluctuations and thus is responsible for the cluster formation.

Another difference between the thermal model and coalescence model is also apparent in the system size-dependence of the hypertriton ratio, ${}^3_\Lambda\text{H}/\Lambda$. The coalescence model predicts a stronger suppression than the canonical thermal model. Also, the study of the critical behavior and the constraint for the low energy EoS (neutron star conditions) involve not only normal nuclei but also hypernuclei and their interactions, e.g., YN — and/or YYN —interaction. Hence, our last Ch. VIII begins by highlighting the need for low energy and a small system for hypernuclei formation. We employ the UrQMD v3.5 transport model to simulate the same collisions of $\pi^- + \text{C}$ and $\pi^- + \text{W}$ at $p_{\text{lab}} = 1.7$ GeV as at HADES and contrast the results with the SMM model for the (hyper)nuclei formation. We found that the extrapolation fit function needs to be adjusted due to the residue protons sitting in the target region, which is outside of the detector acceptance. The light nuclei rapidity distributions further show that the incoming pions can only knock one or two nucleons off the target region, which is a favorable condition for cluster formation or fragmentation. This is further supported by the integrated total yields that (hyper)nuclei, produced with pion-induced reactions, are comparable and even higher than those at p+A and A+A collisions. These indicate that the pion beam at HADES provides a conducive environment to explore these rare probes. Finally, we end our investigation by showing that the ${}^3_\Lambda\text{H}/\Lambda$ from pion-induced reactions could indeed provide a new measurement at a lower system size and also exhibit a strong suppression following the prediction of the coalescence model.



REFERENCES

REFERENCES

- Abbott, T., Akiba, Y., Beavis, D., Bloomer, M., Bond, P., Chasman, C., Chen, Z., Chu, Y., Cole, B., and Costales, J. (1992). "Bose-Einstein correlations in Si + Al and Si + Au collisions at 14.6A GeV/c". *Phys. Rev. Lett.* 69, 1030–1033.
- Abelev, B. I., Aggarwal, M. M., Ahammed, Z., Anderson, B. D., Arkhipkin, D., Averichev, G. S., Balewski, J., Barannikova, O., Barnby, L. S., Baudot, J., Baumgart, S., Beavis, D. R., Bellwied, R., Benedosso, F., Betancourt, M. J., et al. (2010). "Observation of an Antimatter Hypernucleus". *Science* 328, 58–62.
- Abelev, B. I., Aggarwal, M. M., Ahammed, Z., Anderson, B. D., Arkhipkin, D., Averichev, G. S., Balewski, J., Barannikova, O., Barnby, L. S., Baudot, J., Baumgart, S., Beavis, D. R., Bellwied, R., Benedosso, F., Betancourt, M. J., et al. (2005). "Pion interferometry in Au+Au collisions at $\sqrt{s_{NN}} = 200$ GeV". *Phys. Rev. C* 71, 044906.
- Abyazimov, T., Abuhoza, A., Adak, R. P., Adamczyk, M., Agarwal, K., Aggarwal, M. M., Ahammed, Z., Ahmad, F., Ahmad, N., Ahmad, S., Akindinov, A., Akishin, P., Akishina, E., Akishina, T., Akishina, V., et al. (2017). "Challenges in QCD matter physics –The scientific programme of the Compressed Baryonic Matter experiment at FAIR". *Eur. Phys. J. A* 53(3), 60.
- Acharya, S., Adamová, D., Adhya, S., Adler, A., Adolfsson, J., Aggarwal, M., Aglieri Rinella, G., Agnello, M., Agrawal, N., Ahammed, Z., Ahmad, S., Ahn, S., Aiola, S., Akindinov, A., Al-Turany, M., et al. (2022). "Hypertriton Production in p-Pb Collisions at $\sqrt{s_{NN}}=5.02$ TeV". *Phys. Rev. Lett.* 128(25), 252003.
- Acharya, S., Adamová, D., Adhya, S., Adler, A., Adolfsson, J., Aggarwal, M., Aglieri Rinella, G., Agnello, M., Agrawal, N., Ahammed, Z., Ahmad, S., Ahn, S., Aiola, S., Akindinov, A., Al-Turany, M., et al. (2019). "Study of the Λ - Λ interaction with femtoscopy correlations in pp and p-Pb collisions at the LHC". *Phys. Lett. B* 797, 134822.

- Ackermann, K., Adams, N., Adler, C., Ahammed, Z., Ahmad, S., Allgower, C., Amonett, J., Amsbaugh, J., Anderson, B., Anderson, M., Anderssen, E., Arnesen, H., Arnold, L., Averichev, G., Baldwin, A., et al. (2003). “STAR detector overview”. *Nucl. Instrum. Meth. A* 499, 624–632.
- Adam, J., Adamová, D., Aggarwal, M., Agnello, M., Agrawal, N., Ahammed, Z., Ahn, S., Aimo, I., Aiola, S., Ajaz, M., Akindinov, A., Alam, S., Aleksandrov, D., Alessandro, B., Alexandre, D., et al. (2016). “ ${}^3_{\Lambda}\text{H}$ and ${}^3_{\Lambda}\bar{\text{H}}$ production in Pb-Pb collisions at $\sqrt{s_{\text{NN}}} = 2.76$ TeV”. *Phys. Lett. B* 754, 360–372.
- Adam, J., Adamová, D., Aggarwal, M., Agnello, M., Agrawal, N., Ahammed, Z., Ahn, S., Aimo, I., Aiola, S., Ajaz, M., Akindinov, A., Alam, S., Aleksandrov, D., Alessandro, B., Alexandre, D., et al. (2021). “Flow and interferometry results from Au+Au collisions at $\sqrt{s_{\text{NN}}} = 4.5$ GeV”. *Phys. Rev. C* 103(3), 034908.
- Adam, J., Adamová, D., Aggarwal, M., Agnello, M., Agrawal, N., Ahammed, Z., Ahn, S., Aimo, I., Aiola, S., Ajaz, M., Akindinov, A., Alam, S., Aleksandrov, D., Alessandro, B., Alexandre, D., et al. (2020). “Measurement of the mass difference and the binding energy of the hypertriton and antihypertriton”. *Nature Phys.* 16(4), 409–412.
- Adamczewski-Musch, J., Arnold, O., Behnke, C., Belounnas, A., Belyaev, A., Berger-Chen, J., Biernat, J., Blanco, A., Blume, C., Böhmer, M., Bordalo, P., Chernenko, S., Chlad, L., Deveaux, C., Dreyer, J., et al. (2017). “A facility for pion-induced nuclear reaction studies with HADES”. *Eur. Phys. J. A* 53(9), 188.
- Adamczewski-Musch, J., Arnold, O., Behnke, C., Belounnas, A., Belyaev, A., Berger-Chen, J., Biernat, J., Blanco, A., Blume, C., Böhmer, M., Bordalo, P., Chernenko, S., Chlad, L., Deveaux, C., Dreyer, J., et al. (2020). “Identical pion intensity interferometry at $\sqrt{s_{\text{NN}}} = 2.4$ GeV: HADES collaboration”. *Eur. Phys. J. A* 56(5), 140.
- Adamczewski-Musch, J., Arnold, O., Behnke, C., Belounnas, A., Belyaev, A., Berger-Chen, J., Biernat, J., Blanco, A., Blume, C., Böhmer, M., Bordalo, P., Chernenko, S., Chlad, L., Deveaux, C., Dreyer, J., et al. (2019). “Identical pion intensity interferometry in central Au + Au collisions at 1.23 A GeV”. *Phys. Lett. B* 795, 446–451.

- Adamczyk, L., Adkins, J. K., Agakishiev, G., Aggarwal, M. M., Ahammed, Z., Alekseev, I., Alford, J., Anson, C. D., Aparin, A., Arkhipkin, D., Aschenauer, E. C., Averichev, G. S., Banerjee, A., Beavis, D. R., Bellwied, R., et al. (2015). “Beam-energy-dependent two-pion interferometry and the freeze-out eccentricity of pions measured in heavy ion collisions at the STAR detector”. *Phys. Rev. C* 92(1), 014904.
- Adamczyk, L., Adkins, J. K., Agakishiev, G., Aggarwal, M. M., Ahammed, Z., Alekseev, I., Alford, J., Anson, C. D., Aparin, A., Arkhipkin, D., Aschenauer, E. C., Averichev, G. S., Banerjee, A., Beavis, D. R., Bellwied, R., et al. (2014a). “Energy Dependence of Moments of Net-proton Multiplicity Distributions at RHIC”. *Phys. Rev. Lett.* 112, 032302.
- Adamczyk, L., Adkins, J. K., Agakishiev, G., Aggarwal, M. M., Ahammed, Z., Alekseev, I., Alford, J., Anson, C. D., Aparin, A., Arkhipkin, D., Aschenauer, E. C., Averichev, G. S., Banerjee, A., Beavis, D. R., Bellwied, R., et al. (2017). “Global Λ hyperon polarization in nuclear collisions: evidence for the most vortical fluid”. *Nature* 548, 62–65.
- Adamczyk, L., Adkins, J. K., Agakishiev, G., Aggarwal, M. M., Ahammed, Z., Alekseev, I., Alford, J., Anson, C. D., Aparin, A., Arkhipkin, D., Aschenauer, E. C., Averichev, G. S., Banerjee, A., Beavis, D. R., Bellwied, R., et al. (2014b). *Studying the Phase Diagram of QCD Matter at RHIC*.
- Adare, A., Afanasiev, S., Aidala, C., Ajitanand, N. N., Akiba, Y., Akimoto, R., Al-Bataineh, H., Alexander, J., Al-Ta'ani, H., Angerami, A., Aoki, K., Apadula, N., Aramaki, Y., Asano, H., Aschenauer, E. C., et al. (2016). “Measurement of higher cumulants of net-charge multiplicity distributions in Au+Au collisions at $\sqrt{s_{NN}} = 7.7 - 200$ GeV”. *Phys. Rev. C* 93(1), 011901.
- Adhikary, H., Adrich, P., Allison, K., Amin, N., Andronov, E., Antičić, T., Arsene, I.-C., Bajda, M., Balkova, Y., and Baszczyk, M. (2023). “Two-pion femtoscopic correlations in Be+Be collisions at $\sqrt{s_{NN}} = 16.84$ GeV measured by the NA61/SHINE at CERN”. *Eur. Phys. J. C* 83(10), 919.
- Afanasiev, S., Anticic, T., Bächler, J., Barna, D., Barnby, L., Bartke, J., Barton, R., Betev, L., Bialkowska, H., Billmeier, A., Blume, C., Blyth, C., Boimska, B., Bracinik, J., Brady, F.,

- et al. (2000). “Deuteron production in central Pb + Pb collisions at 158 AGeV”. *Phys. Lett. B* 486, 22–28.
- Agakichiev, G., Agodi, C., Alvarez-Pol, H., Atkin, E., Badura, E., Balanda, A., Bassi, A., Bassini, R., Bellia, G., Belver, D., Belyaev, A. V., Benovic, M., Bertini, D., Bielcik, J., Böhmer, M., et al. (2009). “The High-Acceptance Dielectron Spectrometer HADES”. *Eur. Phys. J. A* 41, 243–277.
- Agakishiev, G., Aggarwal, M. M., Ahammed, Z., Alekseev, I., Alford, J., Anson, C. D., Aparin, A., Arkhipkin, D., Aschenauer, E. C., Averichev, G. S., Banerjee, A., Beavis, D. R., Bellwied, R., Bhasin, A., Bhati, A. K., et al. (2011). “Observation of the antimatter helium-4 nucleus”. *Nature* 473. [Erratum: *Nature* 475, 412 (2011)], 353.
- Aguilar, M., Ali Cavasonza, L., Alpat, B., Ambrosi, G., Arruda, L., Attig, N., Aupetit, S., Azzarello, P., Bachlechner, A., Barao, F., Battarbee, M., Battiston, R., Bazo, J., Becker, U., Behlmann, M., et al. (2016). “Antiproton Flux, Antiproton-to-Proton Flux Ratio, and Properties of Elementary Particle Fluxes in Primary Cosmic Rays Measured with the Alpha Magnetic Spectrometer on the International Space Station”. *Phys. Rev. Lett.* 117(9), 091103.
- Ahle, L., Akiba, Y., Ashktorab, K., Baker, M., Beavis, D., Britt, H., Chang, J., Chasman, C., Chen, Z., and Chi, C.-Y. (1999). “Proton and deuteron production in Au + Au reactions at 11.6 AGeV/c”. *Phys. Rev. C* 60, 064901.
- Aichelin, J. (1991). “‘Quantum’ molecular dynamics: A Dynamical microscopic n body approach to investigate fragment formation and the nuclear equation of state in heavy ion collisions”. *Phys. Rept.* 202, 233–360.
- Aichelin, J., Bratkovskaya, E., Le Fèvre, A., Kireyeu, V., Kolesnikov, V., Leifels, Y., Voronyuk, V., and Coci, G. (2020). “Parton-hadron-quantum-molecular dynamics: A novel microscopic n-body transport approach for heavy-ion collisions, dynamical cluster formation, and hypernuclei production”. *Phys. Rev. C* 101(4), 044905.
- Akkelin, S. V., Hama, Y., Karpenko, I. A., and Sinyukov, Y. M. (2008). “Hydro-kinetic approach to relativistic heavy ion collisions”. *Phys. Rev. C* 78, 034906.

- Alford, M. G., Rajagopal, K., and Wilczek, F. (1999). “Color flavor locking and chiral symmetry breaking in high density QCD”. *Nucl. Phys. B* 537, 443–458.
- Allton, C. R., Doring, M., Ejiri, S., Hands, S. J., Kaczmarek, O., Karsch, F., Laermann, E., and Redlich, K. (2005). “Thermodynamics of two flavor QCD to sixth order in quark chemical potential”. *Phys. Rev. D* 71, 054508.
- Almaalol, D., Hippert, M., Noronha-Hostler, J., Noronha, J., Speranza, E., Basar, G., Bass, S., Cebra, D., Dexheimer, V., Keane, D., Radhakrishnan, S., Sheikh, A. I., Strickland, M., Tsang, C. Y., Dong, . X., et al. (2022). “QCD Phase Structure and Interactions at High Baryon Density: Continuation of BES Physics Program with CBM at FAIR”. *arXiv preprint arXiv:2209.05009*.
- Alpher, R. A. and Herman, R. (1948). “Evolution of the Universe”. *Nature* 162(4124), 774–775.
- Ambrosini, G., Arsenescu, R., Baglin, C., Beringer, J., Bohm, C., Borer, K., Bussiere, A., Dittus, F., Elsener, K., and Frei, D. (1998). “Baryon and anti-baryon production in lead-lead collisions at 158 A-GeV/c”. *Phys. Lett. B* 417, 202–210.
- Amsden, A., Bertsch, G., Harlow, F., and Nix, J. (1975). “Relativistic hydrodynamic theory of heavy-ion collisions”. *Physical Review Letters* 35(14), 905.
- Andersson, B., Gustafson, G., Ingelman, G., and Sjöstrand, T. (1983). “Parton fragmentation and string dynamics”. *Physics Reports* 97(2-3), 31–145.
- Andronic, A., Braun-Munzinger, P., Redlich, K., and Stachel, J. (2017). “Hadron yields, the chemical freeze-out and the QCD phase diagram”. *J. Phys. Conf. Ser.* 779(1), 012012.
- Andronic, A., Braun-Munzinger, P., and Stachel, J. (2010). “The Horn, the hadron mass spectrum and the QCD phase diagram: The Statistical model of hadron production in central nucleus-nucleus collisions”. *Nucl. Phys. A* 834, 237C–240C.

- Andronic, A., Braun-Munzinger, P., and Stachel, J. (2009). “Thermal hadron production in relativistic nuclear collisions: The Hadron mass spectrum, the horn, and the QCD phase transition”. *Phys. Lett. B* 673. [Erratum: *Phys.Lett.B* 678, 516 (2009)], 142–145.
- Andronic, A., Braun-Munzinger, P., Stachel, J., and Stocker, H. (2011). “Production of light nuclei, hypernuclei and their antiparticles in relativistic nuclear collisions”. *Phys. Lett. B* 697, 203–207.
- Andronic, A. (2014). “An overview of the experimental study of quark-gluon matter in high-energy nucleus-nucleus collisions”. *Int. J. Mod. Phys. A* 29, 1430047.
- Andronic, A., Braun-Munzinger, P., Friman, B., Lo, P. M., Redlich, K., and Stachel, J. (2019). “The thermal proton yield anomaly in Pb-Pb collisions at the LHC and its resolution”. *Phys. Lett. B* 792, 304–309.
- Andronic, A., Braun-Munzinger, P., Redlich, K., and Stachel, J. (2018). “Decoding the phase structure of QCD via particle production at high energy”. *Nature* 561(7723), 321–330.
- Anticic, T., Bächler, J., Barna, D., Barnby, L., Bartke, J., Barton, R., Betev, L., Bialkowska, H., Billmeier, A., Blume, C., Blyth, C., Boimska, B., Bracini, J., Brady, F., Brun, R., et al. (2004). “Energy and centrality dependence of deuteron and proton production in Pb + Pb collisions at relativistic energies”. *Phys. Rev. C* 69, 024902.
- Anticic, T., Bächler, J., Barna, D., Barnby, L., Bartke, J., Barton, R., Betev, L., Bialkowska, H., Billmeier, A., Blume, C., Blyth, C., Boimska, B., Bracini, J., Brady, F., Brun, R., et al. (2016). “Production of deuterium, tritium, and He3 in central Pb + Pb collisions at 20A, 30A, 40A, 80A, and 158A GeV at the CERN Super Proton Synchrotron”. *Phys. Rev. C* 94(4), 044906.
- Aoki, M. (1992). “Measurements at 0 degrees of negatively charged particles and anti-nuclei produced in collision of 14.6A GeV/c Si on Al, Cu, and Au targets”. *Phys. Rev. Lett.* 69, 2345–2348.

- Aoki, Y., Endrodi, G., Fodor, Z., Katz, S. D., and Szabo, K. K. (2006). “The Order of the quantum chromodynamics transition predicted by the standard model of particle physics”. *Nature* 443, 675–678.
- Ardid, M., Yahlali, N., Díaz, J., and Álvarez, M. (1999). “Results of the commissioning of the Pion Beam Factory at SIS/GSI”. *AIP Conf. Proc.* 495(1), 401.
- Armstrong, T. A., Barish, K. N., Batsouli, S., Bennett, S. J., Bertaina, M., Chikanian, A., Coe, S. D., Cormier, T. M., Davies, R., Dover, C. B., Fachini, P., Fadem, B., Finch, L. E., George, N. K., Greene, S. V., et al. (2000). “Measurements of light nuclei production in 11.5A GeV/c Au + Pb heavy ion collisions”. *Phys. Rev. C* 61, 064908.
- Armstrong, T., Barish, K., Batsouli, S., Bennett, S., Chikanian, A., Coe, S., Cormier, T., Davies, R., Dover, C., and Fachini, P. (1999). “Measurements of neutrons in 11.5 A GeV/c Au + Pb heavy ion collisions”. *Phys. Rev. C* 60, 064903.
- Balberg, S., Lichtenstadt, I., and Cook, G. B. (1999). “Roles of hyperons in neutron stars”. *Astrophys. J. Suppl.* 121, 515.
- Bally, B., Jia, J., Giacalone, G., Brandenburg, J. D., Heinz, U., Huang, S., Lee, D., Lee, Y.-J., Loizides, C., Li, W., Luzum, M., Nijs, G., Noronha-Hostler, J., Ploskon, M., Schee, W. van der, et al. (2024). “Imaging the initial condition of heavy-ion collisions and nuclear structure across the nuclide chart”. *Nuclear Science and Techniques* 35(12), 1–17.
- Barrette, J., Bellwied, R., Bennett, S., Bersch, R., Braun-Munzinger, P., Chang, W., Cleland, W., Clemen, M., Cole, J., and Cormier, T. (2000). “Light fragment yields from Au + Au collisions at 11.5A GeV/c”. *Phys. Rev. C* 61, 044906.
- Barz, H. W., Bondorf, J. P., Donangelo, R., Mishustin, I. N., and Schulz, H. (1986). “Statistical multifragmentation of nuclei”. *Nucl. Phys. A* 448, 753–763.
- Bass, S., Belkacem, M., Bleicher, M., Brandstetter, M., Bravina, L., Ernst, C., Gerland, L., Hofmann, M., Hofmann, S., Konopka, J., Mao, G., Neise, L., Soff, S., Spieles, C., Weber, H., et al. (1998). “Microscopic models for ultrarelativistic heavy ion collisions”. *Prog. Part. Nucl. Phys.* 41, 255–369.

- Batyuk, P., Blaschke, D., Bleicher, M., Ivanov, Y. B., Karpenko, I., Merts, S., Nahrgang, M., Petersen, H., and Rogachevsky, O. (2016). “Event simulation based on three-fluid hydrodynamics for collisions at energies available at the Dubna Nuclotron-based Ion Collider Facility and at the Facility for Antiproton and Ion Research in Darmstadt”. *Phys. Rev. C* 94, 044917.
- Baym, G. and Braun-Munzinger, P. (1996). “Physics of Coulomb corrections in Hanbury-Brown-Twiss interferometry in ultrarelativistic heavy ion collisions”. *Nucl. Phys. A* 610, 286C–296C.
- Bazavov, A., Ding, H.-T., Hegde, P., Kaczmarek, O., Karsch, F., Karthik, N., Laermann, E., Lahiri, A., Larsen, R., Li, S.-T., Mukherjee, S., Ohno, H., Petreczky, P., Sandmeyer, H., Schmidt, C., et al. (2019). “Chiral crossover in QCD at zero and non-zero chemical potentials”. *Physics Letters B* 795, 15–21.
- Bazavov, A., Bhattacharya, T., Cheng, M., DeTar, C., Ding, H.-T., Gottlieb, S., Gupta, R., Hegde, P., Heller, U. M., and Karsch, F. (2012). “The chiral and deconfinement aspects of the QCD transition”. *Phys. Rev. D* 85, 054503.
- Bearden, I., Bøggild, H., Boissevain, J., Christiansen, P., Conin, L., Dodd, J., Erasmus, B., Esumi, S., Fabjan, C., and Ferenc, D. (2002). “Deuteron and triton production with high energy sulphur and lead beams”. *Eur. Phys. J. C* 23, 237–247.
- Becattini, F., Gazdzicki, M., and Sollfrank, J. (1998). “On chemical equilibrium in nuclear collisions”. *Eur. Phys. J. C* 5, 143–153.
- Belenkij, S. Z. and Landau, L. D. (1955). “Hydrodynamic theory of multiple production of particles”. *Usp. Fiz. Nauk* 56, 309.
- Bellini, F. (2022). “Light Antinuclei from the Laboratory to the Cosmos”. *Nucl. Phys. News* 32(1), 11–15.
- Berges, J. and Rajagopal, K. (1999). “Color superconductivity and chiral symmetry restoration at nonzero baryon density and temperature”. *Nucl. Phys. B* 538, 215–232.

- Bertsch, G. and Cugnon, J. (1981). “Entropy production in high energy collisions”. *Phys. Rev. C* 24, 2514–2520.
- Bertsch, G., Gong, M., and Tohyama, M. (1988). “Pion Interferometry in Ultrarelativistic Heavy Ion Collisions”. *Phys. Rev. C* 37, 1896–1900.
- Biswas, B. (2021). “Impact of PREX-II and Combined Radio/NICER/XMM-Newton’s Mass-radius Measurement of PSR J0740+6620 on the Dense-matter Equation of State”. *Astrophys. J.* 921(1), 63.
- Blaschke, D., Röpke, G., Ivanov, Y., Kozhevnikova, M., and Liebing, S. (2020). “Strangeness and light fragment production at high baryon density”. *Springer Proc. Phys.* 250, 183–190.
- Bleicher, M., Zabrodin, E., Spieles, C., Bass, S. A., Ernst, C., Soff, S., Bravina, L., Belkacem, M., Weber, H., Stöcker, H., and Greiner, W. (1999). “Relativistic hadron hadron collisions in the ultrarelativistic quantum molecular dynamics model”. *J. Phys. G* 25, 1859–1896.
- Bleicher, M., Spieles, C., Jahns, A., Mattiello, R., Sorge, H., Stoecker, H., and Greiner, W. (1995). “Phase space correlations of anti-deuterons in heavy ion collisions”. *Phys. Lett. B* 361, 10–13.
- Bleicher, M. and Bratkovskaya, E. (2022). “Modelling relativistic heavy-ion collisions with dynamical transport approaches”. *Prog. Part. Nucl. Phys.* 122, 103920.
- Bluhm, M., Kalweit, A., Nahrgang, M., Arslanok, M., Braun-Munzinger, P., Floerchinger, S., Fraga, E. S., Gazdzicki, M., Hartnack, C., and Herold, C. (2020). “Dynamics of critical fluctuations: Theory – phenomenology – heavy-ion collisions”. *Nucl. Phys. A* 1003, 122016.
- Boal, D. H., Gelbke, C. K., and Jennings, B. K. (1990). “Intensity interferometry in subatomic physics”. *Rev. Mod. Phys.* 62, 553–602.

- Boercker, D. B. and Dufty, J. W. (1979). “Degenerate quantum gases in the binary collision approximation”. *Annals of Physics* 119(1), 43–70.
- Bombaci, I. (2017). “The Hyperon Puzzle in Neutron Stars”. *JPS Conf. Proc.* 17, 101002.
- Bond, R., Johansen, P. J., Koonin, S. E., and Garpman, S. (1977). “Breakup Densities of Nuclear Fireballs”. *Phys. Lett. B* 71, 43–47.
- Bondorf, J. P., Botvina, A. S., Ilinov, A. S., Mishustin, I. N., and Sneppen, K. (1995). “Statistical multifragmentation of nuclei”. *Phys. Rept.* 257, 133–221.
- Borsanyi, S., Fodor, Z., Hoelbling, C., Katz, S. D., Krieg, S., and Szabo, K. K. (2014). “Full result for the QCD equation of state with 2+1 flavors”. *Phys. Lett. B* 730, 99–104.
- Borsanyi, S., Fodor, Z., Guenther, J. N., Kara, R., Katz, S. D., Parotto, P., Pasztor, A., Ratti, C., and Szabo, K. K. (2020). “QCD Crossover at Finite Chemical Potential from Lattice Simulations”. *Phys. Rev. Lett.* 125(5), 052001.
- Botvina, A. S., Buyukcizmeci, N., and Bleicher, M. (2021). “Coupling dynamical and statistical mechanisms for baryonic cluster production in nucleus collisions of intermediate and high energies”. *Phys. Rev. C* 103(6), 064602.
- Botvina, A. S., Buyukcizmeci, N., and Bleicher, M. (2022). “Evolution of the statistical disintegration of finite nuclei toward high energy”. *Phys. Rev. C* 106(1), 014607.
- Botvina, A. S., Steinheimer, J., Bratkovskaya, E., Bleicher, M., and Pochodzalla, J. (2015). “Formation of hypermatter and hypernuclei within transport models in relativistic ion collisions”. *Phys. Lett. B* 742, 7–14.
- Bowler, M. G. (1991). “Coulomb corrections to Bose-Einstein correlations have been greatly exaggerated”. *Phys. Lett. B* 270, 69–74.
- Brachmann, J., Dumitru, A., Maruhn, J. A., Stoecker, H., Greiner, W., and Rischke, D. H. (1997). “Nonequilibrium fluid dynamics in the early stage of ultrarelativistic heavy ion collisions”. *Nucl. Phys. A* 619, 391–412.

- Bratskovskaya, E. (2019a). *Introduction to the dynamical models of heavy-ion collisions - Part1*.
- Bratskovskaya, E. (2019b). *Introduction to the dynamical models of heavy-ion collisions - Part2*.
- Braun-Munzinger, P. and Dönigus, B. (2019). “Loosely-bound objects produced in nuclear collisions at the LHC”. *Nucl. Phys. A* 987, 144–201.
- Bravina, L. V., Zabrodin, E. E., Gorenstein, M. I., Bass, S. A., Belkacem, M., Bleicher, M., Brandstetter, M., Ernst, C., Hofmann, M., Neise, L., Soff, S., Weber, H., Stöcker, H., and Greiner, W. (1999). “Local equilibrium in heavy ion collisions: Microscopic model versus statistical model analysis”. *Phys. Rev. C* 60, 024904.
- Brown, G. E. and Rho, M. (1996). “Chiral restoration in hot and/or dense matter”. *Phys. Rept.* 269, 333–380.
- Brown, R. H. and Twiss, R. Q. (1956). “Correlation between Photons in two Coherent Beams of Light”. *Nature* 177, 27–29.
- Buballa, M. (2005). “NJL model analysis of quark matter at large density”. *Phys. Rept.* 407, 205–376.
- Buss, O., Gaitanos, T., Gallmeister, K., Hees, H. van, Kaskulov, M., Lalakulich, O., Larionov, A. B., Leitner, T., Weil, J., and Mosel, U. (2012). “Transport-theoretical Description of Nuclear Reactions”. *Phys. Rept.* 512, 1–124.
- Busza, W., Rajagopal, K., and Schee, W. van der (2018). “Heavy Ion Collisions: The Big Picture, and the Big Questions”. *Ann. Rev. Nucl. Part. Sci.* 68, 339–376.
- Butler, S. T. and Pearson, C. A. (1961). “Deuterons from High-Energy Proton Bombardment of Matter”. *Phys. Rev. Lett.* 7, 69–71.
- Butler, S. T. and Pearson, C. A. (1963). “Deuterons from High-Energy Proton Bombardment of Matter”. *Phys. Rev.* 129, 836–842.

- Buyukcizmeci, N., Botvina, A. S., Ogul, R., and Bleicher, M. (2020). “Evaluation of hypernuclei in relativistic ion collisions”. *Eur. Phys. J. A* 56(8), 210.
- Buyukcizmeci, N., Reichert, T., Botvina, A. S., and Bleicher, M. (2023). “Nucleosynthesis of light nuclei and hypernuclei in central Au+Au collisions at $\sqrt{s_{NN}} = 3 \text{ GeV}$ ”. *Phys. Rev. C* 108(5), 054904.
- Bzdak, A., Esumi, S., Koch, V., Liao, J., Stephanov, M., and Xu, N. (2020). “Mapping the Phases of Quantum Chromodynamics with Beam Energy Scan”. *Phys. Rept.* 853, 1–87.
- Cabibbo, N. and Parisi, G. (1975). “Exponential Hadronic Spectrum and Quark Liberation”. *Phys. Lett. B* 59, 67–69.
- Capano, C. D., Tews, I., Brown, S. M., Margalit, B., De, S., Kumar, S., Brown, D. A., Krishnan, B., and Reddy, S. (2020). “Stringent constraints on neutron-star radii from multimessenger observations and nuclear theory”. *Nature Astron.* 4(6), 625–632.
- Carlson, E., Coogan, A., Linden, T., Profumo, S., Ibarra, A., and Wild, S. (2014). “Antihelium from Dark Matter”. *Phys. Rev. D* 89(7), 076005.
- Chapman, S., Nix, J. R., and Heinz, U. W. (1995). “Extracting source parameters from Gaussian fits to two particle correlations”. *Phys. Rev. C* 52, 2694–2703.
- Chapman, S., Scotto, P., and Heinz, U. W. (1995). “A New cross term in the two particle HBT correlation function”. *Phys. Rev. Lett.* 74, 4400–4403.
- Chatterjee, D. and Vidaña, I. (2016). “Do hyperons exist in the interior of neutron stars?” *Eur. Phys. J. A* 52(2), 29.
- Chen, J., Keane, D., Ma, Y.-G., Tang, A., and Xu, Z. (2018). “Antinuclei in Heavy-Ion Collisions”. *Phys. Rept.* 760, 1–39.

- Cho, S., Hyodo, T., Jido, D., Ko, C. M., Lee, S. H., Maeda, S., Miyahara, K., Morita, K., Nielsen, M., Ohnishi, A., Sekihara, T., Song, T., Yasui, S., and Yazaki, K. (2017). “Exotic hadrons from heavy ion collisions”. *Progress in Particle and Nuclear Physics* 95, 279–322.
- Cimernan, J., Karpenko, I., Tomasik, B., and Huovinen, P. (2023). “Next-generation multi-fluid hydrodynamic model for nuclear collisions at sNN from a few GeV to a hundred GeV”. *Phys. Rev. C* 107(4), 044902.
- Cleymans, J., Oeschler, H., Redlich, K., and Wheaton, S. (2006). “Comparison of chemical freeze-out criteria in heavy-ion collisions”. *Phys. Rev. C* 73, 034905.
- Cleymans, J. and Satz, H. (1993). “Thermal hadron production in high-energy heavy ion collisions”. *Z. Phys. C* 57, 135–148.
- Cooper, F. and Frye, G. (1974). “Single-particle distribution in the hydrodynamic and statistical thermodynamic models of multiparticle production”. *Physical Review D* 10(1), 186.
- Csernai, L. P. and Kapusta, J. I. (1986). “Entropy and Cluster Production in Nuclear Collisions”. *Phys. Rept.* 131, 223–318.
- Csernai, L., Lukacs, B., and Zimanyi, J. (1980). “On the relativistic hydrodynamical description of energetic heavy-ion reactions”. *Lettere al Nuovo Cimento (1971-1985)* 27, 111–116.
- Csorgo, T. (2006). “Review of HBT or Bose-Einstein correlations in high energy heavy ion collisions”. *J. Phys. Conf. Ser.* 50, 259–270.
- Csorgo, T., Hegyi, S., Novak, T., and Zajc, W. A. (2006). “Bose-Einstein or HBT correlation signature of a second order QCD phase transition”. *AIP Conf. Proc.* 828(1), 525–532.
- Csorgo, T., Hegyi, S., and Zajc, W. A. (2004). “Bose-Einstein correlations for Levy stable source distributions”. *Eur. Phys. J. C* 36, 67–78.
- Csorgo, T. (2008). “Correlation Probes of a QCD Critical Point”. *PoS HIGH-PTLHC08*, 027.

- Danielewicz, P. and Bertsch, G. F. (1991). "Production of deuterons and pions in a transport model of energetic heavy-ion reactions". *Nuclear Physics A* 533(4), 712–748.
- Danielewicz, P. and Schuck, P. (1992). "Formulation of particle correlation and cluster production in heavy-ion-induced reactions". *Phys. Lett. B* 274, 268–274.
- Davis, D. (2005). "50 years of hypernuclear physics: I. The early experiments". *Nuclear Physics A* 754, 3–13.
- DeTar, C. E. and Donoghue, J. F. (1983). "BAG MODELS OF HADRONS". *Ann. Rev. Nucl. Part. Sci.* 33, 235–264.
- Dinh, P. M., Borghini, N., and Ollitrault, J.-Y. (2000). "Effects of HBT correlations on flow measurements". *Phys. Lett. B* 477, 51–58.
- Dönigus, B. (2013). "(Anti-)matter and hyper-matter production at the LHC with ALICE". *Nucl. Phys. A* 904-905, 547c–550c.
- Dönigus, B. (2020). "Selected highlights of the production of light (anti)-(hyper-)nuclei in ultra-relativistic heavy-ion collisions". *Eur. Phys. J. A* 56(11), 280.
- Dover, C. B., Heinz, U. W., Schnedermann, E., and Zimanyi, J. (1991). "Relativistic coalescence model for high-energy nuclear collisions". *Phys. Rev. C* 44, 1636–1654.
- Durante, M., Indelicato, P., Jonson, B., Koch, V., Langanke, K., Meißner, U.-G., Nappi, E., Nilsson, T., Stöhlker, T., Widmann, E., and Wiescher, M. (2019). "All the fun of the FAIR: fundamental physics at the facility for antiproton and ion research". *Phys. Scripta* 94(3), 033001.
- Fai, G. I. and Randrup, J. (1983). "Statistical Simulation of Complete Events in Energetic Nuclear Collisions". *Nucl. Phys. A* 404, 551–577.
- Feldmeier, H. (1990). "Fermionic molecular dynamics". *Nuclear Physics A* 515(1), 147–172.

- Feynman, R. P. (2018). *Statistical mechanics: a set of lectures*. CRC press.
- Florkowski, W., Broniowski, W., and Michalec, M. (2002). “Thermal analysis of particle ratios and $p(t)$ spectra at RHIC”. *Acta Phys. Polon. B* 33, 761–769.
- Fodor, Z. and Katz, S. D. (2002). “Lattice determination of the critical point of QCD at finite T and μ ”. *JHEP* 03, 014.
- Forcrand, P. de (2009). “Simulating QCD at finite density”. *PoS LAT2009*, 010.
- Forcrand, P. de and Philipsen, O. (2010). “Constraining the QCD phase diagram by tricritical lines at imaginary chemical potential”. *Phys. Rev. Lett.* 105, 152001.
- Freedman, B. A. and McLerran, L. D. (1977). “Fermions and Gauge Vector Mesons at Finite Temperature and Density. 3. The Ground State Energy of a Relativistic Quark Gas”. *Phys. Rev. D* 16, 1169.
- Friman, B., C. Hohne, J. Knoll, S. Leupold, J. Randrup, R. Rapp, and P. Senger, eds. (2011). *The CBM physics book: Compressed baryonic matter in laboratory experiments*. Vol. 814. Springer.
- Fritzsch, H., Gell-Mann, M., and Leutwyler, H. (1973). “Advantages of the Color Octet Gluon Picture”. *Phys. Lett. B* 47, 365–368.
- Fujiwara, Y., Nakamoto, C., and Suzuki, Y. (1996a). “A Unified description of NN and YN interactions in a quark model with effective meson exchange potentials”. *Phys. Rev. Lett.* 76, 2242–2245.
- Fujiwara, Y., Nakamoto, C., and Suzuki, Y. (1996b). “Effective meson exchange potentials in the SU(6) quark model for NN and YN interactions”. *Phys. Rev. C* 54, 2180–2200.
- Fuke, H., Maeno, T., Abe, K., Haino, S., Makida, Y., Matsuda, S., Matsumoto, H., Mitchell, J. W., Moiseev, A. A., Nishimura, J., Nozaki, M., Orito, S., Ormes, J. F., Sasaki, M., Seo, E. S., et al. (2005). “Search for cosmic-ray antideuterons”. *Phys. Rev. Lett.* 95, 081101.

- Fukushima, K. (2004). "Chiral effective model with the Polyakov loop". *Phys. Lett. B* 591, 277–284.
- Gaebel, V., Bonne, M., Reichert, T., Burnic, A., Hillmann, P., and Bleicher, M. (2021). "Understanding the energy dependence of B_2 in heavy ion collisions: Interplay of volume and space-momentum correlations". *Eur. Phys. J. A* 57(2), 55.
- Gal, A., Hungerford, E. V., and Millener, D. J. (2016). "Strangeness in nuclear physics". *Rev. Mod. Phys.* 88(3), 035004.
- Gibson, B. F. and Hungerford, E. V. (1995). "A Survey of hypernuclear physics". *Phys. Rept.* 257, 349–388.
- Goldhaber, G., Goldhaber, S., Lee, W.-Y., and Pais, A. (1960). "Influence of Bose-Einstein statistics on the anti-proton proton annihilation process". *Phys. Rev.* 120, 300–312.
- Goulianos, K. (1983). "Diffractive interactions of hadrons at high energies". *Physics Reports* 101(3), 169–219.
- Grassi, F., Hama, Y., and Kodama, T. (1996). "Particle emission in the hydrodynamical description of relativistic nuclear collisions". *Z. Phys. C* 73, 153–160.
- Gross, D. H. E. (1984). "Nuclear physics with heavy ions – Many body systems with specific flavour". *Nucl. Phys. A* 428, 313–325.
- Gross, D. J. and Wilczek, F. (1973). "Ultraviolet Behavior of Nonabelian Gauge Theories". *Phys. Rev. Lett.* 30, 1343–1346.
- Gutbrod, H. H., Sandoval, A., Johansen, P. J., Poskanzer, A. M., Gosset, J., Meyer, W. G., Westfall, G. D., and Stock, R. (1976). "Final State Interactions in the Production of Hydrogen and Helium Isotopes by Relativistic Heavy Ions on Uranium". *Phys. Rev. Lett.* 37, 667–670.
- Gyulassy, M., Frankel, K., and Reimler, E. a. (1983). "Deuteron Formation in Nuclear Collisions". *Nucl. Phys. A* 402, 596–611.

- Hagedorn, R. (1960). "Deuteron Production in High-Energy Collisions". *Phys. Rev. Lett.* *5*, 276–277.
- Hagel, K., Wada, R., Qin, L., Natowitz, J. B., Shlomo, S., Bonasera, A., Röpke, G., Typel, S., Chen, Z., Huang, M., Wang, J., Zheng, H., Kowalski, S., Bottosso, C., Barbui, M., et al. (2012). "Experimental Determination of In-Medium Cluster Binding Energies and Mott Points in Nuclear Matter". *Phys. Rev. Lett.* *108*, 062702.
- Hama, Y., Peterson G. Andrade, R., Grassi, F., Qian, W.-L., Osada, T., Aguiar, C. E., and Kodama, T. (2008). "NeXSPheRIO Results on Elliptic-Flow Fluctuations at RHIC". *Phys. Atom. Nucl.* *71*, 1558–1564.
- Hanbury Brown, R. and Twiss, R. Q. (1956). "A Test of a new type of stellar interferometer on Sirius". *Nature* *178*, 1046–1048.
- Hartnack, C., Aichelin, J., Stoecker, H., and Greiner, W. (1994). "Out of plane squeeze of clusters in relativistic heavy ion collisions". *Phys. Lett. B* *336*, 131–135.
- Hartnack, C., Zhuxia, L., Neise, L., Peilert, G., Rosenhauer, A., Sorge, H., Aichelin, J., Stöcker, H., and Greiner, W. (1989). "Quantum molecular dynamics a microscopic model from UNILAC to CERN energies". *Nuclear Physics A* *495*(1), 303–319.
- Hatsuda, T. and Kunihiro, T. (1994). "QCD phenomenology based on a chiral effective Lagrangian". *Phys. Rept.* *247*, 221–367.
- Heinz, U. W., Hummel, A., Lisa, M. A., and Wiedemann, U. A. (2002). "Symmetry constraints for the emission angle dependence of HBT radii". *Phys. Rev. C* *66*, 044903.
- Heinz, U. W. and Jacob, M. (2000). "Evidence for a new state of matter: An Assessment of the results from the CERN lead beam program". *arXiv preprint nucl-th/0002042*.
- Heinz, U. W. and Kolb, P. F. (Apr. 2002). "Two RHIC puzzles: Early thermalization and the HBT problem". *18th Winter Workshop on Nuclear Dynamics*.

- Herold, C., Kittiratpattana, A., Kobdaj, C., Limphirat, A., Yan, Y., Nahrgang, M., Steinheimer, J., and Bleicher, M. (2019). “Entropy production and reheating at the chiral phase transition”. *Phys. Lett. B* 790, 557–562.
- Hildenbrand, F. and Hammer, H. -. (2019). “Three-Body Hypernuclei in Pionless Effective Field Theory”. *Phys. Rev. C* 100(3). [Erratum: Phys.Rev.C 102, 039901 (2020)], 034002.
- Hillery, M., O’Connell, R., Scully, M., and Wigner, E. (1984). “Distribution functions in physics: Fundamentals”. *Physics Reports* 106(3), 121–167.
- Hillmann, P., Käfer, K., Steinheimer, J., Vovchenko, V., and Bleicher, M. (2022). “Coalescence, the thermal model and multi-fragmentation: the energy and volume dependence of light nuclei production in heavy ion collisions”. *J. Phys. G* 49(5), 055107.
- Hillmann, P., Steinheimer, J., and Bleicher, M. (2018). “Directed, elliptic and triangular flow of protons in Au+Au reactions at 1.23A GeV: a theoretical analysis of the recent HADES data”. *J. Phys. G* 45(8), 085101.
- Hirano, T., Heinz, U. W., Kharzeev, D., Lacey, R., and Nara, Y. (2006). “Hadronic dissipative effects on elliptic flow in ultrarelativistic heavy-ion collisions”. *Phys. Lett. B* 636, 299–304.
- Hodgson, P. E., Gadioli, E., and Gadioli Erba, E. (1997). *Introductory nuclear physics*. OUP Higher Education Division.
- Hornung, S. (2021). “Understanding the background in dark matter searches by studying antinucleosynthesis in the laboratory with ALICE”. *PoS ICHEP2020*, 634.
- Hou, S. Q., He, J. J., Parikh, A., Kahl, D., Bertulani, C. A., Kajino, T., Mathews, G. J., and Zhao, G. (2017). “Non-extensive Statistics to the Cosmological Lithium Problem”. *Astrophys. J.* 834(2), 165.
- Hung, C. M. and Shuryak, E. V. (1998). “Equation of state, radial flow and freezeout in high-energy heavy ion collisions”. *Phys. Rev. C* 57, 1891–1906.

- Huth, S., Pang, P. T. H., Tews, I., Dietrich, T., Le Fèvre, A., Schwenk, A., Trautmann, W., Agarwal, K., Bulla, M., Coughlin, M. W., and Van Den Broeck, C. (2022). “Constraining Neutron-Star Matter with Microscopic and Macroscopic Collisions”. *Nature* 606, 276–280.
- Iancu, E. (2014). “QCD in heavy ion collisions”. *2011 European School of High-Energy Physics*, 197–266.
- Ibarra, A. and Wild, S. (2013). “Prospects of antideuteron detection from dark matter annihilations or decays at AMS-02 and GAPS”. *JCAP* 02, 021.
- Ivanov, Y. B., Russkikh, V. N., and Toneev, V. D. (2006). “Relativistic heavy-ion collisions within 3-fluid hydrodynamics: Hadronic scenario”. *Phys. Rev. C* 73, 044904.
- Johnson, K. (1975). “The M.I.T. Bag Model”. *Acta Phys. Polon. B* 6, 865.
- Jurič, M., Bohm, G., Klabuhn, J., Krecker, U., Wysotzki, F., Coremans-Bertrand, G., Sacton, J., Wilquet, G., Cantwell, T., Esmael, F., Montwill, A., Davis, D., Kietczewska, D., Pniewski, T., Tymieniecka, T., et al. (1973). “A new determination of the binding-energy values of the light hypernuclei ($A \leq 15$)”. *Nuclear Physics B* 52(1), 1–30.
- Kapusta, J. I. (1980). “Mechanisms for deuteron production in relativistic nuclear collisions”. *Phys. Rev. C* 21, 1301–1310.
- Karsch, F. (2002). “Lattice QCD at high temperature and density”. *Lect. Notes Phys.* 583, 209–249.
- Katscher, U., Rischke, D. H., Maruhn, J. A., Greiner, W., Mishustin, I. N., and Satarov, L. M. (1993). “The Three-dimensional (2+1) fluid model for relativistic nuclear collisions”. *Z. Phys. A* 346, 209–216.
- Kincses, D., Nagy, M. I., and Csanád, M. (2020). “Coulomb and strong interactions in the final state of Hanbury-Brown-Twiss correlations for Lévy-type source functions”. *Phys. Rev. C* 102(6), 064912.

- Kireyeu, V., Steinheimer, J., Aichelin, J., Bleicher, M., and Bratkovskaya, E. (2022). “Deuteron production in ultrarelativistic heavy-ion collisions: A comparison of the coalescence and the minimum spanning tree procedure”. *Phys. Rev. C* 105(4), 044909.
- Kittiratpattana, A., Reichert, T., Buyukcizmeci, N., Botvina, A., Limphirat, A., Herold, C., Steinheimer, J., and Bleicher, M. (2024). “Production of nuclei and hypernuclei in pion-induced reactions near threshold energies”. *Phys. Rev. C* 109(4), 044913.
- Kittiratpattana, A., Reichert, T., Li, P., Limphirat, A., Herold, C., Steinheimer, J., and Bleicher, M. (2023). “Investigating the cluster production mechanism with isospin triggering: Thermal models versus coalescence models”. *Phys. Rev. C* 107(4), 044911.
- Kittiratpattana, A., Reichert, T., Steinheimer, J., Herold, C., Limphirat, A., Yan, Y., and Bleicher, M. (2022). “Correcting the B_A coalescence factor at energies relevant for the GSI-HADES experiment and the RHIC Beam Energy Scan”. *Phys. Rev. C* 106(4), 044905.
- Kittiratpattana, A., Wondrak, M. F., Hamzic, M., Bleicher, M., Herold, C., and Limphirat, A. (2020). “Deuteron and Antideuteron Coalescence in Heavy-Ion Collisions: Energy Dependence of the Formation Geometry”. *Eur. Phys. J. A* 56(10), 274.
- Klevansky, S. P. (1992). “The Nambu-Jona-Lasinio model of quantum chromodynamics”. *Rev. Mod. Phys.* 64, 649–708.
- Knoll, J., Munchow, L., Ropke, G., and Schulz, H. (1982). “Deuteron Production - An Entropy Puzzle?” *Phys. Lett. B* 112, 13–16.
- Knoll, J. (2009). “Continuous Decoupling of Dynamically Expanding Systems”. *Nucl. Phys. A* 821, 235–250.
- Koch, P., Muller, B., and Rafelski, J. (1986). “Strangeness in Relativistic Heavy Ion Collisions”. *Phys. Rept.* 142, 167–262.
- Koch, V. (1997). “Aspects of chiral symmetry”. *Int. J. Mod. Phys. E* 6, 203–250.

- Kolb, P. F. and Heinz, U. (2004). “Hydrodynamic description of ultrarelativistic heavy-ion collisions”. *Quark-Gluon Plasma 3*. World Scientific, 634–714.
- Kopylov, G. I. and Podgoretsky, M. I. (1972). “Correlations of identical particles emitted by highly excited nuclei”. *Sov. J. Nucl. Phys.* 15, 219–223.
- Korsmeier, M., Donato, F., and Fornengo, N. (2018). “Prospects to verify a possible dark matter hint in cosmic antiprotons with antideuterons and antihelium”. *Phys. Rev. D* 97(10), 103011.
- Lacey, R. A. (2015). “Indications for a Critical End Point in the Phase Diagram for Hot and Dense Nuclear Matter”. *Phys. Rev. Lett.* 114(14), 142301.
- Laermann, E. and Philipsen, O. (2003). “The Status of lattice QCD at finite temperature”. *Ann. Rev. Nucl. Part. Sci.* 53, 163–198.
- Letessier, J. and Rafelski, J. (1999). “Chemical nonequilibrium and deconfinement in 200A GeV sulphur induced reactions”. *Phys. Rev. C* 59, 947–954.
- Leupold, S. and Heinz, U. W. (1994). “Coalescence model for deuterons and anti-deuterons in relativistic heavy ion collisions”. *Phys. Rev. C* 50, 1110–1128.
- Li, P., Steinheimer, J., Reichert, T., Kittiratpattana, A., Bleicher, M., and Li, Q. (2023). “Effects of a phase transition on two-pion interferometry in heavy ion collisions at $\sqrt{s_{NN}} = 2.4 - 7.7$ GeV”. *Sci. China Phys. Mech. Astron.* 66(3), 232011.
- Li, Q.-f., Li, Z.-x., Soff, S., Bleicher, M., and Stoecker, H. (2006). “Probing the equation of state with pions”. *J. Phys. G* 32(2), 151–164.
- Linyk, O., Bratkovskaya, E. L., and Cassing, W. (2016). “Effective QCD and transport description of dilepton and photon production in heavy-ion collisions and elementary processes”. *Prog. Part. Nucl. Phys.* 87, 50–115.
- Lisa, M. A., Ajitanand, N. N., Alexander, J. M., Anderson, M., Best, D., Brady, F. P., Case, T., Caskey, W., Cebra, D., Chance, J. L., Chung, P., Cole, B., Crowe, K., Das, A. C., Draper,

- J. E., et al. (2000). “Bombarding energy dependence of pi-minus interferometry at the Brookhaven AGS”. *Phys. Rev. Lett.* *84*, 2798–2802.
- Lisa, M. A., Pratt, S., Soltz, R., and Wiedemann, U. (2005). “Femtoscopy in relativistic heavy ion collisions”. *Ann. Rev. Nucl. Part. Sci.* *55*, 357–402.
- Liu, H., Zhang, D., He, S., Sun, K.-j., Yu, N., and Luo, X. (2020). “Light nuclei production in Au+Au collisions at $\sqrt{s_{NN}} = 5 - 200$ GeV from JAM model”. *Phys. Lett. B* *805*. [Erratum: *Phys.Lett.B* 829, 137132 (2022)], 135452.
- Luo, X. (2016). “Exploring the QCD Phase Structure with Beam Energy Scan in Heavy-ion Collisions”. *Nucl. Phys. A* *956*, 75–82.
- Luo, X. and Xu, N. (2017). “Search for the QCD Critical Point with Fluctuations of Conserved Quantities in Relativistic Heavy-Ion Collisions at RHIC : An Overview”. *Nucl. Sci. Tech.* *28*(8), 112.
- Lyuboshits, V. L. (1988). “Narrow Pair Correlations and Bound State Generation in the Model of One Particle Sources”. *Sov. J. Nucl. Phys.* *48*, 956.
- Ma, Y., Wei, Y., Shen, W., Cai, X., Chen, J., Chen, J., Fang, D., Guo, W., Ma, C., and Ma, G. (2006). “Surveying the nucleon-nucleon momentum correlation function in the framework of quantum molecular dynamics model”. *Phys. Rev. C* *73*, 014604.
- Machleidt, R. and Entem, D. R. (2011). “Chiral effective field theory and nuclear forces”. *Phys. Rept.* *503*, 1–75.
- Malaney, R. A. and Mathews, G. J. (1993). “Probing the early universe: A Review of primordial nucleosynthesis beyond the standard Big Bang”. *Phys. Rept.* *229*, 145–219.
- Matsui, T. and Satz, H. (1986). “ J/ψ Suppression by Quark-Gluon Plasma Formation”. *Phys. Lett. B* *178*, 416–422.

- McLerran, L. D. (1986). “The Physics of the Quark - Gluon Plasma”. *Rev. Mod. Phys.* 58, 1021–1064.
- Meisinger, P. N., Miller, T. R., and Ogilvie, M. C. (2002). “Phenomenological equations of state for the quark gluon plasma”. *Phys. Rev. D* 65, 034009.
- Meisinger, P. N. and Ogilvie, M. C. (1996). “Chiral symmetry restoration and Z(N) symmetry”. *Phys. Lett. B* 379, 163–168.
- Meisinger, P. N., Ogilvie, M. C., and Miller, T. R. (2004). “Gluon quasiparticles and the polyakov loop”. *Phys. Lett. B* 585, 149–154.
- Mihaylov, D. L., Mantovani Sarti, V., Arnold, O. W., Fabbietti, L., Hohlweger, B., and Mathis, A. M. (2018). “A femtosopic Correlation Analysis Tool using the Schrödinger equation (CATS)”. *Eur. Phys. J. C* 78(5), 394.
- Mishra, A. P., Mohapatra, R. K., Saumia, P. S., and Srivastava, A. M. (2008). “Super-horizon fluctuations and acoustic oscillations in relativistic heavy-ion collisions”. *Phys. Rev. C* 77, 064902.
- Mishustin, I. N., Russkikh, V. N., and Satarov, L. M. (1987). “RELATIVISTIC HEAVY ION COLLISIONS WITHIN TWO-FLUID DYNAMICS”. *International Symposium on Multiparticle Dynamics*.
- Mishustin, I. N., Russkikh, V. N., and Satarov, L. M. (1989). “Ultrarelativistic Heavy Ion Collisions Within Two Fluid Model With Pion Emission”. *Nucl. Phys. A* 494, 595–619.
- Mishustin, I. N. and Scavenius, O. (1999). “Chiral fluid dynamics and collapse of vacuum bubbles”. *Phys. Rev. Lett.* 83, 3134–3137.
- Mocsy, A., Sannino, F., and Tuominen, K. (2004). “Confinement versus chiral symmetry”. *Phys. Rev. Lett.* 92, 182302.
- Most, E. R., Motorenko, A., Steinheimer, J., Dexheimer, V., Hanauske, M., Rezzolla, L., and Stoecker, H. (2023). “Probing neutron-star matter in the lab: Similarities

- and differences between binary mergers and heavy-ion collisions”. *Phys. Rev. D* 107(4), 043034.
- Motornenko, A., Steinheimer, J., Vovchenko, V., Schramm, S., and Stoecker, H. (2020). “Equation of state for hot QCD and compact stars from a mean field approach”. *Phys. Rev. C* 101(3), 034904.
- Mrowczynski, S. (1993). “Anti-nucleon sources in heavy ion collisions”. *Phys. Lett. B* 308, 216–219.
- Mrowczynski, S. (1987). “Deuteron formation mechanism”. *J. Phys. G* 13(9), 1089–1097.
- Mrowczynski, S. (1992). “On the neutron proton correlations and deuteron production”. *Phys. Lett. B* 277, 43–48.
- Mrowczynski, S. (1990). “Anti-deuteron Production and the Size of the Interaction Zone”. *Phys. Lett. B* 248, 459–463.
- Mrowczynski, S. (2017). “Production of light nuclei in the thermal and coalescence models”. *Acta Phys. Polon. B* 48, 707.
- Mrowczynski, S. and Slon, P. (2020). “Hadron-Deuteron Correlations and Production of Light Nuclei in Relativistic Heavy-ion Collisions”. *Acta Phys. Polon. B* 51(8), 1739–1755.
- Muller, B., Schukraft, J., and Wyslouch, B. (2012). “First Results from Pb+Pb collisions at the LHC”. *Ann. Rev. Nucl. Part. Sci.* 62, 361–386.
- Nagels, M. M., Rijken, T. A., and Swart, J. J. de (1977). “Baryon Baryon Scattering in a One Boson Exchange Potential Approach. 2. Hyperon-Nucleon Scattering”. *Phys. Rev. D* 15, 2547.
- Nagels, M. M., Rijken, T. A., and Swart, J. J. de (1979). “Baryon Baryon Scattering in a One Boson Exchange Potential Approach. 3. A Nucleon-Nucleon and Hyperon - Nucleon Analysis Including Contributions of a Nonet of Scalar Mesons”. *Phys. Rev. D* 20, 1633.

- Nagle, J. L., Kumar, B. S., Bennett, M. J., Coe, S. D., Diebold, G. E., Pope, J. K., Jahns, A., and Sorge, H. (1994). “Anti-deuteron production in high-energy heavy ion collisions”. *Phys. Rev. Lett.* *73*, 2417–2420.
- Nahrgang, M., Leupold, S., Herold, C., and Bleicher, M. (2011). “Nonequilibrium chiral fluid dynamics including dissipation and noise”. *Phys. Rev. C* *84*, 024912.
- Nambu, Y. and Jona-Lasinio, G. (1961). “Dynamical Model of Elementary Particles Based on an Analogy with Superconductivity. 1.” *Phys. Rev.* *122*, 345–358.
- Nara, Y., Otuka, N., Ohnishi, A., Niita, K., and Chiba, S. (1999). “Relativistic nuclear collisions at 10A GeV energies from p+Be to Au+Au with the hadronic cascade model”. *Phys. Rev. C* *61* (2), 024901.
- Nemura, H., Suzuki, Y., Fujiwara, Y., and Nakamoto, C. (2000). “Study of light Lambda and Lambda-Lambda hypernuclei with the stochastic variational method and effective ΛN potentials”. *Prog. Theor. Phys.* *103*, 929–958.
- Nonaka, C. and Bass, S. A. (2006). “3-D hydro + cascade model at RHIC”. *Nucl. Phys. A* *774*, 873–876.
- Noronha-Hostler, J., Noronha, J., and Gyulassy, M. (2016). “The unreasonable effectiveness of hydrodynamics in heavy ion collisions”. *Nuclear Physics A* *956*, 890–893.
- Oertel, M., Gulminelli, F., Providência, C., and Raduta, A. R. (2016). “Hyperons in neutron stars and supernova cores”. *Eur. Phys. J. A* *52*(3), 50.
- Oh, Y. and Ko, C. M. (2007). “Elliptic flow of deuterons in relativistic heavy-ion collisions”. *Phys. Rev. C* *76*, 054910.
- Oliinychenko, D. (2021). “Overview of light nuclei production in relativistic heavy-ion collisions”. *Nucl. Phys. A* *1005*, 121754.
- Oliinychenko, D., Shen, C., and Koch, V. (2021). “Deuteron production in AuAu collisions at $\sqrt{s_{NN}} = 7 - 200$ GeV via pion catalysis”. *Phys. Rev. C* *103*(3), 034913.

- Ollitrault, J.-Y. (1992). “Anisotropy as a signature of transverse collective flow”. *Phys. Rev. D* 46, 229–245.
- Omana Kuttan, M., Motornenko, A., Steinheimer, J., Stoecker, H., Nara, Y., and Bleicher, M. (2022). “A chiral mean-field equation-of-state in UrQMD: effects on the heavy ion compression stage”. *Eur. Phys. J. C* 82(5), 427.
- Omana Kuttan, M., Steinheimer, J., Zhou, K., and Stoecker, H. (2023). “QCD Equation of State of Dense Nuclear Matter from a Bayesian Analysis of Heavy-Ion Collision Data”. *Phys. Rev. Lett.* 131(20), 202303.
- Ono, A. and Horiuchi, H. (2004). “Antisymmetrized molecular dynamics for heavy ion collisions”. *Progress in Particle and Nuclear Physics* 53(2), 501–581.
- Ono, A., Horiuchi, H., Maruyama, T., and Ohnishi, A. (1992). “Antisymmetrized version of molecular dynamics with two nucleon collisions and its application to heavy ion reactions”. *Prog. Theor. Phys.* 87, 1185–1206.
- Özel, F. and Freire, P. (2016). “Masses, Radii, and the Equation of State of Neutron Stars”. *Ann. Rev. Astron. Astrophys.* 54, 401–440.
- Petersen, H., Steinheimer, J., Baur, G., Bleicher, M., and Stöcker, H. (2008). “A Fully Integrated Transport Approach to Heavy Ion Reactions with an Intermediate Hydrodynamic Stage”. *Phys. Rev. C* 78, 044901.
- Petrán, M., Letessier, J., Petráček, V., and Rafelski, J. (2013). “Hadron production and quark-gluon plasma hadronization in Pb-Pb collisions at $\sqrt{s_{NN}} = 2.76$ TeV”. *Phys. Rev. C* 88(3), 034907.
- Philipsen, O. (2021). “Lattice Constraints on the QCD Chiral Phase Transition at Finite Temperature and Baryon Density”. *Symmetry* 13(11), 2079.
- Philipsen, O. (2006). “The QCD phase diagram at zero and small baryon density”. *PoS LAT2005*, 016.

- Pochodzalla, J. (2005). "Future hypernuclear physics at MAMI-C and PANDA-GSI". *Nucl. Phys. A* 754, 430–442.
- Politzer, H. D. (1973). "Reliable Perturbative Results for Strong Interactions?" *Phys. Rev. Lett.* 30, 1346–1349.
- Pospelov, M. and Pradler, J. (2010). "Big Bang Nucleosynthesis as a Probe of New Physics". *Ann. Rev. Nucl. Part. Sci.* 60, 539–568.
- Pratt, S. (1986). "Pion Interferometry of Quark-Gluon Plasma". *Phys. Rev. D* 33, 1314–1327.
- Pratt, S. (2009). "Resolving the HBT Puzzle in Relativistic Heavy Ion Collision". *Phys. Rev. Lett.* 102, 232301.
- Pratt, S., Sangaline, E., Sorensen, P., and Wang, H. (2015). "Constraining the Eq. of State of Super-Hadronic Matter from Heavy-Ion Collisions". *Phys. Rev. Lett.* 114, 202301.
- Rafelski, J. (1991). "Strange anti-baryons from quark - gluon plasma". *Phys. Lett. B* 262, 333–340.
- Rafelski, J. and Yang, C. T. (2022). "Reactions Governing Strangeness Abundance in Primordial Universe". *EPJ Web Conf.* 259, 13001.
- Ratti, C., Thaler, M. A., and Weise, W. (2006). "Phases of QCD: Lattice thermodynamics and a field theoretical model". *Phys. Rev. D* 73, 014019.
- Reichert, T., Hillmann, P., and Bleicher, M. (2021). " Δ resonances in Ca+Ca, Ni+Ni and Au+Au reactions from 1 AGeV to 2 AGeV: Consistency between yields, mass shifts and decoupling temperatures". *Nucl. Phys. A* 1007, 122058.
- Reichert, T., Hillmann, P., Lymphirat, A., Herold, C., and Bleicher, M. (2019). "Delta mass shift as a thermometer of kinetic decoupling in Au + Au reactions at 1.23 AGeV". *J. Phys. G* 46(10), 105107.

- Reichert, T., Inghirami, G., and Bleicher, M. (2021). “A first estimate of η/s in Au+Au reactions at $E_{\text{lab}} = 1.23A \text{ GeV}$ ”. *Phys. Lett. B* 817, 136285.
- Reichert, T., Inghirami, G., and Bleicher, M. (2020). “Probing chemical freeze-out criteria in relativistic nuclear collisions with coarse grained transport simulations”. *Eur. Phys. J. A* 56(10), 267.
- Reichert, T., Kittiratpattana, A., Li, P., Steinheimer, J., and Bleicher, M. (2023). “Probing system size dependence at high baryon density by systematic comparison of Ag+Ag and Au+Au reactions at 1.23A GeV”. *J. Phys. G* 50(2), 025104.
- Reichert, T., Savchuk, O., Kittiratpattana, A., Li, P., Steinheimer, J., Gorenstein, M., and Bleicher, M. (2023). “Decoding the flow evolution in Au+Au reactions at 1.23A GeV using hadron flow correlations and dileptons”. *Phys. Lett. B* 841, 137947.
- Reichert, T., Steinheimer, J., Herold, C., Limphirat, A., and Bleicher, M. (2022). “Harmonic flow correlations in Au+Au reactions at 1.23A GeV: a new testing ground for the equation-of-state and expansion geometry”. *Eur. Phys. J. C* 82(6), 510.
- Reichert, T., Steinheimer, J., Vovchenko, V., Dönigus, B., and Bleicher, M. (2023a). “Energy dependence of light hypernuclei production in heavy-ion collisions from a coalescence and statistical-thermal model perspective”. *Phys. Rev. C* 107(1), 014912.
- Reichert, T., Steinheimer, J., Vovchenko, V., Dönigus, B., and Bleicher, M. (2023b). “Light hypernuclei in heavy-ion collisions”. *EPJ Web Conf.* 276, 04008.
- Remler, E. A. (1981). “Composite Particle Cross-sections From the Density Operator”. *Annals Phys.* 136, 293.
- Retiere, F. and Lisa, M. A. (2004). “Observable implications of geometrical and dynamical aspects of freeze out in heavy ion collisions”. *Phys. Rev. C* 70, 044907.
- Rischke, D. H. (1999). “Fluid dynamics for relativistic nuclear collisions”. *Lect. Notes Phys.* 516, 21.

- Rischke, D. H., Gorenstein, M. I., Stoecker, H., and Greiner, W. (1991). “Excluded volume effect for the nuclear matter equation of state”. *Z. Phys. C* 51, 485–490.
- Rogochaya, E. P., Acharya, S., Adamová, D., Adhya, S., Adler, A., Adolfsson, J., Aggarwal, M., Aglieri Rinella, G., Agnello, M., Agrawal, N., Ahammed, Z., Ahmad, S., Ahn, S., Aiola, S., Akindinov, A., et al. (Oct. 2017). “Charged kaon femtoscopic correlations in p—Pb collisions at $\sqrt{s_{NN}} = 5.02$ TeV with ALICE at the LHC”. *12th Workshop on Particle Correlations and Femtoscopy*.
- Roland, G. (1994). “Rapidity and transverse momentum dependence of the two pi-correlation function in 200 GeV/nucleon S+A collisions”. *Nucl. Phys. A* 566, 527C–530C.
- Rufa, M., Schaffner, J., Maruhn, J., Stöcker, H., Greiner, W., and Reinhard, P.-G. (1990). “Multi-lambda hypernuclei and the equation of state of hypermatter”. *Phys. Rev. C* 42(6), 2469.
- Sarabura, M., Atherton, H. W., Bøggild, H., Boissevain, J. G., Cherney, M., Chesi, E. G., Dodd, J., Downing, J. N., Fabjan, C. W., Franz, A., Hansen, K. H., Humanic, T. J., Ikemoto, T., Jacak, B. V., Kalechofsky, H., et al. (1992). “Results from CERN experiment NA44”. *Nucl. Phys. A* 544, 125C–136C.
- Sato, H. and Yazaki, K. (1981). “On the coalescence model for high-energy nuclear reactions”. *Phys. Lett. B* 98, 153–157.
- Schaffner-Bielich, J. and Gal, A. (2000). “Properties of strange hadronic matter in bulk and in finite systems”. *Phys. Rev. C* 62, 034311.
- Schenke, B., Jeon, S., and Gale, C. (2011). “Elliptic and triangular flow in event-by-event (3+1)D viscous hydrodynamics”. *Phys. Rev. Lett.* 106, 042301.
- Schmidt, C. (2006). “Lattice QCD at finite density”. *PoS LAT2006*, 021.
- Schnedermann, E., Sollfrank, J., and Heinz, U. W. (1993). “Thermal phenomenology of hadrons from 200A GeV S+S collisions”. *Phys. Rev. C* 48, 2462–2475.

- Šerkšnytė, L., Königstorfer, S., Doetinchem, P. von, Fabbietti, L., Gomez-Coral, D. M., Herms, J., Ibarra, A., Pöschl, T., Shukla, A., and Strong, A. (2022). “Reevaluation of the cosmic antideuteron flux from cosmic-ray interactions and from exotic sources”. *Phys. Rev. D* 105(8), 083021.
- Seyboth, P., Baechler, J., Bartke, J., Bialkowska, H., Bloomer, M., Bock, R., Brockmann, R., Buncic, P., Chase, S., and Cramer, J. (1992). “Recent results from experiment NA35”. *Nucl. Phys. A* 544, 293C–307C.
- Shen, C. and Heinz, U. (2012). “Collision Energy Dependence of Viscous Hydrodynamic Flow in Relativistic Heavy-Ion Collisions”. *Phys. Rev. C* 85. [Erratum: *Phys.Rev.C* 86, 049903 (2012)], 054902.
- Shinmura, S., Akaishi, Y., and Tanaka, H. (1984). “A Study of S-Shell Hypernuclei Based on the Realistic NN AND Λ N Interactions”. *Prog. Theor. Phys.* 71, 546–560.
- Shuryak, E. and Torres-Rincon, J. M. (2020). “Baryon preclustering at the freeze-out of heavy-ion collisions and light-nuclei production”. *Phys. Rev. C* 101(3), 034914.
- Shuryak, E. V. (1999). “New Phases of QCD; the Tricritical Point; and Rhic as a “Nutcracker””. *15th Winter Workshop on Nuclear Dynamics*. Springer, 179–188.
- Shuryak, E. V. (1978). “Quark-Gluon Plasma and Hadronic Production of Leptons, Photons and Psions”. *Phys. Lett. B* 78, 150.
- Shuryak, E. V. (1973). “The Correlation of identical pions in multibody production”. *Phys. Lett. B* 44, 387–389.
- Sinyukov, Y., Lednicky, R., Akkelin, S. V., Pluta, J., and Erazmus, B. (1998). “Coulomb corrections for interferometry analysis of expanding hadron systems”. *Phys. Lett. B* 432, 248–257.
- Skokov, V., Friman, B., and Redlich, K. (2013). “Volume Fluctuations and Higher Order Cumulants of the Net Baryon Number”. *Phys. Rev. C* 88, 034911.

- Soff, S., Bass, S. A., Bleicher, M., Bravina, L., Gorenstein, M., Zabrodin, E., Stoecker, H., and Greiner, W. (1999). “Strangeness enhancement in heavy ion collisions: Evidence for quark gluon matter?” *Phys. Lett. B* 471, 89–96.
- Sombun, S., Steinheimer, J., Herold, C., Limphirat, A., Yan, Y., and Bleicher, M. (2020). “Influence of centrality definition and detector efficiency on the net-proton kurtosis”. *Springer Proc. Phys.* 250, 335–343.
- Sorensen, A., Agarwal, K., Brown, K. W., Chajecki, Z., Danielewicz, P., Drischler, C., Gandolfi, S., Holt, J. W., Kaminski, M., Ko, C.-M., Kumar, R., Li, B.-A., Lynch, W. G., McIntosh, A. B., Newton, W. G., et al. (2024). “Dense nuclear matter equation of state from heavy-ion collisions”. *Prog. Part. Nucl. Phys.* 134, 104080.
- Sorensen, P. (2010a). “Elliptic Flow: A Study of Space-Momentum Correlations In Relativistic Nuclear Collisions”. *Quark-gluon plasma 4*. World Scientific, 323–374.
- Sorensen, P. (2010b). “Implications of space-momentum correlations and geometric fluctuations in heavy-ion collisions”. *J. Phys. G* 37, 094011.
- Spieles, C. and Bleicher, M. (2020). “Effects of the QCD phase transition on hadronic observables in relativistic hydrodynamic simulations of heavy-ion reactions in the FAIR/NICA energy regime”. *Eur. Phys. J. ST* 229(22-23), 3537–3550.
- Staudenmaier, J., Oliinychenko, D., Torres-Rincon, J. M., and Elfner, H. (2021). “Deuteron production in relativistic heavy ion collisions via stochastic multiparticle reactions”. *Phys. Rev. C* 104(3), 034908.
- Steinheimer, J., Bleicher, M., Petersen, H., Schramm, S., Stocker, H., and Zschesche, D. (2008). “(3+1)-dimensional hydrodynamic expansion with a critical point from realistic initial conditions”. *Phys. Rev. C* 77, 034901.
- Steinheimer, J., Botvina, A., and Bleicher, M. (2017). “Sub-threshold charm production in nuclear collisions”. *Phys. Rev. C* 95(1), 014911.

- Steinheimer, J., Nahrgang, M., Gerhard, J., Schramm, S., and Bleicher, M. (2012). “Recent developments on the UrQMD hybrid model”. *Phys. Atom. Nucl.* 75, 759–763.
- Steinheimer, J., Motornenko, A., Sorensen, A., Nara, Y., Koch, V., and Bleicher, M. (2022). “The high-density equation of state in heavy-ion collisions: constraints from proton flow”. *Eur. Phys. J. C* 82(10), 911.
- Steinheimer, J., Wang, Y., Mukherjee, A., Ye, Y., Guo, C., Li, Q., and Stoecker, H. (2018). “Nuclear interactions and net-proton number fluctuations in heavy ion collisions at the SIS18 accelerator”. *Phys. Lett. B* 785, 40–45.
- Stephanov, M. A. (2009). “Non-Gaussian fluctuations near the QCD critical point”. *Phys. Rev. Lett.* 102, 032301.
- Stephanov, M. A. (2006). “QCD phase diagram: An Overview”. *PoS LAT2006*, 024.
- Stephanov, M. A., Rajagopal, K., and Shuryak, E. V. (1999). “Event-by-event fluctuations in heavy ion collisions and the QCD critical point”. *Phys. Rev. D* 60, 114028.
- Sun, K.-J., Chen, L.-W., Ko, C. M., and Xu, Z. (2017). “Probing QCD critical fluctuations from light nuclei production in relativistic heavy-ion collisions”. *Phys. Lett. B* 774, 103–107.
- Sun, K.-J., Ko, C. M., and Dönigus, B. (2019). “Suppression of light nuclei production in collisions of small systems at the Large Hadron Collider”. *Phys. Lett. B* 792, 132–137.
- Teaney, D. A. (2010). “Viscous Hydrodynamics and the Quark Gluon Plasma”. *Quark-gluon plasma 4*. World Scientific, 207–266.
- Tolos, L. and Fabbietti, L. (2020). “Strangeness in Nuclei and Neutron Stars”. *Prog. Part. Nucl. Phys.* 112, 103770.
- Vidaña, I. (2018). “Hyperons: the strange ingredients of the nuclear equation of state”. *Proc. Roy. Soc. Lond. A* 474, 0145.

- Vogl, U. and Weise, W. (1991). “The Nambu and Jona Lasinio model: Its implications for hadrons and nuclei”. *Prog. Part. Nucl. Phys.* 27, 195–272.
- Von Doetinchem, P., Perez, K., Aramaki, T., Baker, S., Barwick, S., Bird, R., Boezio, M., Boggs, S., Cui, M., Datta, A., Donato, F., Evoli, C., Fabris, L., Fabbietti, L., Bueno, E. F., et al. (2020). “Cosmic-ray antinuclei as messengers of new physics: status and outlook for the new decade”. *JCAP* 08, 035.
- Vovchenko, V., Anchishkin, D. V., and Gorenstein, M. I. (2015). “Van der Waals Equation of State with Fermi Statistics for Nuclear Matter”. *Phys. Rev. C* 91(6), 064314.
- Vovchenko, V., Begun, V. V., and Gorenstein, M. I. (2016). “Hadron multiplicities and chemical freeze-out conditions in proton-proton and nucleus-nucleus collisions”. *Phys. Rev. C* 93(6), 064906.
- Vovchenko, V., Dönigus, B., Kardan, B., Lorenz, M., and Stoecker, H. (2020). “Feeddown contributions from unstable nuclei in relativistic heavy-ion collisions”. *Phys. Lett. B*, 135746.
- Vovchenko, V., Dönigus, B., and Stoecker, H. (2018). “Multiplicity dependence of light nuclei production at LHC energies in the canonical statistical model”. *Phys. Lett. B* 785, 171–174.
- Vovchenko, V., Gorenstein, M. I., and Stoecker, H. (2017). “van der Waals Interactions in Hadron Resonance Gas: From Nuclear Matter to Lattice QCD”. *Phys. Rev. Lett.* 118(18), 182301.
- Vovchenko, V., Motornenko, A., Alba, P., Gorenstein, M. I., Satarov, L. M., and Stoecker, H. (2017). “Multicomponent van der Waals equation of state: Applications in nuclear and hadronic physics”. *Phys. Rev. C* 96(4), 045202.
- Vovchenko, V., Steinheimer, J., Philipsen, O., and Stoecker, H. (2018). “Cluster Expansion Model for QCD Baryon Number Fluctuations: No Phase Transition at $\mu_B/T < \pi$ ”. *Phys. Rev. D* 97(11), 114030.

- Vovchenko, V. and Stoecker, H. (2019). “Thermal-FIST: A package for heavy-ion collisions and hadronic equation of state”. *Comput. Phys. Commun.* 244, 295–310.
- Wang, S., Albergo, S., Bieser, F., Brady, F., Caccia, Z., Cebra, D., Chacon, A., Chance, J., Choi, Y., and Costa, S. (1995). “Light fragment production and power law behavior in Au + Au collisions”. *Phys. Rev. Lett.* 74, 2646–2649.
- Weber, F. (2005). “Strange quark matter and compact stars”. *Prog. Part. Nucl. Phys.* 54, 193–288.
- Weil, J., Steinberg, V., Staudenmaier, J., Pang, L. G., Oliinychenko, D., Mohs, J., Kretz, M., Kehrenberg, T., Goldschmidt, A., Bäuchle, B., Auvinen, J., Attems, M., and Petersen, H. (2016). “Particle production and equilibrium properties within a new hadron transport approach for heavy-ion collisions”. *Phys. Rev. C* 94 (5), 054905.
- Weiner, R. M. (2000). “Boson interferometry in high-energy physics”. *Phys. Rept.* 327, 249–346.
- Werner, K., Karpenko, I., Pierog, T., Bleicher, M., and Mikhailov, K. (2010). “Event-by-Event Simulation of the Three-Dimensional Hydrodynamic Evolution from Flux Tube Initial Conditions in Ultrarelativistic Heavy Ion Collisions”. *Phys. Rev. C* 82, 044904.
- Wiedemann, U. A. (2010). “Jet Quenching in Heavy Ion Collisions”. *arXiv preprint arXiv:0908.2306*, 521–562.
- Wiedemann, U. A. and Heinz, U. W. (1999). “Particle interferometry for relativistic heavy ion collisions”. *Phys. Rept.* 319, 145–230.
- Wolter, H., Colonna, M., Cozma, D., Danielewicz, P., Ko, C. M., Kumar, R., Ono, A., Tsang, M. B., Xu, J., Zhang, Y.-X., Bratkovskaya, E., Feng, Z.-Q., Gaitanos, T., Ikeno, N., Kim, Y., et al. (2022). “Transport model comparison studies of intermediate-energy heavy-ion collisions”. *Prog. Part. Nucl. Phys.* 125, 103962.
- Wong, C.-Y. (1982). “Dynamics of nuclear fluid. VIII. Time-dependent Hartree-Fock approximation from a classical point of view”. *Phys. Rev. C* 25, 1460–1475.

- Wong, C., Maruhn, J., and Welton, T. (1975). “Dynamics of nuclear fluid:(l). Foundation”. *Nuclear Physics A* 253(2), 469–489.
- Xu, J. (2019). “Transport approaches for the description of intermediate-energy heavy-ion collisions”. *Prog. Part. Nucl. Phys.* 106, 312–359.
- Yagi, K., Hatsuda, T., and Miake, Y. (2005). *Quark-gluon plasma: From big bang to little bang*. Vol. 23. Cambridge University Press.
- Yang, J.-M., Turner, M. S., Steigman, G., Schramm, D. N., and Olive, K. A. (1984). “Primordial Nucleosynthesis: A Critical Comparison of Theory and Observation”. *Astrophys. J.* 281, 493–511.
- Yano, F. B. and Koonin, S. E. (1978). “Determining Pion Source Parameters in Relativistic Heavy Ion Collisions”. *Phys. Lett. B* 78, 556–559.
- Yassine, R. A., Adamczewski-Musch, J., Arnold, O., Atomssa, E. T., Becker, M., Behnke, C., Berger-Chen, J. C., Blanco, A., Blume, C., Böhmer, M., Chlad, L., Chudoba, P., Ciepala, I., Deveaux, C., Dittert, D., et al. (2024). “Hadron production and propagation in pion-induced reactions on nuclei”. *The European Physical Journal A* 60(7), 156.
- Ye, Y., Wang, Y., Li, Q., Lu, D., and Wang, F. (2020). “Beam energy dependence of cumulants of the net-baryon, net-charge, and deuteron multiplicity distributions in Au+Au collisions at $\sqrt{s_{NN}} = 3.0 - 5.0$ GeV”. *Phys. Rev. C* 101(3), 034915.
- Yen, G. D. and Gorenstein, M. I. (1999). “The Analysis of particle multiplicities in Pb + Pb collisions at CERN SPS within hadron gas models”. *Phys. Rev. C* 59, 2788–2791.
- Yen, G. D., Gorenstein, M. I., Greiner, W., and Yang, S.-N. (1997). “Excluded volume hadron gas model for particle number ratios in A+A collisions”. *Phys. Rev. C* 56, 2210–2218.
- Zhaba, V. I. (2017). “Deuteron: properties and analytical forms of wave function in coordinate space”. *arXiv preprint arXiv:1706.08306*.

Zhu, L., Ko, C. M., and Yin, X. (2015). "Light (anti-)nuclei production and flow in relativistic heavy-ion collisions". *Phys. Rev. C* 92(6), 064911.



CURRICULUM VITAE

- Name** : Mr. Apiwit Kittiratpattana
- Date of Birth** : February 24, 1996
- Place of Birth** : Nakhon Ratchasima, Thailand
- Education** :
- 2021 - 2024 Doctor of Philosophy (Cotutelle Program),
Goethe University Frankfurt, Germany with
Suranaree University of Technology, Thailand
Advisors: Marcus Bleicher and Christoph Herold
- 2018 - 2021 Master of Science, Suranaree University of Technology
Advisor: Christoph Herold
- 2014 - 2018 Bachelor of Science, Suranaree University of Technology
Advisor: Christoph Herold
- Awards & Honors** :
- 2014 - 2024 DPST (Development and Promotion of Science and Technology
Talents Project, Thai government scholarship)
- 2023 - 2024 HGS-HiRe for FAIR (The Helmholtz Graduate School for Hadron
and Ion Research)
- Publications** :
1. Reichert, T., Savchuk, O., **Kittiratpattana, A.** et al. (2023). *Physics Letters B*, 841, 137947.
 2. **Kittiratpattana, A.** et al. (2023). *Physical Review C*, 107(4), 044911.
 3. Li, P., Steinheimer, J., Reichert, T., **Kittiratpattana, A.** et al. (2023). *Science China Physics, Mechanics & Astronomy*, 66(3), 232011.
 4. Reichert, T., **Kittiratpattana, A.** et al. (2023). *Journal of Physics G: Nuclear and Particle Physics*, 50(2), 025104.
 5. **Kittiratpattana, A.** et al. (2022). *Physical Review C*, 106(4), 044905.
 6. **Kittiratpattana, A.** et al. (2020). *The European Physical Journal A*, 56(10), 274.
 7. Herold, C., **Kittiratpattana, A.** et al. (2019). *Physics Letters B*, 790, 557-562.